Measurement back action and feedback in superconducting circuits

Philippe Campagne-Ibarcq

Cette thèse décrit une série d'expériences mettant en lumière l'***action en retour*** de la mesure et la ***décohérence*** pour un système quantique ouvert élémentaire, le ***qubit supraconducteur***. Ces observations sont rendues possibles grâce au développement récent d'***amplificateurs Josephson*** proches de la limite quantique. L'information extraite du système peut être utilisée dans des boucles de ***rétroaction quantique***.

Pour stabiliser un état arbitraire prédéterminé du qubit, une mesure projective est réalisée périodiquement et une boucle de rétroaction permet de corriger les erreurs détectées.

En se substituant à l'environnement et en réalisant une mesure hétérodyne continue de la fluorescence du qubit, nous reconstituons des ***trajectoires quantiques*** individuelles lors de sa relaxation.

En conditionnant cette détection au résultat d'une mesure projective postérieure, nous déterminons les ***weak values*** du signal de fluorescence.

En formant une boucle de rétroaction continue à partir de ce signal, nous stabilisons également un état arbitraire du qubit.

Enfin, nous observons dans une dernière expérience la ***dynamique quantique Zénon*** d'un mode micro-onde, induite par son couplage au qubit.

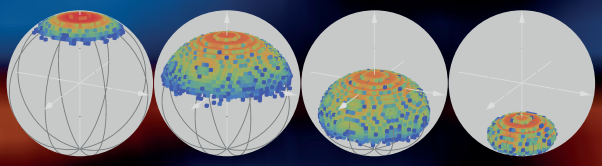

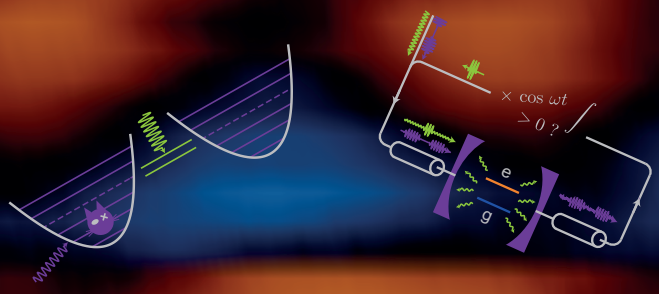

Measurement back action and feedback in superconducting circuits

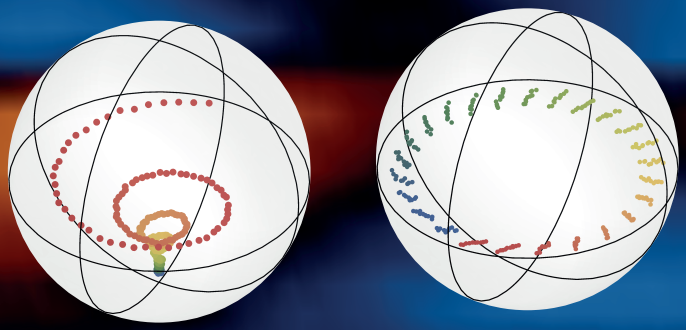

This thesis presents a series of experiments highlighting measurement ***back action*** and ***decoherence*** in a basic open quantum system, the ***superconducting qubit***. These observations are enabled by recent advances in amplification close to the quantum limit using ***Josephson circuits***. The information extracted from the system can then be used as input in ***quantum feedback***.

A stroboscopic projective readout is performed and a feedback loop is used to correct for detected errors, thus stabilizing an arbitrary predetermined state of the qubit.

When monitoring continuously the environment of the qubit by heterodyne detection of its fluorescence, we reconstruct individual ***quantum trajectories*** during relaxation.

Conditioning this detection to the outcome of a following projective measurement, we access the ***weak values*** of the fluorescence signal.

Included in a continuous feedback loop, this detection is also used to stabilize an arbitrary state of the qubit.

Finally, a last experiment witnesses ***quantum Zeno dynamics*** of a resonant microwave mode, entailed by its coupling to the qubit.

Philippe Campagne-Ibarcq
Quantum Electronics Group
LPA-ENS Paris

Département de Physique
École Normale Supérieure

Laboratoire Pierre Aigrain

THÈSE de DOCTORAT

Spécialité : Physique Quantique

Measurement back action and feedback in superconducting circuits

---

présentée par

Philippe Campagne-Ibarcq

pour obtenir le grade de docteur de l'École Normale Supérieure

sous la direction de Benjamin Huard et de Michel Devoret

Soutenue le 26 Juin 2015

Devant le jury composé de :

Leonardo	**Di Carlo**	Rapporteur
Steven	**Girvin**	Rapporteur
John	**Martinis**	Examinateur
Jean-Michel	**Raimond**	Examinateur
Denis	**Vion**	Examinateur
Benjamin	**Huard**	Directeur de thèse
Michel	**Devoret**	Co-directeur de thèse

ABSTRACT

In quantum physics, a measurement corresponds to the interaction of a system with an observer, who is part of its environment. In general, this measurement disturbs the state of the system in a an effect known as the quantum back action. This perturbation is stochastic and cannot be predicted a priori. However, if the observer efficiently extracts the information from the measurement, he can know about the back action a posteriori, and thus keep track of the system's evolution.
As flexible quantum machines, whose collective behavior follows the laws of quantum physics, superconducting circuits are promising systems to investigate this subject. A particular superconducting qubit, the 3D transmon, reaches coherence times over 100 microseconds. Combined with the development of near quantum limited parametric amplifiers, also based on superconducting circuits, it is possible to coherently control, measure and react on a 3D transmon before it loses its coherence.
In this thesis, we describe several experiments performing such tasks on a 3D transmon. In particular, a stroboscopic and non demolition measurement with high fidelity in a single shot is used in a feedback loop to stabilize an arbitrary state of the qubit. In another experiment, the fluorescence signal of the qubit is used to track its state during a single relaxation event. This signal is also used to implement continuous analog feedback, again to stabilize an arbitrary state of the qubit. When averaged conditionally to a final projective measurement outcome, the fluorescence signal displays weak values out of range for unconditional average. Last, the qubit is used as an auxiliary system to induce Zeno dynamics of an electromagnetic mode of a resonant cavity with which it is coupled.

ACKNOWLEDGEMENTS

Quand je considère ces années de thèse au sein de l'équipe *Electronique quantique*, je m'estime extrêmement chanceux. Sur le plan scientifique, chaque projet auquel j'ai participé m'a permis d'aborder un nouvel aspect de la théorie quantique, toujours plus passionnant et stimulant. Par ailleurs, l'atmosphère particulière de ce groupe où tout le monde travaille dans la même salle est propice aux échanges, et la compréhension des sujets les plus complexes devient un jeu. Toutes les personnes avec qui j'ai travaillé ont ainsi contribué à rendre ces années fantastiques, aussi bien dans le laboratoire qu'en dehors.

Pour tout cela, je tiens avant tout à remercier Benjamin Huard. Merci pour m'avoir fait confiance en me prenant en thèse alors que je ne connaissais pas le moindre de ces instruments qui s'entassaient sur le rack, ni même ce qu'était un rack. Ta patience, ta disponibilité et ta maîtrise aussi bien des aspects théoriques les plus complexes que des raccords du circuit de refroidissement des cryostats m'ont permis de progresser très rapidement et continueront de m'inspirer. La liberté que tu m'a laissée dans l'orientation des projets doublée de conseils avisés et d'enthousiasme dans les moments difficiles m'a, je pense, donné le meilleur départ possible pour une carrière de physicien.

Merci à François Mallet pour son encadrement dès les premiers moments de ma thèse. En travaillant à plein temps avec toi sur mon premier projet, j'ai acquis non seulement de grandes connaissances, mais surtout les méthodes de travail qui ont fait de moi un expérimentateur.

Merci à Michel Devoret pour les discussions toujours extrêmement enrichissantes que nous avons eues et pour ses réponses éclairantes sur les sujets les plus complexes.

Merci à Nicolas Roch, Jean-Damien Pillet, Landry Bretheau et Sébastien Jézouin, les post-docs qui se sont succédés au laboratoire et qui ont rivalisé de compétence, d'efforts pour expliquer les théories ou techniques expérimentales les plus variées, de disponibilité pour des discussions fructueuses, et d'humour pour tous les moments de la journée et bien souvent de la soirée.

Merci à mes co-thésards Emmanuel Flurin, Danijela Markovic et Igor Ferrier-Barbut pour leur soutien, leur aide et leurs conseils immanquablement offerts, et pour les interminables discussions à propos de physique ou de tout autre sujet, au laboratoire ou autour d'une pinte-frites à la Montagne.

Merci à tous les stagiaires avec qui j'ai eu la chance de travailler, et en particulier Quentin Ficheux, Nathanaël Cottet et Théau Peronnin qui assurent désormais la relève.

I also thank Vladimir Manucharyan for his efforts in introducing me to fluxonium theory and fabrication, and all the great discussions we have had.

Un grand merci aux théoriciens avec qui j'ai collaboré, Alexia Auffèves, Pierre Rouchon, Mazyar Mirrahimi et Alain Sarlette, ainsi qu'à leurs doctorants. A leur contact j'ai fini par comprendre et même apprécier le formalisme des *Past quantum states* et des équations stochastiques maîtresses.

Je souhaite aussi remercier tous les membres du laboratoire Pierre Aigrain et des ser-

vices du département de physique de l'ENS. En particulier, merci à Pascal Morfin pour son aide lors de l'assemblage et la mise en route du cryostat, à David Darson pour la programmation de la carte FPGA et à Michaël Rosticher pour ses conseils et son encadrement en salle blanche. Merci à toute l'équipe HQC pour leur accueil et les bons moments autour de la machine à café.
Merci à mes colocataires et à ma famille pour leur soutien durant la rédaction du manuscrit.
Finally I thank all the members of the defense committee for accepting the position and for carefully reviewing the manuscript.

CONTENTS

1 INTRODUCTION 1
1.1 Monitored qubit 2
1.1.1 Qubit coupled to an environment 2
1.1.2 Prediction from past measurements 4
1.1.3 Influence of post-selection 6
1.2 Quantum feedback 8
1.2.1 Measurement-based feedback and reservoir engineering 9
1.2.2 Quantum Zeno Dynamics 11

i OPEN SYSTEM AND QUANTUM TRAJECTORIES 13

2 OPEN QUBIT 15
2.1 Quantum Bit of Information : the simplest quantum system 15
2.1.1 TLS representation 15
2.1.2 Entropy 16
2.1.3 Lindblad Master Equation 17
2.1.3.1 Quantum operations 17
2.1.3.2 Continuous time evolution 19
2.2 3D transmon 21
2.2.1 Resonant cavity and LC resonator 21
2.2.2 3D cavity coupled to transmission lines 23
2.2.2.1 Lossy resonators 23
2.2.2.2 Master equation for a cavity mode 25
2.2.2.3 Choosing the coupling to the lines 25
2.2.3 Transmon qubit in 3D cavity 27
2.2.3.1 Transmon regime 27
2.2.3.2 Circuit Black Box Quantization 30
2.2.3.3 Designing the experiment: BBQ VS two-mode model 32
2.2.4 AC Stark shift and measurement induced dephasing 37
2.2.5 Other decoherence channels and thermal effects 40

3 MEASUREMENT AND QUANTUM TRAJECTORIES 45
3.1 Stochastic Master Equations 45
3.1.1 Measurement efficiency - discussion based on the Stern and Gerlach experiment 45
3.1.2 SME with a jump detector 47
3.2 Dispersive measurement 49
3.2.1 Linear detection 49
3.2.2 Homodyne detection 51
3.2.3 Heterodyne measurement 55
3.2.3.1 Single-shot Non Demolition readout 56
3.2.3.2 Quantum jumps 59
3.3 High-power readout 60

3.4 Monitoring the fluorescence 62
3.4.1 Mean fluorescence signal 64
3.4.2 Quantum trajectories for fluorescence 68
3.4.2.1 Integrable quantity for measurement records 70
3.4.2.2 From measurement record to trajectory 72
3.4.2.3 Particle filtering for the estimation of η 75
3.4.2.4 Trajectories statistics 77
4 POST-SELECTED QUANTUM TRAJECTORIES 81
4.1 Past quantum state 82
4.1.1 Discrete time version 82
4.1.2 Continuous time version 84
4.2 Weak values of the fluorescence signal 88
4.2.1 Master equation 88
4.2.2 Post-selected fluorescence traces 91
4.2.3 Pre and post-selected fluorescence traces 92
4.2.4 Time asymmetry for a dissipative system 96
4.3 Conclusion 100
ii QUANTUM CONTROL 103
5 MEASUREMENT BASED FEEDBACK 107
5.1 Stroboscopic digital feedback using dispersive measurement 107
5.1.1 Feedback loop 107
5.1.2 Qubit reset 110
5.1.3 Rabi oscillations 112
5.1.4 Ramsey oscillations 116
5.2 Continuous analog feedback using the fluorescence signal 117
5.2.1 Effective master equation in presence of feedback 118
5.2.1.1 SISO Markovian feedback with diffusive measurements 118
5.2.1.2 MIMO Markovian feedback and arbitrary state stabilization 120
5.2.2 Experimental implementation 122
5.2.2.1 Stabilization of $|e\rangle$ 122
5.2.2.2 Arbitrary state stabilization 125
6 RESERVOIR ENGINEERING 129
6.1 Double Drive Reset of Population 129
6.1.1 Principle and limits 129
6.1.2 Heating up the transmon 131
6.1.3 Cooling performances 133
6.2 Autonomous feedback versus MBF 136
6.2.1 Swap reset 136
6.2.2 Engineering dissipation with continuous feedback 138
7 QUANTUM ZENO DYNAMICS 141
7.1 Zeno dynamics of a microwave mode 141
7.1.1 Zeno dynamics by repeated measurements 141
7.1.2 Zeno dynamics by strong coherent driving 142

7.1.2.1 Phase randomization 142
7.1.2.2 Zeno dynamics using an ancillary system 143
7.2 Oscillations in levels occupation for a driven N-level system 147
7.2.1 Fock states occupation for a coherent field 147
7.2.2 Fock state occupation for a field under QZD 150
7.3 Wigner tomography 153
7.3.1 Photon parity measurement 154
7.3.2 Wigner function of a field under QZD 156
7.3.3 A tailorable infinite Hilbert space? 159
7.4 Conclusion 160

iii APPENDIX 163

A EXPERIMENTAL TECHNIQUES 165
A.1 Qubits fabrication and characterization 165
A.1.1 Nanofabrication 167
A.1.2 Wafer probing 169
A.1.3 Cavity machining and surface treatment 170
A.2 Wiring and cryogenics 171
A.2.1 Wiring the dilution refrigerator 171
A.2.2 Room temperature pulse generation and measurement setup 172
A.3 Electromagnetic simulations 177

B QUANTUM CIRCUITS 181
B.1 Capacitively coupled transmission line 181
B.2 Input output formalism 182

C STOCHASTIC MASTER EQUATIONS FOR DISPERSIVE MEASUREMENT 187
C.1 Jump operators for detection with a photocounter 187
C.2 Derivation of the SME for homodyne detection 188

iv BIBLIOGRAPHY 193

BIBLIOGRAPHY 195

1 INTRODUCTION

The state of a closed quantum system evolves in a deterministic and reversible manner. Physically, this state constitutes a description of the statistics of outcomes for any following measurement on the system. In the Copenhagen interpretation, a measurement irreversibly projects, or *collapses*, the wavefunction onto a particular set of states. A paradox then arises when considering the measurement apparatus as part of the system itself, so that the global evolution should be reversible. About these issues, Bell and Nauenberg considered in 1966 that "the typical physicist feels that they have been long answered, and that he will fully understand just how, if ever he can spare twenty minutes to think about it." Yet, this paradox has since fueled heated debates, and interpretations such as many worlds theory [1] or the more recent work on Quantum Darwinism [2].

Already that same year, Daneri *et al.* [3, 4] argued that the measurement problem is key to understanding the boundary between the classical and quantum worlds. Their claim that one has to take into account the *macroscopicity* of the measurement apparatus is the starting point of modern decoherence theory. Fully quantum behavior is usually observed in systems containing only a small number of degrees of freedom. The irreversible evolution during a measurement comes from the difficulty to monitor a great number of auxiliary degrees of freedom, or *ancillas*, on which information on the system has been imprinted through reversible evolution in interaction. Dismissing the information thus carried away effectively induces a collapse toward the *pointer states*, which are immune to distant operations on the ancillas[1].

In the past decades, experiments using various systems have succeeded in decomposing the information extraction process [6, 7, 8], which now plays a central role in attempts to axiomatize the quantum theory [9, 5]. As flexible *quantum machines*, whose collective behavior follows the laws of quantum physics, superconducting circuits [10] are promising systems to investigate further these issues. The rapid improvement of their coherence times combined with efficient detectors now allows to recover a large fraction of the information leaking out from such a system through controlled dissipation or dephasing channels [11], and to feed it back before it looses its coherence.

In this thesis, we describe experiments performed on a particular superconducting circuit, the *transmon* [12]. When cooled down at dilution refrigerator base temperature, it behaves as an anharmonic resonator that, properly addressed with microwave radiations, implements a controllable *quantum bit*. It is enclosed in an off-resonant 3 dimensional microwave cavity [13] probed via transmission lines, which provide a con-

1 more precisely the states that are stable under local operations that can be unmade by action on the distant ancillas [5].

trolled and monitored environment for the qubit. In these conditions, the transmon is a good test-bed to investigate quantum measurement and feedback. In particular, the dynamics of an open quantum system is analyzed in the situation where the main relaxation and dephasing channels are efficiently monitored. Combined with single-shot readout schemes, we study the effect of post-selection on these dynamics. The extracted information is also used via a feedback loops to stabilize arbitrary states and to effectively engineer dissipation.

1.1 MONITORED QUBIT

1.1.1 *Qubit coupled to an environment*

The system used in the experiments described throughout this thesis follows the design of the 3D transmon [12, 13]. It consists in a Josephson junction (JJ) linking two antennas. The JJ behaves as a non linear inductor and the antennas form a large shunting capacitance so that this circuit is a weakly anharmonic oscillator. Its resonance frequency is in the GHz range and it thus needs to be cooled down at dilution refrigerator base temperature to be used for quantum information experiments. Via the antennas, this circuit couples to the electromagnetic field so that it can be controlled with microwave radiations. Its energy levels are not evenly spaced and, if addressing only the transition at ω_q between the ground state $|g\rangle$ and the first excited state $|e\rangle$, it forms an effective qubit whose hamiltonian reads $H_q = \hbar\omega_q \frac{\sigma_Z}{2}$.

This circuit is fabricated on a sapphire chip, enclosed in a 3 dimensional resonant cavity of high quality factor (see Fig. 10a). The electromagnetic modes of the cavity can be modeled as harmonic oscillators. They are coupled to semi infinite transmission lines via 2 ports, whose coupling rates can be tuned over a wide range. In the experiment, one of the ports, called the *output* port has a much larger coupling rate than the other one and than the cavity internal losses. Thus, the leak through this output port dominates the damping of the cavity modes photons and the qubit radiative decay. The cavity dimensions were chosen so that its first mode resonates at $\omega_r = \omega_q + \Delta$, above the qubit transition. Its hamiltonian reads $H_r = \hbar\omega_r a^\dagger a$, where a is the photon annihilation operator.

The detuning Δ is far larger than the coupling between this mode and the qubit via the antennas. It is thus in the *dispersive regime* and the total system hamiltonian reads

$$\boxed{H = \hbar\omega_r a^\dagger a + \hbar\omega_q \frac{\sigma_Z}{2} - \hbar\frac{\chi}{2}\sigma_Z a^\dagger a}, \tag{1}$$

where we neglected the other modes of the cavity, farther detuned, and the higher order terms in $a^\dagger a$. The dispersive shift χ makes the cavity resonance frequency dependent of the qubit state. Probing the cavity in transmission then provides a measurement scheme of the σ_Z operator of the qubit. If the information carried by this transmitted signal is dismissed, it leads to dephasing of the qubit at rate Γ_d, proportional to the

probe power [11].

Another role of the cavity is to control the electromagnetic environment of the qubit [14]. In particular, the noise power at ω_q is filtered by the off resonant cavity. As a result, the relaxation rate γ_1 of the qubit is considerably lowered, enabling us to coherently manipulate it much faster than its lifetime. In the Purcell limit [15, 16, 17], this rate is dominated by the relaxation into the modes of the output line, where fluorescence can be detected.

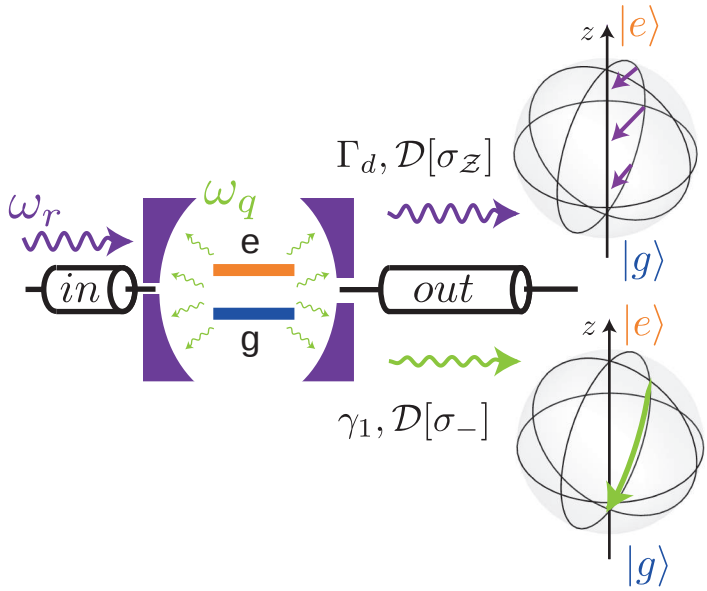

Figure 1: Schematic representation of the qubit in the 3 dimensional cavity. The output port couples with a high rate the first mode of the cavity to the output line. It is used to channel the fluorescence field of the qubit (in green, at ω_q) and the transmitted signal at cavity resonance frequency which comes from the input port (in purple, at ω_r). If dismissed, the information and energy contained in these fields leaking out of the system leads to relaxation at a rate γ_1 (collapse of the state toward $|g\rangle$) and dephasing with rate Γ_d that scales with the input field power (collapse of the state on the z-axis of the Bloch sphere).

When considering the qubit as the system, and the cavity and the lines as its environment, it implements a two-level system in presence of a dephasing and a relaxation channel [18] as schematized on Fig. 1b. The system dynamics is governed by the *Lindblad Master Equation* reading

$$\boxed{\frac{\mathrm{d}\rho}{\mathrm{d}t} = -\frac{i}{\hbar}[H_q, \rho] + \gamma_1 \mathcal{D}[\sigma_-]\rho + \frac{\Gamma_d}{2}\mathcal{D}[\sigma_Z]\rho}, \tag{2}$$

where the damping super-operator $\mathcal{D}$ is defined by

$$\mathcal{D}[L]\rho = L\rho L^\dagger - \frac{1}{2}L^\dagger L\rho - \frac{1}{2}\rho L^\dagger L. \tag{3}$$

These rates can be increased by other uncontrolled processes (non radiative decay, pure dephasing). For a qubit at finite temperature, a third channel associated with

the σ_+ operator is opened. Note that in H_q, the qubit frequency is now dressed by its hybridization with the cavity mode and depends on its occupation (AC Stark shift).

These channels ultimately lead to the erasure of the information initially encoded by the qubit and constitute a limit to quantum information processing. However, if one monitors efficiently these channels, the qubit state can be followed in time so that its purity remains of order 1.

1.1.2 *Prediction from past measurements*

The damping terms in Eq. (2) originate from the coupling between the qubit and the *bath* of traveling modes in the probe lines[2]. Over a time-step longer than the bath auto-correlation time, they can be modeled as a series of unread *generalized measurements* involving these modes as ancillas [18]. In order to retrieve the information contained in the ancillas, we detect the output field from the cavity.

We place on the output line a phase preserving parametric amplifier, the Josephson Parametric Converter (JPC) [19, 20]. The JPC performs *heterodyne detection* of the field on a finite amplification bandwidth. It has been showed to work near the quantum limit, so that if the signal that we want to detect is properly collected and transmitted to its input, the detection efficiency η is of order 1. The experiments described in this thesis use two types of detection, depending on the measured frequency range.

When the JPC is tuned at the cavity frequency, it is used to detect the transmitted field at ω_r, shifted by the dispersive interaction with the qubit (see Eq. (1)). The two measured signals, called the *measurement records*, integrated over a time step $\mathrm{d}t$, read [21]

$$\begin{cases} \mathrm{d}I &= i_0 \mathrm{d}t + \mathrm{d}W_{t,I} \\ \mathrm{d}Q &= \sqrt{\Gamma_m}\langle\sigma_Z\rangle \mathrm{d}t + \mathrm{d}W_{t,Q} \end{cases}, \tag{4}$$

where i_0 is a constant depending on the system parameters that will be detailed in Sec. 3.2.3, and $W_{t,I,Q}$ are independent Wiener processes, or *idealized random walks*, verifying

$$\begin{cases} \overline{\mathrm{d}W_t} &= 0 \\ \mathrm{d}W_t^2 &= \mathrm{d}t \end{cases}. \tag{5}$$

The measurement is thus noisy when integrated on a finite time step. This noise ultimately originates from the quantum fluctuations of the detected field. Γ_m is the total measurement rate. It defines the time scale on which the measurement can discriminate between the two states of the qubit[3]. One can show that $\Gamma_m = \eta\Gamma_d$ [11], so that for perfect measurement efficiency, no information is lost and the observer acquires information as fast as the dephasing induced by the measurement. For finite efficiency, one

2 In the case of the dephasing term, the coupling is mediated by the cavity mode

3 With this convention, the same measurement rate requires to integrate the signal twice longer to discriminate between $|g\rangle$ and $|e\rangle$ compared to homodyne detection.

needs to integrate further the readout signal after that the qubit has been projected by measurement in order to get a good readout fidelity in a single shot.

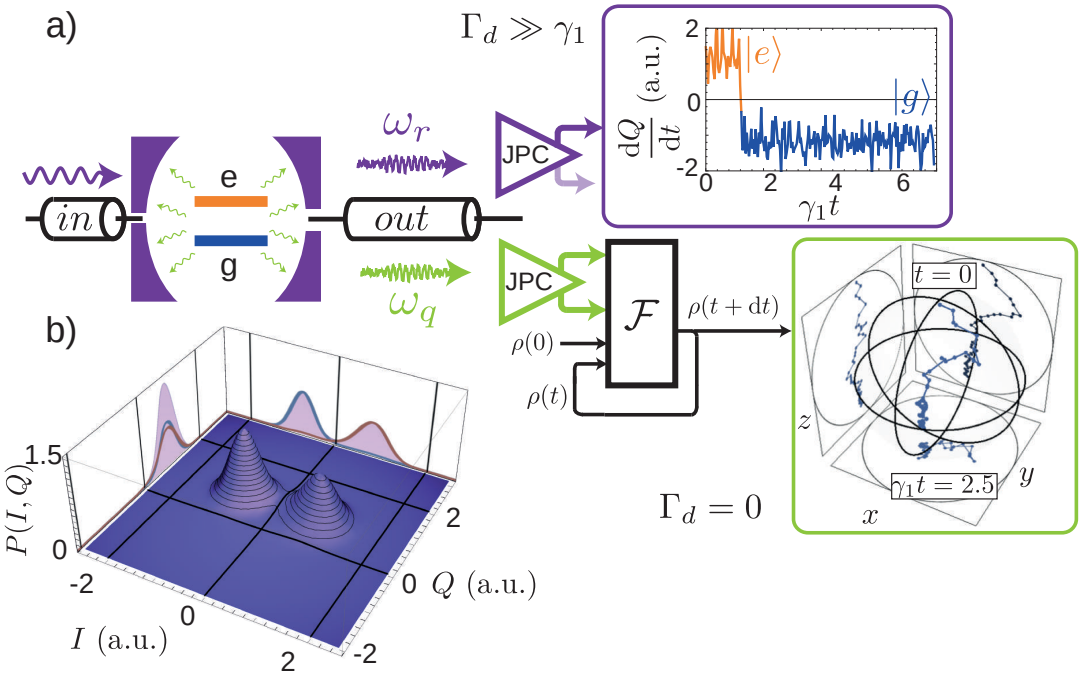

Figure 2: **a**) Detection of the field associated with dispersive measurement (in purple) or the fluorescence field (in green). The upper inset shows a measurement record associated with the first detection, on a time scale larger than T_1 and for a large measurement rate. It reveals quantum jumps [22]. The second, from a different experiment, shows a quantum trajectory associated with the fluorescence detection when no dispersive measurement takes place. A quantum filter $\mathcal{F}$ is used to propagate the density matrix from t to $t + \mathrm{d}t$ knowing $\mathrm{d}I_t$ and $\mathrm{d}Q_t$. The qubit state diffuses continuously toward $|g\rangle$. **b**) Density of probability for $I(T_{\mathrm{meas}})$ and $Q(T_{\mathrm{meas}})$ extracted from 10^6 measurement outcomes when the qubit is prepared in states $|g\rangle$ or $|e\rangle$ with equal probability. The halved probability density corresponding to the preparation of $|g\rangle$ only (resp. $|e\rangle$) is plotted in blue (red) together with the marginals along the I and Q axes. The distributions are well separated, indicating that when integrating the dispersive measurement record over a sufficiently long time $T_{\mathrm{meas}} \ll T_1$, one gets a high fidelity, non-destructive, single shot readout of the qubit.

A particular *quantum filter*, the Stochastic Master Equation (SME) [23, 24], is used to translate the measurement records in *quantum trajectories*. These are the states occupied by the qubit in time during the measurement. If one collects efficiently the information ($\eta \simeq 1$), these states can be deduced accurately and their purity remains of order 1 *during the collapse* on $|g\rangle$ or $|e\rangle$. The measurement record presented on Fig. 2a (purple inset) would lead to a trajectory displaying abrupt variations or *jumps* [22] between $|g\rangle$ and $|e\rangle$. This limit is reached when the integration time step $\mathrm{d}t$ is much larger than the measurement time $1/\Gamma_m$.

A second measurement scheme used in these experiments is performed by heterodyne detection of the *fluorescence field* emitted by the qubit when relaxing into the output line [25, 26]. The JPC is then tuned to the qubit resonance frequency. In that case, the measurement records read [24]

$$\begin{cases} \mathrm{d}I &= \sqrt{\frac{\eta\gamma_1}{2}}\langle\sigma_X\rangle\mathrm{d}t + \mathrm{d}W_{t,I} \\ \mathrm{d}Q &= \sqrt{\frac{\eta\gamma_1}{2}}\langle\sigma_Y\rangle\mathrm{d}t + \mathrm{d}W_{t,Q} \end{cases}, \tag{6}$$

so that it can be understood as a measurement of the hermitian and anti-hermitian parts of the σ_- operator of the qubit. This measurement is weak on a timescale shorter than T_1. Therefore it is not QND in the sense that it eventually collapses the qubit state to $|g\rangle$. The typical trajectory displayed on Fig. 2a (green inset) corresponds to a diffusion of this state from the initial preparation in $|e\rangle$ at $t = 0$, to $|g\rangle$ at $t = 2.5\ T_1$.

The SME allows us to predict the state of the qubit at time t using the measurement records from 0 to t. We now show how to infer this state *a posteriori*, conditioned on the outcome of a measurement taking place *after* t.

1.1.3 *Influence of post-selection*

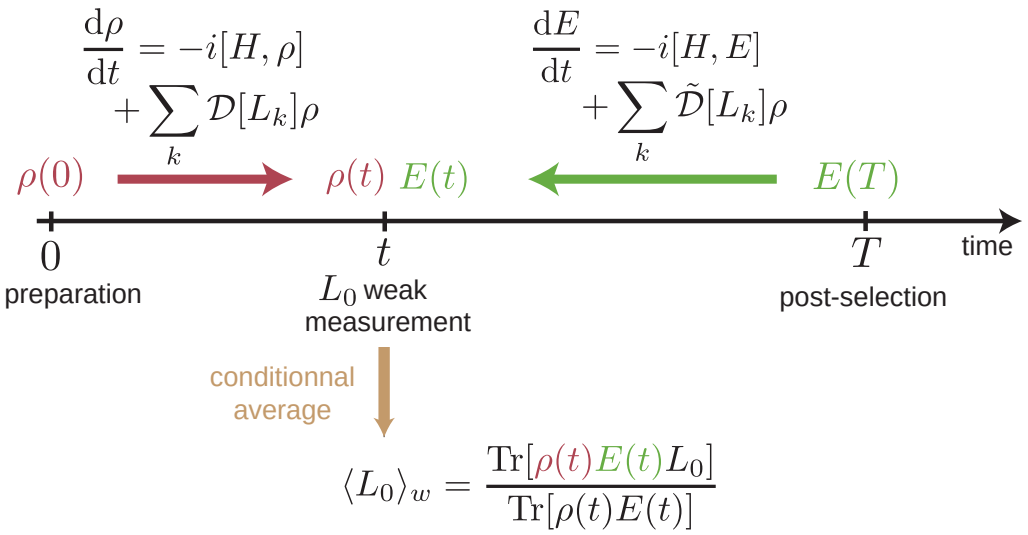

Figure 3: The density matrix ρ and effect matrix E are propagated respectively forward and backward from initial state (resp. final post selection) toward t. They allow to predict the average value of the detected signal at time t for the post-selected experiments.

In 1964, Aharonov *et al.* noticed that post-selection on the final state of a closed quantum system played a time symmetric role to preparation [27]. This paved the way for the still controversial *weak value* physics [28]. Recently, this theoretical framework was extended to open quantum systems [29, 30, 31]. The information of the final measurement at time T is encoded in an *effect matrix* E(T), similar to the density matrix. This matrix is then propagated backward in time until a given time t, taking

into account the damping by a set of jump operators $\{L_k\}$, as depicted on Fig. 3. In this expression, the modified damping super operator $\tilde{D}$ reads

$$\tilde{D}[L]E = -L^\dagger E L + \frac{1}{2}(L^\dagger L E + E L^\dagger L). \tag{7}$$

It is similar to the Lindblad master equation, but *does not lead to a time-symmetric* evolution for E compared to the one for ρ if $L \neq L^\dagger$, which is the case for a relaxation process.

Both ρ and E are used to make predictions on post-selected sub ensembles of experiments. The conditional average value of a weak measurement at time t, such as the continuous monitoring of a jump operator L_0 over a small integration time step, reads $\langle L_0 \rangle_w = \mathrm{Tr}[\rho_E L_0]$ where

$$\rho_E = \frac{\rho E}{\mathrm{Tr}[\rho E]} \tag{8}$$

is not hermitian, which entails counter intuitive properties [32].

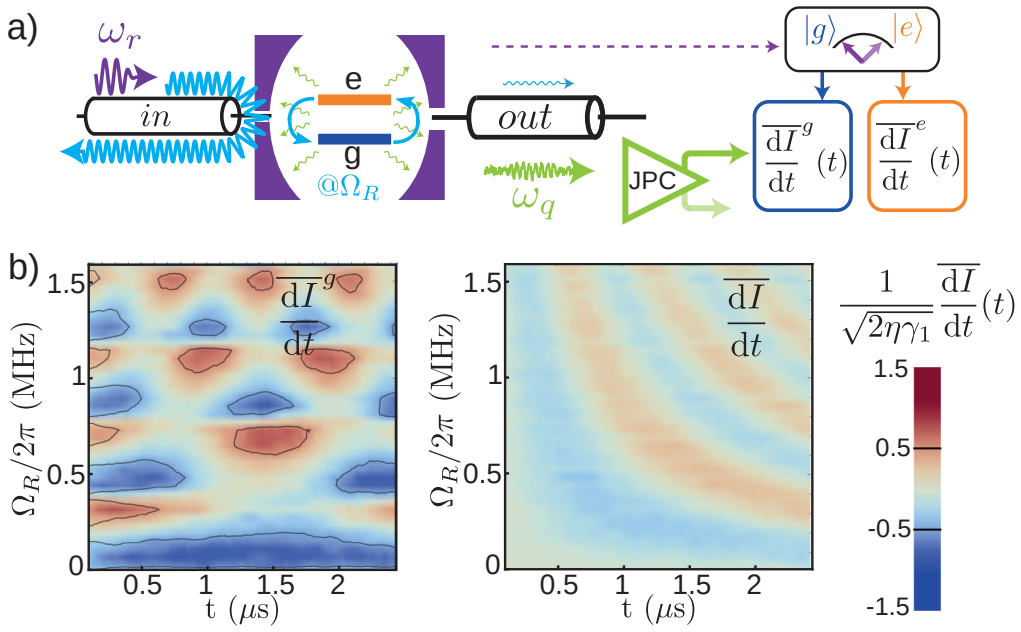

Figure 4: **a**)The resonance fluorescence of a driven qubit is detected on the output line (in green) from 0 to $T = 2.5\mu$s ($T \ll T_1$). The traces are averaged conditionally to a final projective measurement outcome using the dispersive shift of the cavity (in purple). For a qubit driven around σ_Y, only the I measurement record contains information about the qubit dynamics on average. **b**) The conditional fluorescence signal (to the left) displays features from both preparation and post-selection. It can take much larger values than the unconditionally averaged signal (to the right). Lines surround regions with weak values beyond the accessible range for unconditional average.

In order to test this theory on the monitored relaxation channel ($L_0 = \sqrt{\gamma_1}\sigma_-$), we modify the detection setup schematized on Fig. 2a as represented on Fig. 4a. The qubit is driven resonantly so that it undergoes Rabi oscillations from time 0 to T

(blue arrows). At T, it is measured projectively along σ_z using the dispersive shift of the cavity resonance (high power readout method, described in Sec. 3.3). On a large number of experiments, the measurement records from the fluorescence detection are then averaged according to this final measurement outcome. For a qubit initially in $|e\rangle$ and when varying the Rabi pulsation Ω_R, the probability to post select the qubit, say, in $|g\rangle$, becomes very low when $\Omega_R T = 2n\pi$. Such events would not be possible if not for the decoherence induced by the relaxation channel, which is the only decoherence channel in the present case. As a result, the average fluorescence signal conditioned on this post-selection then takes large values (dark colors in the right panel of Fig. 4b compared to the unconditioned case on the left), in quantitative agreement with the predicted weak value.

Now that both the dispersive and fluorescence detections have been characterized, we describe in the next section how they were used in feedback loops to stabilize an arbitrary state of the qubit. We compare these feedback protocols to *reservoir engineering* and to coherent engineering of the system energy levels.

1.2 QUANTUM FEEDBACK

Classically, feedback loops are used indifferently either to prepare a system in a *target state* starting from an unknown state, or to protect an unknown initial state from external noise. In the quantum domain, one might distinguish these two situations when the state to protect should not be measured in order to preserve the information that it carries.

In the first situation, it is necessary to evacuate the entropy from the initial unknown state, so that the loop includes either a measurement, implementing *measurement based feedback* [33, 24] (MBF), or a specifically designed dissipative channel, which defines *reservoir engineering* [34], also called *autonomous feedback*. We present two experiments using MBF loops to stabilize arbitrary states (even dynamic ones), and compare them to reservoir engineering techniques. Their performances are similar when using efficient detectors and we show that continuous MBF allows to effectively engineer dissipation.

On the other hand, protecting an unknown state can be done coherently[4]. We present an experiment witnessing Zeno dynamics[35, 36, 37, 38, 39] of a microwave mode, entailed by coherent control only. Seen as *coherent feedback* inhibiting departure from a stabilized subspace, it only protects from spurious transitions induced by coherent processes. However, since decoherence and relaxation can ultimately be described as coherent evolution with ancillary modes, inhibiting coherently these interactions effectively decreases the rate of induced errors. A trivial example is the use of an off resonant cavity to control the electromagnetic environment of the qubit. Another device commonly used is the so called Purcell filter, which can lower considerably the relaxation rate into the probe lines [16, 17].

4 We do not consider here *correcting codes* that make use of a larger Hilbert space to protect a logical qubit by careful measurement or dissipation, stabilizing a coding subspace.

1.2.1 *Measurement-based feedback and reservoir engineering*

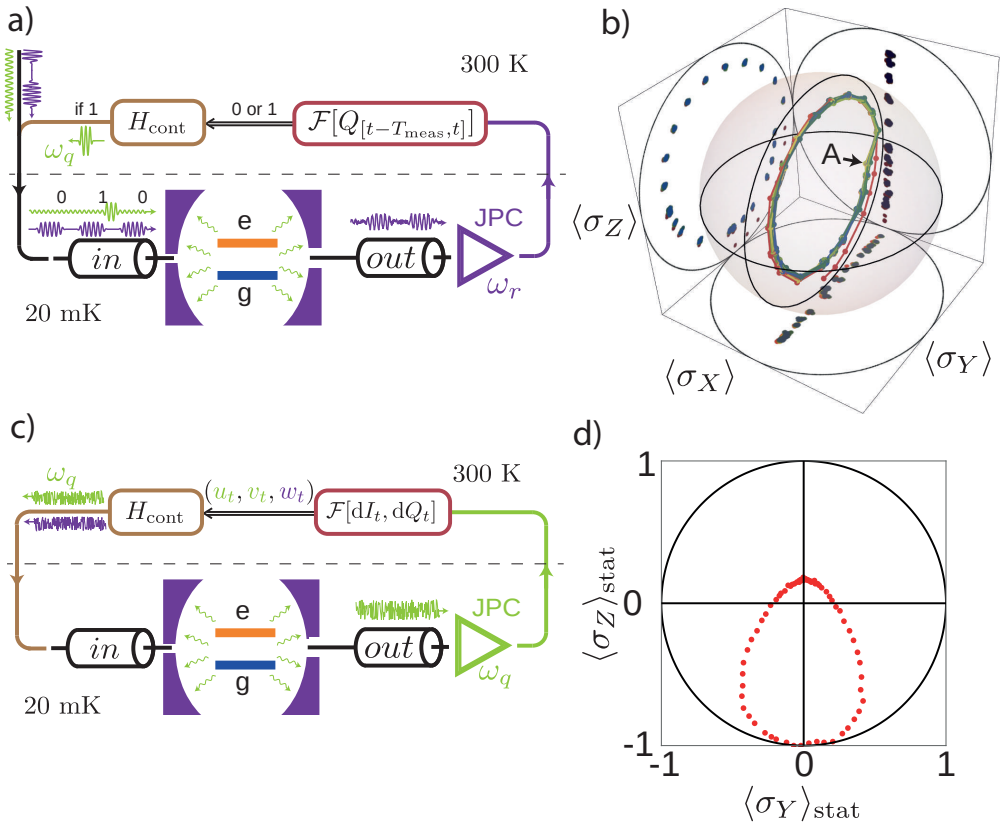

Figure 5: **a**) Stroboscopic MBF using a pulsed dispersive measurement (purple waves). The controller (in red) integrates the signal on Q and instructs the actuator (in brown) to trigger a fast correcting π-pulse (large green wave) if the qubit is in $|e\rangle$. This pulse is combined with the readout signals and, in the present case, a weak constant drive to induce Rabi oscillations. More complex operations by the FPGA could allow for more elaborate bayesian feedback schemes. **b**) Bloch sphere representation of stabilized Rabi oscillations from the setup described in **a**. Time is encoded in color from $t = 0$ (in red) to $t \simeq 4\,T_1$ (in blue). Actuations "A" correspond to the application of the correcting pulse and compensate for the purity loss during each oscillation. **c**) Continuous markovian feedback using the fluorescence field (in green) detection. The controls u_t, v_t and w_t are proportional to the current values ${\rm d}I_t$ and ${\rm d}Q_t$ of the records. The control hamiltonian is $H_{\rm cont} = u_t\sigma_X + v_t\sigma_Y + w_t\sigma_Z$. Rotations around $\sigma_{X,Y}$ are implemented by drives at ω_q (in green) and around σ_Z by *dressing* the qubit frequency with a field near ω_r (purple). **d**) Stabilized states represented as red dots in the (y,z) plane of the Bloch sphere, in the stationary state of the feedback schematized in **c**.

A measurement based feedback loop can be decomposed in three parts. A *sensor* extracts efficiently information from the system. It transmits it to a *controller* that "decides" of the strategy to adopt in order to steer the system toward the target state. This decision is communicated classically to an *actuator* that applies coherent drives on the system accordingly. Realizations of MBF were recently performed using Ryd-

berg atoms [40, 41] and superconducting circuits [42].

First, we implement stroboscopic feedback using the dispersive measurement. It is schematized on Fig. 5a. At discrete times, a readout pulse at the cavity resonance frequency is sent through the input line. The transmitted field is amplified by a JPC (the sensor) and the resulting signal is digitized at room temperature by an FPGA board (the controller). The board integrates the signal so as to determine the state of the qubit in a single-shot with high fidelity. If it is detected in $|e\rangle$, it sets a control bit to 1. This bit is transferred on to the board's DAC (the actuator) that generates a pulse at qubit frequency so as to perform a π rotation of the state if the bit is 1.
With this strategy, we can reset the qubit efficiently as was done in [42], which implements the removal of entropy needed as quantum information protocols first step [43]. Moreover, by applying measurement pulses at predefined times only, which are when the qubit is expected to be in the ground state, we can stabilize a non trivial trajectory such as Rabi or Ramsey oscillations (see Fig. 5b).
This measurement based feedback loop is similar to the discrete time version of an autonomous scheme previously realized in [44] and that we reproduced in the *resolved photon number regime* [45] (see Fig. 52). Making use of a dispersive shift larger than the cavity linewidth, we first drive the cavity at $\omega_{r,g} = \omega_r + \chi/2$ so that a large coherent state $|\alpha\rangle$ develops only if the qubit is in $|g\rangle$. A π pulse on the qubit is then applied conditioned on the cavity being in the vacuum. This sequence effectively swaps the qubit state with an effective qubit formed by the orthogonal cavity states $|0\rangle$ and $|\alpha\rangle$. The performances are similar to the measurement based scheme for high efficiency detection. Indeed, both protocols are limited by thermal excitations during the necessary delay before using the qubit for other operations in order for the cavity field to leak out. The minimal amplitude of this field is in both cases set by a distinguishability criterion between $|0\rangle$ and $|\alpha\rangle$. Moreover, the autonomous scheme relies on having a cold ancilla (the cavity in the present case) to swap states with the qubit. This ancilla needs to be reset or replaced to repeat the scheme, requiring a cold bath to dissipate into. The complete loop is thus not coherent, and the ancilla effectively plays the same role as a bit of memory in the FPGA board.

A second experiment uses the fluorescence field measurement. The feedback is continuous and markovian, in the sense that the controller does not have a memory and sets the control drives as a function of the current values of the detected signal only. One can show that [23, 24, 46], when considering a perfect detection of a single jump operator L and a simple proportional controller, the feedback loop results in an effective master equation for the qubit in which L has been modified as

$$L \leftarrow L - iH_d, \tag{9}$$

where H_d is an arbitrary drive hamiltonian[5]. In the case of the heterodyne detection used in this experiment, which corresponds to the simultaneous detection of $L_1 = \sqrt{\frac{\gamma_1}{2}}\sigma_-$ and $L_2 = i\sqrt{\frac{\gamma_1}{2}}\sigma_-$, we can still define a proportional controller that stabilizes an arbitrary state of the Bloch sphere for perfect detection efficiency. With

5 In general, a constant drift in the qubit hamiltonian also needs to be compensated.

the limited efficiency of our setup, we stabilize the states with finite purity as represented on Fig. 5d.

Note that by canceling the imaginary part of a jump operator with the right drive hamiltonian, it is possible to effectively transform a dissipation process into a QND continuous measurement. Conversely, when considering, for example, the case $L = \sqrt{\frac{\Gamma_d}{2}}\sigma_z$ as for a dispersive measurement with homodyne detection, and choosing $H_d = \sqrt{\frac{\Gamma_d}{2}}\sigma_Y$, one could stabilize the state $|+x\rangle$, on the equator of the Bloch sphere. Thus, efficient detection, combined with continuous markovian measurement based feedback, allows to engineer dissipation just as autonomous techniques [47]. Such a scheme was first used by Vijay *et al.* to stabilize Rabi oscillations [48].

1.2.2 *Quantum Zeno Dynamics*

A last experiment led us to the observation of Quantum Zeno Dynamics (QZD) of the microwave mode of a cavity. This experiment demonstrates a similar effect for light than was previously done for atomic levels [49, 50]. In its original definition, the quantum Zeno effect corresponds to the inhibition of coherent transitions from, or to, the pointer states of a strong measurement or dissipative process. Instead of freezing the dynamics, one can restrict it to a given subspace by choosing a measurement with degenerate eigenvalues.

Similar behavior can also be induced by rapid unitary "kicks" [37, 38], leaving the subspace to protect unaffected. It can be understood considering a model for the original Zeno measurement as a series of coherent interactions with ancillary systems. When the interactions are strong enough, departure from the subspace is perfectly suppressed, so that the outcome of the detector is always the same. Therefore, the ancillas are all left in the same state after the interaction and they do not need to be reset. One can then enforce Zeno dynamics by performing repeatedly unitary operations controlling the state of an auxiliary degree of freedom. This amounts to re-using the same ancilla, at the condition that the unitary evolutions are fast enough to effectively *randomize* the phase of coherences created with the system. In that sense, QZD is a coherent feedback, which engineers the energy level landscape of a system or its environment by coherent coupling with an ancillary degree of freedom.

In the experiment, a qubit in the resolved photon number regime [45] plays the role of the ancillary system. A strong Rabi drive is applied on its transition conditioned on the cavity mode hosting N photons ($N = 3$ on Fig. 6a). The drive hybridizes the levels $|N, g\rangle$ and $|N, e\rangle$ that repel each other. The level $|N\rangle$ is then moved out from the harmonic ladder of the cavity mode. When starting in the vacuum and applying a coherent drive at ω_r, the generated state cannot contain N photons so that it is restricted to N levels.

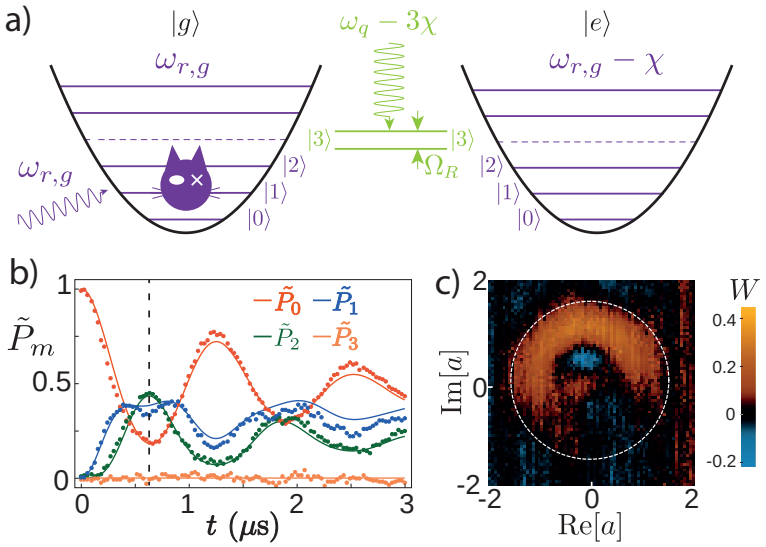

Figure 6: **a**) Combined energy level diagram for the qubit and cavity. By applying a strong Rabi drive on the $|3, g\rangle \leftrightarrow |3, e\rangle$ transition, the $|2\rangle \leftrightarrow |3\rangle$ transition of the cavity becomes off resonant at $\omega_{r,g}$. **b**) Oscillations of the Fock state occupation when driving the cavity mode from the vacuum and blocking $|3\rangle$. **c**) Wigner tomography of the field at half period of oscillation (dashed line in **b**). The quasi-probability density is confined within a circular barrier of radius $\sqrt{3}$ (white circle). Negativities (in blue) reveal a non classical state.

When measuring the Fock state occupation probabilities as a function of time for this effective driven N-level system, characteristic oscillations appear (see Fig. 6b). Quantum coherence of the field is revealed by direct Wigner tomography [51] (see Fig. 6c). At half-period of the oscillations, fringes with negativities can be observed. This non classical state is similar to a "Schrödinger cat state", confined in phase space within a circular barrier of radius $\sqrt{N}$.

This thesis is organized as follows. Chapters 1 and 2 describe the formalism adopted in this work, the system and its decoherence channels, and the two types of detections used in the experiments. Chapter 3 focusses on a weak value experiment and describes the framework to combine information from past and future measurements. Chapters 4 and 5 report experiments implementing measurement based feedback and reservoir engineering. Chapter 6 describes the Zeno dynamics of the microwave mode. Chapter 7 gives a brief overview of experimental techniques used throughout the experiments.

Part I

OPEN SYSTEM AND QUANTUM TRAJECTORIES

2

OPEN QUBIT

2.1 QUANTUM BIT OF INFORMATION : THE SIMPLEST QUANTUM SYSTEM

We will define here the notations used throughout this thesis, describe the representations for a qubit state and formally derive a Master Equation as a general framework to model open qubit dynamics.

2.1.1 *TLS representation*

A two level system, which will be referred to in this thesis as a *quantum bit* (qubit) for it can be used to carry one bit of information, has exactly 2 steady states. If non degenerate, they are called ground $|g\rangle$ and excited $|e\rangle$ by order of energy. If the qubit state is perfectly known, it is in a pure state and can be written $\alpha|g\rangle + \beta|e\rangle$ with α and β some complex coefficients such that $\sqrt{|\alpha|^2 + |\beta|^2} = 1$. In order to describe the qubit state even in the case of imperfect knowledge, we use the density matrix formalism. For a pure state $|\psi\rangle$, the density matrix is simply $\rho = |\psi\rangle\langle\psi|$. With the above decomposition on the eigenbasis $\{|e\rangle, |g\rangle\}$, the density matrix then reads

$$\rho = \begin{pmatrix} |\beta|^2 & \alpha^*\beta \\ \alpha\beta^* & |\alpha|^2 \end{pmatrix}. \tag{10}$$

When considering a statistical mixture of states $|\psi_i\rangle$, the density matrix becomes $\rho = \sum_i p_i |\psi_i\rangle\langle\psi_i|$ where $\{p_i\}$ is a set of (classical) probabilities of sum 1. Since ρ is hermitian, positive and of trace 1, it can be decomposed on the Pauli matrice basis

$$\rho = \frac{1}{2}(\mathbb{1} + x\sigma_x + y\sigma_y + z\sigma_z) \text{ with } \sigma_x = \begin{pmatrix} 0 & 1 \\ 1 & 0 \end{pmatrix}, \ \sigma_y = \begin{pmatrix} 0 & -i \\ i & 0 \end{pmatrix}, \sigma_z = \begin{pmatrix} 1 & 0 \\ 0 & -1 \end{pmatrix}. \tag{11}$$

A convenient graphical representation for these density matrices uses the so-called Bloch sphere, which is a ball of radius 1. A state is then represented by a vector of coordinates $\{x, y, z\}$ (Fig. 7). A density matrix ρ being hermitian, it can be diagonalized on an orthonormal basis. This means that there exist 2 orthogonal states $|+\rangle$ and $|-\rangle$ such that

$$\rho = p\ |+\rangle\langle+| + (1-p)\ |-\rangle\langle-|, \tag{12}$$

where $p \in [0, 1]$ since ρ is positive and of trace 1. This decomposition is in fact unique, except for the maximally entropic state $\rho = \frac{1}{2}\mathbb{1}$. Indeed, as orthogonal pure states, $|+\rangle\langle+|$ and $|-\rangle\langle-|$ are represented by two Bloch vectors $\overrightarrow{B_+}$ and $\overrightarrow{B_-}$ of length 1 (Eqs. (10,11)), and the Bloch vector for ρ is $\overrightarrow{B} = p\overrightarrow{B_+} + (1-p)\overrightarrow{B_-}$: any Bloch vector remains inside the sphere.

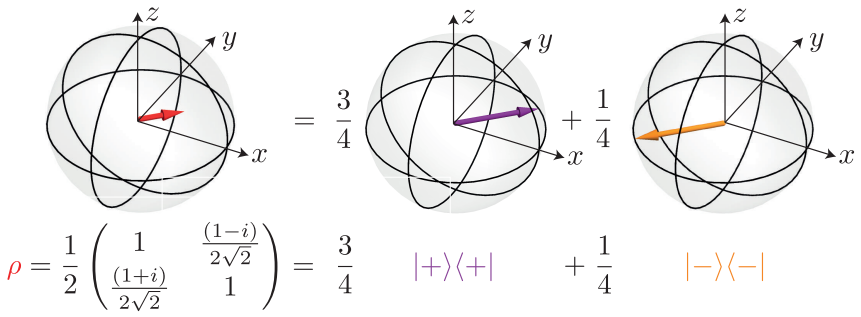

Figure 7: Bloch sphere representation of the mixed state $\rho = \frac{1}{2}(\mathbb{1} + \frac{1}{2\sqrt{2}}\sigma_x + \frac{1}{2\sqrt{2}}\sigma_y)$ (to the left) and its decomposition on a basis in which ρ is diagonal (to the right): noting $|+\rangle = \frac{1}{\sqrt{2}}(|g\rangle + \frac{1-i}{\sqrt{2}}|e\rangle)$ and $|-\rangle = \frac{1}{\sqrt{2}}(|g\rangle - \frac{1-i}{\sqrt{2}}|e\rangle)$ the two pure states whose Bloch vectors are collinear to the one of ρ, these states are orthogonal so that they form a basis and their Bloch vectors are opposed. It is the basis on which the outcomes of a projective measurement of the qubit will yield the minimum Shannon entropy.

2.1.2 *Entropy*

The possibility to consider mixed states can first appear as a practical way to take into account experimental imperfections. However, we will see throughout this thesis that, on a fundamental level, variation of entropy is unavoidable when considering an open-system. If a system interacts with its environment and that the information thus imprinted in auxiliary degrees of freedom is not fed back to the system, it can result in an increase of entropy.

There are several definitions for entropy that quantify the lack of knowledge of an observer. In this thesis, we will use the Von Neumann definition

$$S = -\mathrm{Tr}[\rho \mathrm{Log}_2[\rho]] = -p\mathrm{Log}_2[p] - (1-p)\mathrm{Log}_2[1-p], \tag{13}$$

where p is the probability entering the decomposition of Eq. (12). Hence, the entropy of a qubit state lies between 0 for a pure state and 1 bit for the maximally entropic state $\rho = \frac{1}{2}\mathbb{1}$. Moreover, it corresponds to the Shannon entropy associated to the statistics of the outcome of a measurement along the basis $\{|+\rangle, |-\rangle\}$. Any other projective measurement along a different basis $\{|a\rangle, |b\rangle\}$ would yield the outcome a with probability $p' = \mathrm{Tr}[\rho|a\rangle\langle a|] = pq + (1-p)(1-q)$ where $q = |\langle +|a\rangle|^2$, so that $|p' - \frac{1}{2}| < |p - \frac{1}{2}|$, and the corresponding Shannon entropy would be larger than S. This excess uncertainty about the outcome of a measurement on an imperfect basis is sometimes referred to as *measurement entropy*[52].

An important feature of the entropy associated to a density matrix is that its value does not depend on the choice of the basis on which it is written. As a consequence, any unitary operation on a density matrix preserves entropy.
The purification principle states that apparition of entropy for a system A can always be modeled as the entanglement of A in a pure state with an auxiliary system B, followed by an unread measurement of B. This is even the only postulate that differs

between quantum and classical information theory in the axioms of Chiribella *et al*[9]. Such an unread measurement is mathematically described by the partial trace operation. Given an orthonormal basis $\{|\phi_i\rangle\}$ on which B will be measured, and a density matrix ρ_{AB} describing a potentially entangled state of A and B, it is defined by:

$$\mathrm{Tr}_B[\rho_{AB}] = \sum_i \langle\phi_i|\rho_{AB}|\phi_i\rangle \tag{14}$$

The resulting matrix ρ_A represents a state of the system A only. This operation is trace preserving so that the density matrix ρ_A is well defined, but not unitary so that the entropy is not preserved. Another important feature is that ρ_A does not depend of the choice of the basis $\{|\phi_i\rangle\}$. This means that which measurement will actually be performed on B does not matter. As long as one gives up all information on any future measurement on system B, the knowledge about A is be encoded by ρ_A. For instance, a qubit that interacts with an electromagnetic mode will undergo the same evolution (namely submitted to relaxation and/or decoherence), whatever the fate of the light in this mode as long as all info about it is dismissed. That it be measured along a particular basis, absorbed by the environment or let to travel in free space indefinitely does not change the state of A. Thus, in this formalism, a quantum state is defined relatively to an observer: it is no more than the knowledge that we have about it. As a consequence, entropy is also defined relatively to an observer.

Another notion from information theory that will be of interest is the relative entropy [52]. Considering two density matrices ρ and σ, we define

$$S(\rho||\sigma) = -\mathrm{Tr}[\rho \mathrm{Log}_2(\sigma)] + \mathrm{Tr}[\rho \mathrm{Log}_2(\rho)]. \tag{15}$$

This quantity is a measure of the "distance"[1] between the states represented by ρ and σ. In particular, $S(\rho||\sigma) \geq 0$, with equality when $\rho = \sigma$. We will see that without extracting any information about an open quantum system, the relative entropy of two different initial states, which can be understood as the distinguishability between two initial preparations, can only decrease with time. This is in contrast to the entropy of a particular state that, depending on the interaction with the environment, can increase due to decoherence, or decrease in presence of dissipation.

In order to describe in a compact way the effects of the interaction of a qubit with its environment, which makes it an open quantum system, we will now establish a Lindblad master equation that describes its dynamics.

2.1.3 *Lindblad Master Equation*

2.1.3.1 *Quantum operations*

Nielsen and Chuang [18] proposed three equivalent ways to describe *quantum operations*, that is any physical transformation acting on a system A. These are represented by a super operator $\mathcal{L}$, also referred to as a *map*, acting on the density matrices of A. They must, in the axiomatic way, have the 3 following properties.

1 but the relative entropy is not a proper metric since it is not symmetric

- $\mathcal{L}$ is *trace-preserving*[2]: $\forall \rho, \mathrm{Tr}[\mathcal{L}[\rho]] = 1$
- $\mathcal{L}$ is *completely positive*. This property means that for any auxiliary system B with which our system is potentially entangled, the map $\mathcal{L}_A \otimes \mathbb{1}_B$ acting on the whole system must preserve positivity (that is ρ_{AB} with non-negative eigenvalues). The 2 previous properties ensure that the eigenvalues of $\mathcal{L}[\rho]$ can still be interpreted as classical probabilities of a mixed state.
- $\mathcal{L}$ is *convex linear*: for a set of probabilities $\{p_i\}$ and states $\{\rho_i\}$, $\mathcal{L}[\sum_i p_i \rho_i] = \sum_i p_i \mathcal{L}[\rho_i]$. This means that picking randomly from an ensemble of initial states with some given probability distribution, one expects to get one of the transformed states with the same probability after the operation .

Then, they show that for such a map, if the system is not initially entangled with the rest of the universe (its environment), there exists a finite set of so-called 'Kraus operators' $\{M_i\}$ which are linear operators acting on the states of A, such that, for any density matrix ρ_A,

$$\mathcal{L}[\rho_A] = \sum_i M_i \rho_A M_i^\dagger, \tag{16}$$

with the normalisation relationship

$$\sum_i M_i^\dagger M_i = \mathbb{1}. \tag{17}$$

A simple example is the one of a unitary evolution U. In this case, a single Kraus operator $M_0 = U$ is enough. Note that the assumption that system and environment are initially in a separable state does not imply that they cannot be correlated due to prior interaction. This model just does not account for the pre-existing entanglement and the environment needs to be first traced out. In practice, the system is supposed not to interact with a part of the environment to which it is already entangled. Thus, we need the entanglement with the system to be either diluted in a large number of degrees of freedom, or that the modes entangled with the system do not interact anymore: these two possibilities are formally equivalent [11].

This decomposition is very convenient for calculations and will be used to derive a master equation. To get some physical insight and to introduce a method used in Sec. 4.1.2, let us present a last description of quantum operations and show its equivalence with the Kraus operators. The idea is that a quantum operation can always be modeled as a *generalized measurement* that is a unitary evolution of the system A coupled to an auxiliary system B, followed by a projective measurement of B. Indeed, starting from the decomposition of Eq. (16), one can introduce a sufficiently large auxiliary system B and associate to each M_i a base state $|\phi_i^B\rangle$ of B[3]. B is initially supposed

2 Nielsen and Chuang give a less strict property $0 \leq \mathrm{Tr}[\mathcal{L}[\rho]] \leq 1$ to allow the trace of ρ to encode the probability that a series of quantum operations occur. Those will be described in chapter 3. For now we suppose that no information is extracted from the system.

3 this system can be the physical environment of the qubit or a fictitious auxiliary system used for calculations

to be in a pure state $|\psi_0^B\rangle$. Then, the operator defined on $\mathcal{H}_A \otimes \mathrm{Vect}(|\psi_0^B\rangle)$, for any vector $|\psi^A\rangle$ of $\mathcal{H}_A$, by

$$U : |\psi^A\rangle \otimes |\psi_0^B\rangle \mapsto \sum_i M_i |\psi^A\rangle \otimes |\phi_i^B\rangle \tag{18}$$

can be extended into a unitary operator over $\mathcal{H}_A \otimes \mathcal{H}_B$ thanks to the normalization relation on $\{M_i\}$. The action of this unitary evolution on a density matrix ρ_A, followed by an unread projective measurement on the basis $\{|\phi_i^B\rangle\}$ of B then has the same effect as the operator $\mathcal{L}$ of Eq. (16). Indeed, if the measurement outcome i is known, the state is projected to the matrix

$$\rho_i = \frac{M_i \rho_A M_i^\dagger}{\mathrm{Tr}[M_i \rho_A M_i^\dagger]}, \tag{19}$$

and the measurement yields this outcome with probability

$$p_i = \mathrm{Tr}[M_i \rho_A M_i^\dagger] \tag{20}$$

(this result will be used in Sec. 3.1.2). On the other hand, if the measurement result is unread, one encodes the resulting state as a statistical mix $\sum_i p_i \rho_i = \mathcal{L}(\rho_A)$. This result is quite remarkable since it shows that any *physical* evolution of a system initially separated from its environment can be understood as a unitary evolution followed by a measurement of one of the environment observables.

Note that it is actually this unread measurement that can imply a change in the system entropy. This description also explains the theorem mentioned in Sec. 2.1.2: starting from 2 initial states ρ_A and σ_A, the unitary operator U preserves the relative entropy so that the potentially entangled states ρ_{AB} and σ_{AB} resulting from this evolution verify

$$S(\rho_{AB} \,||\, \sigma_{AB}) = S(\rho_A \otimes |\psi_B\rangle\langle\psi_B| \,||\, \sigma_A \otimes |\psi_B\rangle\langle\psi_B|) = S(\rho_A \,||\, \sigma_A). \tag{21}$$

On the other hand, the unread measurement, mathematically realized by tracing out the auxiliary system B, can only decrease the relative entropy. We then get

$$S(\mathcal{L}[\rho_A] \,||\, \mathcal{L}[\sigma_A]) = S(\mathrm{Tr}_B[\rho_{AB}] \,||\, \mathrm{Tr}_B[\sigma_{AB}]) \leq S(\rho_A \,||\, \sigma_A). \tag{22}$$

A physical evolution can therefore only decrease the relative entropy of 2 states.

2.1.3.2 *Continuous time evolution*

Up to now, we have considered a measurement occurring abruptly. What if we can track the measurement in time? We will apply the previous results to the evolution of a qubit between time t and $t + \mathrm{d}t$, where $\mathrm{d}t$ is a short time-step compared to the typical time T on which its state evolves (due to intrinsic hamiltonian evolution or to the interaction with its environment). In order for the above assumptions to be verified, we will restrict our model to Markovian environments. This essentially means that the part of the environment that interacts with the system does not have any memory

after a typical time τ_c, which is much shorter than the time step $\mathrm{d}t$. It implies that one cannot take the limit $\mathrm{d}t \to 0$ rigorously, but instead will have to settle with the hierarchy $\tau_c \ll \mathrm{d}t \ll T$. This is called a *coarse-grained* description. In the Heisenberg picture, the Markovian hypothesis reads that, for any observable A appearing in the interaction hamiltonian, in the absence of interaction,

$$\mathrm{Tr}[\rho_E A(t)A(t+\tau)] \simeq 0, \tag{23}$$

for $\tau > \tau_c$.

Then, considering the evolution of the qubit state during a time interval $\mathrm{d}t$, we consider that the interaction with the environment is first turned off during τ_c. This does not affect the evolution since $\tau_c \ll T$, and it gives time for the environment to get back to its steady state and trace out any entanglement. Then, during $\mathrm{d}t - \tau_c \simeq \mathrm{d}t$, the map $\rho(t) \mapsto \rho(t+\mathrm{d}t)$ can be written

$$\rho(t+\mathrm{d}t) = \sum_{i=0}^{3} M_i \rho(t) M_i^\dagger. \tag{24}$$

Note that we restrict the number of Kraus operators to 4 which is universal for a qubit evolution. The M_i's do not depend on t since the environment is in a steady state. Moreover, since $\rho(t+\mathrm{d}t) = \rho(t) + O(\mathrm{d}t)$, we can choose M_0 of the order of unity[53], and separating the hermitian and anti-hermitian parts of the first-order term (resp. H and J), we write it as

$$M_0 = \mathbb{1} - i\frac{H}{\hbar}\mathrm{d}t - J\mathrm{d}t + O(\mathrm{d}t^2), \tag{25}$$

and the other terms appearing in (24) are of order $\mathrm{d}t$ so that we can write the other Kraus operators

$$M_i = \sqrt{\mathrm{d}t} L_i, \tag{26}$$

where the L_i's are of order unity. Then, the normalization relation (17) gives $J = \frac{1}{2}\sum_{i=1}^{3} L_i^\dagger L_i$, and we get the Lindblad form of the master equation [54]

$$\boxed{\frac{\mathrm{d}\rho(t)}{\mathrm{d}t} = -\frac{i}{\hbar}[H,\rho] + \sum_{i=1}^{3} \mathcal{D}[L_i]\rho,} \tag{27}$$

where we have defined the Lindblad superoperator $\mathcal{D}[L]$ acting on a matrix ρ as

$$\mathcal{D}[L]\rho = L\rho L^\dagger - \frac{1}{2}L^\dagger L\rho - \frac{1}{2}\rho L^\dagger L. \tag{28}$$

In this equation, H can be identified to the hamiltonian of the qubit which is *dressed* by its coupling to the environment. In particular, it accounts for the Lamb shift of energy levels when the environment is an electromagnetic mode. Finally, we choose "arbitrarily" a particular set of L_i's so that each term might be easily interpreted:

- $L_1 = \sqrt{\Gamma_\downarrow}\sigma_- = \sqrt{\Gamma_\downarrow}\,|g\rangle\langle e|$ for relaxation

- $L_2 = \sqrt{\Gamma_\uparrow}\sigma_+ = \sqrt{\Gamma_\uparrow}|e\rangle\langle g|$ for excitation
- $L_3 = \sqrt{\Gamma_\phi/2}\,\sigma_z$ for pure dephasing.

The master equation then reads

$$\frac{\mathrm{d}\rho(t)}{\mathrm{d}t} = -\frac{i}{\hbar}[H,\rho] + \Gamma_\downarrow \mathcal{D}[\sigma_-]\rho + \Gamma_\uparrow \mathcal{D}[\sigma_+]\rho + \frac{\Gamma_\phi}{2}\mathcal{D}[\sigma_z]\rho. \tag{29}$$

We can already identify the characteristic timescales of the qubit.

- $T_1 = \frac{1}{\Gamma_\downarrow + \Gamma_\uparrow}$ is the typical time for energy decay.
- $T_2 = \frac{1}{\frac{\Gamma_\downarrow + \Gamma_\uparrow}{2} + \Gamma_\phi}$ is the typical time for coherence decay.

In order to discuss these rates further, one needs to be more specific and describe the physical implementation of the qubit.

2.2 3D TRANSMON

The system that is used for the experiments described throughout this thesis follows the design of the 3D transmon [13]. A single Josephson junction is shunted by a large capacitance and is coupled to the lowest resonant electromagnetic mode of a high Q cavity made out of bulk aluminum or copper, cooled down at 20 mK.

2.2.1 *Resonant cavity and LC resonator*

The field of cavity quantum electrodynamics (CQED) studies the interaction of a light mode confined between two highly reflective mirrors (Faby-Perot cavity) with an atom or other particles. Electromagnetic confinement allows for an enhanced coupling to the particle of interest and has led to ground-breaking experiments [51, 55, 56] that implement the thought experiments of the quantum physics pioneers. Fully quantum behaviors that were thought unreachable and entailing "ridiculous consequences" by Erwin Schrödinger have been observed. With superconducting circuits, strong coupling of a qubit to a microwave mode confined on chip was achieved in 2004 by Wallraff *et al.* [57], and many experiments have since succeeded in reproducing, and sometimes going beyond, CQED achievements [58, 59, 60, 61, 10]. In our experiments, even if we use superconducting circuits on chip to implement *artificial atoms*, the cavity design is similar to CQED setup.
A parallelepipedic cavity is machined out of bulk aluminum as can be seen on Fig. 8a. Its lowest resonant modes are transverse electric (TE) and characterized by 3 integers $\{n_x, n_y, n_z\}$ such that the wave vectors are (on a basis defined by the orientation of the walls): $\vec{k} = n_x\frac{\pi}{l_x}\vec{e_x} + n_y\frac{\pi}{l_y}\vec{e_y} + n_z\frac{\pi}{l_z}\vec{e_z}$, where $l_{x,y,z}$ are the 3 dimensions of the cavity. Maxwell's laws impose that one of the n_i's is zero and the direction of the electric field is along the corresponding axis. We chose the dimensions of the cavity to be $(26.5 \times 26.5 \times 9.6)$ mm^3 so that the first resonant mode is TE110, resonating at $f = \frac{c}{2\pi}\sqrt{k_x^2 + k_y^2} \simeq 8$ GHz. Distribution of the electric field can be simulated using full 3D electromagnetic simulations and is represented on Fig. 8b. Its maximum amplitude

is at the centre of the cavity.

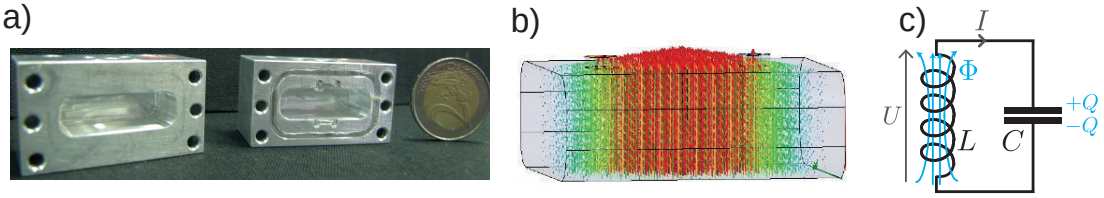

Figure 8: a) Picture of the two blocks of aluminum from which the cavity is machined out. When pressed together, they form a cavity whose first mode resonates at 8 GHz. b) Calculated distribution of the electric field of mode TE110 using full 3D electromagnetic simulation of the cavity. Electric field direction is represented by the arrow direction, amplitude encoded in color (from strong to weak: red to blue). c) LC resonator equivalent of a cavity mode. Φ is the magnetic flux threading the coil and Q is the charge on the capacitance electrode.

In order to quantize this mode, one can write down the electromagnetic lagrangian

$$\mathcal{L} = \int_V \frac{\epsilon_0}{2} E^2 - \frac{1}{2\mu_0} B^2 \mathrm{d}\overrightarrow{r}^3, \tag{30}$$

and decompose $\overrightarrow{E}$ and $\overrightarrow{B}$ over the basis of the TE modes. We then get the Lagrangian of N uncoupled harmonic oscillators, N being the number of resonant modes of the cavity ($N \to \infty$ for a full description [62]). The dynamics of these modes is thus the same as the one of LC resonators and we will model them so. This apparently formal identification has in fact a physical significance since the upper and lower walls of the cavity which are orthogonal to $\overrightarrow{E}$ play the role of a charged capacitor, and current flows in the vertical walls as in an inductor.

In order to quantize the LC circuit depicted on Fig. 8c , one has to introduce the flux Φ and charge Q defined by

$$\left\{ \begin{array}{rcl} \Phi & = & \int_{-\infty}^{t} U(t')\mathrm{d}t' \\ Q & = & \int_{-\infty}^{t} I(t')\mathrm{d}t' \end{array} \right. . \tag{31}$$

Then, the Lagrangian for this LC circuits reads

$$\mathcal{L} = \frac{Q^2}{2C} - \frac{\Phi^2}{2L}, \tag{32}$$

and the Kirchoff laws and constitutive relations of the elements imply that

$$\left\{ \begin{array}{rcccl} \dfrac{\partial \mathcal{L}}{\partial \dot{Q}} & = & -LI & = & \Phi \\ \dfrac{\partial \mathcal{L}}{\partial \dot{\Phi}} & = & CU & = & Q \end{array} \right. \tag{33}$$

so that Φ and Q are the two canonically conjugated variables for the system quantization. We can then promote them to quantum observables verifying the commutation relation [63, 64, 65]

$$[\Phi, Q] = i\hbar. \tag{34}$$

Note that this commutation relation in fact holds for any element and does not depend on the particular circuit under study: it can be directly derived from microscopic commutation relations of $\overrightarrow{E}$ and $\overrightarrow{B}$ in quantum electrodynamics[66]. The hamiltonian of the LC circuit is

$$H = \dot{\Phi}Q - \mathcal{L} = \frac{Q^2}{2C} + \frac{\Phi^2}{2L}. \tag{35}$$

Following the classical method for the second quantization of an harmonic oscillator, we introduce the annihilation operator defined as

$$a = \sqrt{\frac{1}{2\hbar Z_r}}\Phi + i\sqrt{\frac{Z_r}{2\hbar}}Q, \tag{36}$$

where we note $Z_r = \sqrt{L/C}$ the characteristic impedance of the resonator. We also drop the hat notation for operators as it can be implicitly understood from now on. From Eq. (34), we get the commutation relation with the creation operator $a^\dagger$

$$[a, a^\dagger] = \mathbb{1}. \tag{37}$$

Then we can write the hamiltonian of the mode in a canonic way as

$$H_0 = \hbar\omega_r(a^\dagger a + \frac{1}{2}). \tag{38}$$

Here, $\omega_r = 1/\sqrt{LC} \simeq 2\pi \times 8$ GHz is the resonance pulsation of the mode and $n = a^\dagger a$ is the number of energy quanta in the mode. Note that in order to witness non-classical behavior, the typical energy associated to the temperature of the cavity needs to be much smaller than the energy of a photon: $k_B T \ll \hbar\omega_R$ so that $T \ll 400$ mK. Thus, the quantum properties of microwave modes are hidden at room temperature in contrast with electromagnetic modes in the optical domain. This temperature is routinely reached in properly equipped dilution refrigerators (see A.2). Besides, at this temperature, typical energies are well below the gap of superconducting aluminum ($\simeq 1.2\ K$) so that losses inside the aluminum cavity are considerably lowered and the Josephson effect provides us with the non linear and non dissipative element at the base of our quantum circuit (see Sec. 2.2.3).
However, in the model presented above, we neglected the spurious internal losses of the cavity and the coupling to the outside world. We will see in the next section that these two phenomena can be simply modeled in the same way.

2.2.2 *3D cavity coupled to transmission lines*

2.2.2.1 *Lossy resonators*

In practice, the cavities are intrinsically lossy due to finite conductivity for copper cavities and impurities on the surface or quasi-particules for aluminum ones. To model these internal losses, we add in parallel to the LC model a resistor R. Resistors are not as simple to model in quantum mechanics as inductors or capacitors. Indeed, we cannot write down a hamiltonian since its dynamics is not reversible and it is intrinsically

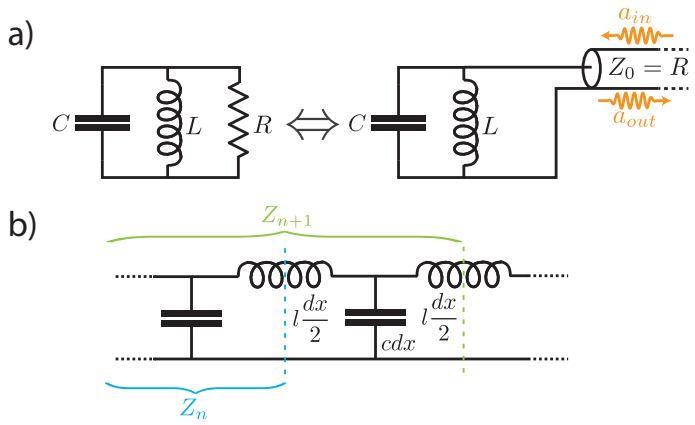

Figure 9: a) To include the losses inside the cavity in our model, we add a resistor R to the resonator. This resistor can be modeled as a semi-infinite transmission line of characteristic impedance $Z_0 = R$. b) Telegraph model for a transmission line of characteristic impedance $Z_0 = \sqrt{\frac{l}{c}}$. l is the inductance per unit length and c the capacitance to the ground per unit length.

an open-system since it dissipates energy. However, such an element of purely real impedance is in fact equivalent to a lossless semi-infinite transmission line, that is an infinite collection of purely reactive elements. To show this, we consider the telegraph model of a transmission line (e.g. a coaxial cable) as depicted on Fig. 9b. It has an inductance per unit length l and a capacitance to the ground per unit length c. We model it by a periodic pattern of period δx. Then we have the recursive relation between the impedance of a length $n\delta x$ and $(n+1)\delta x$

$$Z_{n+1}(\omega) = [(Z_n(\omega) + i\omega l\frac{\delta x}{2}) \quad || \quad \frac{1}{i\omega c\delta x}] + i\omega l\frac{\delta x}{2}. \tag{39}$$

This directly leads, for an infinite and continuous line, to

$$Z_0 = \lim_{\substack{\delta x\to 0\\ n\to\infty}} [Z_n] = \sqrt{\frac{l}{c}}. \tag{40}$$

Here, the resistor R is galvanically coupled to the LC resonator. Therefore, it is modeled by a galvanically coupled semi-infinite line of characteristic impedance $Z_0 = R$.

In fact, this basic RLC model can also represent a capacitively coupled line such as the ones we use to probe our system (Fig. 10a). Noting Z_c the characteristic impedance of the line, if the coupling capacitance C_κ is much smaller than $1/Z_c\omega_r$, we show in appendix B.1 that, as seen from the cavity, the circuit is equivalent to a galvanically coupled line of characteristic impedance Z_0 with

$$Z_0 = \frac{1}{C_\kappa^2\omega_r^2 Z_c} \gg Z_c. \tag{41}$$

Thus, a capacitive coupling to a transmission line is equivalent to a galvanic coupling to a high impedance line[4].

4 The cavity mode capacitance is slightly renormalized by the coupling capacitance.

2.2.2.2 *Master equation for a cavity mode*

A coupled semi-infinite line induces a non-unitary evolution for the intra-cavity field. These dynamics can be taken into account by a Lindblad master equation. For a zero temperature line, it reads [24]

$$\frac{\mathrm{d}\rho(t)}{\mathrm{d}t} = -\frac{i}{\hbar}[H,\rho] + \kappa\mathcal{D}[a]\rho, \tag{42}$$

where

$$\kappa = \omega_r \frac{Z_r}{Z_0} \tag{43}$$

is the photon exit rate. Note that when the coupling capacitance C_κ to the transmission line decreases, the impedance mismatch between the resonator and its environment increases so that the damping rate κ is reduced.

In Eq. (42), we suppose that the environment is Markovian. In appendix B.2, we show that this imposes to choose a coarse time step $\mathrm{d}t$ that respects the hierarchy

$$\frac{1}{\omega_r} \ll \mathrm{d}t \ll \frac{1}{\kappa}. \tag{44}$$

In this formalism, a coherent drive through one of the lines can be taken into account by adding up to the hamiltonian of the cavity a drive term [67]

$$H_d = \hbar(\epsilon_d e^{-i\omega_d t}a^\dagger + \epsilon_d^* e^{+i\omega_d t}a), \tag{45}$$

where the displacement rate ϵ_d is proportional to the drive amplitude, so that $H = H_0 + H_d$.

In appendix B.2, we show the Heisenberg picture counterpart of the master equation (42) for the field amplitude,

$$\partial_t a = \frac{1}{i\hbar}[a, H_0] - \frac{\kappa}{2}a + \sqrt{\kappa}a_{in}, \tag{46}$$

which is the quantum Langevin equation. We also define the incoming and outgoing mode operators and show that a_{in}[5] and a_{out} are linked by the input/output relation

$$\sqrt{\kappa}a = a_{in} + a_{out}. \tag{47}$$

2.2.2.3 *Choosing the coupling to the lines*

Using the quantum Langevin equation, we show in this section how to infer the coupling rates through the ports of the cavity from its scattering properties.

In our devices, 2 tunnels are drilled through the upper wall of the cavity and two standard SMA connectors whose pins go through these tunnels are mounted on the

5 Equivalence with the Schrödinger picture is made by setting $\epsilon_d e^{-i\omega_d t} = i\sqrt{\kappa}\langle a_{in}\rangle$ in Eq. (45).

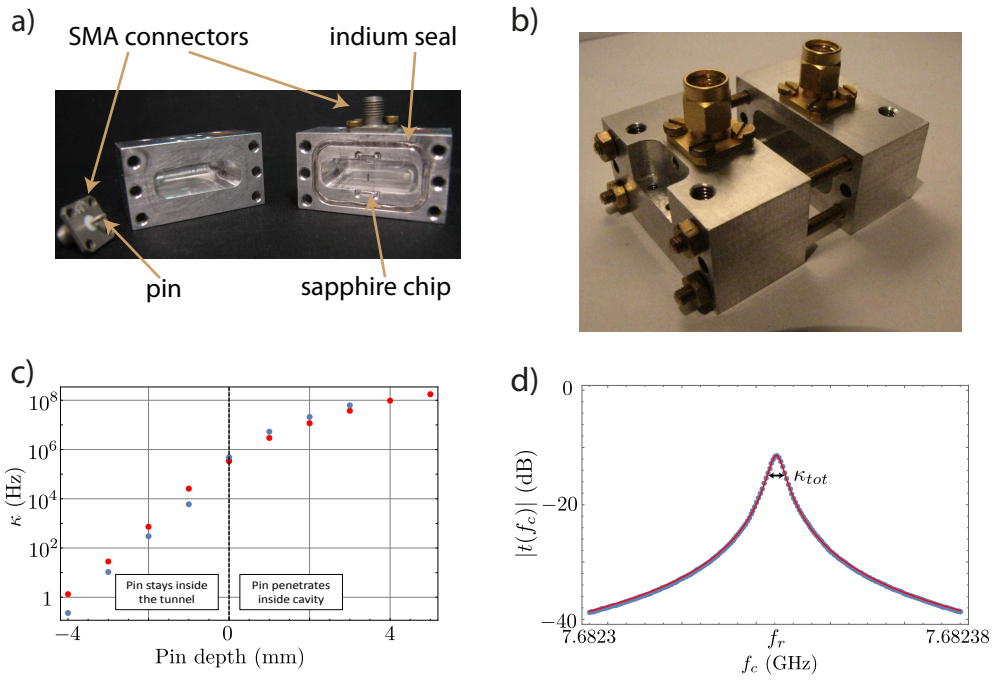

Figure 10: a) Picture of the 2 halves of the cavity and SMA connectors. A transmon qubit is fabricated on the sapphire chip. An indium thread is used to seal the two halves. b) Cavity with 2 connectors before closure. c) Measured (blue) and simulated (red) coupling rates through a port as a function of the pin length inside the cavity. d) Transmission measurement (blue dots) on the aluminum cavity at fridge base temperature (20 mK). Coupling through the ports was calibrated at room temperature. Red line: fit with internal losses rate $\kappa_L = 2.6$ kHz. Internal quality factor is $Q = f_r/\kappa_L \simeq 2.5 \times 10^6$

.

cavity (see Fig. 10a). These pins interact capacitively with the cavity modes. Connecting a coaxial line on these connectors, we get the situation described in Appendix B.2. Moreover, by changing the length of the pins so that their tip stays in the tunnel or dips inside the cavity, one can modulate the coupling rates κ_1 and κ_2 between the cavity and lines 1 and 2 over more than 8 orders of magnitude (see Fig. 10c). The internal losses can be seen as a virtual third line that cannot be monitored with a coupling rate κ_L. With this 3-port situation, the Langevin equation becomes

$$\partial_t a = \frac{1}{i\hbar}[a, H_0] - \frac{\kappa_1 + \kappa_2 + \kappa_L}{2} a + \sqrt{\kappa_1} a_{in,1} + \sqrt{\kappa_1} a_{in,2} + \sqrt{\kappa_1} a_{in,L}, \tag{48}$$

with the input/output relations

$$\sqrt{\kappa_i} a = a_{in,i} + a_{out,i} \quad (i = 1, 2, L). \tag{49}$$

When driving the harmonic cavity mode with a classical source at zero temperature, the intra cavity field is a coherent state $|\alpha\rangle$[6]. If we drive only through port 1 at an

6 On the Fock state basis, it reads $|\alpha\rangle = e^{-\frac{|\alpha|^2}{2}} \sum_{n=0}^{+\infty} \frac{\alpha^n}{\sqrt{n!}} |n\rangle$

amplitude $\alpha_{in,1}$while line 2 and the cavity dissipative part are at zero temperature, the equation for the now classical fields becomes

$$\dot{\alpha}(t) = -i\omega_r\alpha(t) - \frac{\kappa_1+\kappa_2+\kappa_L}{2}\alpha(t) + \sqrt{\kappa_1}\alpha_{in,1}(t), \tag{50}$$

which reads in the spectral domain

$$\alpha(\omega) = \frac{2\sqrt{\kappa_1}}{\kappa_1+\kappa_2+\kappa_L-2i(\omega-\omega_r)}\alpha_{in,1}(\omega). \tag{51}$$

Using the input/output relations, we get the scattering coefficients of our cavity

$$\begin{cases} S_{11}(\omega) \overset{\text{def}}{=} \dfrac{\alpha_{out,1}}{\alpha_{in,1}} = \dfrac{\kappa_1-\kappa_2-\kappa_L+2i(\omega-\omega_r)}{\kappa_1+\kappa_2+\kappa_L-2i(\omega-\omega_r)} & \text{(reflection)} \\ S_{21}(\omega) \overset{\text{def}}{=} \dfrac{\alpha_{out,2}}{\alpha_{in,1}} = \dfrac{2\sqrt{\kappa_1\kappa_2}}{\kappa_1+\kappa_2+\kappa_L-2i(\omega-\omega_r)} & \text{(transmission)} \end{cases}. \tag{52}$$

We can characterize precisely the coupling strengths through the ports and the internal losses of the cavity by measuring the reflection coefficients on the ports 1 and 2 and the transmission coefficient from 1 to 2 as a function of ω. The internal quality factors of our cavity have been measured to be $Q \sim 2.5\times10^6$ for aluminum and $Q \sim 40000$ for the copper at 20 mK and $|\alpha| \sim 1$.

2.2.3 *Transmon qubit in 3D cavity*

2.2.3.1 *Transmon regime*

The transmon is made of a single $Al/Al_2O_3/Al$ Josephson Junction (JJ) connected to 2 antennas. This circuit is fabricated through standard e-beam lithography techniques (see Sec. A.1) on a sapphire chip. The device is then enclosed in the 3D cavity (see Fig. 10a).

A tunnel junction between two superconducting electrodes at zero temperature has a single collective degree of freedom, which is the superconducting phase difference φ across the junction. It is linked to its electromagnetic phase Φ_J by

$$\varphi = \frac{\Phi_J}{\varphi_0} \bmod 2\pi, \tag{53}$$

where $\varphi_0 = \frac{\hbar}{2e}$ is the reduced flux quantum.
In practice, the electrodes have a finite capacitance C (see Fig. 11a). The corresponding charge energy $E_c = \frac{e^2}{2C}$ corresponds to 1 excess charge on one of the electrodes. Then, taking into account this shunting capacitance, the JJ forms a non-linear resonator that can store energy. Noting n the number of excess Cooper pairs ($Q = 2en$ for the corresponding circuit node), its hamiltonian reads

$$H = 4E_C(n-n_g)^2 - E_J\cos\varphi. \tag{54}$$

In this expression,

- from the commutation relation $[\Phi, Q] = i\hbar$, one gets the conjugation relation $[n, \exp i\varphi] = \exp i\varphi$[7].
- noting $\{|n\rangle, n \in \mathbb{Z}\}$ the charge states of the JJ, we have

$$-E_J \cos\varphi = -\frac{E_J}{2}(e^{i\varphi} + e^{-i\varphi}) = -\frac{E_J}{2}\sum_n (|n+1\rangle\langle n| + |n\rangle\langle n+1|), \quad (55)$$

  so that $\frac{E_J}{2}$ can be interpreted as the energy associated with the tunneling of a Cooper pair.
- the value of E_J depends on the geometry of the junction and on the thickness of the insulating barrier. Both parameters can be be adjusted during fabrication.
- n_g is an offset in the number of Cooper pairs due to the uncontrolled electrostatic environment of the junction (e.g. trapped charges in the substrate) that tends to attract charges on one of the electrodes.

The hamiltonian (54) is often referred to as the Cooper-Pair Box hamiltonian. It is exactly solvable in terms of Mathieu functions [68]. The energy levels depend on the charge offset n_g so that charge offset fluctuations induce decoherence. However, the sensitivity of energy levels on n_g decreases exponentially with $\frac{E_J}{E_C}$. For $\frac{E_J}{E_C} \sim 80$, we reach the *transmon* regime [12, 69, 70], in which this dispersion with n_g becomes negligible. In our geometry, E_C can be increased independently of E_J by increasing the size of the antennas that form a large capacitance shunting the junction. As depicted on Fig. 11c, this shunting capacitance simply renormalizes the junction intrinsic capacitance and lowers the charging energy. Moreover, in this regime, eigenstates will be quite close to phase states. In other words, the charge Q is uncertain, whereas Φ is well defined, in agreement with the Heisenberg uncertainty principle.

We can then represent the energy levels of the circuit in a cosine potential (Fig. 11b) as a function of Φ_J. At low temperature ($k_B T \ll \hbar\omega_{eg}$), its state is bounded at the bottom of a well. It can therefore be understood as an anharmonic oscillator whose magnetic term reads

$$H = E_J \frac{\Phi^2}{2\varphi_0^2} + H_1. \quad (56)$$

The first term correspond to the energy stored in an inductor $L_J = \varphi_0^2/E_J$ and, developing up to the fourth order in Φ/φ_0,

$$H_1 = -\frac{E_J}{24}\frac{\Phi^4}{\varphi_0^4} \quad (57)$$

is a purely non linear perturbation. We represent it as a spider element [71] in the circuit of Fig. 11b. Due to this term, the levels of the oscillator are not evenly spaced (Fig. 11c) so that we can address specifically the transition between ground $|g\rangle$ and first excited $|e\rangle$ states. These will be the 2 states of our qubit.

7 In the case of the transmon, the variable φ is strictly speaking compact. φ and $\varphi + 2\pi$ are the same physical state and equivalently, n is a well-defined integer. Therefore, there is no operator ϕ and only periodic operators such as $\exp i\varphi$ or $\cos\varphi$ exist.

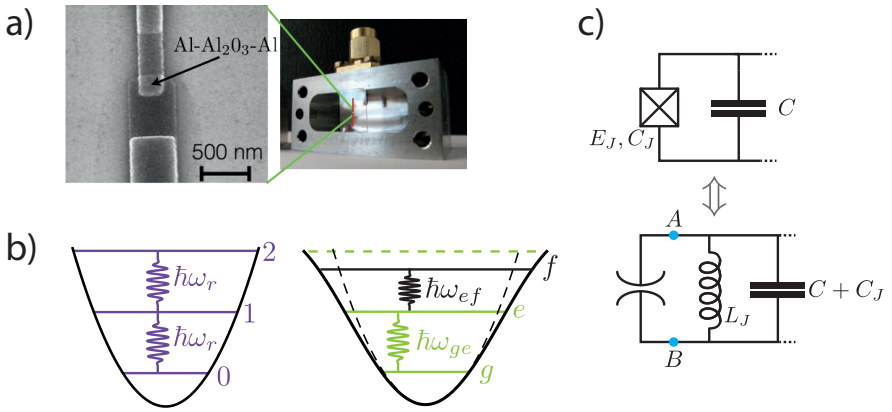

Figure 11: a) E-beam microscope image of a Josephson junction fabricated on a sapphire chip. It links 2 aluminum antennas (each $\sim 1.5 \times 0.05$ mm on this sample) also on chip, and colored in red on the picture. The sapphire substrate is pinched between the two cavity halves. b) Representation of the cavity mode (to the left) and transmon (to the right) energy levels in their electromagnetic phase potentials. Cavity levels, in a parabolic potential, are evenly spaced, in contrast with transmon levels in a cosine potential. The first transmon transition can be addressed selectively. c) Josephson junction circuit element in parallel with a large shunting capacitance C that limits sensitivity to charge fluctuations. The small intrinsic Josephson capacitance ($C_J \sim$ 1fF) only slightly contributes to this capacitance. In the transmon regime, the junction can be seen as an inductor $L_J = \varphi_0^2/E_J$ in parallel with a purely non linear element ("spider" symbol) that will lead to the perturbation H_1 in its hamiltonian.

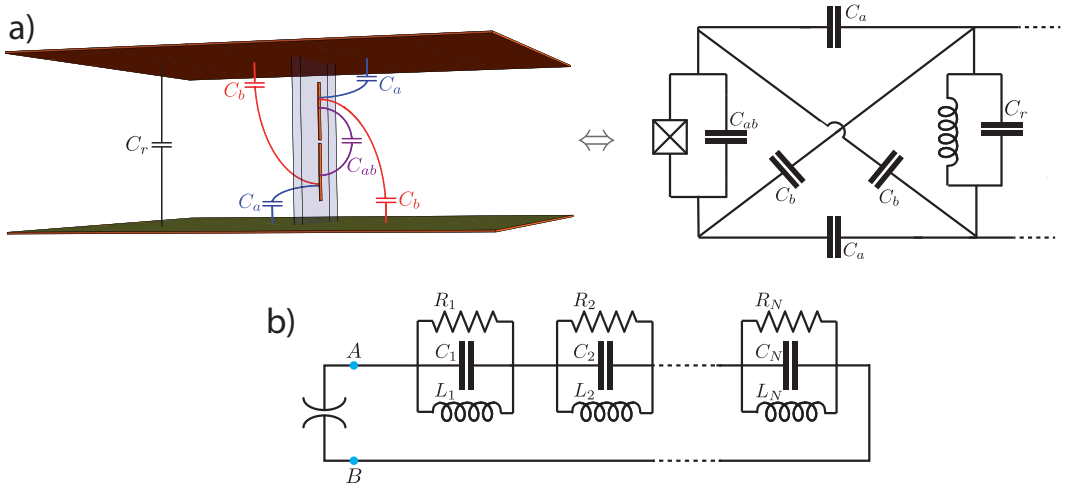

Figure 12: a) Schematic representation of the capacitive interactions created by the antennas with a single cavity mode. The coupling capacitances C_a, C_b and the cavity capacitance C_r depend on the cavity mode under consideration. On the electrical circuit, only one mode of the cavity is represented. b) Foster equivalent circuit seen by the non-linear element, taking into account N cavity modes.

The antennas play another crucial role in the setup, which is capacitively coupling the JJ to the cavity modes. A simplified representation of the capacitive network in-

side the cavity is represented on Fig. 12a. It only takes into account a single mode of the cavity. However, the same pattern applies for the coupling of the JJ mode to any cavity mode: the interaction is that of a dipole in the sense that the direct coupling capacitance C_a from an antenna to the closest cavity wall is shunted by C_b, the one of the other antenna to same wall. Thus, the effective coupling capacitance between the junction and a given mode ($\sim \frac{C_a - C_b}{2} \simeq 1$ fF) remains in practice more than an order of magnitude lower than the one of the coupled modes (respectively $\sim C_{ab}$ and C_r, which are both of about 100 fF).
Note that in the limit of a small gap between the antennas compared to their length, the gap size has a very small impact on these capacitances. Similarly, the sapphire substrate, which has a dielectric constant $\epsilon_r \simeq 10$, only slightly increases the capacitances because of its small thickness compared to the cavity size. A full analysis of this network could lead us to the full hamiltonian of the system.

Though this analysis can give some physical insight on the system's properties (see Sec. 2.2.3.3), it becomes very complex as one wants to include the effect of higher cavity modes, and it needs to account for the distortion of these modes due to the presence of the antennas. Moreover, the intrinsic quantities on which it will depend are not directly measurable in our system. We will rather derive the hamiltonian of the system following a Black-Box Quantization method[62, 72, 73].

2.2.3.2 *Circuit Black Box Quantization*

The general principle of the BBQ method is the following. In the transmon regime, the JJ is decomposed as an inductor in parallel with a purely non linear "spider" element. This element will be treated perturbatively. The rest of the circuit, which is made of the linear part of the junction with its shunting capacitance and N modes of the cavity, can be decomposed as N+1 LC resonators in series (Fig. 12b). This so-called Foster decomposition is equivalent to diagonalizing the N+1 coupled modes into N+1 hybrid but decoupled modes. First neglecting the losses represented by the R_p's, the hamiltonian of this system reads

$$H_{lin} = \sum_{p=1}^{N+1} \hbar\omega_p (a_p^\dagger a_p + 1/2), \tag{58}$$

$\omega_p = \frac{1}{\sqrt{L_p C_p}}$ being the resonant pulsation of mode p, $Z_p = \sqrt{\frac{L_p}{C_p}}$ its characteristic impedance and $a_p = \sqrt{\frac{1}{2\hbar Z_p}}\Phi_p + i\sqrt{\frac{Z_p}{2\hbar}}Q_p$ the corresponding annihilation operator. The eigenstates are definite numbers of excitations for each of these oscillators $|n_1, n_2, ...n_{N+1}\rangle$. From Kirchoff laws, we find the following relation for the flux at the poles of the spider element,

$$\Phi = \sum_{p=1}^{N+1} \Phi_p. \tag{59}$$

We can now treat the leading order hamiltonian H_1 Eq. (57) of the spider element as first order perturbation, assuming non-degenerate modes. Then, expanding it using

Eq. (59) and keeping only the terms that conserve the number of excitations in each mode and using the commutation relation $[a_p, a_p^\dagger] = 1$, it reads

$$H_1 = \sum_p \Delta_p n_p + \frac{1}{2}\sum_{p,p'} \chi_{pp'} n_p n_{p'}, \tag{60}$$

$n_p = a_p^\dagger a_p$ being the excitation number operator of mode p. Here, $\Delta_p = -\frac{e^2}{2L_J}[Z_p \sum_{p'} Z_{p'} - \frac{Z_p^2}{2}]$ is a slight correction to the frequencies of the oscillators and

$$\begin{cases} \chi_{pp} &= -\dfrac{L_p}{L_J}\dfrac{C_{||}}{C_p} E_{C_{||}} & \text{the anharmonicity (self-Kerr) of mode p} \\ \chi_{pp'} &= 2\sqrt{\chi_{pp}\chi_{p'p'}} & \text{the pull (cross-Kerr) between modes p and p'} \end{cases}. \tag{61}$$

where $C_{||} = C_{ab} + C_J$ is the capacitance shunting the junction[8]. Thus, all the oscillators being hybridized, they inherit some anharmonicity from the junction and the number of excitations in an oscillator shifts the resonant frequency of the others. This last behavior enables to readout non destructively the state of the qubit (see Sec. 3.2.3) or conversely to measure the number of photons in a cavity mode (see Sec. 7.2.1).

However, in a regime in which the coupling between the physical modes is small and the detuning important, which is the case in practice, one particular mode (that we label q) has a much higher anharmonicity than the others: $\chi_{qq} \gg \chi_{p'p'}$ for $p' \neq q$. It can be interpreted as the mode of the junction (and its capacitance) *dressed* by the cavity modes.

In order to connect with the notations used in the following section, let us note that this much larger anharmonicity for the qubit mode implies that $\forall p' \neq q$,

$$\frac{L_{p'}}{C_{p'}} \gg \frac{L_q}{C_q} \tag{62}$$

Thus, the impedances Z_p of the dressed cavity modes seen by the junction are much greater than the ones of the original bare modes which are only weakly coupled with the junction through small capacitances. Then, considering the low and high frequency limit of the circuit on Fig. 12b, we find that

$$\begin{cases} \sum\limits_p L_p &= L_J & \text{(from the low frequency limit)} \\ \sum\limits_p C_p^{-1} &= C_\Sigma^{-1} & \text{(from the high frequency limit)} \end{cases}, \tag{63}$$

where C_Σ is the total capacitance in parallel with the junction[9]. It follows that the qubit resonator inductance reads, to the first order, $L_q \simeq L_J$ and its capacitance $C_q \simeq C_\Sigma$. Letting $E_C = \frac{e^2}{2C_\Sigma}$ the corresponding charging energy, the qubit mode parameters are

$$\begin{cases} f_q &= \frac{1}{h}\sqrt{8E_J E_C} & \text{(resonance frequency)} \\ \alpha &= E_C & \text{(anharmonicity)} \end{cases}. \tag{64}$$

8 this convention is not the one used in [62], but $C \times E_C$ does not depend on C

9 $C_\Sigma = C_{||} + C_c$ in the following section

Dissipation or leakage through external ports can now be modeled by resistors R_p on each of these modes. Note that a more general model for losses goes beyond the Foster decomposition[73]. These resistors induce non coherent decay of each mode, so that we get the Lindblad master equation for the whole system

$$\frac{\mathrm{d}\rho(t)}{\mathrm{d}t} = -\frac{i}{\hbar}[H_0 + H_1, \rho] + \sum_{p=1}^{N+1} \kappa_p \mathcal{D}[a_p]\rho, \tag{65}$$

with $\kappa_p = \omega_p \frac{Z_p}{R_p}$ (see Eq. (43)). Note that even in absence of internal dissipation inside the junction, it inherits some dissipative part due to the hybridization to cavity modes[10]. This relaxation of the "cavity part" of the qubit into the probe lines is known as the Purcell effect [15, 16, 17].

This very general description led us to a simple master equation. If one includes higher order terms in H_1, it can account for more subtle non-linear effects such as cross-Kerr shifts in the straddling regime[12, 74, 75]. All the terms of the equation can be measured independently. We will now see how this model can be used to predict the characteristic values of a system according to its geometry, and compare it to a less refined but more intuitive 2-mode model.

2.2.3.3 *Designing the experiment: BBQ VS two-mode model*

Now that the form of the master equation has been established, we want to connect the physical parameters of the experiment (dimensions of the cavity, length of the antennas, inductance of the JJ...) to the effective parameters of this equation (ω_p, κ_p...). One of the main advantages of using 3D cavities in circuit-QED experiments is that the electromagnetic environment of the Josephson junction is well controlled and can be simulated exactly by performing full 3D electromagnetic simulations using finite elements methods (see Sec. A.3). Thus, inputing the above physical parameters in the model and replacing the JJ by a port with an attached lumped inductor, one can simulate the response of the linear part of the system to an excitation at any frequency ω. Then, the resonance frequencies can be identified and it comes directly [62] from the decomposition depicted in Fig. 12b that[11]

$$\begin{cases} R_p &= \dfrac{1}{\mathrm{Re}[Y(\omega_p)]} \\ C_p &= \frac{1}{2}\mathrm{Im}[Y'(\omega_p)] \end{cases}. \tag{66}$$

This can in principle determine the full behavior of the system for a given set of parameters. We then tune the physical parameters of the system to get the desired effective parameters in the master equation. However, dissipation being very small, the response of the system is nearly divergent at resonances and the measurement of

10 Here, non radiative decay, thermal excitation and pure dephasing of the qubit are not taken into account.

11 valid for small dissipation, that is $R_p \gg Z_p$, which is the case for our experiments

$R_p \to \infty$ gets imprecise for reasonable simulation times. Moreover, it is difficult with this black-box method to know on which physical parameter to act in order to get to the desired effective parameters.

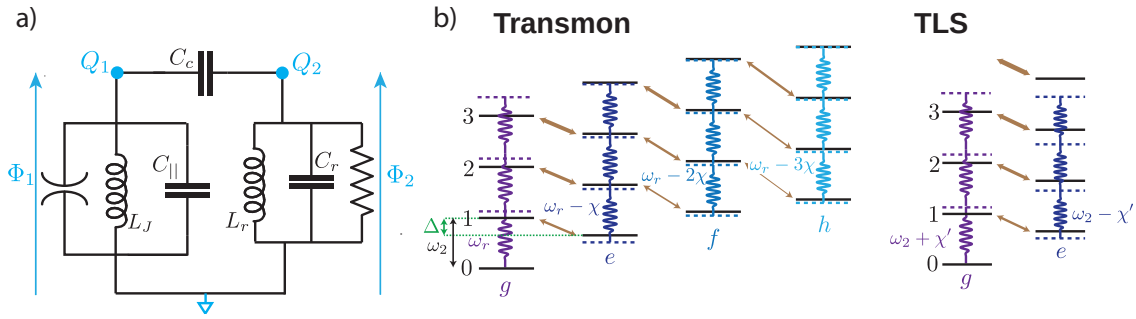

Figure 13: a) Equivalent circuit for a junction mode coupled to a single mode of the cavity. Fluxes and charges on the nodes are conjugated $[\Phi_i, Q_i] = i\hbar$ for $i = 1, 2$. b) Combined energy level diagram for the two coupled modes. Cavity levels are noted with numbers (0,1,2,...), transmon levels with letters (g,e,...). The cavity pull χ can be understood as repulsion (double head brown arrows) between levels: original coupled levels (black lines) become hybrid ones (dotted lines). If $\omega_r > \omega_q$, hybridization increases cavity resonant frequency $\omega_r > \omega_{bare}$. Cavity pull is reduced for transmon compared to a two-level system (Jaynes-Cummings hamiltonian) due to higher levels.

To enable an analytic approach, we limit ourselves to the first resonant mode of the cavity. This is particularly relevant in the experiments described throughout this thesis since the qubits considered are chosen to resonate at $f_q \sim 4 - 6$ GHz which is below the first cavity mode TE110 at $f_r \sim 8$ GHz. The electrical field direction for this mode is along the antenna axis and maximum amplitude of the field occurs at the centre of the cavity where the qubit is located. The qubit is therefore much better coupled to this mode than to the next excited modes TE210, TE120, TE011 or TE101 at $f \sim 12 - 15$ GHz that have either a node at the centre of the cavity or an orthogonal electric field [76]. Thus the next coupled modes are far detuned and hybridize only marginally with the qubit mode.

With only one cavity mode only, the equivalent circuit is depicted on Fig. 13, where the effective capacitances are $C_c = \frac{C_a - C_b}{2}$ and $C_{||} = \frac{C_a + C_b}{2} + C_{ab}$ (in reference to Fig. 12c). It is then possible to calculate analytically the transmon energy levels. A detailed calculation by Kurtis Geerlings, based on prior study by Shyam Shankar and Michel Devoret, can be found in Sec.2.2.1 of [77]. Here, we outline briefly the used method and give its main results.
The hamiltonian of the circuit reads

$$H = \frac{\Phi_2^2}{2L_r} + \frac{Q_r^2}{2C_r} - E_J \cos\frac{\Phi_1}{\varphi_0} + \frac{Q_{||}^2}{2C_{||}} + \frac{Q_c^2}{2C_c}, \tag{67}$$

where Q_r (resp. Q_c, $Q_{||}$) is the charge on a plate of the capacitor C_r (resp. C_c, $C_{||}$), linked to the canonically conjugated nodes variables $\Phi_{1,2}$ and $Q_{1,2}$ by

$$\begin{cases} Q_1 &= Q_{||} - Q_c \\ Q_2 &= Q_r + Q_c \end{cases} . \tag{68}$$

Introducing the corresponding annihilation operators a_1 and a_2[12] and assuming the transmon regime $\frac{e^2}{2(C_{||}+C_c)} = E_C \ll E_J$ and in the rotating wave approximation, the hamiltonian transforms into

$$H = \hbar\omega_2(a_2^\dagger a_2 + 1/2) + \hbar\omega_1(a_1^\dagger a_1 + 1/2) + \hbar g(a_2^\dagger a_1 + a_2 a_1^\dagger) - \frac{E_c}{12}(a_1 + a_1^\dagger)^4, \tag{70}$$

with, in the limit $C_r \gg C_c$,

$$\begin{cases} \omega_2 &= \dfrac{1}{\sqrt{L_r C_r}} \\ \omega_1 &= \sqrt{8E_J E_C}/\hbar \\ g &= \dfrac{C_c}{2\sqrt{C_r(C_{||}+C_c)}}\sqrt{\omega_1\omega_2} \end{cases} . \tag{71}$$

We recognize the hamiltonian of two coupled oscillators, one being anharmonic. We can then define 2 uncoupled but hybridized oscillators a and b. In the experiment, the detuning $\Delta = \omega_r - \omega_q$ is much larger than g, which is called the dispersive regime. In this regime, oscillator a is a cavity-like mode dressed by a small qubit part, and b a qubit-like mode dressed by the cavity. The hybrid annihilation operators read

$$\begin{cases} a &\simeq -a_2 + \frac{g}{\Delta} a_1 \\ b &\simeq \frac{g}{\Delta} a_2 + a_1 \end{cases} . \tag{72}$$

These operators obey canonical commutation relations up to the first order in $\frac{g}{\Delta}$. The corresponding resonance frequencies ω_r and ω_q are slightly renormalized compared to the bare resonance frequencies ω_2 and ω_1 as

$$\begin{cases} \omega_r &\simeq \omega_2 + \frac{g^2}{\Delta} \\ \omega_q &\simeq \omega_1 - \frac{g^2}{\Delta} \end{cases} . \tag{73}$$

Note that experimentally, we only have access to these resonance frequencies. They correspond to the ω_p's of the BBQ Foster decomposition.

12

$$\begin{cases} a_2 &= \sqrt{\frac{1}{2\hbar}\sqrt{\frac{C_r}{L_r}}}\Phi_2 + i\sqrt{\frac{1}{2\hbar}\sqrt{\frac{L_r}{C_r}}}Q_2 & \text{cavity mode} \\ a_1 &= \sqrt{\frac{1}{2\hbar}\sqrt{\frac{C_c+C_{||}}{L_J}}}\Phi_1 + i\sqrt{\frac{1}{2\hbar}\sqrt{\frac{L_J}{C_c+C_{||}}}}Q_1 & \text{junction mode} \end{cases} \tag{69}$$

Now treating the non-linear term $-\frac{E_c}{12}(a_1 + a_1^\dagger)^4$ as a perturbation, one finds a hamiltonian of the same form as $H_{lin}^{(58)} + H_1^{(60)}$ with[13]

$$\begin{cases} -\alpha & \stackrel{\text{def}}{=} & \chi_{qq} & = & -\frac{1}{\hbar}E_C \\ -\chi & \stackrel{\text{def}}{=} & \chi_{rq} & = & -2\alpha\frac{g^2}{\Delta^2} \end{cases} . \tag{74}$$

Another effect of this hybridization is that the drive hamiltonian (45) splits into two parts:

$$H_d = -\hbar(\epsilon_d e^{-i\omega_d t}a^\dagger + \epsilon_d^* e^{+i\omega_d t}a) + \hbar\frac{g}{\Delta}(\epsilon_d e^{-i\omega_d t}b^\dagger + \epsilon_d^* e^{+i\omega_d t}b), \tag{75}$$

so that both cavity and qubit can be driven through the cavity ports. Moreover, adding up a resistor in parallel to the cavity LC resonator to take into account the losses into the lines, one gets,

$$\gamma_{1,\text{Purcell}} \simeq \kappa\frac{g^2}{\Delta^2}, \tag{76}$$

where $\gamma_{1,\text{Purcell}}$ and κ are respectively the decay rates of qubit and of the cavity associated with photon leakage out of the cavity [14]. With this simple formula and Eq. (74), one can compute the expected bound on T_1 due to the Purcell effect by measuring χ, α and κ on the system. It has been shown however to be inaccurate. Indeed, qubit decay time measured to exceed $1/\gamma_{1,\text{Purcell}}$ computed with this simple model have been reported in [77], and have also been observed with the qubits used in this thesis (see Sec.A.1). A more rigorous approach consists in characterizing the qubit electromagnetic environment with simulations (see Sec. A.3) and using [78]

$$\gamma_{1,\text{Purcell}} = \frac{\text{Re}[Y[\omega_q]]}{C_{||} + C_c}, \tag{77}$$

which generalizes Eq. (43).

This analytical treatment gives us some insight on the constraints and choosable parameters of our system.

- In order to remain in the transmon regime, we impose $E_C \leq 50E_J$.
- We want thermal excitation to remain as low as possible at refrigerator base temperature. We thus need that $hf_q \ll k_B T$, so that $\frac{1}{h}\sqrt{8E_J E_C} \geq 4$ GHz.
- To remain in the situation described above of a qubit coupled to a single cavity mode, we want the qubit to resonate at lower frequency than the cavity first mode. The coupling strength being set (see below), we need a sufficiently large detuning in order for the interaction to be dispersive. In practice, all the qubits described in this thesis are designed so that $f_q \leq 6$ GHz.

13 α and χ are chosen to be positive so that $\omega_{ef} - \omega_{ge} = -\alpha$ and $\omega_{r,e} - \omega_{r,g} = -\chi$ with $\omega_{r,g}$ and $\omega_{r,e}$ defined in Eq. (81)

14 This can be understood considering that in Eq.(72), $\frac{g^2}{\Delta^2}$ is the participation ratio of the cavity photon number (leaking out into the lines with rate κ) in the qubit-like mode excitation.

- To use the anharmonic oscillator as a qubit, we need to address specifically its first transition on a time scale much shorter than all decoherence (typically $T_{1,2} \sim 10\ \mu$s). This sets a lower bound for the anharmonicity: $E_C = \alpha \geq 100$ MHz.

These requirements put strong constraints on the choice of E_C. Therefore, all the qubits used in the experiments described in this thesis have an anharmonicity $\alpha \simeq 2\pi \times 150 - 200$ MHz. Resonance frequency is then finely tuned by adjusting E_J through the size of the Josephson Junction.
This value $\alpha = E_C$ much constraints the size of the antennas, which also determines the coupling capacitances and thus the value of g. However, some margin exists by tuning the aspect ratio of the antennas. Effectively, the shunting capacitance C_{ab} (Fig. 12d) depends mostly on the surface of the antennas whereas the coupling capacitance $C_c \propto C_a - C_b$ essentially depends on their length. In practice, we used 2 different geometries in the experiments presented here, both leading to the same charging energy E_C mentioned above

- 1.5×0.05 mm leading to $g \sim 2\pi \times 300$ MHz
- 1×0.4 mm leading to $g \sim 2\pi \times 200$ MHz

These orders of magnitude do not take into account a correction in $E_J^{1/4}$ (see Eq. (71)). The last tunable parameter is the cavity damping rate κ, which is set by the connector pin length (Fig. 10 a). As we will see in the next chapter, it can be set in order to optimize the readout efficiency of the qubit. A list of measured qubits and their properties is presented on Tab.3. We can summarize the choice of parameters and their physical origin in the following table.

Parameter	Value Range	Control
E_C/h	150-200 MHz	Antenna area
E_J/h	10-25 GHz	Junction size
f_q	4-6 GHz	$\sqrt{8E_JE_C}/h$
f_r	7.5 GHz	Cavity dimensions
g	200-300 MHz	Antennas length
κ	1 kHZ - 10 MHz	Connector pin length

A final constraint revealed by this model is the fact that, in order to remain in the dispersive regime of hamiltonian (70), one needs the detuning Δ to be much larger than the Rabi splitting $2g\sqrt{n+1}$, where $n+1$ is the number of photons inside the cavity. We then find that the photon number should remain much smaller than a critical value n_c in order for the cavity and qubit not to exchange energy. In practice, cavity photons will be used to readout the qubit state and this readout is non destructive only if

$$n \ll n_c = \frac{\Delta^2}{4g^2}. \tag{78}$$

Within this range of parameters, we now have a system implementing the open two-level system described in Sec. 2.1. Indeed, probing the transmon only around its first

transition frequency effectively transforms the anharmonic oscillator into a qubit. We then get an effective Lindblad master equation for the qubit coupled to a single cavity mode [79]

$$\frac{\mathrm{d}\rho(t)}{\mathrm{d}t} = -\frac{i}{\hbar}[H,\rho] + \kappa\mathcal{D}[a]\rho + \gamma_{1,\mathrm{Purcell}}\mathcal{D}[\sigma_-]\rho, \tag{79}$$

with

$$\begin{aligned} H &= \hbar\omega_r a^\dagger a + \hbar\tfrac{\omega_q}{2}\sigma_z - \hbar\tfrac{\chi}{2}a^\dagger a\sigma_z \\ &\quad + \hbar(\epsilon_c e^{-i\omega_c t}a^\dagger + \epsilon_c^* e^{+i\omega_c t}a) + \hbar(\epsilon_d e^{-i\omega_d t}\sigma_+ + \epsilon_d^* e^{+i\omega_d t}\sigma_-). \end{aligned} \tag{80}$$

The frequencies ω_r and ω_q are slightly modified compared to Eq. (71) since they are the dressed cavity and qubit frequencies. In the drive part of the hamiltonian, we distinguished a tone at frequency ω_c around ω_r and a tone at ω_d around ω_q. Note that, according to Eq. (75), for identical drive powers P_{drive} referenced at the cavity input port, $\epsilon_d \ll \epsilon_c$ since $\epsilon_d = \frac{g}{\Delta}\epsilon_c \propto \sqrt{P_{\mathrm{drive}}}$. Finite anharmonicity of the cavity-like mode is neglected, but its value can be computed from Eq. (61). Finally, compared to the exact equation Eq. (65), other cavity modes are traced out. Extra modes result in an increase of $\gamma_{1,\mathrm{Purcell}}$ and the apparition of dephasing terms in Eq. (80), but this will be taken into account later on as unmonitored sources of relaxation and decoherence.

2.2.4 *AC Stark shift and measurement induced dephasing*

In the previous section, we saw that the free evolution of our system entangles the qubit and cavity modes. Indeed, in the hamiltonian (80), the cross-Kerr term $-\hbar\frac{\chi}{2}a^\dagger a\sigma_z$ can be seen as a qubit state dependent shift of the cavity resonance frequency. Thus,

$$\begin{cases} \omega_r \rightarrow \omega_{r,g} \overset{\mathrm{def}}{=} \omega_r + \frac{\chi}{2} & \text{if qubit state is } |g\rangle \\ \omega_r \rightarrow \omega_{r,e} \overset{\mathrm{def}}{=} \omega_r - \frac{\chi}{2} & \text{if qubit state is } |e\rangle \end{cases}. \tag{81}$$

If we probe the cavity in transmission with, say, a coherent drive at frequency ω_c near ω_r, such as the one in hamiltonian (80), the transmitted field will acquire a phase-shift dependent on the qubit state (see Eq. (52)). This will provide us with a non destructive measurement scheme for the σ_z operator of the qubit [80] as described in 3.2.3. In the present section, we focus on the back-action of this measurement on the conjugated operator, which is measurement induced dephasing of the qubit.

Let us first note that the same cross-Kerr term $-\hbar\frac{\chi}{2}a^\dagger a\sigma_z$ can, alternatively to Eq. (81), be seen as a cavity photon number dependent shift of the qubit frequency. When the cavity mode is in Fock state $|n\rangle$,

$$\omega_q \rightarrow \omega_{q,n} \overset{\mathrm{def}}{=} \omega_q - n\chi. \tag{82}$$

Driving the cavity with a coherent tone at ω_c puts the cavity mode in a coherent state as well (see Eq. (51)), so that the number of photons is not determined. If we do not collect and measure the output field from the cavity, the information on the cavity is dismissed. This procedure is taken into account by tracing out the cavity state. Then,

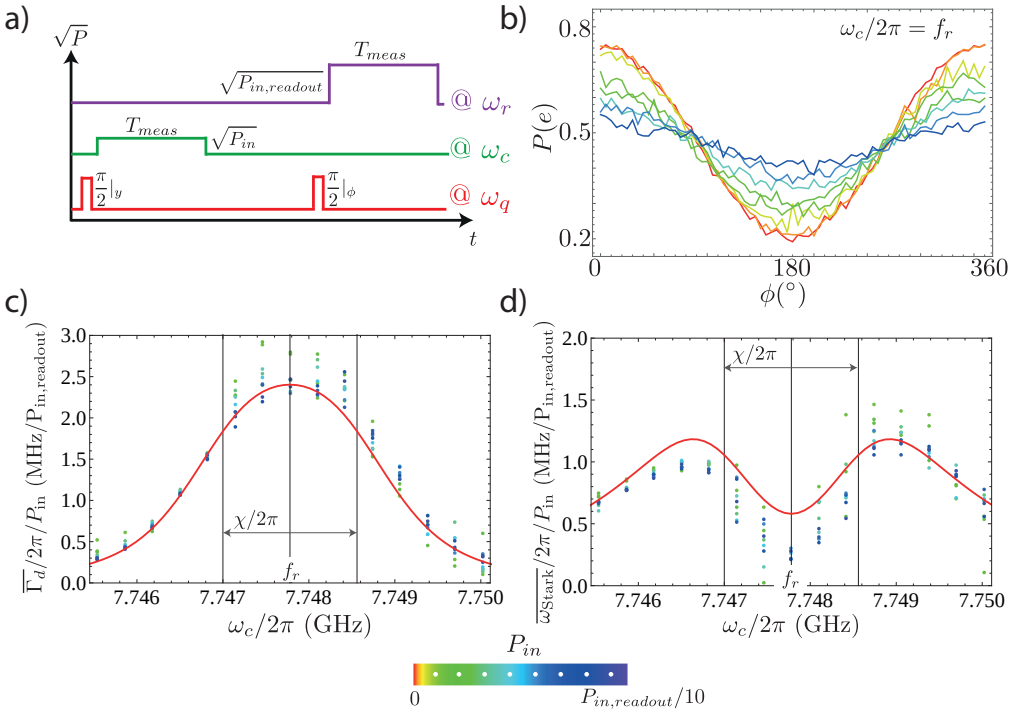

Figure 14: Measurement induced dephasing and ac-Stark shift. a) Scheme of the pulse sequence. The cavity pulse is arbitrarily chosen to have the same duration as the readout pulse at ω_r. The second $\pi/2$ pulse at ω_q is phase shifted by an angle ϕ compared to the initial $\pi/2$ pulse. b) Final occupation of the $|e\rangle$ state as a function of ϕ and for several cavity pulse powers encoded in color according to the color scale at bottom. The amplitude (resp. phase) of the oscillation is proportional to $\exp(-\overline{\Gamma_d}T_{meas})$ (resp. $\overline{\omega_{\rm Stark}}T_{meas}$), where $\overline{\Gamma_d}$ is the average extra dephasing rate (resp. $\overline{\omega_{\rm Stark}}$ the average frequency shift) at that power compared to $P_{\rm in} = 0$. c) For values of $P_{\rm in}$ varying from 0 to $P_{\rm in,readout}/10$, $\overline{\Gamma_d}$ as a function of ω_c. Red line: theoretical prediction using (87) with μ adjusted to $\frac{\mu}{2\pi} = 1.25$ MHz$/\sqrt{P_{\rm in,readout}}$. d) Idem for the ac-Stark shift $\overline{\omega_{\rm Stark}}$.

the qubit frequency becomes a stochastic variable and the qubit state gets dephased.

More quantitatively, starting from Eq. (79), Gambetta *et al.* have shown [21] how to derive a qubit master equation of the form (29). In the frame rotating at ω_c, the coherent states $|\alpha_g(t)\rangle$ (resp. $|\alpha_e(t)\rangle$) developing in the cavity when the qubit is in $|g\rangle$ (resp. $|e\rangle$) verify Eq. (50)[15]

$$\begin{aligned} \dot{\alpha_g}(t) &= i(\omega_c - \omega_r - \tfrac{\chi}{2})\alpha_g(t) - \tfrac{\kappa}{2}\alpha_g(t) + \epsilon_c \\ \dot{\alpha_e}(t) &= i(\omega_c - \omega_r + \tfrac{\chi}{2})\alpha_e(t) - \tfrac{\kappa}{2}\alpha_e(t) + \epsilon_c \end{aligned} \quad . \tag{83}$$

Thus, they find that the effective master equation for the qubit reads [21]

$$\frac{\mathrm{d}\rho(t)}{\mathrm{d}t} = -i[\frac{\omega_q + \omega_{\rm Stark}(t)}{2}\sigma_z, \rho] + \gamma_{1,\rm Purcell}\mathcal{D}[\sigma_-]\rho + \Gamma_d(t)\mathcal{D}(t)[\sigma_z]\rho, \tag{84}$$

15 For the sake of simplicity, compared to the hamiltonian (80), we shifted the drive term by $\frac{\pi}{2}$, that is $\epsilon_c \to i\epsilon_c$ with $\epsilon_c \in \mathbb{R}$

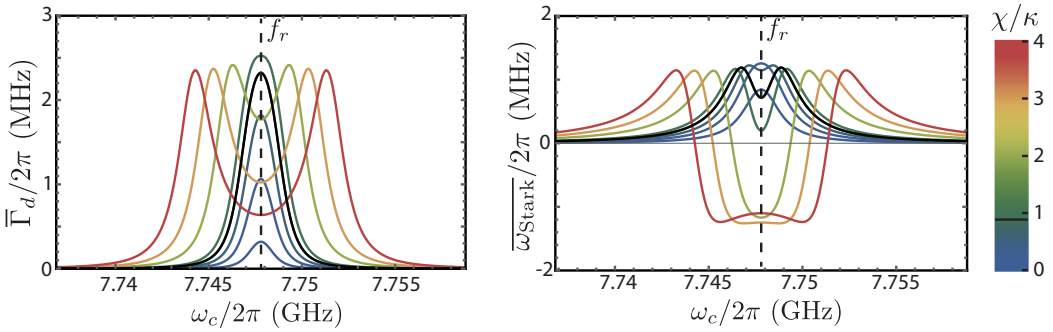

Figure 15: Numerical simulation of the average measurement induced dephasing (to the left) and AC Stark shift (to the right) for the readout pulse ($P_{\text{in}} = P_{\text{in,readout}}$) as a function of the probe frequency. The parameters of the qubit are the one of the experiment except for χ that is varied from $\kappa/5$ to 4κ (encoded in color). In black: experimental value of χ.

where

$$\begin{cases} \Gamma_d(t) &= \chi \text{Im}[\alpha_g^*(t)\alpha_e(t)] \\ \omega_{\text{Stark}}(t) &= \chi \text{Re}[\alpha_g^*(t)\alpha_e(t)] \end{cases}. \tag{85}$$

Note that counter-intuitively, when probing the cavity at ω_r, the qubit frequency is increased when driving the cavity near resonance in the regime $\chi < \kappa$ (see Fig. 15).

The measurement induced dephasing and Stark shift can be used to calibrate the attenuation of the line probing the cavity, that is the factor μ linking the power P_{in} at the refrigerator input to the amplitude displacement rate ϵ_c for the cavity field: $\epsilon_c = \mu\sqrt{P_{\text{in}}}$. This method is illustrated in [81] and on Fig. 14 (Qubit 1 in Tab. 3) as follows. The qubit is first prepared in a state close to $\frac{1}{\sqrt{2}}(|e\rangle + |g\rangle)$ by applying a fast $\frac{\pi}{2}$ pulse to rotate the qubit around the y axis of the Bloch sphere. This is done by driving at ω_q with a tone of large amplitude $\epsilon_d \in i\mathbb{R}$ during a time $t = \frac{\pi}{4|\epsilon_d|}$). A pulse of power P_{in}, frequency ω_c and duration T_{meas} is then sent to the initially empty cavity. After waiting long enough so that the cavity goes back to its ground state (in practice, $T_{wait} = 1\ \mu\text{s} \simeq 12/(2\pi\kappa)$), we measure the coherence of the qubit ρ_{eg}. This is done by reading out the qubit state (see Sec. 3.2.3.1) after a second $\frac{\pi}{2}$ pulse of phase ϕ. When averaging the result of this readout, and then repeating the experiment for $\phi \in [0, 2\pi]$, the resulting probability as a function of ϕ is a sinusoid whose amplitude is $|\rho_{eg}|$ and phase is $\text{Arg}[\rho_{eg}]$ (see Fig. 14b).

It is useful to define a quantity β that scales with $|\epsilon_c|^2$

$$\beta(\delta) = \chi \int_0^\infty \alpha_g^*(\delta, t)\alpha_e(\delta, t)/\epsilon_0^2 \text{d}t \quad \text{for} \quad \epsilon_c(t) = \theta(t)\theta(1-(t-T))\epsilon_0{}^{16}, \tag{86}$$

which can be numerically computed knowing χ and κ. Following Eq. (85), one gets

$$\rho_{eg}(\delta, P_{\text{in}}) \propto e^{-iP_{\text{in}}|\mu|^2 \text{Re}[\beta(\delta)]} e^{-P_{\text{in}}|\mu|^2 \text{Im}[\beta(\delta)]}. \tag{87}$$

When varying ω_c and P_{in}[17], measured coherences are in good agreement with (87) and consistent with $\frac{\mu}{2\pi} = 1.25\ \text{MHz}/\sqrt{P_{\text{in,readout}}}$[18], where $P_{\text{in,readout}}$ is the power of the tone used for the qubit readout as described in section 3.2.3. This leads to a number of photons inside the cavity in the stationary regime $n = 1.4$ photons when the readout pulse is turned on.

2.2.5 *Other decoherence channels and thermal effects*

Up to now, we have described relaxation and dephasing mechanisms for the qubit due to its coupling to the cavity and the transmission lines. We will see in the next chapter that these channels can be monitored and that we can use the information from this detection to recover our knowledge about the qubit state, that is purify the density matrix. In the ideal situation of perfect monitoring, on a single experiment and starting from a pure state, the qubit remains in a pure state that depends on the continuous measurement record. However, in practice, the system state is not perfectly known and has non-zero entropy. This comes from finite detection efficiency as described in the next chapter, but also from unknown (and thus unmonitored) decay and decoherence channels. In practice, in the Lindblad master equation (29), the experiments are described within the following constraints.

- $\Gamma_\downarrow \geq \gamma_{1,\text{Purcell}}$: there are extra-relaxation events associated with non radiative decay of the qubit. This could be due to dielectric losses in the substrate [77], trapped TLS resonant with the qubit [84, 85], quasi-particles in the superconducting aluminum thin film or cavity [86, 87, 88]...
- $\Gamma_\uparrow \geq 10\ \text{ms}^{-1}$ for aluminum cavities, $\Gamma_\uparrow \geq 2\ \text{ms}^{-1}$ for copper ones (see Tab. 3). The qubit is coupled to unknown hot baths that induce thermal excitation. This could be due to poor thermalization of the substrate phonons or of the systems responsible for cavity losses, or high frequency radiations coming down the control lines and creating "hot" quasi particles [89]. Note that these excitation rates increase when the cavity surface is not properly etched before the cool-down (see Sec. A.1.3).
- $\Gamma_\phi \geq 60\ \text{ms}^{-1}$, even when the cavity mode is empty[19]. This could be due to residual effect of the charge noise, interaction with non-resonant trapped two-level systems, flux noise in the effective superconducting loops formed by the Josephson junction conduction channels, photon shot-noise inside the cavity[77]... It can be accessed by measuring the coherence decay rate Γ_2 during a Ramsey interference experiment (see Fig 16a) and using the relation $\Gamma_2 = \frac{\Gamma_1}{2} + \Gamma_\phi$.

The first two terms can be determined experimentally by measuring the energy decay rate $\Gamma_1 = \Gamma_\downarrow + \Gamma_\uparrow$ (Fig. 16a) and the relative occupancy of the ground and excited

17 We limit ourselves to $P_{\text{in}} < P_{\text{in,readout}}/10$ in order for the first-order approximation (72) to be valid. For larger probe powers, Γ_d and ω_{Stark} do not scale perfectly linearly with P_{in}.

18 The value given in the supplementary material of [81] is erroneous.

19 the dephasing rate also appears to depend strongly on the cavity surface state (see Sec. A.1.3)

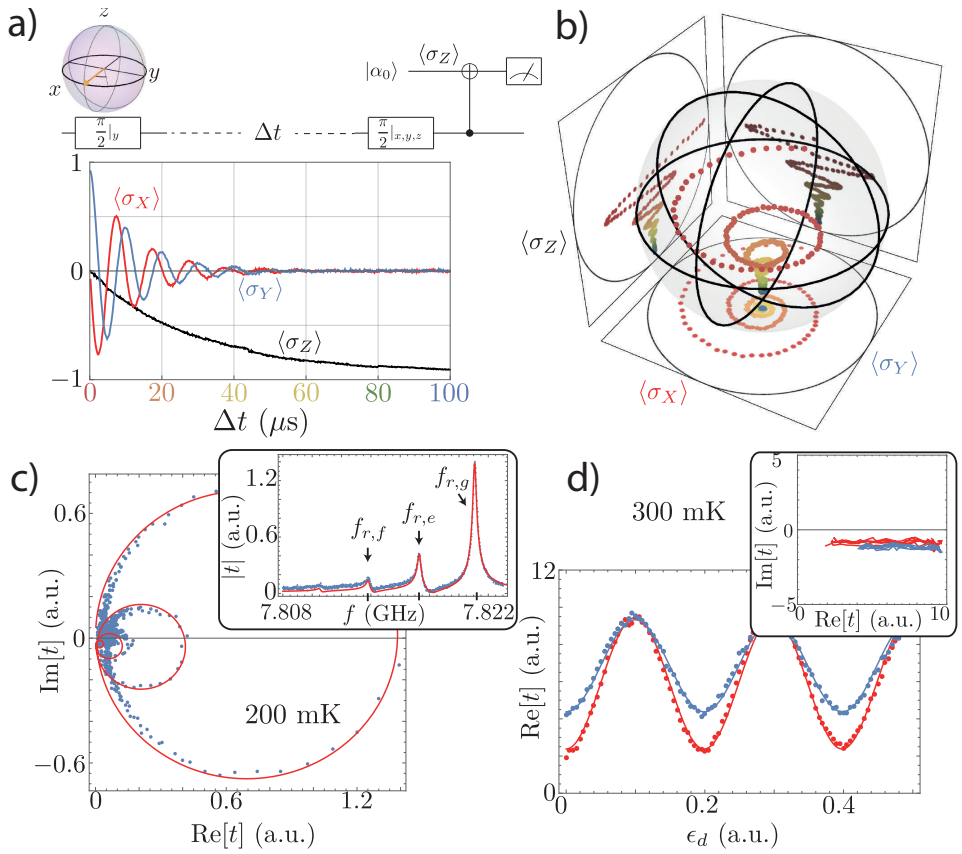

Figure 16: a) Ramsey interference experiment with the qubit used in [81] and Sec. 5.1 (Qubit 1 in Tab. 3). The qubit is first prepared close to the $|+\rangle_x$ state by applying a fast $\pi/2|_y$ pulse to rotate it around the y axis. After a waiting time Δt, each Pauli operator σ_i, $i = x, y, z$ is measured. Since readout only allows direct measurement of σ_z, a fast $\pi/2|_{y,x}$ pulse is applied before the measurement for $\sigma_{x,y}$. Drive pulses are slightly detuned from qubit frequency in order to observe Ramsey interference pattern. Fitting the exponential decay of energy ($\langle\sigma_z\rangle$) we find $T_1 = 26$ μs. Fitting the exponential decay of coherences ($|\langle\sigma_x\rangle + i\langle\sigma_y\rangle|$) we find $T_2 = 11$ μs. b) Bloch sphere representation of the state of the qubit as a function of time (encoded in color) during the same experiment c) Dots: measured amplitude of the cavity transmission coefficient when varying the probe pulsation ω_d with a qubit at thermal equilibrium (Qubit 2 in Tab.3, used in Sec. 4.2.1 and [82]). Red line: theoretical prediction adjusting a ground state occupation at equilibrium of $p_g = 71\%$. Inset: corresponding magnitude of transmission coefficient. d) Amplitude of the transmitted field at $\omega_d = \omega_{r,g}$ after a Rabi drive, varying the drive amplitude for another qubit (Qubit 3 in Tab. 3, used in Sec. 7 and [83]). In blue: qubit initially at equilibrium. In red: initial π pulse on $|e\rangle \leftrightarrow |f\rangle$. Main panel: quadrature of the field containing the information. Dots: experimental data. Line: cosine fit. Oscillation amplitude ratio gives $p_g = 58\%$. Inset: corresponding oscillations in the Fresnel plane.

states at equilibrium, linked by the detailed balance $p_g\Gamma_\uparrow = p_e\Gamma_\downarrow$. We use two different methods to determine this ratio, that are presented on Fig. 16c-d. Note that the given figures correspond to different qubits and different cavity parameters. In both cases, we include higher excited states of the anharmonic transmon mode and assume

a Boltzmann distribution for their occupation: $\frac{p_{i+2}}{p_{i+1}} = \frac{p_{i+1}}{p_i} = r_B = \exp -\frac{\hbar\omega_q}{kT_{\text{eff}}}$. Note that it is possible to directly measure the occupation of the second excited state with a protocol presented in Sec. 6.1.2. In the supplementary material of [81] is presented a method to give an upper bound on this value in the case of very low occupation probability (Qubit 1 in Tab. 3). This bound is found in agreement with the Boltzmann distribution assumption.

In Fig. 16c, the sample corresponds to Qubit 2 in Tab.3, used in Sec. 4.2.1 and in [82]. With the qubit at equilibrium, the cavity is probed with a low power continuous tone around its resonance frequency. Several peaks appear, each corresponding to different occupied qubit levels. Note that contrary to what is predicted by Eq. (60), these peaks are not all exactly separated by the same amount χ. Indeed, due to higher order non linear terms, cavity pull decreases with the number of excitations in the qubit mode. Fitting the relative heights of these peaks yields the ratio $\frac{\Gamma_\uparrow}{\Gamma_\downarrow} = r_B = 0.29$, corresponding to an effective temperature $T_{\text{eff}} = 200$ mK.

In Fig. 16d, the sample corresponds to Qubit 3 in Tab. 3, used in Chap. 7 and [83]. The qubit is resonantly driven with an amplitude ϵ_d for a short time $T_{\text{drive}} = 50$ ns $\ll T_1$. We then probe the cavity during a time $T_{\text{meas}} \leq T_1$ with a tone at $\omega_c = \omega_r + \chi/2$, that is the cavity resonant frequency when the qubit is in $|g\rangle$, and the average complex amplitude of the transmitted field is recorded. Increasing the drive pulse amplitude yields characteristic Rabi oscillations. In blue, the qubit is initially at equilibrium whereas in red we first applied a fast π pulse on its second transition to invert the population of the two first excited states $|e\rangle$ and $|f\rangle$. Calling t_g (resp. t_e) the average amplitude that would be recorded if the qubit were in $|g\rangle$ (resp. $|e\rangle$), the average field amplitude that we measure oscillates between

$$\begin{cases} p_g t_g + p_e t_e + c & \leftrightarrow & p_e t_g + p_g t_e + c & \text{for the blue curve} \\ p_g t_g + p_f t_e + c' & \leftrightarrow & p_f t_g + p_g t_e + c' & \text{for the red curve} \end{cases}, \tag{88}$$

where c and c' are two unknown constants, and $p_{g,e,f}$ are the occupations of the states $|g, e, f\rangle$ at equilibrium. Then the ratio of the blue and red oscillation amplitudes is $\frac{a_{\text{blue}}}{a_{\text{red}}} = \frac{1}{1+r_B}$. We then find $\frac{\Gamma_\uparrow}{\Gamma_\downarrow} = r_B = 0.40$, corresponding to an effective temperature $T_{\text{eff}} = 300$ mK[20].

This second method was better adapted in that particular experiment. Indeed the system was in a regime where the anharmonicity of the cavity was not negligible $\chi_{rr} \sim \kappa$. This implies that to get a similar figure as in c, one would have to probe the cavity with a power corresponding to much less than a photon on average. Otherwise, the Kerr effect would affect the shape of the peaks in a non trivial way. For a reasonable averaging time, it becomes difficult to extract the value of r_B with that first method. In [44], Geerlings *et al.* demonstrate a slightly different method, consisting in comparing the amplitude of the oscillations in the measurement signal when inducing Rabi oscil-

20 Note that when neglecting the occupation of the higher excited states at thermal equilibrium, one gets $\frac{a_{\text{blue}}}{a_{\text{red}}} = \frac{1-2P_{\text{eq}}(|e\rangle)}{1-P_{\text{eq}}(|e\rangle)}$ so that $P_{\text{eq}}(|e\rangle) = 22$ %, which is the figure given in [83] and Chap. 7.

lations between the first and second excited state, starting from thermal equilibrium or after inverting the occupation of $|g\rangle$ and $|e\rangle$ with a fast π-pulse.

3

MEASUREMENT AND QUANTUM TRAJECTORIES

3.1 STOCHASTIC MASTER EQUATIONS

3.1.1 *Measurement efficiency - discussion based on the Stern and Gerlach experiment*

In the seminal experiment by Stern and Gerlach in 1922, the spin of silver atoms is measured along a chosen direction by sending these atoms through a medium with a magnetic field gradient [90]. Under this field, the spin degree of freedom gets entangled to the spatial one that acts as a pointer. Then, by detecting the position of the atom, the σ_Z component of the spin is measured strongly, which means that it gets projected. Thus, if one prepares the spins in a pure state along σ_X[1] and for a sufficiently large field gradient, one gets two separated distributions for the detected positions, each associated with an eigenvalue of σ_Z. (see Fig. 17a).
The extension of these distributions has two origins. An irreducible component is the vacuum fluctuations $\delta z_Q = z_{ZPF}$ of the atom position. Imperfections in the detection setup (atoms in a thermal state for position, fluctuations of the magnetic field, imprecision of the detection panel...) adds up an extra classical noise to this uncertainty so that $\delta z^2 = \delta z_Q^2 + \delta z_C^2$. This noise can be expressed in terms of detection efficiency $\eta = \frac{\delta z_Q^2}{\delta z^2}$. One can then define a dephasing rate Γ_d as the inverse of the flight time that is needed to get two resolved spatial distributions for the detected atom positions in the ideal case $\eta = 1$ [11]. It corresponds to the measurement rate for an observer not subject to classical noise. The rate at which the observer acquires information on the spin state is in general $\eta\Gamma_d$. We can then identify several regimes when comparing these rates to the decoherence rate Γ_2 that is associated with other measurements performed by an unmonitored environment [91], and to the measurement time T_{meas}.

- $\Gamma_d < \Gamma_2$: the spin cannot be measured before it loses its original coherences.
- $\frac{1}{T_{\text{meas}}} > \Gamma_d > \Gamma_2$: the measurement is weak, meaning that the pointer states corresponding to $z = \pm 1$ are not distinguishable (see Fig. 17c) in one shot. The original spin state is affected but not fully projected.
- $\Gamma_d > \frac{1}{T_{\text{meas}}} > \eta\Gamma_d > \Gamma_2$: the spin state is fully collapsed onto $|\pm z\rangle$ but the observer cannot know the outcome for sure (see Fig. 17b). This is a strong but low fidelity readout.
- $\eta\Gamma_d > \frac{1}{T_{\text{meas}}} > \Gamma_2$: strong single-shot readout. This is the regime reached by Stern and Gerlach, even though their measurement efficiency was very low.

1 This was not the case for the experiment by Stern and Gerlach, in which the spins were initially in a maximally mixed state corresponding to thermal equilibrium

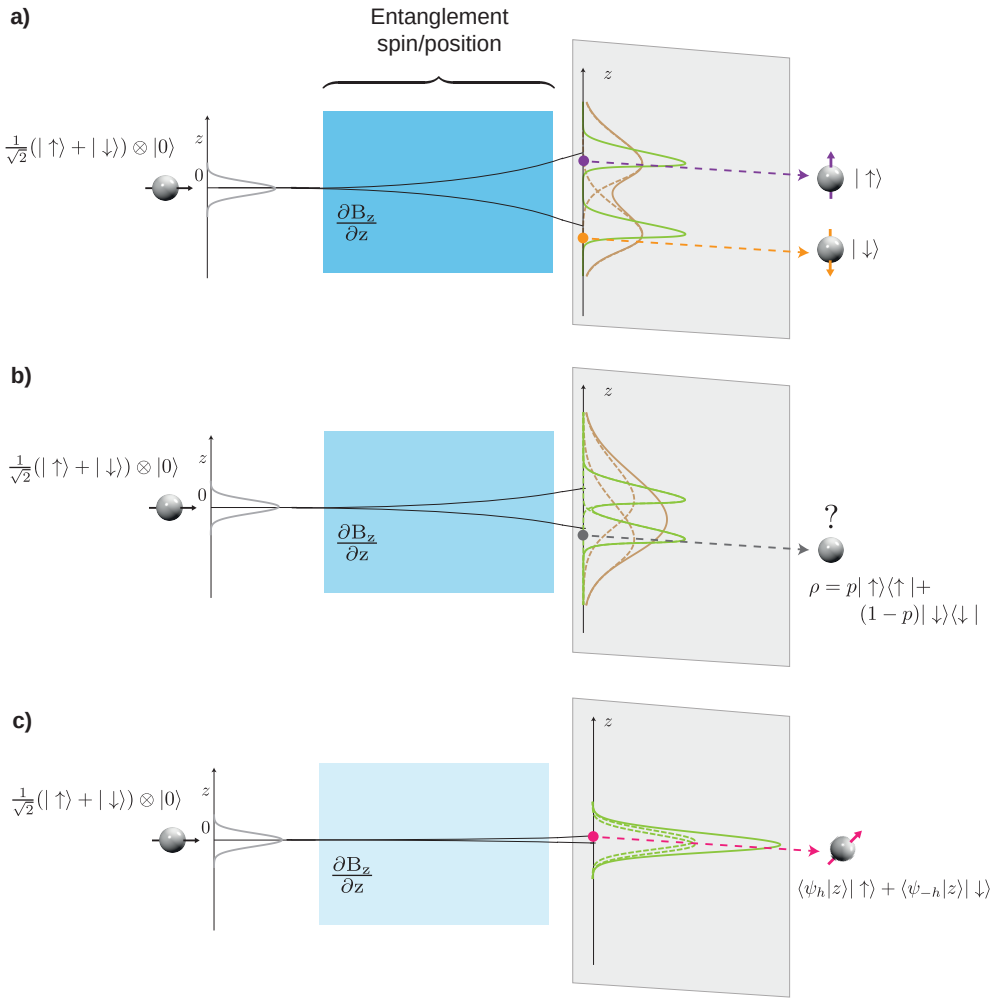

Figure 17: a) Thought experiment inspired by the one of Stern and Gerlach [90]. An atom prepared in a coherent superposition of $|\uparrow\rangle$ and $|\downarrow\rangle$ states is sent through a medium with a magnetic field gradient (in blue). The atom is then deflected upward or downward according to its spin state. The vertical position of the atom is detected on a screen (in gray). When repeating the experiment, a double peak distribution appears (in brown). The width of each peak corresponds to the total noise on the atom position. The incompressible zero point fluctuations are shown as green gaussians. If the two peaks do not overlap (as represented here), the measurement of the spin state is projective and single-shot. Dotted lines: distributions when the atoms are initially prepared in $|g\rangle$ or $|e\rangle$. b) Same experiment with a weaker magnetic gradient. If the brown peaks overlap, the experimenter cannot distinguish between $|e\rangle$ and $|g\rangle$, but if the separation is larger than the zero point fluctuations, the spin is still projected. For the experimenter, the spin is in a mixed state. c) For a perfect measurement ($\eta = 1$), the uncertainty on the atom position only comes from zero point fluctuations. If the magnetic gradient is weak enough that the two peaks overlap, the measurement is not projective, but the state remains pure.

Qubit detectors with efficiency close to 1 have only recently been developed [11], which has permitted to investigate the regime of weak measurement. The back action of the measurement induces a non trivial stochastic evolution of the system but, *a posteri-*

ori, the experimenter can use the measurement outcome to reconstruct the quantum evolution so that purity remains of order 1. The successive states of the system in the Hilbert space during a single experiment form a *quantum trajectory*. In 2008, Katz *et al.* [8] showed that it was possible to cancel the effect of a first partial measurement by a second "symmetric" measurement giving the same outcome. In 2011, Vijay *et al.* [22] observed quantum jumps of a superconducting qubit, which correspond to quantum trajectories in the strong measurement limit. In 2013, Murch *et al.* [92] detected quantum trajectories corresponding to a weak and continuous measurement with homodyne detection (see Sec. 3.2.2). A similar experiment was performed by Hatridge *et al.* [93] with heterodyne detection (see Sec. 3.2.3) while varying the strength of the measurement, illustrating the fact that a strong projective measurement is ultimately an integrated continuous one.

We will now derive the general formalism that describes the evolution of a qubit state under monitoring, which is done through a Stochastic Master Equation (SME).

3.1.2 *SME with a jump detector*

In Eq. (27) we have described the evolution of a qubit under the action of a set of jump operators. In this section, we will describe the evolution of a system for which we know when these jumps occur. The jumps correspond to a measurement as in Eq. (18) and Eq. (19), and we assume that the result of this measurement is known. The derivation presented here follows the notes by D. Steck [94].

Starting from a simplified version of (24), we consider a single jump operator L. Then, we need only two Kraus operators $M_0 = \mathbb{1} - i\frac{H}{\hbar}\mathrm{d}t - \frac{1}{2}LL^\dagger \mathrm{d}t$ and $M_1 = \sqrt{\mathrm{d}t}L$. If these jumps are perfectly detected[2], considering the evolution of the density matrix between t and $t+\mathrm{d}t$ as in Eq. (20) and Eq. (19),

- if no jump occurred, which happens with probability $p_0 = M_0\rho M_0^\dagger = 1 - \mathrm{d}t\langle L^\dagger L\rangle$, developing to the first order in $\mathrm{d}t$,

$$d\rho_0 = \frac{M_0\rho M_0^\dagger}{p_0} = -\frac{i}{\hbar}\mathrm{d}t[H,\rho] - \frac{1}{2}\mathrm{d}t\{L^\dagger L - \langle L^\dagger L\rangle, \rho\} \tag{89}$$

- if a jump occured, which happens with probability $p_1 = M_1\rho M_1^\dagger = \mathrm{d}t\langle L^\dagger L\rangle$

$$d\rho_1 = \frac{M_1\rho M_1^\dagger}{p_1} = \frac{L\rho L^\dagger}{\langle L^\dagger L\rangle} - \rho. \tag{90}$$

Denoting by $\mathrm{d}N_t$ the number of jumps detected during $\mathrm{d}t$[3], for a small enough time step, $\mathrm{d}N_t$ is either 0 or 1, with $E(\mathrm{d}N_t) = \langle L^\dagger L\rangle \mathrm{d}t$, and the evolution of the density matrix reads

$$\mathrm{d}\rho = (1 - \mathrm{d}N_t)\mathrm{d}\rho_0 + \mathrm{d}N_t\mathrm{d}\rho_1 = \mathrm{d}\rho_0 + \mathrm{d}N_t\mathrm{d}\rho_1. \tag{91}$$

2 when $L = \sqrt{\gamma}\sigma_-$, this corresponds to a perfect photocounter at the output of the cavity
3 $\mathrm{d}N_t$ is a Poisson process.

The last equality holds because $\mathrm{d}\rho_0$ is of order $\mathrm{d}t$ when $\mathrm{d}\rho_1$ is of order 1. Then, we get

$$\mathrm{d}\rho = -\frac{i}{\hbar}\mathrm{d}t[H,\rho] - \frac{1}{2}\mathrm{d}t\{L^\dagger L - \langle L^\dagger L\rangle, \rho\} + \mathrm{d}N_t\Big(\frac{L\rho L^\dagger}{\langle L^\dagger L\rangle} - \rho\Big), \tag{92}$$

which can be written in a more common form

$$\dot{\rho} = -\frac{i}{\hbar}[H,\rho] + \mathcal{D}[L]\rho + \Big(\frac{\mathrm{d}N_t}{\mathrm{d}t} - \langle L^\dagger L\rangle\Big)\Big(\frac{L\rho L^\dagger}{\langle L^\dagger L\rangle} - \rho\Big). \tag{93}$$

The last term in this equation, proportional to the deviation of the detector from its expected average value is called *actuation*. It compensates for the purity lost due to from the Lindblad term. Starting from a pure state, the qubit remains in a pure state. This means that if we monitor every interaction of the qubit with its environment, we know its state perfectly. However, this state depends on the random detector outcome, which cannot be predicted *a priori*. When averaging the detected trajectories over many experiments, the actuation term averages out to 0, and we get back the evolution predicted by the Lindblad master equation.

Let us consider two possible cases for L. For simplicity, we consider a non driven qubit, whose hamiltonian in the frame rotating at ω_q reads H=0.

- $\boxed{L = \sqrt{\frac{\gamma_\phi}{2}}\sigma_Z}$, L represents a dephasing jump. Then Eq. (92) simplifies into

  $$\mathrm{d}\rho = \mathrm{d}N_t\Big(\sigma_Z\rho\sigma_Z - \rho\Big). \tag{94}$$

  The state does not change until a jump is detected. In that case, its phase is rotated by π. Since, in the Markov approximation, the environment has no memory of the past jumps and the qubit remains in a state which has the same symmetry as the initial one, the jump rate is constant and the number of jumps after time t follows a Poissonian law of parameter $\frac{\gamma_\phi}{2}t$. Then, considering that after an even number of jumps n, the system gets back its initial phase whereas it takes a minus sign for odd numbers of jump, as a mean, its coherences read

  $$\rho_{eg}(t) = \rho_{eg}(0)\exp(-\frac{\gamma_\phi}{2}t)\sum_n(-1)^n\frac{(\frac{\gamma_\phi}{2}t)^n}{n!} = \rho_{eg}(0)\exp(-\gamma_\phi t). \tag{95}$$

  Thus, its coherences decay with a rate γ_ϕ.

- $\boxed{L = \sqrt{\gamma}\sigma_-}$, L represents a relaxation jump. Then $\mathrm{d}\rho_1 = |g\rangle\langle g| - \rho$. Thus, if a jump occurs, the qubit is projected onto the ground state. The trajectory when no jump is detected is non-trivial. In terms of Bloch coordinates, it reads:

  $$\begin{cases} \dot{x}|_0 &= \frac{\gamma}{2}zx \\ \dot{y}|_0 &= \frac{\gamma}{2}zy \\ \dot{z}|_0 &= -\frac{\gamma}{2}(1-z^2) \end{cases} \tag{96}$$

  We can check that purity remains 1 when the system starts in a pure state (but is not constant otherwise). The steady states are $|g\rangle\langle g|$ (which is stable) and

$|e\rangle\langle e|$ (unstable). Any other state will eventually collapse onto the ground state, even in the absence of a jump! This can be understood with a simple Bayesian argument: detecting no jump is more probable if the qubit is in the ground state so that, starting from a symmetric superposition, detecting no jump implies that the qubit is more probably in $|g\rangle$. In this sense, the absence of a jump event is in fact a signal itself.

In this formalism, finite detection efficiency means that only a fraction η of the jumps are detected. This changes the statistics of $\mathrm{d}N_t$ in the actuation term as

$$\dot{\rho} = -\frac{i}{\hbar}[H,\rho] + \mathcal{D}[L]\rho + \left(\frac{\mathrm{d}N_t^{(\eta)}}{\mathrm{d}t} - \eta\langle L^\dagger L\rangle\right)\left(\frac{L\rho L^\dagger}{\langle L^\dagger L\rangle} - \rho\right), \tag{97}$$

where η is the detector efficiency with $\eta \in [0,1]$, and $E[\mathrm{d}N_t^{(\eta)}] = \eta\langle L^\dagger L\rangle$.

In this section, we described the behavior of a *monitored* qubit with a particular detector, which is a jump detector. In the case of σ_- jumps, it can be realized by collecting the field leaking out of the cavity and sending it to a photo-counter. However, such a diode-like element with good efficiency does not exist yet in the microwave range even though encouraging experiments have been performed [95, 96] and new detection schemes recently proposed [97]. In Appendix C, we propose a Stochastic Master Equation associated to this type of detection.
In the rest of this thesis, we focus on heterodyne detection of the field, which can be performed using linear amplifiers. We will now derive and use a SME formalism for linear detectors in two cases. First when detecting the field at the output port of the cavity at ω_r. This will enable us to perform non-destructive readout of the qubit. Then we will describe the detection of the field around the qubit resonance frequency, which allows us to unravel the relaxation jumps of the qubit using the information contained in the field that leaks out in the process.

3.2 DISPERSIVE MEASUREMENT

3.2.1 *Linear detection*

Non destructive measurement of the σ_Z operator of the qubit is performed using the dispersive interaction of the qubit and cavity. In the hamiltonian (80), the dispersive term $-\hbar\frac{\chi}{2}a^\dagger a\sigma_z$ can be seen as a shift of the cavity mode resonance frequency depending on the qubit state. When probing the cavity around its resonance frequency, the transmitted field a_{out} thus depends on the qubit state. We now focus on the case of a probe field at ω_r. In Fig. 18b, we represent the states of this field corresponding to a qubit in $|g\rangle$ or $|e\rangle$, in the Fresnel plane rotating at ω_r and when driving the cavity at resonance. Measuring the observable $\mathrm{Im}[a_{out}]$ allows one to distinguish between the two states of the qubit as depicted on Fig. 18c. The detection of $\mathrm{Re}[a_{out}]$ does not provide information about σ_Z, but as we will see in the next section, it is associated with a back action on the qubit state so that, if we dismiss the measurement outcome, it leads to dephasing.

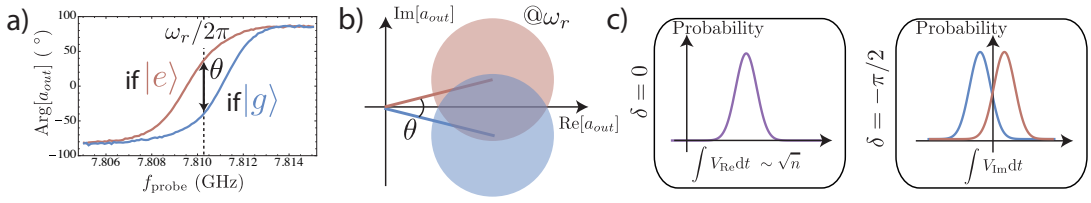

Figure 18: a) Measured phase of the transmitted field in the experiment described in 3.2.3, when the qubit is in $|g\rangle$ (blue) or $|e\rangle$ (red). b) Fresnel plane representation (plane rotating at ω_r) of the calculated transmitted field at ω_r (same color code as in a). Filled circles represent the quantum uncertainty of the field. c) corresponding distributions of the integrated homodyne detection outputs. When the phase of the detection is $\delta = \pi/2$, the observer can distinguish partially between $|g\rangle$ and $|e\rangle$ and gets a weak measurement of σ_Z. When $\delta = 0$, the observer cannot distinguish between $|g\rangle$ and $|e\rangle$, but he gets information about the number of photons in the field, and thus learns about the shifts in the qubit phase induced by measurement back action.

The detection of one of the quadratures of a_{out} is called a *homodyne* detection. For a classical signal, homodyne detection of a microwave field can be performed using a commercial *mixer* that multiplies the signal $s(t) = I\cos\omega_r t + Q\sin\omega_r t$ by a strong carrier $B\cos\omega_r t + \delta$ provided by a Local Oscillator (LO) at the same frequency. Averaging out the fast oscillating components, the resulting signal reads $u \propto I\cos\delta + Q\sin\delta$, so that by varying δ, one can choose the detected quadrature.
Heterodyne detection consists in detecting simultaneously both quadratures. It is performed by an *IQ mixer* that splits the signal and mixes one part with the LO, and another with the LO dephased by $\pi/2$. Note that in our setup, heterodyne detection is performed by another technique, mixing the signal with a slightly detuned LO at $\omega_r + \omega_h$. The output signal $u(t) \propto I\cos\omega_h t + Q\sin\omega_h t$ oscillates at small enough frequency that it can be detected and digitized, leading to a simultaneous measurement of both I and Q by numerical demodulation.

Mixers are based on diodes, which provide the non-linearity needed for the multiplication. However, since these diodes are dissipative, noise is added to the measurement. The field a_{out} being very small, diode based mixers cannot be directly used to perform an efficient detection. A non-linear, non-dissipative element, is thus needed to perform *quantum limited* measurement[11]. For microwave signals, Josephson junctions provide such an element. The field a_{out} can be linearly amplified with no noise added, and the output signal can be detected with commercial mixers at room temperature[4].

The *no-cloning* thorem[98] stating that a quantum state cannot be copied, one needs to specify what quantum limited amplification means. Following the results of Sec. 2.1.3.1, we define it as an operation that does not increase the entropy of the

4 The Josephson device can also be seen as performing the detection by itself and its output as a classical signal. From an informational point of view, the exact position of the limit between quantum and classical worlds is irrelevant since the effect on the qubit state is the same in both cases.

system. Thus, quantum limited amplification is a hamiltonian evolution. In the following sections, we will describe the physical implementations of such amplifiers and the stochastic master equations ruling the evolution of the qubit under such detections.

3.2.2 *Homodyne detection*

Before describing the *heterodyne detection* that is used in the experiments reported in this thesis, it is instructive to describe homodyne detection. A Josephson junction based linear amplifier commonly used for homodyne detection is the so-called Josephson Parametric Amplifier (JPA)[99, 100, 101]. We give here a brief description of its working principle. Alternative designs of the JPA and many other degenerate amplifiers can be used [102, 103, 104, 105, 106, 107, 108, 109, 110, 111, 112, 113, 114].
The field that we want to amplify is directed toward a microwave resonator at ω_r, in which one or several Josephson junctions have been embedded so as to provide some non linearity. Its dynamics is governed by a duffing hamiltonian that reads

$$H_{\text{Duff}} = \hbar\omega_r\ c^\dagger c + \hbar k c^\dagger c^\dagger cc. \tag{98}$$

When pumped on resonance with a strong coherent tone of amplitude p_0 on top of which the signal of interest δc is added, in the limit $p_0 \gg \sqrt{\langle \delta c^\dagger \delta c \rangle}$, it can be approximated as

$$H_{\text{Duff}} = \hbar(\omega_r + 2k|p_0|^2)\delta c^\dagger \delta c + \hbar k(p_0^2 \delta c^{\dagger 2} + p_0^{*2}\delta c^2). \tag{99}$$

The input and output traveling wave operators c_{in} and c_{out} are linked to $c = p_0 + \delta c$ by the input/output relation (47)

$$\sqrt{\kappa_{\text{JPA}}}c = c_{in} + c_{out}. \tag{100}$$

When considering the components δc_{in} and δc_{out} of these traveling waves associated with the signal only, the new input/output relation reads [11]

$$\delta c_{out} = \sqrt{G}\delta c_{in} + e^{i\delta}\sqrt{G-1}\delta c_{in}^\dagger. \tag{101}$$

In this expression, G and δ can be adjusted by p_0 and depend on κ_{JPA}. Due to the pumped non-linearity in H_{Duff}, the signal is squeezed along a direction in the Fresnel plane that is set by the pump phase (see Fig. 19). Thus, amplification of one quadrature of the signal is achieved at the expense of the other quadrature, which is de-amplified. In practice, the large constant pump tone can be removed from the outgoing field by interferometry.

If the signal is the field a_{out} of Fig. 18b and for large gain G, the reflected signal from the JPA[5] reads

$$\delta c_{out} \simeq \sqrt{G}(a_{out} + e^{i\delta}a_{out}^\dagger). \tag{102}$$

5 A circulator is used to direct the amplified field away from the cavity into output lines.

Thus, the JPA is implementing homodyne detection. The detected quadrature is chosen via the pump phase. However, the output of the JPA is not directly the average value $\langle \mathrm{Re}[a_{out}]\rangle$ or $\langle \mathrm{Im}[a_{out}]\rangle$, but is subject to quantum fluctuations. After further amplification and renormalization, when integrated over a time step $\mathrm{d}t$[6], it reads (in the case where $\mathrm{Im}[a_{out}]$ is amplified)[24]

$$J_{\delta=\pi/2}(t)\mathrm{d}t = \sqrt{\eta}\langle 2\mathrm{Im}[a_{out}]\rangle \mathrm{d}t + \mathrm{d}W_t, \tag{103}$$

where $\eta \leq 1$ is the detection efficiency. The ensemble of values taken by $J_{\delta=\pi/2}$ on a given experiment is called a *measurement record*. In this expression, W_t is a *Wiener process* or *idealized random walk* accounting for the quantum fluctuations of p_0. It verifies

$$\begin{cases} \overline{\mathrm{d}W_t} &= 0 \\ \mathrm{d}W_t^2 &= \mathrm{d}t \end{cases}. \tag{104}$$

Before describing the stochastic master equations associated with these measurements, let us compute the measurement rate Γ_m associated with the homodyne detection of $\mathrm{Im}[a_{out}]$. In the absence of input drive through the output port of the cavity, a_{out} is linked to the intra cavity field a by $\langle a_{out}\rangle = \sqrt{\kappa}\langle a\rangle$ where κ is the damping rate of the cavity mode. Moreover, from Eq. (51), when driving the cavity at resonance, we have

$$\langle \mathrm{Im}[a]\rangle = \langle\sigma_z\rangle\sqrt{n}\sin\frac{\theta}{2} = \langle\sigma_z\rangle\sqrt{n\frac{\chi^2}{\kappa^2+\chi^2}} \tag{105}$$

where n is the mean number of photons in the cavity, and θ the angle between α_e and α_g (see Fig. 19). Thus, we can rewrite Eq. (103) as

$$J_{\delta=\pi/2}(t)\mathrm{d}t = 2\langle\sigma_z\rangle\sqrt{\eta n\frac{\kappa\chi^2}{(\kappa^2+\chi^2)}}\mathrm{d}t + \mathrm{d}W_t. \tag{106}$$

Following Clerk *et al.* in [11], we define the measurement rate from the signal to noise ratio of this signal integrated from 0 to t as

$$\Gamma_m \overset{\mathrm{def}}{=} \frac{1}{2}\frac{SNR}{t} = 2n\frac{\kappa\chi^2}{(\kappa^2+\chi^2)}. \tag{107}$$

We can check that $\Gamma_m = \eta\Gamma_d$, where Γ_d is the dephasing rate given in Eq. (85). In the case of perfect detection, we acquire information at the same rate that the qubit is dephased.
The measurement record can be written as [7]

$$J_{\delta=\pi/2}(t)\mathrm{d}t = \sqrt{2\Gamma_m}\langle\sigma_Z\rangle\mathrm{d}t + \mathrm{d}W_t. \tag{108}$$

We now present the Stochastic Master equation associated with each homodyne detection, which is the proper way to actuate our knowledge of the qubit state using

6 in the limit $\mathrm{d}t \gg 1/\omega_r$

7 The global sign of $J(t)$, just as the scaling factor in experimental data, is not relevant for the SME. In practice, it is set by the numerical demodulation performed by the acquisition board. However, changing the sign of $\mathrm{d}W_t$ has a physical significance and must be taken into account in the SME.

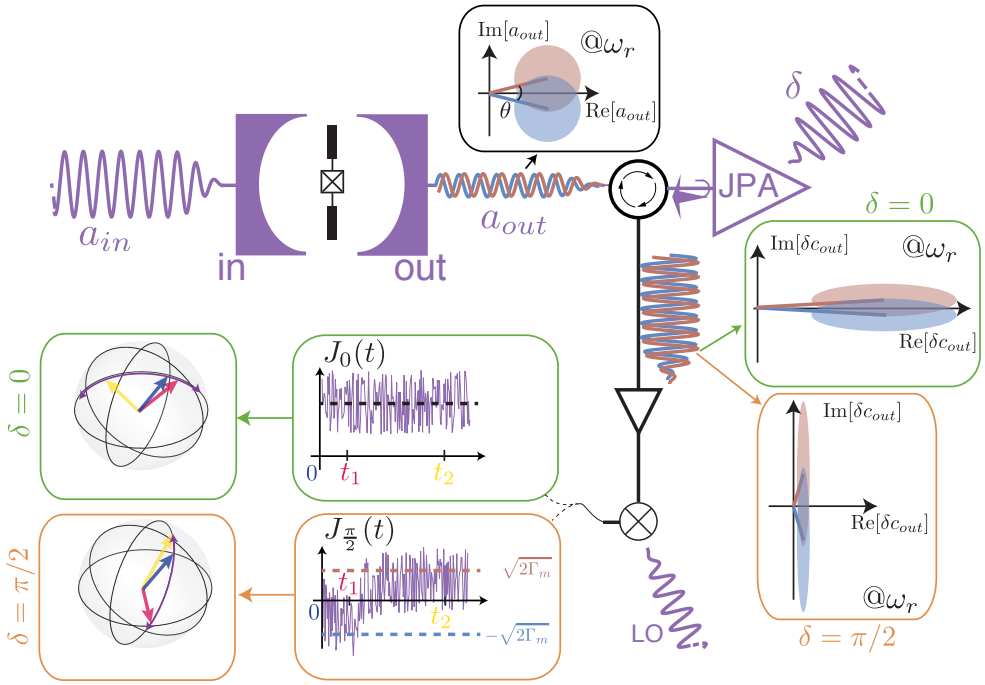

Figure 19: a) Homodyne detection of the transmitted field with a JPA for a qubit initially in $1/\sqrt{2}(|g\rangle + |e\rangle)$. a_{out} is mixed with a strong pump tone at ω_r in a non linear resonator. The output field δc_{out} is squeezed along a direction that depends of the phase δ of the pump. After further amplification, the signal is mixed with a commercial mixer at room temperature and digitized. According to the detected quadrature, the qubit state diffuses along a meridian of the Bloch sphere ($\delta = \pi/2$) or along the equator ($\delta = 0$).

the measurement records. A derivation from the SME of the cavity mode and using a Jayne-Cummings model can be found in [115]. We propose in Appendix C a derivation starting from the SME associated with a detection with a photocounter, and using a model of homodyne detection borrowed from quantum optics, which is equivalent to the one described above.

If $\boxed{\delta = \frac{\pi}{2}}$, the SME reads[8]

$$\mathrm{d}\rho = -\frac{i}{\hbar}\mathrm{d}t[H,\rho] + \frac{\Gamma_d}{2}\mathrm{d}t\mathcal{D}[\sigma_Z]\rho + \mathrm{d}W_t\sqrt{2\Gamma_m}\mathcal{M}[\sigma_Z]\rho, \tag{109}$$

where the measurement super operator $\mathcal{M}$ acts on ρ as

$$\boxed{\mathcal{M}[c]\rho = \frac{1}{2}\Big((c - \langle c\rangle)\rho + \rho(c^\dagger - \langle c^\dagger\rangle)\Big)}. \tag{110}$$

8 For simplicity, we do not include the terms associated with other decoherence channels.

This equation leads to a diffusive behavior for the qubit state which moves stochastically along a meridian of the Bloch sphere according to the value of W_t (see Fig. 19). Indeed, in terms of Bloch coordinates, the actuation term leads to

$$\begin{cases} \mathrm{d}x &= -\mathrm{d}W_t\sqrt{2\Gamma_m}zx \\ \mathrm{d}y &= -\mathrm{d}W_t\sqrt{2\Gamma_m}zy \\ \mathrm{d}z &= +\mathrm{d}W_t\sqrt{2\Gamma_m}(1-z^2) \end{cases} . \tag{111}$$

As an example, starting at time t from a state verifying $y = 0$, let us compute the variation of the squared norm of the Bloch vector using Itô rules. We have $\mathrm{d}y = 0$ and including the contribution of the damping super operator,

$$\mathrm{d}(x^2+z^2) = -2\Gamma_d x^2\mathrm{d}t + 2\sqrt{2\Gamma_m}z(1-z^2-x^2)\mathrm{d}W_t + 2\Gamma_m((1-z^2)^2+z^2x^2)\mathrm{d}t. \tag{112}$$

If $\eta = 1$, $\Gamma_m = \Gamma_d$ so that

$$\mathrm{d}(x^2+z^2) = 2(1-x^2-z^2)(\sqrt{2\Gamma_m}z\mathrm{d}W_t + \Gamma_m\mathrm{d}t). \tag{113}$$

In this case, as a mean, the Bloch vector norm increases until it reaches the surface of the Bloch sphere, that is a pure state. In particular, a pure state remains pure at all time. When $\eta < 1$, the dephasing term is stronger than the actuation term, and the state remains inside the sphere, except when $z = \pm 1$, which is a stable point for Eq. (111) and for the Lindblad super operator.

More generally, after a typical time $\frac{1}{\Gamma_m}$, the state has reached a pole of the Bloch sphere and stays there [21]. It thus corresponds to a non-destructive measurement of the σ_Z operator of the qubit. As stated previously, the measurement record, that is the normalized signal at the output of the detection setup, is $J_{\frac{\pi}{2}}(t)$ with

$$\begin{aligned} J_{\frac{\pi}{2}}(t)\mathrm{d}t &= 2\sqrt{\eta\kappa n}\sin\tfrac{\theta}{2}\langle\sigma_Z\rangle\mathrm{d}t + \mathrm{d}W_t \\ &= \sqrt{2\Gamma_m}\langle\sigma_Z\rangle\mathrm{d}t + \mathrm{d}W_t \end{aligned} . \tag{114}$$

Note that in practice, this record is always scaled by a factor depending on the pump tone for the JPA, the attenuation of the lines and other uncontrolled factors.

If $\boxed{\delta = 0}$, the SME reads

$$\begin{aligned} \mathrm{d}\rho &= -\tfrac{i}{\hbar}\mathrm{d}t[H,\rho] + \tfrac{\Gamma_d}{2}\mathrm{d}t\mathcal{D}[\sigma_Z]\rho - \mathrm{d}W_t\sqrt{2\Gamma_m}\mathcal{M}[i\sigma_Z]\rho \\ &= -\tfrac{i}{\hbar}\mathrm{d}t[H,\rho] + \tfrac{\Gamma_d}{2}\mathrm{d}t\mathcal{D}[\sigma_Z]\rho - \tfrac{i}{2}\mathrm{d}W_t\sqrt{2\Gamma_m}[\sigma_Z,\rho]. \end{aligned} . \tag{115}$$

This equation also leads to a diffusive behavior for the qubit state (see Fig. 19), but along the equator of the Bloch sphere. Indeed, during $\mathrm{d}t$, the evolution is governed by the stochastic hamiltonian $H - \sqrt{\frac{\Gamma_m}{2}}\hbar\sigma_z\mathrm{d}W_t$. Thus, the qubit frequency is now a stochastic parameter so that in the frame rotating at ω_q, its phase shifts randomly. If the measurement record is dismissed, after a typical time $1/\Gamma_d$, the initial phase of the qubit is lost. This phenomenon corresponds to the back action of the measurement of

σ_Z. However, in the present case, the quadrature of the field that contains the information about this back action is measured so that the observer can *a posteriori* know its effect and the state remains pure for $\eta = 1$. Recently, De Lange *et al.* showed that the phase shifts could even be reversed by feedback [116].

In this case, and with the same normalization as in Eq. (114), the measurement record is $J_0(t)$ with

$$J_0(t)\mathrm{d}t = 2\sqrt{\eta\kappa n}\cos\frac{\theta}{2}\mathrm{d}t + \mathrm{d}W_t. \tag{116}$$

The behavior of a qubit under these two homodyne measurements has been beautifully illustrated by an experiment in the Siddiqi group at Berkeley [92].

3.2.3 *Heterodyne measurement*

As stated previously, heterodyne detection can be understood as a simultaneous homodyne detection of both quadratures of the field [117]. Since the observables $\mathrm{Re}[a_{out}]$ and $\mathrm{Im}[a_{out}]$ associated with these quadratures do not commute, one needs to conceptually split the signal in two parts, each one being detected separately. In that sense, a heterodyne detection with efficiency η of a jump operator L is equivalent to 2 simultaneous homodyne detections, *with the same efficiency*, of the jumps

$$\begin{cases} L_I &= \frac{1}{\sqrt{2}}L \\ L_Q &= \frac{i}{\sqrt{2}}L \end{cases}. \tag{117}$$

If $\eta = 1$, any pure state remains pure under perfect heterodyne detection if one uses all the information at his disposal (see [118] for theory and [93] for experimental demonstration).

In the experiments described in this thesis, heterodyne detection is implemented by amplifying the output field from the cavity with a quantum limited *phase preserving* parametric amplifier known as the Josephson Parametric Converter (JPC) [19, 119, 20]. We will not describe its working details here. A complete description can be found in Emmanuel Flurin's PhD thesis [120]. Note however that its working principle is similar to the one of phase sensitive amplifiers. Quantum limited amplification of the signal mode a is achieved by the necessary combination with an auxiliary mode b, usually referred to as the *idler*, and a pump. When $\omega_{\mathrm{pump}} = \omega_{\mathrm{signal}} + \omega_{\mathrm{idler}}$, the JPC performs amplification of both quadratures of the signal mode[9]. When tracing out the idler mode, each quadrature of the amplified signal contains extra noise coming from the idler, or equivalently in the SME, the mean value of the measurement records are divided by $\sqrt{2}$ following Eq. (117) compared to Eqs. (114, 116). However, this extra quantum noise is *not* detrimental to the purity of the state when solving the SME [118].

9 The unitary evolution during the amplification corresponds to squeezing in the phase space of the composite system made of signal and idler [11, 121], so that the overall phase space volume is preserved in agreement with Liouville theorem for a unitary evolution.

The measurement record is now complex and reads

$$J(t)\mathrm{d}t = \sqrt{2\eta\kappa n}\cos\frac{\theta}{2}\mathrm{d}t + \mathrm{d}W_{t,1} + i\Big(\sqrt{2\eta\kappa n}\sin\frac{\theta}{2}\mathrm{d}t\langle\sigma_Z\rangle + \mathrm{d}W_{t,2}\Big), \tag{118}$$

where $\mathrm{d}W_{t,1}$ and $\mathrm{d}W_{t,2}$ are two independent Wiener processes. The SME can be easily deduced from the ones corresponding to homodyne detections. It reads[10]

$$\mathrm{d}\rho = -\frac{i}{\hbar}\mathrm{d}t[H,\rho] + \frac{\Gamma_d}{2}\mathrm{d}t\mathcal{D}[\sigma_Z]\rho + \mathrm{d}W_{t,2}\sqrt{\eta\Gamma_d}\mathcal{M}[\sigma_Z]\rho - \mathrm{d}W_{t,1}\sqrt{\eta\Gamma_d}\mathcal{M}[i\sigma_Z]\rho. \tag{119}$$

Note that in this expression, we have avoided using Γ_m. Indeed, the definition of the measurement rate can be ambiguous, since information is extracted from both quadratures of the measurement field. If considering the measurement of $\langle\sigma_Z\rangle$ only, the measurement rate reads $\eta\Gamma_d/2$, twice smaller than for homodyne detection of $\mathrm{Im}[a_{out}]$.

3.2.3.1 *Single-shot Non Demolition readout*

In the previous section, we saw that heterodyne detection provides a continuous measurement scheme of the σ_Z operator. In the present section, we describe how this measurement can be used as a high-fidelity projective quantum non-demolition (QND) readout and how to calibrate the efficiency η of our detection chain.

On the experiment presented on Fig. 20a, the parameters of the qubit and cavity are the same as those in 2.2.4 and [81], corresponding to Qubit 1 in Tab. 3. Then, starting from an unknown state and not driving the qubit ($H = 0$ in the frame rotating at ω_q), we probe the cavity in transmission with a tone at ω_r that leads to a stationary number of photons calibrated to be $n = 1.4$ photons. This stationary regime is reached in $1/\kappa \simeq 90$ ns and leads to a dephasing rate (see Eq. (85))

$$\Gamma_d = 2n\frac{\chi^2}{\kappa(\kappa^2+\chi^2)} \simeq 1/100 \text{ ns}. \tag{120}$$

Thus after a time $t_{\mathrm{coll}} = 240$ ns, we consider that stationary regime is reached for the cavity field and the qubit has been projected to either $|g\rangle$ or $|e\rangle$, so that, for a single experiment, $\langle\sigma_Z(t_{\mathrm{coll}})\rangle = \pm 1$. We then integrate the readout signal $\alpha J(t)$ (α being an unknown proportionality factor depending on uncontrolled parameters such as the lines attenuation) during $T_{\mathrm{meas}} = 960$ ns. Note that $t_{\mathrm{coll}} + T_{\mathrm{meas}} \ll T_1 = 28$ μs so that the state of the qubit does not evolve during measurement.

The integrated measurement records over many experiments have a mean value

$$\begin{aligned} \overline{a} &= \overline{\alpha\int_{t_{\mathrm{coll}}}^{t_{\mathrm{coll}}+T_{\mathrm{meas}}} J(t)\mathrm{d}t} \\ &= \alpha\sqrt{2\eta\kappa n}(\cos\tfrac{\theta}{2} \pm i\sin\tfrac{\theta}{2})T_{\mathrm{meas}}, \end{aligned} \tag{121}$$

and a variance

$$\mathrm{Var}(\mathrm{Re}[a]) = \mathrm{Var}(\mathrm{Im}[a]) = \alpha^2 T_{\mathrm{meas}}. \tag{122}$$

10 To highlight the equivalence between a heterodyne detection and two homodyne ones, one can note that $\mathcal{D}[\sigma_Z] = \mathcal{D}[\frac{\sigma_Z}{\sqrt{2}}] + \mathcal{D}[i\frac{\sigma_Z}{\sqrt{2}}]$

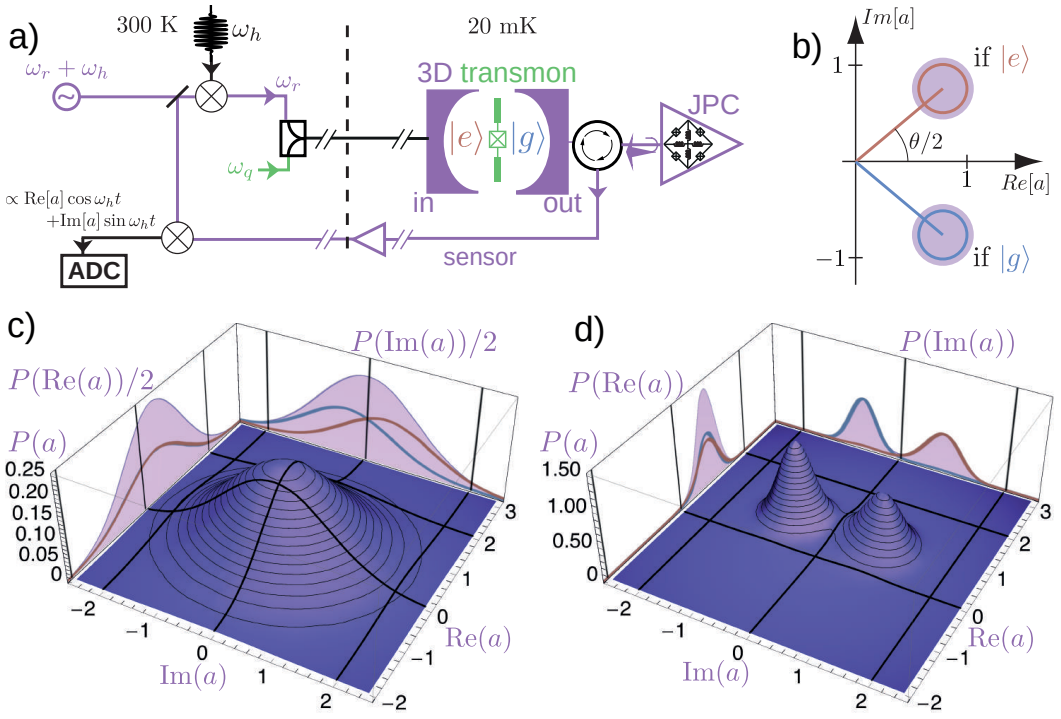

Figure 20: a) Simplified experimental setup. Qubit is prepared with pulses at ω_q and readout at ω_r. These pulses are generated by mixing a LO detuned by a small frequency $\omega_h/2\pi = 62.5$ MHz with a square waveform oscillating at ω_h. This LO is also used for heterodyne detection: both quadratures of the output field are amplified before down-conversion to ω_h by mixing it with the LO. The resulting signal is then digitized and numerically demodulated to recover $\mathrm{Re}[a]$ and $\mathrm{Im}[a]$ up to a constant pre factor α. By adjusting the phase of the arbitrary waveform, one can phase shift a so that only the imaginary part of the field contains information about the qubit state. b) Expected complex amplitude of the integrated signal a (see Eq. (121)). The mean value $\overline{a}$ is represented as the rod of a lollypop for both qubit states, the fluctuations by the purple disks. These fluctuations have an irreducible component originating from the non commutativity of $\mathrm{Re}[a]$ and $\mathrm{Im}[a]$ (Heisenberg principle) and which is represented, for these coherent fields, by the brown and blue circles. The limited measurement efficiency ($\eta = 67\%$) only slightly increases the observed deviations by $\eta^{-1/2} - 1 = 22$ %. Here we have set $\alpha = \sqrt{\frac{1}{2\eta\kappa}}/T_{\mathrm{meas}}$ so that a indeed coincides with the intra-field cavity amplitude. c,d) Probability density with the JPC OFF (c) and ON (d), extracted from 10^6 measurement outcomes when the qubit is prepared in states $|g\rangle$ or $|e\rangle$ with equal probability. The halved probability density corresponding to the preparation of $|g\rangle$ only (resp. $|e\rangle$) is plotted in blue (red) together with the projections along the real and imaginary axes. Turning on the pump of the amplifier (d) results in a great enhancement of the measurement fidelity compared to the case when it if turned off (c).

Thus, if $\sqrt{2\eta\kappa n}\sin\frac{\theta}{2}T_{\mathrm{meas}} \gg \sqrt{T_{\mathrm{meas}}}$, which is equivalent to $T_{\mathrm{meas}} \gg 1/\eta\Gamma_d$, one can use the criterion

$$\begin{cases} \mathrm{Im}[a] < 0 \rightarrow \text{qubit in } |g\rangle \\ \mathrm{Im}[a] > 0 \rightarrow \text{qubit in } |e\rangle \end{cases} . \tag{123}$$

This measurement is always projective since qubit state is collapsed to an eigenstate, but its fidelity depends on the distinguishability between the distributions of a according to the qubit state, and thus on η.

In fact we empirically chose T_{meas} so that the fidelity of the readout beyond relaxation errors is 99.7 %. This can be estimated by fitting the negative part of the probability distribution of the measured $\text{Im}[a]$ values when the qubit is in $|g\rangle$ (blue curve on the projection of Fig 20d) with a gaussian. The overlap of this gaussian with the positive part of the axis gives the probability of error during the detection.

From this gaussian deviation and mean (signal to noise ratio), we can also estimate η. Indeed, we have

$$\frac{\text{Var}(\text{Re}[a]) + \text{Var}(\text{Im}[a])}{|\bar{a}|^2} = \frac{1}{\eta n \kappa T_{\text{meas}}}, \tag{124}$$

which is independent of α. We then find that $\eta = 67$ %.

Let us comment on this readout performances.

- The gain of the parametric amplifier is set to $G \geq 20$ dB. Since the noise temperature of the following HEMT amplifier is about 10K[11], that is ~ 25 photons at 8 GHz, it ensures that this noise is below 0.25 photon referenced to the output of the cavity. Indeed, the signal to noise ratio at the end of the detection setup reads $\text{SNR} = \frac{S}{\frac{1}{2} + n_1 + \frac{n_2}{G_1} + \frac{n_3}{G_1 G_2} + ...}$, where G_i and n_i are the gain and added noise photons by the i^{th} amplifier. In terms of measurement efficiency,

$$\eta^{-1} = \eta_1^{-1} + (\eta_2 G_1)^{-1} + (\eta_3 G_1 G_2)^{-1} + ..., \tag{125}$$

  and $\eta_2 = \eta_{\text{HEMT}} \sim 0.5$ %.

- We do not use the real part of the measurement record (see Eq.(118)) to actuate the density matrix of the qubit according to Eq.(119). Thus our measurement scheme is equivalent to a homodyne measurement of efficiency $\eta/2$, so that the number of added photons by the JPC is $n_1 = 1/2$ at minimum. However, in the convention chosen here, an ideal amplifier corresponds to $\eta = 1$ since the factor 1/2 has already been taken into account in Eq. (119).

- The finite efficiency is partly due to the leak through the unmonitored input port and losses in the cavity. Indeed, not all of the probing photons are collected through the output port so that we can write $\eta = \frac{\kappa_{out}}{\kappa_{in}+\kappa_L+\kappa_{out}} \eta_{\text{detector}}$. This leads to $\eta_{\text{detector}} = 82$ %, which characterizes the efficiency of the output field detector only. In an ideal setup, we would get $\eta = 1$ but 1 dB of loss in the components between the cavity output and the JPC are sufficient to explain this figure.

- A faster readout could in principle be achieved by increasing the number of photons n in the cavity in the stationary regime so as to avoid relaxation or

11 This effective temperature takes into account the losses in the lines between the JPC and the HEMT

excitation during readout. Indeed, in the experiment, $\Gamma_\downarrow(t_{\text{coll}} + T_{\text{meas}}) = 4$ % when the qubit is in $|e\rangle$, leading roughly to an added 2 % of readout errors, and $\Gamma_\uparrow(t_{\text{coll}} + T_{\text{meas}}) = 0.1$ % when the qubit is in $|g\rangle$, leading to negligible readout errors. However the dispersive regime is valid for $n \ll 5$ (Eq. (78)). In practice, $n = 1.4$ was empirically set so that readout induced qubit flips happen less than 0.2 % of the time. Within this limit, our readout remains single shot and QND.

3.2.3.2 *Quantum jumps*

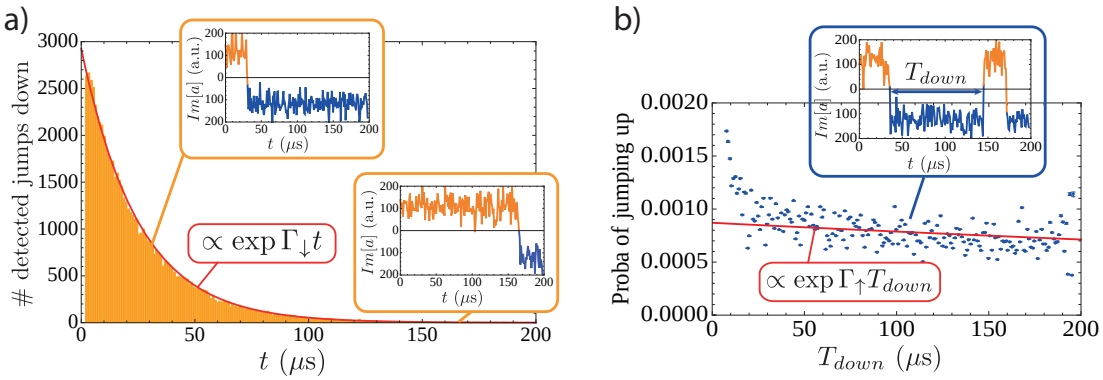

Figure 21: Over 10^5 experiments, the qubit is prepared in $|e\rangle$ and then continuously monitored for 200 μs. a) The imaginary part of the measurement record is integrated over bins of 960 ns, which is the time needed for a high-fidelity readout. The resulting signal is then well above 0 until it switches abruptly to negative values when the qubit relaxes. A typical trajectory and an unusually long-lived excitation of the qubit are presented in orange insets. Histogram of the dates of jumps follows an exponential law of rate $\Gamma_\downarrow$. b) For some trajectories, the qubit then gets thermally re-excited after the jump down (blue inset). The probability of not jumping back up after time T_{down} is supposed to follow an exponential law of rate $\Gamma_\uparrow$.

This non demolition readout allows us to observe *quantum jumps* [22]. Quantum jumps appear when measuring a system strongly enough so that the corresponding measurement rate Γ_m is much larger than the typical rate of non-coherent processes changing its state[12]. In our case, this corresponds to $\Gamma_m T_1 \gg 1$. In that case and on a time scale larger than $1/\Gamma_m$, qubit state is forced to be $|g\rangle$ or $|e\rangle$ but relaxation or excitation events will occasionally flip this state.

Observation of quantum jumps is presented on Fig. 21a. The qubit is initially prepared in $|e\rangle$ and is then left undriven while the cavity contains a readout field with the same characteristics as the one described in the previous section. The value of the imaginary part of the measurement record corresponding to Eq.(118) is represented as a function of time. On a typical trajectory, the signal remains well above 0 (qubit in $|e\rangle$) for about $1/\Gamma_\downarrow$ and then abruptly becomes negative when the qubit relaxes. However, on some trajectories such as the one presented on Fig. 21b, the qubit can remain in $|e\rangle$ for much longer. When constructing the histogram of these jumps dates,

12 coherent departure from a measured state is suppressed due to Zeno effect

one recovers an exponential decay with a rate $\Gamma_\downarrow$. This is another proof of the QNDness of the readout. Jumps up from $|g\rangle$ to $|e\rangle$ also occur, but with a much smaller rate $\Gamma_\uparrow$.

Here, relaxation appears to be an abrupt event, but we will see in 3.4 that this is in fact dependent on the detection scheme that is used. In the present experiment, it is in fact our knowledge of the qubit that evolves on a short time scale $1/\Gamma_m$.

3.3 HIGH-POWER READOUT

In the experiment described in 3.2.3, the parameters of the system were chosen in order to maximize measurement rate with respect to relaxation rate so that $\Gamma_m/\Gamma_1 \gg 1$. Namely, we set $\chi \simeq \kappa$. However, relaxation during the measurement limits this readout fidelity (~ 4 % errors when the qubit is in $|e\rangle$). Moreover, for some experiments such as the one described in 7, parameters are constrained so that such a fidelity cannot be obtained via QND dispersive readout. When the readout does not need to be QND, another scheme designed by Reed *et al.* [122] allows for high-fidelity projective readout, particularly in the regime where $\chi \gg \kappa$. It makes use of the non-trivial regime where the cavity is probed at high power. In this section, we will describe qualitatively this regime and show how it can be used for qubit readout. A detailed theoretical description can be found in [123].

The dispersive hamiltonian $H = \sum_{p=r,q} \omega_p n_p + \frac{1}{2} \sum_{p,p'=r,q} \chi_{pp'} n_p n_{p'}$ found through black-box quantization of the circuit (see Sec. 2.2.3.2) and in which the cavity mode inherits a small constant anharmonicity χ_{rr} from its hybridization with the qubit is only valid in the dispersive limit $n \ll n_c$. When cranking up probe power, cavity resonance frequency is shifted by an amount χ_{rr} per photon, but this anharmonicity decreases down to 0 for large powers [124]. In this regime, cavity resonance frequency is the one of the bare cavity mode f_{bare}[13]. A map showing cavity transmission coefficient as a function of probe power and frequency is presented on Fig. 22a. At low power ($n \sim 1$ photon) the system behavior is well captured by the dispersive hamiltonian (60). Several resonances appear separated by χ due to thermal excitation of the qubit. These frequencies are shifted linearly with increasing power. At large powers, only one resonance remains, at f_{bare}. The physics in between these two limits is still poorly understood. Cavity transmission displays complex pattern as a function of probe frequency probably due to interferences between bistable solutions.

When probing the cavity at f_{bare}, transmission is very low at low power but when approaching the region circled in green, the response displays a strong non-linearity and the cavity switches abruptly to a *bright state* (high transmission). The probe power for which the cavity switches depends on the qubit state. This can be simply understood considering that when in $|e\rangle$, the qubit shifts the cavity low power resonance frequency by $\chi/2\pi$ toward f_{bare}. Thus, the lorentzian filter in Eq. (51) is less strong and intra cavity field is stronger for a given probe power. The cavity switching probability as a

13 but is still affected by the sapphire chip and the antennas

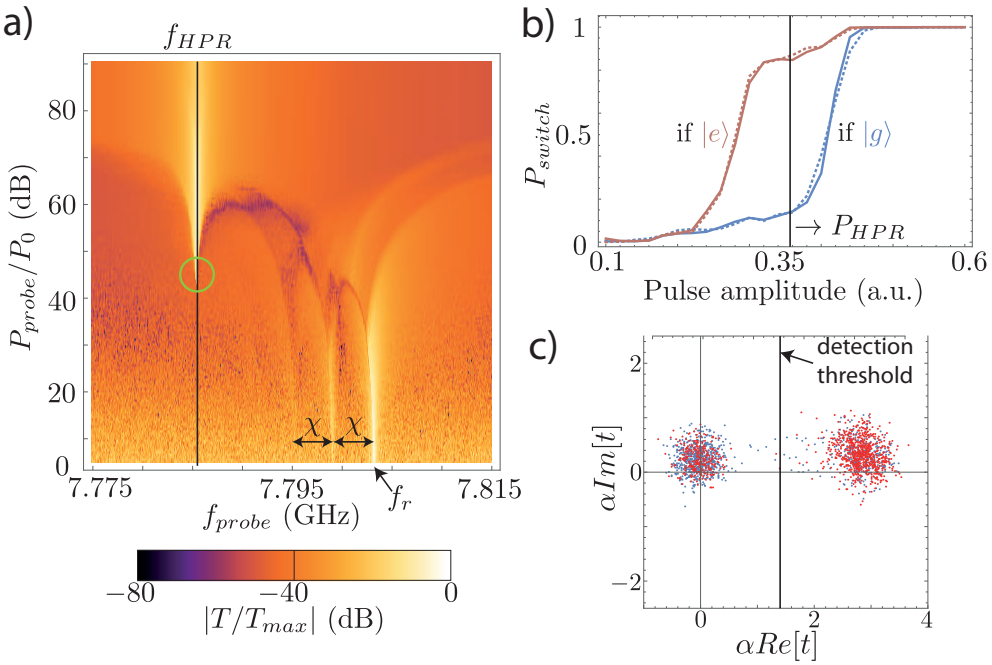

Figure 22: a) Magnitude of the cavity transmission coefficient encoded in color as a function of probe power and frequency, when driving with a continuous tone. We normalize the signal by the bright state transmission. Readout frequency is $f_{HPR} = f_{bare}$ (black line). Readout power is chosen within the region materialized by a green circle. b) Cavity response to pulsed driving (pulse length: is 800 ns). We represent the switching probability as a function of probe pulse amplitude for a qubit at thermal equilibrium (blue) or after a π pulse (red). Switching detection criterion is chosen as in c. Plain lines: cavity initially empty. Dotted lines: cavity containing initially about 5 photons. Readout power P_{HPR} is chosen to maximize contrast. c) Integrated output signal represented in the Fresnel plane rotating at f_{bare} over 1000 experiments for a qubit at thermal equilibrium (blue) and after a π pulse (red). For long enough integration time, two well separated distributions appear. Switching detection threshold is chosen in between. Correcting for thermal population (Qubit 2 in Tab.3, used in Sec. 4.2.1 and [82]), these distributions are consistent with a cavity that is never switching when the qubit is in state $|g\rangle$, and switching in 94 % of the experiments when the qubit is in an excited state (6 % false negatives).

function of the probe pulse amplitude displays a characteristic S-shape (Fig. 22b) that is therefore shifted according to the qubit state. In practice, we choose the amplitude that maximizes the contrast between ground and excited qubit state response.

An advantage of this method is that once the cavity has switched to its bright state, it stays there as long as the field energy has not decreased beyond a given threshold. Thus, we can map the qubit state onto the cavity state and then integrate the output signal for an indefinite amount of time as long as probe power is not turned off. Signal to noise ratio can thus be increased at will so that quantum limited amplification chain is not needed. Errors are then dominated by spurious switching of the cavity but probabilities as low as 2 % of false positives and false negatives have been measured in some

cases. In the experiment corresponding to Fig. 22c, we calibrated 6% of false negatives and no measurable false positive. The origin of these errors needs more investigation. Possible explanations include quasi-particles mediated excitations of the qubit, large probe field fluctuations...

Another advantage of this readout method is that its results depend only weakly on the prior state of the cavity, as long as the photon number is low. If $n\chi_{rr} \ll \kappa$, low power resonance frequency does not depend on n and switching probability is not affected by these photons . On Fig. 22b, plain lines correspond to a cavity mode initially empty of photons, and dotted lines correspond to a intra cavity field of ~ 5 photons before readout. The cavity responses are very similar. Therefore, it is not needed to wait for the cavity to empty before reading out the state of the qubit, which would limit single-shot readout fidelity as it allows for relaxation of the qubit[14].

Beside being destructive for the qubit, the main drawback of this method is that the used power is so large ($\sim 1.5 \times 10^6$ photons on average in the cavity if the excitation were permanent) that it creates quasi-particles in the superconducting aluminum of the cavity or antennas. The relaxation of these quasi-particles has been studied in [126] but the corresponding time constant is not well understood. Their effect is to limit the life time T_1 of the qubit and even more drastically the coherence time T_2. Moreover, qubit resonance frequency sometimes displays low frequency fluctuations, which cannot be described within the Lindblad model. This limits the repetition rate of the experiment. We found an important variation in the relaxation rate of these quasi-particles (from a few μs up to several ms) from a qubit design to another, but also with the same system after cycling it above the critical temperature of superconducting aluminum. This is consistent with recent observation of quasi-particles induced noise suppression due to vortices in aluminum thin films [127, 128]. These vortices are created when cooling down the sample under constant magnetic field and act as quasi-particle traps.

In practice, high fidelity single-shot readout is not always needed. When only occupation probability of the excited state as a mean is needed, a compromise can be found between the experiment repetition rate and the readout fidelity by lowering the readout pulse power. In the intermediate region between high and low power regimes for the cavity, we then adjust readout power and frequency to empirically maximize the readout contrast.

3.4 MONITORING THE FLUORESCENCE

The measurement scheme that was described in 3.2.3 uses the dispersive interaction between qubit and cavity to probe the σ_Z operator. This interaction entails decoherence of the qubit, which is associated to a Lindblad super operator $\mathcal{D}[\sqrt{\frac{\Gamma_d}{2}}\sigma_Z]$ defined in Eq.(84). However, if the measurement signal is efficiently detected, the evolution of the qubit state is not predictable but can be known a posteriori. Instead of decoherence,

14 another method consists in using another empty coupled cavity for readout [125]

the qubit follows a stochastic evolution towards $|g\rangle$ or $|e\rangle$. Therefore, at times longer than $\frac{1}{\eta\Gamma_d}$, the continuous measurement of the field at ω_r constitutes a QND projective readout.

Then what about the other decoherence processes in the master equation (29)? Can we detect the corresponding measurement signal and take it into account to better predict the state of the qubit?
In the model described in 2.2.3.2 an unavoidable relaxation process comes from the hybridization of qubit and cavity modes. Qubit energy decays directly into the probe lines at a rate $\gamma_{1,\text{Purcell}}$. The corresponding jump operator is $L = \sqrt{\gamma_{1,\text{Purcell}}}\sigma_-$. In order to retrieve this information and actuate the density matrix with it, we will once again monitor the electromagnetic field in the output line with a high efficiency detection chain. However, contrary to the scheme pictured in Fig. 19, detection is not made at cavity frequency ω_r but at qubit frequency ω_q.

Starting from Eq. (93), if an ideal photocounter working at ω_q is placed on the output line, it acts as a jump detector and the dynamics is described by Eqs.(93,96). Thus, neglecting for now any relaxation processes but the one into the output line, if no jump is detected, qubit state collapses toward $|g\rangle$ on a typical time-scale $1/\gamma_{1,\text{Purcell}}$ but remains pure for a detection efficiency 1. When a jump is detected, it goes instantaneously to $|g\rangle$.

However, we do not have efficient photo-counters in the microwave range and as in 3.2.3, we rather realize a heterodyne detection. For perfect detection, the SME reads [23, 24]

$$\begin{aligned} \mathrm{d}\rho &= -\tfrac{i}{\hbar}\mathrm{d}t[H,\rho] + \mathrm{d}t\mathcal{D}[\sqrt{\gamma_1}\sigma_-]\rho \\ &+ \sqrt{2}\mathrm{d}W_{t,I}\mathcal{M}[\sqrt{\gamma_{1,\text{Purcell}}}\sigma_-]\rho + \sqrt{2}\mathrm{d}W_{t,Q}\mathcal{M}[i\sqrt{\gamma_{1,\text{Purcell}}}\sigma_-]\rho, \end{aligned} \tag{126}$$

with $\mathcal{M}[c]$ defined, as in 3.2.2, by $\mathcal{M}[c]\rho = \frac{1}{2}((c-\langle c\rangle)\rho + \rho(c^\dagger - \langle c^\dagger\rangle))$ and $W_{t,I}$ and $W_{t,Q}$ two independent Wiener processes. I and Q refer respectively to the *in phase* ($\delta = 0$) and *in quadrature* ($\delta = -\frac{\pi}{2}$) part of the detected signal.

Relaxation into the unmonitored input line, through cavity internal losses and non radiative decay processes have the same effect, which is limiting the overall detection efficiency η. We take this into account along with imperfections of the detection setup whose first amplifier is a JPC designed so that its amplification bandwidth is centred at ω_q. We can indeed decompose

$$\eta = \frac{\gamma_{1,\text{Purcell}}}{\gamma_1} \times \frac{\gamma_{1,\text{Purcell,out}}}{\gamma_{1,\text{Purcell}}} \times \eta_{\text{detec}}, \tag{127}$$

where the first term accounts for the fraction of the energy radiated into the lines when the qubit decays being finite (see Sec. 2.2.5), the second for the finite fraction of the energy leaking through the monitored output line (see Eq. (49)), and the third for the detection setup imperfections (dominated by losses in RF components between the cavity and the JPC). The first and third contributions are impossible to distinguish in

practice due to uncalibrated cavity output impedance, and we only access the value of the overall efficiency η.
Including non-relaxation induced dephasing, we get the full Stochastic Master Equation:

$$\begin{aligned} \mathrm{d}\rho &= -\frac{i}{\hbar}\mathrm{d}t[H,\rho] + \gamma_1 \mathrm{d}t\mathcal{D}[\sigma_-]\rho + \frac{\gamma_\phi}{2}\mathrm{d}t\mathcal{D}[\sigma_Z]\rho \\ &+ \sqrt{\frac{\eta\gamma_1}{2}}(\sigma_-\rho + \rho\sigma_+ - \langle\sigma_X\rangle\rho)\mathrm{d}W_{t,I} + \sqrt{\frac{\eta\gamma_1}{2}}(i\sigma_-\rho - i\rho\sigma_+ - \langle\sigma_Y\rangle\rho)\mathrm{d}W_{t,Q}. \end{aligned} \tag{128}$$

The measurement records are given by

$$\begin{cases} \mathrm{d}I &= \sqrt{\frac{\eta\gamma_1}{2}}\langle\sigma_X\rangle\mathrm{d}t + \mathrm{d}W_{t,I} \\ \mathrm{d}Q &= \sqrt{\frac{\eta\gamma_1}{2}}\langle\sigma_Y\rangle\mathrm{d}t + \mathrm{d}W_{t,Q} \end{cases}. \tag{129}$$

3.4.1 *Mean fluorescence signal*

The fluorescence signal of an atom, which is the light that it emits when de-exciting, is commonly observed and used in physics, but also in biology, chemistry... However, due to limited measurement efficiency for linear detection setups, it has mostly been characterized through its power spectrum. When driven on resonance, the signature of fluorescence is the so-called Mollow triplet [129]. With superconducting qubits, it has recently been observed on the single "atom" level [26], and efficient linear detection with a sufficiently large bandwidth has allowed to resolve temporally the fluorescence signal [25, 130].

In the experiment reported in [82] and described in Fig. 23, a qubit resonating at $\omega_q/2\pi = 5.2$ GHz (Qubit 2 in Tab.3) is embedded in a 3D aluminum cavity whose first mode resonates at $\omega_r/2\pi = 7.8$ GHz. When the qubit is resonantly driven, it undergoes Rabi oscillations that can be revealed by measuring the occupation of the levels after a time t varying from 0 to $T = 2.5\ \mu\mathrm{s} < T_1 = 16\ \mu\mathrm{s}$. This is done using a high power readout method (see Sec. 3.3), whose fidelity has been calibrated as in Fig. 22. Measured Rabi oscillations for a qubit initially in $|g\rangle$ (in purple) or $|e\rangle$ (in orange) are presented in Fig. 23b. The qubit is actually in $|g\rangle$ only $f_g = 91\%$ of the experiments when preparing the ground state, and in $|e\rangle$ only $f_e = 85\%$ of the times when preparing the excited state. This limited preparation fidelity comes from an important thermal excitation rate in this experiment that results in about 30% spurious occupation of the excited state at thermal equilibrium, which is partially lowered using the cool down scheme described in 6.1 prior to every experiment. This imperfect preparation fidelity lowers the contrast of the oscillations.

In a separate experiment, we drive the qubit during the whole time interval $[0, T]$. While this drive is applied through a lowly coupled transmission line labelled *in* on Fig. 23a, the resonance fluorescence is collected on the strongly coupled *out* line and measured continuously using a JPC tuned at qubit frequency. The coupling rate $\kappa_{out}/2\pi = 0.25$ MHz to this line far dominates the coupling rates κ_{in}, κ_L to other

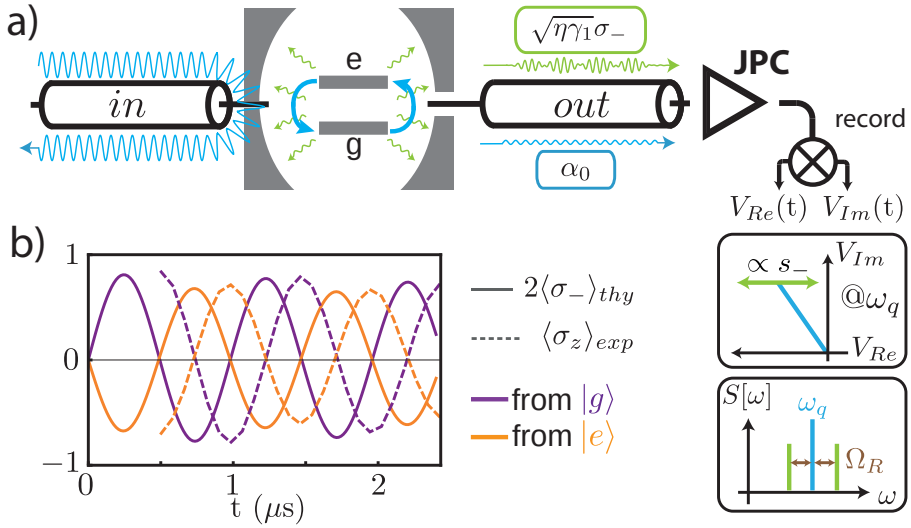

Figure 23: a) Schematic of the experimental setup. A 3D transmon is driven through the *in* line and its fluorescence signal (in green) is collected on the *out* line, along with the small portion of the drive field that is transmitted through the cavity (in blue). In the Fresnel plane rotating at ω_q, the transmitted signal has a constant complex amplitude (peak at ω_q in the power spectrum), whereas the fluorescence signal has a complex amplitude oscillating at the Rabi frequency (in the frequency domain, 2 side bands appear around ω_q). Note that in the experiment, the signal is down-converted by mixing with a LO before being digitized (not represented: see 3.4.2 and Fig. 25b for detailed description). b) Measured occupation of the qubit levels during the drive (dotted line) and predicted value of the fluorescence signal (plain lines) for a qubit initially in $|g\rangle$ or $|e\rangle$.

decay channels of the cavity. However, qubit decay rate is measured to be dominated by unknown non radiative processes. Quantitatively, $\gamma_1 > \gamma_{1,\text{Purcell}} \simeq 50\ \mu\text{s}^{-1}$, so that signal collection efficiency in Eq. (129) is quite small. However, here we are only interested in the fluorescence signal as a mean so that the efficiency η only modifies the *a priori* unknown scaling factor relating the output cavity field to the voltage measured by the acquisition board.

Considering a drive field a_{in} in a large coherent state $|\alpha_{in}\rangle$ whose phase is set to 0 ($\alpha_{in} > 0$), it results in an added drive term in the qubit hamiltonian that reads, as in Eqs. (45, 75), $H_{\text{drive}} = \hbar(i\sqrt{\kappa_{in}}\alpha_{in}\frac{g}{\Delta}(\sigma_+ - \sigma_-)) = -\hbar\sqrt{\kappa_{in}}\alpha_{in}\frac{g}{\Delta}\sigma_Y$, so that the unitary evolution operator for the qubit after time t is

$$U(t) = \exp(i\sqrt{\kappa_{in}}\alpha_{in}\frac{g}{\Delta}\sigma_Y t) = \cos(\frac{\Omega_R}{2}t)\ \mathbb{1} + i\sin(\frac{\Omega_R}{2}t)\ \sigma_Y, \tag{130}$$

where $\Omega_R = 2\sqrt{\kappa_{in}}\alpha_{in}\frac{g}{\Delta}$ is the Rabi pulsation. Thus, the qubit rotates around the y-axis of the Bloch sphere. Following Eq. (129), the corresponding mean fluorescence record is

$$\begin{cases} \overline{\frac{\mathrm{d}I}{\mathrm{d}t}}_{\text{fluo}} = \sqrt{\frac{\eta\gamma_1}{2}}\langle\sigma_X\rangle = \sqrt{\frac{\eta\gamma_1}{2}}\sin\Omega_R t \\ \overline{\frac{\mathrm{d}Q}{\mathrm{d}t}}_{\text{fluo}} = \sqrt{\frac{\eta\gamma_1}{2}}\langle\sigma_Y\rangle = 0 \end{cases}. \tag{131}$$

The finite transmission of the cavity at ω_q implies that a fraction of the drive field is also detected and adds up to the fluorescence signal. This contribution can essentially be understood classically. Indeed, the transmitted field is in a coherent state $|\alpha_{out,0}\rangle$ at ω_q, which reads, according to Eq. (52),

$$\alpha_{out,0} = \frac{\sqrt{2\kappa_{in}\kappa_{out}}}{\kappa_{tot} - 2i(\omega_q - \omega_r)} \simeq -i\Omega_R \frac{\sqrt{\kappa_{out}}}{2g}. \tag{132}$$

Here, we have used that $\Delta = \omega_r - \omega_q \gg \kappa_{tot}$, where Δ is the detuning between qubit and cavity. In the Q measurement record defined in Eq. (129), this transmitted field yields a constant term

$$\begin{cases} \overline{\frac{\mathrm{d}I}{\mathrm{d}t}}_{\mathrm{trans}} &= 0 \\ \overline{\frac{\mathrm{d}Q}{\mathrm{d}t}}_{\mathrm{trans}} &= -\sqrt{\frac{\eta\kappa_{tot}}{2}}\frac{\Omega_R}{g} \end{cases}. \tag{133}$$

Thus, the fluorescence signal and the transmitted signal should each be detected on a different quadrature. However, in our experiment, the transmission between input and output port is dominated by a -50 dB aerial cross-talk so that the transmitted signal has an unknown amplitude and phase. In terms of measurement record, both I and Q have an unknown constant component from the transmitted field. Combining with Eq. (131), and taking into account an unknown scaling factor V_0, the mean complex signal detected by the JPC thus reads

$$\begin{aligned} S(t) &= V_0\sqrt{\tfrac{1}{2\eta\gamma_1}}\left(\overline{\tfrac{\mathrm{d}I}{\mathrm{d}t}} + i\overline{\tfrac{\mathrm{d}Q}{\mathrm{d}t}}\right) \\ &= \langle\sigma_-(t)\rangle + \beta_0, \end{aligned} \tag{134}$$

where V_0 is defined so that $S(t)/V_0$ matches with the value of $\langle\sigma_-(t)\rangle$. The complex number β_0 scales with Ω_R and needs to be determined as explained below.

This record is not directly the digitized signal at the output of the detection setup. Indeed, the measurement has a finite bandwidth $\delta f = 1.6$ MHz, which is dominated by the JPC amplification bandwidth and which acts as a low-pass filter for the signal. In the filtered signal $\tilde{S}(t)$,

- the transmitted field contribution $V_0\beta_0\theta(t)$ results in a non constant signal $\tilde{S}_0(t) = V_0\beta_0(1 - \exp -t/(2\pi\delta f))$ during a transient regime that lasts about 100 ns after turning on the drive at $t = 0$. Note that it still does not depend on the qubit state.

- after the short transient, the oscillating part $V_0\langle\sigma_-(t)\rangle$ gets its amplitude decreased for Rabi frequencies beyond δf.

On Fig. 24a, we represent the averaged measured output signals for a qubit prepared with finite fidelity in $|g\rangle$ or $|e\rangle$ for three different drive amplitudes. In order to keep only the interesting oscillating part, we subtract the state independent transmitted field contribution, which corresponds to the output signal for a qubit initially in the most entropic state $\rho = \frac{1}{2}\mathbb{1}$. In practice, this is not done in a separate experiment but by averaging the signals corresponding to a qubit in $|g\rangle$ or $|e\rangle$ with the proper

coefficients to compensate for the imperfect preparation fidelities f_g and f_e[15].

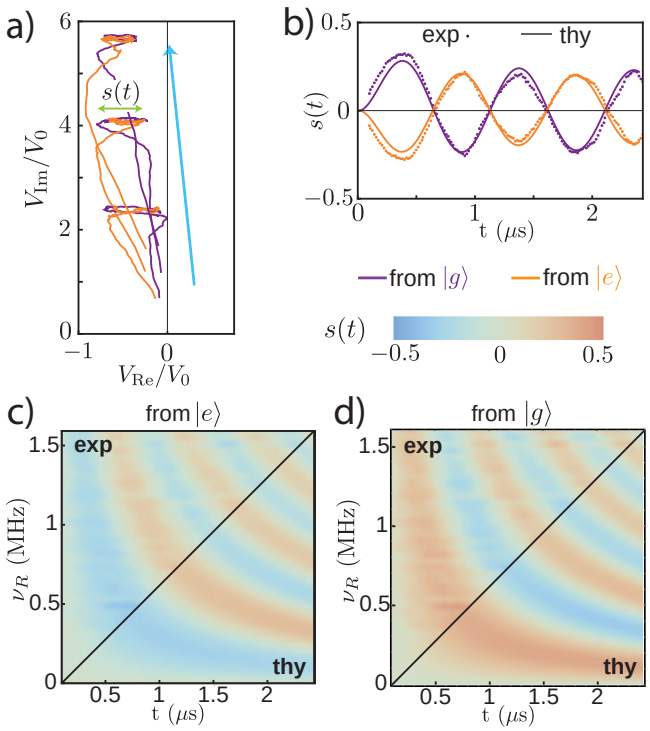

Figure 24: a) Measured complex fluorescence signal for a qubit initially in $|g\rangle$ or $|e\rangle$, and for increasing drive amplitudes (blue arrow) leading to Rabi frequencies 0.6, 1 and 1.4 MHz. Due to the detection setup finite bandwidth, the oscillation amplitude decreases when Ω_R increases. The scaling factor V_0 is chosen as in b, so that the signal matches the predicted and numerically filtered signal using Eq. (134). b) Normalized signal $s(t)$ after subtraction of the constant contribution from the transmitted field and for a Rabi frequency of 1 MHz. Reduced contrast is due to initial finite purity and filtering of the signal by the amplifier acting as a low pass filter. c) -d) Predicted and measured fluorescence signal encoded in color, for Rabi frequencies ranging from 0 to 1.6 MHz.

Then, taking the real part of the oscillating term and dividing by V_0, we get the normalized signal $s(t) = \mathrm{Re}[(\tilde{S}(t) - \tilde{S}_0(t))/V_0)]$. Note that V_0 is constant over all experiments when varying Ω_R.

To calibrate the factor V_0, we compute the expected value of $\langle\sigma_-(t)\rangle$ using the Lindblad master equation

$$\mathrm{d}\rho = -\frac{i}{\hbar}\mathrm{d}t[H + H_{\mathrm{drive}}, \rho] + \gamma_1 \mathrm{d}t\mathcal{D}[\sigma_-], \tag{135}$$

where the pure dephasing term is neglected and we set $\rho(0) = f_g|g\rangle\langle g| + (1 - f_g)|e\rangle\langle e|$ for a qubit prepared near $|g\rangle$. The resulting signal is numerically filtered to mimic the

15 $\frac{1}{2}\mathbb{1} = a_g\rho^g + a_e\rho^e$ where $\rho^{g,e}$ is the density matrix representing the finite fidelity preparation of $|g, e\rangle$ and the coefficients are $a_g = \frac{1/2-(1-f_e)}{f_g+f_e-1}$ and $a_e\frac{1/2-(1-f_g)}{f_g+f_e-1}$.

finite bandwidth of the measurement. V_0 is then adjusted over all data so that this predicted signal matches $s(t)$. On Fig. 24b, we represent the measured $s(t)$ (dotted line) and the numerically filtered predicted signal for a drive amplitude corresponding to a Rabi frequency of $\Omega_R/2\pi = 1$ MHz. On Fig. 24c-d the predicted and measured signals are encoded in color for Rabi frequencies ranging from 0 to 1.6 MHz. Theoretical predictions (lower right corner of the panel) and experimental data (upper left) show good agreement.

3.4.2 *Quantum trajectories for fluorescence*

In the experiment described in the previous section, the detection efficiency of $\sqrt{\gamma_1}\sigma_-$ is degraded by non radiative decay processes of the qubit since $\eta = \eta_{\text{detec}}\frac{\gamma_{1,\text{Purcell}}}{\gamma_1} \leq 0.3\ \eta_{\text{detec}}$. This prevents us from using individual measurement records to get reasonably pure quantum trajectories. We thus design a more adapted experiment (Qubit 4 in Tab. 3). In order to increase $\gamma_{1,\text{Purcell}}$, the qubit frequency is chosen closer to the cavity mode. It was set at $\omega_q/2\pi = 6.3$ GHz. The coupling to the *out* line is also increased. This larger coupling allows us to use a copper cavity with more important losses while keeping the condition $\kappa_{out} \gg \kappa_L \simeq 2\pi \times 200$ kHz.

With this setup, we observed a far better thermalization of the qubit, with a probability of thermal excitation at equilibrium $p(e) \leqslant 1$ %, so that $T_{qubit} \leqslant 70$ mK. We also measure the decay time $T_1 = 4$ μs and the pure dephasing time $T_\phi = 35$ μs. Here, the qubit decay time is actually longer than the upper bound set by the Purcell decay rate computed with Eq. (76), $T_{1,\text{Purcell}} = 1.3$ μs. Such discrepancies have also been reported in [77] and are attributed to the coupling of the transmon mode to other cavity modes, which are neglected in Eq. (76). Here, the large value $\frac{g}{\Delta} \sim \frac{1}{5}$ may also make some approximations assuming the dispersive regime inaccurate (see Sec. 2.2.3.3).

The experimental setup, similar to the one depicted on Fig. 23a is represented on Fig. 25a.

- The qubit is prepared in $|e\rangle$ or in $(|g\rangle + |e\rangle)/\sqrt{2}$ by applying a fast π or $\pi/2$ resonant pulse. This pulse is generated using a LO at $\omega_q/2\pi + 100$ MHz that is mixed with a temporally windowed 100 MHz sine.
- The fluorescence field is measured for a time ranging from 1 to 10 μs. The signal at the output of the cavity is amplified using a JPC and several commercial amplifiers. It is then down-converted to 100 MHz by mixing with the same LO that was used to generate preparation pulse, before being sampled and digitized. In order to limit the amount of recorded data, the resulting record is integrated over $\mathrm{d}t = 200$ ns bins chosen so that $\mathrm{d}t \ll T_1$. Since the only monitored jump operator is σ_- and $\sigma_-^2 = 0$, a simple quantum filter [131] that we describe in Sec. 3.4.2.2 will yield accurate quantum trajectories even for such large time steps [132].
- The qubit state is measured using the high-power readout method described in Sec. 3.3. On 1/3 of the experiments, this readout is directly realized at the end of

trajectories (σ_Z measurement), on 1/3 after a fast $\frac{\pi}{2}|_y$ pulse to rotate the qubit around y-axis (σ_X measurement) and 1/3 after a $\frac{\pi}{2}|_x$ pulse to rotate it around the x-axis (σ_Y measurement)[16]. Note that in this experiment, the high power readout pulse degraded the coherence time of the qubit for tens of milliseconds after the readout, limiting the repetition rate of the experiment. This is attributed to quasi particles creation, whose relaxation was recently shown to occur on such long timescales [133, 128]. We chose to decrease the amplitude of this pulse in order to limit this effect, at the expense of the readout fidelity. Thus, in a single-shot, the fidelity of the readout is about 85 % (15 % probability of false positive or false negative). However, since we will only use this final readout as a mean over a given ensemble, this imperfection can be taken into account and corrected for.

A great number of such trajectories are then recorded. For each initial state of the qubit, each trajectory duration and each type of final tomographic measurement, 10^6 trajectories are recorded on a dedicated hardware. This important amount of data can be challenging to process but this figure was chosen to sample sufficiently every possible final density matrix of the qubit (see Sec. 3.4.2.2). Moreover, we need to keep the whole measurement record for each experiment.

In [134], Murch *et al.* show that for trajectories associated with a dispersive measurement of the qubit, it is possible to reconstruct the final density matrix from the integral of the measurement record only. Indeed, for a homodyne detection of the imaginary part of the field at cavity frequency as is done in this experiment, and neglecting the relaxation, the SME reads (see Eq. (109))

$$\mathrm{d}\rho = -\frac{i}{\hbar}\mathrm{d}t[H,\rho] + \frac{\Gamma_d}{2}\mathrm{d}t\mathcal{D}[\sigma_Z]\rho + \mathrm{d}W_t\sqrt{2\eta\Gamma_d}\mathcal{M}[\sigma_Z]\rho, \tag{136}$$

and the measurement record is (see Eq. (108))

$$\mathrm{d}J_t = \sqrt{2\eta\Gamma_d}z\mathrm{d}t + \mathrm{d}W_t. \tag{137}$$

Then, letting $\zeta = \mathrm{ArcTanh}(z)$, a direct Itô calculation leads to

$$\mathrm{d}\zeta = \sqrt{2\Gamma_d\eta}\ \mathrm{d}J_t, \tag{138}$$

so that

$$z(T) = \tanh\Big(\zeta(0) + \int_0^T \frac{\mathrm{d}J_t}{\sqrt{2\Gamma_d\eta}}\Big). \tag{139}$$

It is also possible to show that $x(T)$ is directly linked to $z(T)$. Thus, a single scalar number is enough to reconstruct the state of the qubit.

In the present case of records associated with the fluorescence of the qubit, the integral of the measurement record does not allow to actuate ρ from 0 to T. Indeed,

16 The σ_Z measurement is delayed so that the time between the end of the trajectory and the projective measurement is the same for the 3 axis

the measurement being destructive, the value of $I(T)$ and $Q(T)$ does not depend on ρ for $T \gg T_1$ since it is then dominated by noise. In the following section, following a calculation by Mazyar Mirrahimi, we define a scalar value that is directly correlated to the tomographic averaged outcomes. This will enable us to validate the stochastic master equation model. Moreover, it will lead to a first estimation of η. An efficient way of estimating η is crucial in this experiment, since a brute force strategy consisting in running a maximum likelihood algorithm so that the fluorescence signal for each experiment matches with the final tomographic measurement statistics is time consuming. In Sec. 3.4.2.3, we describe another method using quantum particle filtering to estimate η.

3.4.2.1 *Integrable quantity for measurement records*

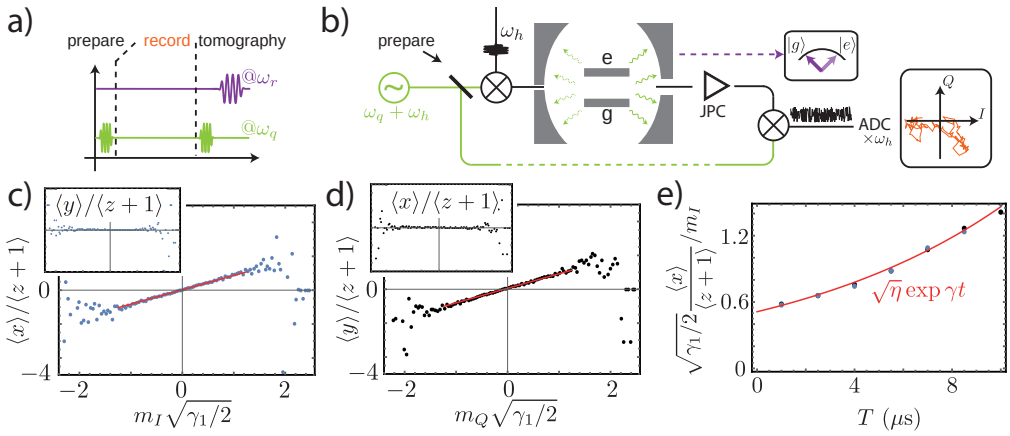

Figure 25: a) Pulse sequence for recorded fluorescence trajectories. The qubit is first prepared in $|e\rangle$ or $(|e\rangle + |g\rangle)/\sqrt{2}$ and its fluorescence signal is then recorded for a time T. Qubit is eventually projectively measured along either σ_X, σ_Y or σ_Z. b) Schematic of the experimental setup (full wiring can be found on Fig. 67). The same LO that is used to prepare the qubit is used to down convert the fluorescence signal before digitization. After numerical demodulation we obtain the record $\{I_t, Q_t\}$. c) For a qubit prepared in $|e\rangle$, the fluorescence signal is integrated for $T = 4$ μs with a decreasing exponential weight (see Eq. (142)). Experiments with the same resulting integral m_I are binned and we plot the mean value per bin of $\frac{x}{z+1}$ given by the final readout against m_I. When statistics is sufficient (low $|m_I|$) a slope appears. Red line: linear fit. Inset: no correlation is observed between m_I and $\frac{y}{z+1}$. d) Idem for m_Q and $\frac{y}{z+1}$. e) Dots : fitted slopes for m_I's (in blue) and m_Q's (in black) as a function of trajectory length T. Red line: exponential fit with time constant $1/(\gamma_1/2 - \gamma_{phi})$ leading to $\eta = 26\%$.

Starting from Eq. (128), in terms of Bloch coordinates, we find that

$$\begin{cases} \mathrm{d}x &= -(\frac{\gamma_1}{2} + \gamma_\phi)x\mathrm{d}t - \sqrt{\frac{\eta\gamma_1}{2}}(z + 1 - x^2)\mathrm{d}W_t \\ \mathrm{d}z &= -\gamma_1(z+1)\mathrm{d}t - \sqrt{\frac{\eta\gamma_1}{2}}x(z+1)\mathrm{d}W_t \end{cases} . \tag{140}$$

Then, letting $\xi = \frac{x}{z+1}$ and applying Itô rules, we find that

$$\begin{aligned} \mathrm{d}\xi &= (\tfrac{\gamma_1}{2} - \gamma_\phi)\xi \mathrm{d}t + \sqrt{\tfrac{\eta\gamma_1}{2}}\mathrm{d}W_t + \tfrac{\eta\gamma_1}{2} x \mathrm{d}t \\ &= (\tfrac{\gamma_1}{2} - \gamma_\phi)\xi \mathrm{d}t + \sqrt{\tfrac{\eta\gamma_1}{2}}\mathrm{d}I_t, \end{aligned} \tag{141}$$

where I_t is the measurement record defined in Eq. (129). Integrating this equation between time 0 and T, on a single trajectory we get

$$e^{-(\frac{\gamma_1}{2}-\gamma_\phi)T}\frac{x(T)}{z(T)+1} - \frac{x(0)}{z(0)+1} = \sqrt{\frac{\eta\gamma_1}{2}}\int_0^T e^{-(\frac{\gamma_1}{2}-\gamma_\phi)t}\mathrm{d}I_t \overset{\text{def}}{=} \sqrt{\frac{\eta\gamma_1}{2}} m_I. \tag{142}$$

Let us note here that $x(t) = \mathrm{Tr}[\rho(t)\sigma_X]$ and $z(t) = \mathrm{Tr}[\rho(t)\sigma_Z]$ are not directly measurable on a single experiment. Yet, when considering a great number N of trajectories from the same initial state and giving the same measured m_I, if we were to use all information in the measurement record, we would find N different ρ_k's with

$$\forall k, \sqrt{\frac{\eta\gamma_1}{2}} m_I = e^{-(\frac{\gamma_1}{2}-\gamma_\phi)T}\frac{\mathrm{Tr}[\rho_k\sigma_X]}{\mathrm{Tr}[\rho_k\sigma_Z]+1} - \frac{x(0)}{z(0)+1}, \tag{143}$$

so that averaging both sides of the equation over k[17]

$$\begin{aligned} \sqrt{\tfrac{\eta\gamma_1}{2}} m_I &= e^{-(\frac{\gamma_1}{2}-\gamma_\phi)T}\frac{\frac{1}{N}\sum_k \mathrm{Tr}[\rho_k\sigma_X]}{\frac{1}{N}\sum_k \mathrm{Tr}[\rho_k\sigma_Z]+1} - \frac{x(0)}{z(0)+1} \\ &= e^{-(\frac{\gamma_1}{2}-\gamma_\phi)T}\frac{\mathrm{Tr}[\overline{\rho}\sigma_X]}{\mathrm{Tr}[\overline{\rho}\sigma_Z]+1} - \frac{x(0)}{z(0)+1}, \end{aligned} \tag{144}$$

where $\overline{\rho}$ is the density matrix corresponding to the statistical mixture of all the selected final states. Thus, $\mathrm{Tr}[\overline{\rho}\sigma_\alpha]$ corresponds to the average value of the σ_α measurement outcomes ($\alpha = x, z$) for the selected experiments.

Similarly, defining $m_Q = \int_0^T e^{-(\frac{\gamma_1}{2}-\gamma_\phi)t}\mathrm{d}Q$, when selecting experiments giving the same m_Q, we have

$$\sqrt{\frac{\eta\gamma_1}{2}} m_Q = e^{-(\frac{\gamma_1}{2}-\gamma_\phi)T}\frac{\mathrm{Tr}[\overline{\rho}\sigma_Y]}{\mathrm{Tr}[\overline{\rho}\sigma_Z]+1} - \frac{y(0)}{z(0)+1}. \tag{145}$$

On Fig. 25c-d, for trajectories starting in $\rho_0 = \frac{1}{2}(\mathbb{1} + \sigma_X)$ and recording the fluorescence field for $T = 4$ μs, we sort the trajectories according to the value of m_I and place them into 111 bins. For each bin i and using the trajectories for which we measured σ_Z (resp. σ_X) at T, we compute the average value z_i (resp. x_i). Plotting $\frac{x_i}{z_i+1}$ as a function of m_{I_i}, a linear dependance clearly appears. We also check that no correlation exists with the associated $\frac{y_i}{z_i+1}$. Symmetrically, when sorting the trajectories according to the values of m_Q and placing them into the bins j, the same slope appears when plotting $\frac{y_j}{z_j+1}$ as a function of m_{Q_j}. Note that due to the electrical delay between the cavity output and the end of the detection chain, the phase of the measurement record needs to be adjusted. Since $\langle\sigma_Y\rangle = 0$, it can be done by setting to 0 the phase of

17 if $\forall k$, $\frac{a_k}{b_k} = \epsilon$, then $\frac{\sum_k a_k}{\sum_k b_k} = \epsilon$

the average signal $\mathrm{d}I_t + i\mathrm{d}Q_t = \sqrt{\frac{\eta\gamma_1}{2}}(\langle\sigma_X\rangle + i\langle\sigma_Y\rangle)\mathrm{d}t$ when the qubit is prepared in $(|g\rangle + |e\rangle)/\sqrt{2}$.

The measured slopes in this experiment are directly proportional to η, but the digitized measurement record is also scaled by an undetermined factor α (cables attenuation, LO power...). This factor can be determined by measuring the variance of $\alpha I(\tau) = \alpha \int_0^\tau \mathrm{d}I_\tau$ over many experiments. For a qubit in its ground state, we directly have:

$$\mathrm{Var}[\alpha I(\tau)] = \alpha^2 \mathrm{Var}[W_{\tau,I} - W_{0,I}] = \alpha^2 \tau. \tag{146}$$

Note that the finite amplification bandwidth $\delta\omega$ of the JPC induces correlations in the measured signal over a typical time $\tau_c = 1/\delta\omega$ so that we have to choose $\tau \gg \tau_c$.

Repeating this process for trajectories ending up at different times $T \in [1\ \mu\mathrm{s}, 10\ \mu\mathrm{s}]$ and fitting the measured slopes with $\sqrt{\frac{\eta\gamma_1}{2}} e^{(\frac{\gamma_1}{2} - \gamma_\phi)T}$, we extract $\boxed{\eta = 26 \pm 2\ \%}$ (see Fig. 25e). This value is consistent with the more precise estimation given in Sec. 3.4.2.3.

3.4.2.2 *From measurement record to trajectory*

Now that detection efficiency is known, we want to translate all the measurement records $\{\mathrm{d}I_t, \mathrm{d}Q_t\}$ into quantum trajectories $\{\rho(t)\}$.
Up to now, we have neglected the finite bandwidth of the JPC which was about $2\pi \times 3$ MHz $\gg \gamma_1$. However, the time constant τ_c of the effective low pass filter can be extracted along with the scaling factor α and its effect can then be corrected for. Indeed, considering two successive time steps $t - \mathrm{d}t$ and t (in practice, $\mathrm{d}t = 200$ ns, which matches the constraints given in Sec. 2.1.3.2), the digitized records $\tilde{I}$ and $\tilde{Q}$ amplified and filtered by the JPC finite bandwidth are given at first order by

$$\begin{cases} \mathrm{d}\tilde{I}_t &= \lambda\alpha \mathrm{d}I_t + (1-\lambda)\mathrm{d}\tilde{I}_{t-\mathrm{d}t} \\ \mathrm{d}\tilde{Q}_t &= \lambda\alpha \mathrm{d}Q_t + (1-\lambda)\mathrm{d}\tilde{Q}_{t-\mathrm{d}t}, \end{cases} \tag{147}$$

where λ is defined by $\tau_c = -\frac{\mathrm{d}t}{\log 1-\lambda}$ and $\{\mathrm{d}I_t, \mathrm{d}Q_t\}$ would be the records for an infinite bandwidth detector. We then consider records much longer than τ_c and for a qubit prepared in $|g\rangle$ so that there is no signal on average. In that case, $\mathrm{d}I_t = \mathrm{d}W_t$ at all times t. By definition, $\mathbb{E}[\mathrm{d}W_t \mathrm{d}W_{t'}] = \delta_{t,t'}\mathrm{d}t$. Then, for $t \gg \tau_c$,

$$\begin{aligned} \mathbb{E}[\mathrm{d}\tilde{I}_t^2] &= \mathbb{E}[(\alpha\lambda \sum_{k=0}^{t/\mathrm{d}t} (1-\lambda)^k \mathrm{d}I_{t-k\mathrm{d}t})^2] \\ &= \alpha^2\lambda^2 \sum_{k=0}^{t/\mathrm{d}t} (1-\lambda)^{2k}\mathrm{d}t \\ &= \tfrac{\alpha^2\lambda\mathrm{d}t}{2-\lambda}\left(1 - (1-\lambda)^{2t/\mathrm{d}t+1}\right) \\ &= \tfrac{\alpha^2\lambda\mathrm{d}t}{2-\lambda}, \end{aligned} \tag{148}$$

and similarly,

$$\mathbb{E}[\mathrm{d}\tilde{I}_t \mathrm{d}\tilde{I}_{t-\mathrm{d}t}] = \frac{\alpha^2\lambda(1-\lambda)\mathrm{d}t}{2-\lambda}. \tag{149}$$

We can then extract the value of α which is consistent with what was found in Eq. (146), and the value of $\tau_c = 100$ ns. We then recover the measurement records before any amplification or filtering

$$\begin{cases} \mathrm{d}I_t &= \frac{\mathrm{d}\tilde{I}_t + (\lambda-1)\mathrm{d}\tilde{I}_{t-\mathrm{d}t}}{\lambda\alpha} \\ \mathrm{d}Q_t &= \frac{\mathrm{d}\tilde{Q}_t + (\lambda-1)\mathrm{d}\tilde{Q}_{t-\mathrm{d}t}}{\lambda\alpha} \end{cases} . \tag{150}$$

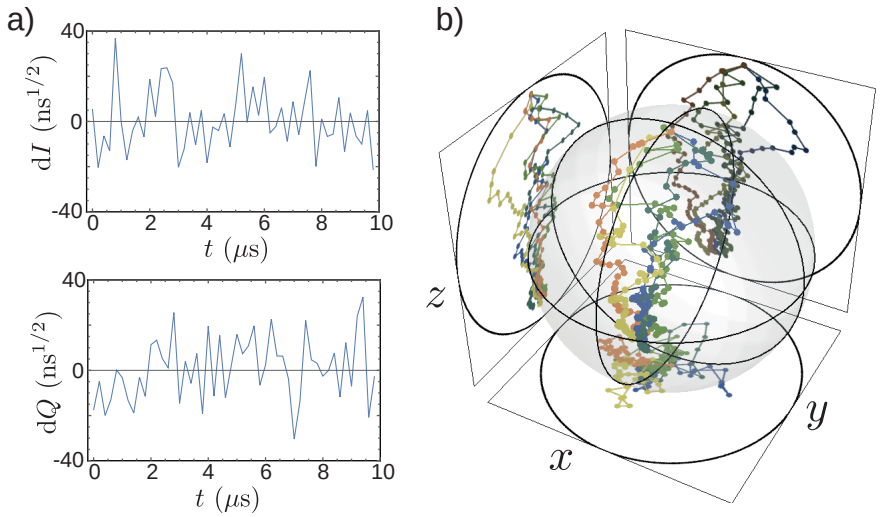

Figure 26: **a**) A typical 10 μs-long measurement record, rescaled and corrected for finite detection bandwidth according to Eq. (150). **b**) Bloch sphere representation of 5 random 10 μs trajectories (each in a different color) for a qubit initially in $|e\rangle$. The blue trajectory corresponds to the measurement record shown in (a).

We can then recover the quantum trajectories using a more practical formulation of the general SME

$$\mathrm{d}\rho = -\frac{i}{\hbar}\mathrm{d}t[H,\rho] + \mathrm{d}t\sum_\nu \mathcal{D}[L_\nu]\rho + \sum_\nu 2\mathrm{d}W_{\nu,t}\sqrt{\eta_\nu}\mathcal{M}[L_\nu]\rho, \tag{151}$$

where $\{L_\nu\}$ is a set of jump operators and $\{W_\nu\}$ a set of independent Wiener processes associated with the jump operators. Following Amini, Mirrahimi and Rouchon [131], we can show applying Itô rules that this equation can be written as

$$\rho(t+\mathrm{d}t) = \frac{M_t\rho(t)M_t^\dagger + \sum_\nu(1-\eta_\nu)L_\nu\rho(t)L_\nu^\dagger\mathrm{d}t}{\mathrm{Tr}[M_t\rho(t)M_t^\dagger + \sum_\nu(1-\eta_\nu)L_\nu\rho(t)L_\nu^\dagger\mathrm{d}t]}, \tag{152}$$

with the Kraus operator M_t depending on the measurement records at time t as

$$M_t = \mathbb{1} - (iH + \sum_\nu \frac{1}{2}L_\nu^\dagger L_\nu)\mathrm{d}t + \sum_\nu \sqrt{\eta_\nu}L_\nu \mathrm{d}J_{\nu,t}. \tag{153}$$

Here, $\mathrm{d}J_{\nu,t} = \sqrt{\eta_\nu}\langle L_\nu + L_\nu^\dagger\rangle\mathrm{d}t + \mathrm{d}W_{\nu,t}$ is the measurement record associated with jump ν.

This formulation of the SME is more adapted for data analysis [132] which is always acquired with a finite bandwidth detector so that we cannot take the limit $\mathrm{d}t \to 0$. For example, in Eq. (109) and for a finite time step $\mathrm{d}t$, it can occur that for a state $\rho(t)$ nearby the surface of the Bloch sphere, the state $\rho(t+\mathrm{d}t)$ lies outside of the sphere. On the other hand, Eq. (152) ensures that the Bloch vector remains inside of the sphere and the density matrix remains positive at each time step. It is also more adapted for numerical simulation .

In the case of the monitored fluorescence signal, with heterodyne detection of efficiency η, and taking into account extra dephasing at a rate γ_ϕ, it reads

$$\rho(t+\mathrm{d}t) = \frac{M_t \rho(t) M_t^\dagger + (1-\eta)\gamma_1 \sigma_- \rho(t) \sigma_+ \mathrm{d}t + \frac{\gamma_\phi}{2}\sigma_Z \rho(t) \sigma_Z \mathrm{d}t}{\mathrm{Tr}[M_t \rho(t) M_t^\dagger + (1-\eta)\gamma_1 \sigma_- \rho(t) \sigma_+ \mathrm{d}t + \frac{\gamma_\phi}{2}\sigma_Z \rho(t) \sigma_Z \mathrm{d}t]}, \tag{154}$$

where the operator M_t is similar to a Kraus operator (see 4.1.2) and depends on the measurement record as

$$M_t = \mathbb{1} - (iH + \frac{\gamma_1}{2}\sigma_+\sigma_- + \frac{\gamma_\phi}{4}\mathbb{1})\mathrm{d}t + \sqrt{\frac{\eta\gamma_1}{2}}\sigma_-(\mathrm{d}I_t + i\mathrm{d}Q_t). \tag{155}$$

We applied this quantum filter to all the measurement records rescaled and corrected for the detection finite bandwidth according to Eq. (150). We present here the resulting trajectories for a qubit prepared in $|e\rangle$ at $t = 0$. Note that we adjusted finely the qubit decay time to $T_1 = 4.15\ \mu s$ on the whole set of data. Imperfections in qubit preparation due to spurious thermal excitation at equilibrium and decoherence during the preparation π pulse are neglected so that $\rho(0) = |e\rangle\langle e|$.

On Fig. 26b, we give a Bloch sphere representation of 5 random 10 μs long trajectories. Each one is plotted in a different color, and the blue one corresponds to the record plotted on Fig. 26a. Starting from $|e\rangle$, the qubit state diffuses randomly in the Bloch sphere, but each trajectory eventually ends up in $|g\rangle$ at infinite time. For a given trajectory, the initial rotational symmetry around the z-axis is spontaneously broken by the quantum noise.

In order to verify our model, we compare the predictions made from the trajectories with the results of the final tomography (see Fig. 25a). The trajectories that ended at time T with a σ_Z measurement (resp. σ_X, σ_Y) are sorted according to the value of $z_{\mathrm{traj}} = \mathrm{Tr}[\rho(T)\sigma_Z]$ (resp. $x_{\mathrm{traj}} = \mathrm{Tr}[\rho(T)\sigma_X]$, $y_{\mathrm{traj}} = \mathrm{Tr}[\rho(T)\sigma_Z]$) and grouped in 20 bins of 5×10^5 trajectories each, with similar values of z_{traj} (resp. x_{traj}, y_{traj})[18]. In each bin, we average the final projective measurement outcome, corrected for finite readout fidelity. The average value z_{tomo} (resp. x_{tomo}, y_{tomo}) is then compared with the value predicted from the trajectories. On Fig. 27b-c, we plot z_{tomo} against z_{traj} and x_{tomo} against x_{traj} for the 4 μs long trajectories. In both cases, the tomography results match quantitatively with the predictions from the trajectories. The agreement is also quantitative for the predictions on σ_Y and for all trajectory durations, which we did not plot here. Note that on Fig. 27a, we plot 5 trajectories with similar final value of

18 With this choice, the bins thus have a variable width Δz_{traj}

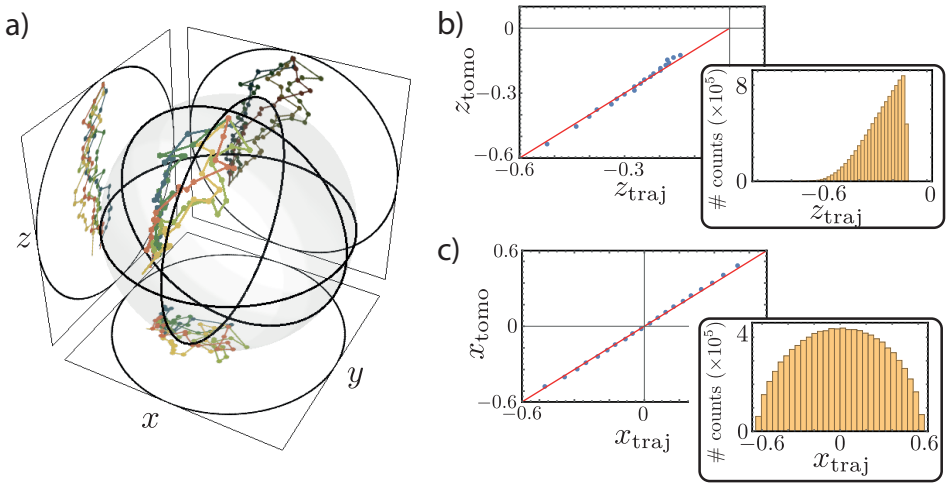

Figure 27: a) Bloch sphere representation of 5 trajectories (each in a different color) for a qubit initially in $|e\rangle$ and with similar final value of $\rho(T) = \frac{\mathbb{1}}{2} + \frac{1}{2}\vec{\sigma}.(-0.6 \pm 0.05, 0 \pm 0.05, -0.2 \pm 0.05)$ at $T = 4$ μs . b) Comparison of the predicted values z_{traj} of $\langle \sigma_Z \rangle$ with the final projective measurement result z_{tomo} averaged over bins containing 5×10^5 trajectories each. The red line has slope 1. Inset: distribution of z_{traj} for the 10^6 trajectories. The bins have a constant width 0.02 and do not correspond to the bins used in the main panel). c) Idem for predicted x_{traj} and measured x_{tomo} at final time.

ρ (same x_{traj}, y_{traj} *and* z_{traj} within ± 0.05), but on Fig. 27b-c, trajectories are binned according to the value of z_{traj} *only* for the top panel and x_{traj} *only* for the bottom panel.

3.4.2.3 *Particle filtering for the estimation of η*

In this section, we describe the method proposed by Six *et al.* [135] to determine η, which uses quantum particle filtering principles [136, 137]. The idea of this method is to compare the likelihood of different test values of η by comparing the probability of having measured a given record for each considered value η_i.

If η is known, for a given value $\mathrm{d}y_t$ of the measurement records at time t[19], we can map the density matrix from t to $t + \mathrm{d}t$ as (see Eq. (152))

$$\rho(t + \mathrm{d}t) = \frac{K_{\mathrm{d}y_t}[\rho(t)]}{\mathrm{Tr}[K_{\mathrm{d}y_t}[\rho(t)]]}, \tag{156}$$

where the so-called *partial Kraus map* $K_{\mathrm{d}y_t}$ [24] is given by

$$K_{\mathrm{d}y_t}[\rho(t)] = M_{\mathrm{d}y_t}\rho(t)M_{\mathrm{d}y_t}^\dagger + \sum_\nu (1 - \eta_\nu) L_\nu \rho(t) L_\nu^\dagger \mathrm{d}t. \tag{157}$$

Here, the L_ν's are the jump operators, η_ν the yet undetermined detection efficiency associated with each one, and the Kraus operator $M_{\mathrm{d}y_t}$ is defined as in Eq. (153) and

19 in the case of heterodyne detection, $\mathrm{d}y_t$ is a two components vector

also depends on the choice of the η_ν's. In Eq. (156), we now note that the denominator $\mathrm{Tr}[K_{\mathrm{d}y_t}[\rho(t)]]$ corresponds to the "density of probability"[20] of having found the outcome $\mathrm{d}y_t$ at time t. It depends on the η_ν's.

We now want to determine the most likely value of η given a set of possible values. For simplicity, let us assume that there is a single jump operator L, and that η is one of two possibilities η_1 and η_2 that we want to test. At time t, we associate with each one a probability $\pi_i(t)_{i=1,2}$ to be the true value of η *knowing* the measurement record from 0 to t. Then, following Bayes rules, we have at time $t+\mathrm{d}t$

$$\begin{aligned}
\pi_i(t+\mathrm{d}t) &= P(\eta=\eta_i|\mathrm{d}y_t) \\
&= \frac{P(\mathrm{d}y_t|\eta=\eta_i)\times P(\eta=\eta_i)}{P(\mathrm{d}y_t)} \\
&= \frac{P(\mathrm{d}y_t|\eta=\eta_i)\times P(\eta=\eta_i)}{P(\mathrm{d}y_t|\eta=\eta_1)+P(\mathrm{d}y_t|\eta=\eta_2)} \\
&= \frac{\mathrm{Tr}[K_{\mathrm{d}y_t}^{\eta=\eta_i}[\rho(t)]]\times\pi_i(t)}{\mathrm{Tr}[K_{\mathrm{d}y_t}^{\eta=\eta_1}[\rho(t)]]+\mathrm{Tr}[K_{\mathrm{d}y_t}^{\eta=\eta_2}[\rho(t)]]},
\end{aligned} \tag{158}$$

where, for simplicity, all the probabilities P are implicitly *conditioned on* the measurement record from 0 to t. We thus process the measurement records in a similar way to what is done in Sec. 3.4.2.2, but applying the extended filter keeping track of both $\rho^{\eta=\eta_i}(t)$ and the corresponding probability $\pi_i(t)$ for each i. For a long trajectory, eventually, one of the π_i's goes to 1, and it is the most likely value of η. By repeating this method, we can perform a dichotomic search of the value of η.

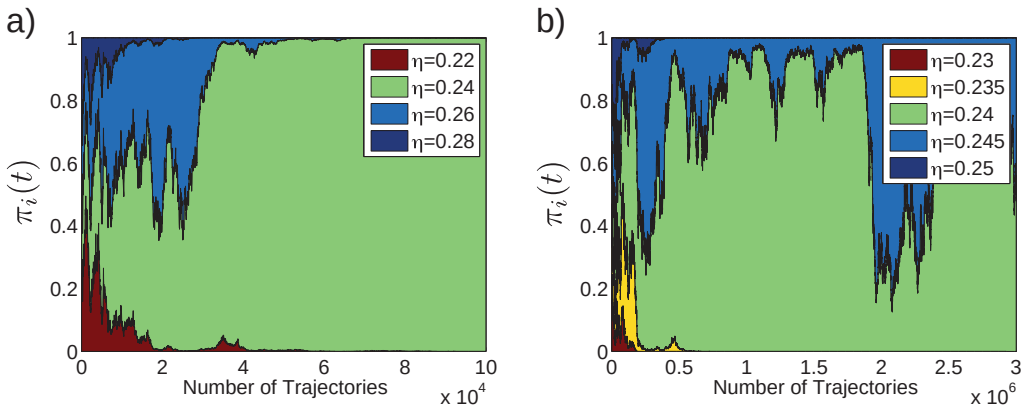

Figure 28: a) Quantum particle filter applied to 10 μs long records corresponding to a qubit prepared in $\rho(0)=\frac{1}{2}(\mathbb{1}+\sigma_X)$. One of the π_i's converges toward 1 rapidly, singling out the most likely value $\eta=0.24$. b) After scanning the whole set of records for more refined test values, the filter cannot decide between $\eta=0.24$ and $\eta=0.245$.

The method that we have described can easily be adapted to the heterodyne measurement with several jump operators and can also account for a finite pure dephasing

20 For a density of probability to be rigorously defined, one would need to normalize $\mathrm{d}y_t$ by $\sqrt{\mathrm{d}t}$

rate, which is simply the effect of the jump operator $\sqrt{\gamma_\phi/2}\sigma_Z$ monitored with efficiency $\eta_\phi = 0$. Note that in our data, we do not have a single long trajectory, but a great number of short ones. The method is then applied to the concatenated measurement records and ρ_i is reset to $\rho(0)$ at the end of each individual trajectory. On Fig. 28a, we represent the π_i's for a set of tested values of η. After scanning 5×10^4 individual records, the value $\eta = 0.24$ is clearly chosen by the filter as the most likely value for η. In Fig. 28b, we test more refined values of η around this first estimation. After scanning the whole set of data, the filter cannot decide between $\eta = 0.24$ and $\eta = 0.245$. This gives us the estimated value of η and the corresponding uncertainty.

3.4.2.4 *Trajectories statistics*

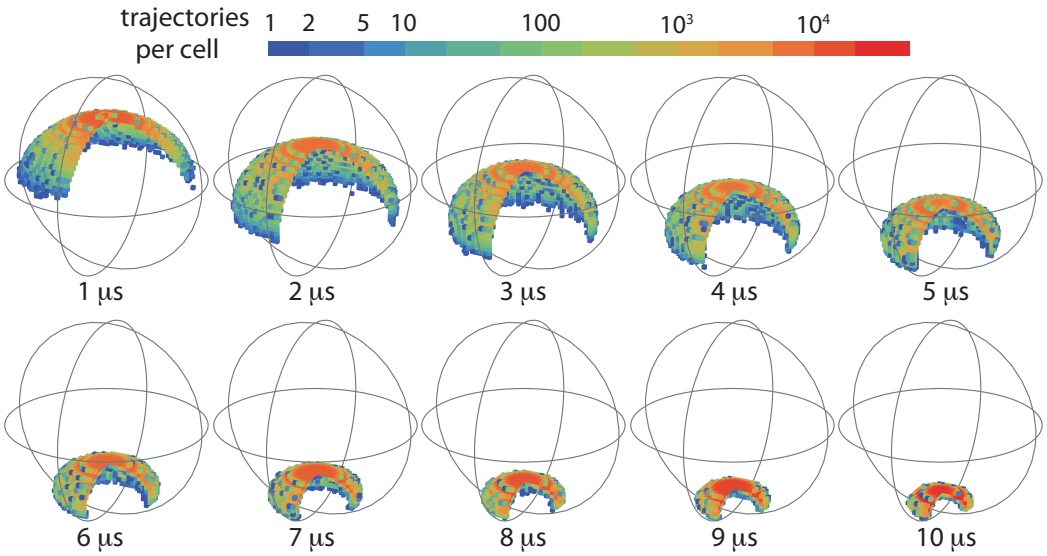

Figure 29: Distribution of the qubit states in the Bloch sphere for 10^6 repeated experiments with a qubit initially in $|e\rangle$ and after a time t from 0 to 10 μs. The Bloch sphere is paved with cells of size $\mathrm{d}x = \mathrm{d}y = \mathrm{d}z = 0.02$, and the number of trajectories in each cell is encoded in color.

We now consider only the 10 μs long trajectories. A proper model to describe the statistics of these trajectories would require a Fokker-Planck equation, which is a work still in progress at the time of this writing. In this section, we give a representation of the distribution of the qubit states during the decay from $|e\rangle$ to $|g\rangle$.

On Fig. 29, we represent at different times t the distribution of the qubit states in the Bloch sphere for 10^6 repeated experiments. To do so, we first pave the Bloch sphere with cubic cells whose size are given by $\mathrm{d}x = \mathrm{d}y = \mathrm{d}z = 0.02$. In color, we represent the number of experiments for which the trajectory predicts a value of $(x(t), y(t), z(t))$ lying inside a given cell. We do not represent a fourth of the cells $(x > 0 > y)$ for better visibility.

The overall rotational symmetry around the z-axis is respected. At each time t, the trajectories are dispersed on a cap of finite thickness (several cells), and this cap collapses down to $|g\rangle$ at large times t. To get some qualitative understanding of this shape, let us note that for the $\sqrt{\gamma_1/2}\sigma_-$ jump operator alone (corresponding to the quadrature I only of the fluorescence signal), the evolution of the density matrix over a time step $\mathrm{d}t$ is given by (see Eq. (128))

$$\mathrm{d}\rho = \frac{\gamma_1}{2}\mathrm{d}t\mathcal{D}[\sigma_-]\rho + \sqrt{\frac{\eta\gamma_1}{2}}(\sigma_-\rho + \rho\sigma_+ - \langle\sigma_X\rangle\rho)\mathrm{d}W_{t,I}, \tag{159}$$

which leads to an evolution of the Bloch coordinates

$$\left\{\begin{array}{rcl} \mathrm{d}x &=& -\frac{\gamma_1}{4}x\mathrm{d}t + \sqrt{\frac{\eta\gamma_1}{2}}(1+z-x^2)\mathrm{d}W_{t,I} \\ \mathrm{d}z &=& -\frac{\gamma_1}{2}(1+z)\mathrm{d}t + \sqrt{\frac{\eta\gamma_1}{2}}(1+z)x\mathrm{d}W_{t,I} \end{array}\right. . \tag{160}$$

A similar evolution of the y and z coordinates is associated with the $i\sqrt{\gamma_1/2}\sigma_-$ jump operator. We can check that, beside the deterministic evolution proportional to $\mathrm{d}t$, the qubit states receives stochastic "kicks" proportional to $\mathrm{d}W_{t,I}$. Along the x-axis, these kicks are stronger near the center of the Bloch sphere. This tends to push apart the trajectories in the (x,y) plane. Along the z-axis, the kicks are stronger in the upper part of the Bloch sphere and farther from the z-axis. This will cause the trajectories to go down faster near the surface of the Bloch sphere, and thus to form a cap.
In this experiment, η being quite small ($\eta = 24$ %), the dynamics is dominated by the deterministic evolution associated with the damping operator $\mathcal{D}[\sigma_-]$. As a result, the trajectories are well inside of the sphere, whereas they would remain on the surface for $\eta = 1$. Moreover, the corresponding variation of $(\mathrm{d}x, \mathrm{d}z)$ proportional to $\mathrm{d}t$ in Eq. (160) pulls the trajectories toward $|g\rangle$ along a parabola so that the distribution ends up wrapped upon itself.
Naively, one could think that the evolution of the statistics of trajectories can be understood as an overall shrinking of the Bloch sphere due to the unmonitored relaxation with a rate proportional to $1-\eta$, and stochastic diffusion on this reduced sphere. However, the experiment demonstrates that there is a non-zero thickness to the deformed sphere, which informs the too simple picture of well decoupled equations of evolution for $P(\rho(T))$.

During relaxation, we can check that the trajectories first spread out in the Bloch sphere before gathering down toward $|g\rangle$. To be more quantitative, we use the relative entropy between two matrices ρ and σ defined in Eq. (15) as

$$S(\rho||\sigma) = -\mathrm{Tr}[\rho\mathrm{Log}_2(\sigma)] + \mathrm{Tr}[\rho\mathrm{Log}_2(\rho)] \tag{161}$$

as a measure of distance. Then, calling ρ_k the density matrix corresponding to the k^{th} cell, p_k the probability of a trajectory being in this cell at time t and ρ the mean density matrix over all trajectories, which is the matrix one gets when not using the fluorescence records, we have

$$\begin{array}{rcl} \overline{S(\rho_k||\rho)}^k &=& -\sum_k p_k \mathrm{Tr}[\rho_k \mathrm{Log}(\rho)] + \sum_k p_k \mathrm{Tr}[\rho_k \mathrm{Log}(\rho_k)] \\ &=& -\mathrm{Tr}[\sum_k p_k\rho_k \mathrm{Log}(\rho)] - \sum_k p_k S(\rho_k) \\ &=& S(\rho) - \overline{S(\rho_k)}^k. \end{array} \tag{162}$$

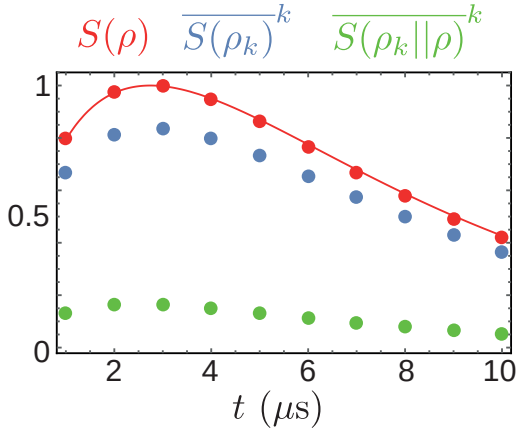

Figure 30: For 10^6 experiments of monitored relaxation, evolution of the Von Neumann entropy of the density matrix when dismissing the measurement records (red dots), the mean entropy of a trajectory (blue dots) and the mean relative entropy from a trajectory to the mean density matrix (green dots). Red line: calculated Shannon entropy $S = p\text{Log}_2 p + (1-p)\text{Log}_2(1-p)$ for p the occupation of the $|e\rangle$ state decaying with rate T_1

For a perfect detection, the trajectories remain on the surface of the Bloch sphere and we have $\overline{S(\rho_k)}^k = 0$. In that case, since the relative entropy can be seen as a distance in the Bloch sphere, the entropy of the unconditioned density matrix ρ can be interpreted as the dispersion of the trajectories around their mean value $\overline{S(\rho_k||\rho)}^k$. In this sense, the increase of entropy during relaxation corresponds to an increase in the volume occupied by the trajectories in the Bloch sphere. When these trajectories gather down to the ground state, the entropy decreases down to 0. For finite efficiency, the trajectories are themselves entropic, which compensates for their smaller dispersion. On Fig. 30, we plot the mean relative entropy extracted from the ensemble of trajectories (green dots), the mean entropy of the trajectories (blue dots) and the entropy of the unconditioned matrix (red dots). This last value is, as expected, strictly equal to the sum of the two previous ones. It follows the expected law for a qubit initially in $|e\rangle$ and decaying on a time scale T_1 (red line).

In this chapter, we have seen how the outcomes of measurements of the qubit performed until the time t can be used to estimate its state. The *actuated* density matrix $\rho(t)$ then allows us to make predictions about the statistics of future measurements conditioned on the history of past measurements. In the next chapter, we will see how to use the knowledge from measurements performed both *before* and *after* time t to predict the statistics of a measurement at t. This knowledge about past and future will be encoded in two matrices $\rho(t)$ and $E(t)$, forming the *Past Quantum State* of the system.

4

POST-SELECTED QUANTUM TRAJECTORIES

The reversibility of time evolution for a closed quantum system is an essential feature of quantum physics. Open systems such as ones under measurement evolve irreversibly. In 1964, Aharonov *et al.* noticed that post-selection using a final projective measurement plays the time symmetric role of an initial preparation [27]. In 1988, in a seminal paper, they showed that when considering a system prepared and post-selected in eigenstates of two non-commuting operators, a weak measurement in between could yield on average a result far outside of the allowed range for pre or post selection only [28]. This non trivial property of the mean, which is called *weak value*, is a quantum feature that cannot be observed with strong disrupting measurements [138]. It was experimentally observed for the first time in 1991 [139] and has since then been shown to contradict macro-realism in the hypothesis of a non-invasive detector, using the violation of Leggett-Garg inequality [140, 141, 142, 143]. Other interesting features of the weak values have also been put forward (summarized in [144]) and experimentally used, such as noiseless amplification [145, 146] or direct tomography of an operator or wave function [147]. However, usefulness of these weak values as well as their purely quantum origin are still the subject of heated debates [148, 32, 149, 150, 151].

In this chapter, we present the results of an experiment illustrating some of these properties for pre and post-selected ensembles of quantum trajectories. The weak measurement here is the heterodyne detection of the fluorescence field (see Sec. 3.4).

In order to make predictions about this weak measurement using all available information, extracted both before and after it took place, one needs to design an *acausal Bayesian filter* [152], in the same way that a historian tries to reconstruct the thread of events in the recent past scanning both records from the far past and from the current situation.
It is possible to formulate this filter to render explicit the symmetry between the processing of the information from both sides of the timeline around the weak measurement date. Using a recently developed framework generalizing to open quantum systems the backward propagation in time of the information from *a posteriori* measurements [29, 30, 31], we establish a time reversed version of the stochastic master equation (154). It generalizes the quantum trajectory approach described in Sec. 3.4.2. When considering the average value of a weak measurement on post selected ensembles, the time evolution of the *effect matrix*, which encodes the information on the final measured state of the qubit, is governed by a master equation similar to the Lindblad form (see Eq. (27)). We show however that for a non QND weak measurement such as the one used here, this evolution is not time symmetric to the one of the density matrix.

4.1.1 *Discrete time version*

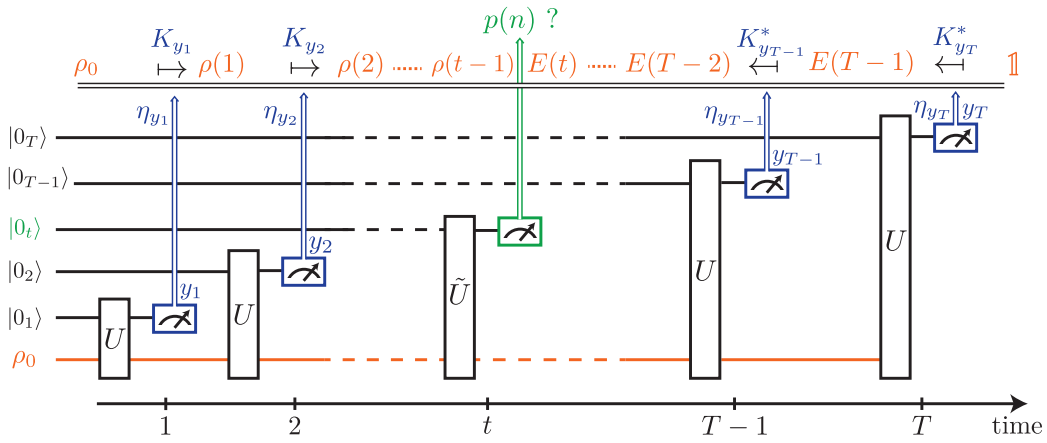

Figure 31: Prediction and retrodiction from discrete time measurements. A system (in orange) is measured at discrete times $k \in \{1..., T\}$. These generalized measurements are modeled by unitary evolutions in interaction with ancillary systems, the meters, which are then measured projectively with finite efficiency (equivalence with the Kraus decomposition shown in Sec. 2.1.3.1 and [18]). We want to predict the probability of a given outcome n at time t, knowing all the other outcomes y_k's. The observer information on the system (in the upper part of the diagram) comes both from measurements before t (information encoded in the density matrix $\rho(t-1)$), and after t (information encoded in the effect matrix $E(t)$). ρ and E are found respectively starting from the initial state ρ_0 (resp. the final effect matrix $E(T) = \mathbb{1}$) and actuating with the measured y_k's as $\rho(k) = K_{y_k}[\rho(k-1)]$ if $k < t$ (resp. $E(k-1) = K^*_{y_k}[E(k)]$ if $k > T$) until time t.

We want to describe the situation represented on Fig. 31. A quantum system is prepared at time 0 in a state encoded by the density matrix ρ_0 and then measured at discrete times $k = 1, 2, ..., T$. Here, these measurements are any *generalized measurement* [18], from weak to fully projective. We want to make predictions about the statistics of the outcomes of the one taking place at $t \in [0, T]$ when post-selecting the experiments that yielded a particular measurement record $(y_1, ..., y_{t-1}, y_{t+1}, ...y_T)$ for the $T-1$ others. For now, we suppose that there is no hamiltonian evolution or decoherence processes beyond these measurements. We will see in the following section how to take those into account as continuous detection back-action.

We model the $T-1$ measurements with the same set of Kraus operators $\{M_\nu\}$ (see Sec. 2.1.3.1)[1]. We take into account finite efficiencies encoded in a matrix η which coefficients are $\eta_{y,\nu} = P(y|\nu)$, corresponding to the probability of detecting the outcome y when a ν jump actually occurred. Thus η, has coefficients between 0 and 1, and verifies $\forall \nu, \sum_y \eta_{y,\nu} = 1$. Note that η does not need to be a square matrix. Indeed, there

1 For simplicity, we suppose that all measurements follow the same procedure. If one wants to model measurements of, say, different operators, a different set of Kraus operators is needed for each time.

can be cases for which some jumps are not detected whereas others are with efficiency 1 (in this case η has more columns than lines) or other situations when a jump can trigger many outcomes for the measurement, each one indicating a jump with a given confidence (in this case η has more lines than columns).
Then, knowing the density matrix of the system just before time k and the measurement outcome y_k, ρ reads after time k

$$\begin{aligned}\rho_k &= \sum_\nu P(\nu|y_k)\frac{M_\nu\rho(k-1)M_\nu^\dagger}{\mathrm{Tr}[M_\nu\rho(k-1)M_\nu^\dagger]}\\ &= \sum_\nu \frac{P(\nu|y_k)}{P(\nu)}M_\nu\rho(k-1)M_\nu^\dagger\\ &= \frac{\sum_\nu \eta_{y_k,\nu}M_\nu\rho(k-1)M_\nu^\dagger}{P(y_k)}\\ &\stackrel{\text{def}}{=} \frac{K_{y_k}[\rho(k-1)]}{\mathrm{Tr}[K_{y_k}[\rho(k)]]},\end{aligned} \tag{163}$$

where K_{y_k} is a completely positive map. Here, we can identify the probability of the outcome y_k as $P(y_k) = \mathrm{Tr}[\sum_\nu \eta_{y_k,\nu}M_\nu\rho(k-1)M_\nu^\dagger]$.
We then write the state of the qubit just before the measurement at time t

$$\rho(t-1) = \frac{K_{y_{t-1}}\circ K_{y_{t-2}}\circ ...\circ K_{y_1}[\rho_0]}{\mathrm{Tr}[K_{y_{t-1}}\circ K_{y_{t-2}}\circ ...\circ K_{y_1}[\rho_0]]}. \tag{164}$$

To model the measurement at time t, we suppose that the system interacts with an ancillary system called the *meter*. This representation is equivalent to the Kraus decomposition (see Sec. 2.1.3.1 and [18]). Following Eq. (18), we suppose that the meter is initially in a pure state that we call $|0\rangle$, and that there is a set of Kraus operators $\{\Omega_m\}$[2] and an orthogonal basis of the meter space $\{|m\rangle\}$ so that the interaction transforms the whole system as

$$\rho(t-1)\otimes|\psi_0\rangle \mapsto \sum_{m,m'}\Omega_m\rho(t-1)\Omega_{m'}^\dagger\otimes|m\rangle\langle m'|. \tag{165}$$

We then postpone the projection of the meter and instead, following Gammelmark *et al.*, place it into an imaginary safe while the system continues to evolve. At time T, the whole density matrix reads

$$\rho_{tot}(T) = \frac{\sum\limits_{m,m'} K_{y_T}\circ ...\circ K_{y_{t+1}}[\Omega_m\rho(t-1)\Omega_{m'}^\dagger]\otimes|m\rangle\langle m'|}{D}, \tag{166}$$

with

$$\begin{aligned}D &= \mathrm{Tr}[\sum_{m,m'} K_{y_T}\circ ...\circ K_{y_{t+1}}[\Omega_m\rho(t-1)\Omega_{m'}^\dagger]\otimes|m\rangle\langle m'|]\\ &= \mathrm{Tr}[\sum_m K_{y_T}\circ ...\circ K_{y_{t+1}}[\Omega_m\rho(t-1)\Omega_m^\dagger]].\end{aligned} \tag{167}$$

Eventually, after time T we look at the meter state in the safe, which projects on the basis $\{|m\rangle\}$. For now we suppose that this measurement has perfect fidelity. Errors

2 We thus let the possibility for the measurement at time t to be different from the $t-1$ others.

in the measurement can indeed easily be taken into account by mixing the outcomes probabilities. We then get a particular outcome n with probability

$$p(n|y_1,...,y_{T_1},\rho_0) = \frac{\mathrm{Tr}[K_{y_T} \circ ... \circ K_{y_{t+1}}[\Omega_n \rho(t-1)\Omega_n^\dagger]]}{D}. \tag{168}$$

Letting K_y^* be the adjoint map of K_y, which is defined by its action on a matrix A as

$$K_y^*[A] \stackrel{def}{=} \sum_\nu \eta_{y,\nu} M_\nu^\dagger A M_\nu, \tag{169}$$

we note that for two hermitian matrices A and B,

$$\mathrm{Tr}[AK_y[B]] = \mathrm{Tr}[K_y^*[A]B]. \tag{170}$$

We can then rewrite the numerator in Eq. (168) as

$$\begin{aligned} p(n|y_1,...,y_T,\rho_0) &= \mathrm{Tr}[K_{y_T} \circ ... \circ K_{y_{t+1}}[\Omega_n \rho(t-1)\Omega_n^\dagger]]/D \\ &= \mathrm{Tr}[\mathbb{1}\ K_{y_T} \circ ... \circ K_{y_{t+1}}[\Omega_n \rho(t-1)\Omega_n^\dagger]]/D \\ &= \mathrm{Tr}[K_{y_T}^*[\mathbb{1}]\ K_{y_{T-1}} \circ ... \circ K_{y_{t+1}}[\Omega_n \rho(t-1)\Omega_n^\dagger]]/D \\ &= ... \\ &= \mathrm{Tr}[K_{y_{t+1}}^* \circ ... \circ K_{y_{T-1}}^* \circ K_{y_T}^*[\mathbb{1}]\ \Omega_n \rho(t-1)\Omega_n^\dagger]/D, \end{aligned} \tag{171}$$

so that

$$p(n|y_1,...,y_T,\rho_0) = \frac{\mathrm{Tr}[E(t)\Omega_n \rho(t-1)\Omega_n^\dagger]}{\sum_m \mathrm{Tr}[E(t)\Omega_m \rho(t-1)\Omega_m^\dagger]}. \tag{172}$$

Here, we have introduced the so-called *effect matrix* $E(t)$ [29] which is propagated backward in time according to

$$E(t) = K_{y_{t+1}}^* \circ ... \circ K_{y_{T-1}}^* \circ K_{y_T}^*[\mathbb{1}]. \tag{173}$$

Like ρ, E is hermitian, but it is not normalized. Gammelmark *et al* named Past Quantum State (PQS) the association of both matrices $\Big(\rho(t-1), E(t)\Big)$. It contains all the available information in order to make predictions about a measurement at time t, knowing the measurement outcomes prior and after t.

4.1.2 *Continuous time version*

We now want to transpose the previous reasoning to weak continuous monitoring of the system. Note that the actual experiment described in the next section contains one discrete measurement of the σ_Z operator of the qubit at time T, preceded by a continuous heterodyne detection of the fluorescence field from time 0 to T. We will thus need to combine both models.

We now suppose that the system evolves continuously under the action of several homodyne detections labelled ν, which are associated to the jump operators L_ν and

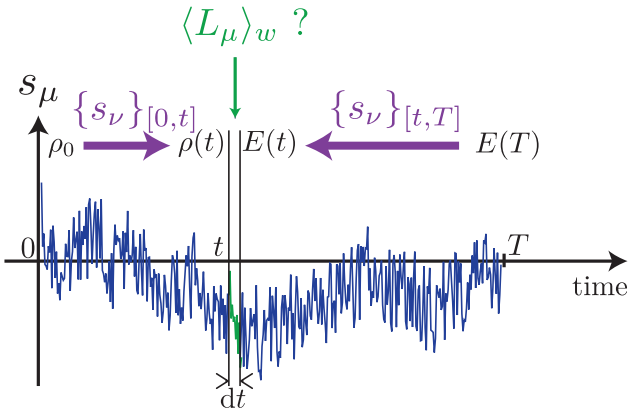

Figure 32: Prediction and retrodiction for continuous detections. The system is weakly and continuously probed using homodyne detections schemes. These are associated with a set of jump operators $\{L_\nu\}$ and yield a set of measurement records $\{s_{\nu,[0,T]}\}$ according to which one propagates the density matrix ρ (resp. the effect matrix E) forward (resp. backward) in time starting from time 0 (resp. T). Propagation depends on detection efficiencies η_ν's. If measurement channels are left unread (see section 4.2.1), it only represents hamiltonian evolution and decoherence. The weak value of a given detection labelled μ can then be predicted at time t. It is the average of the green portion of the curve for experiments that yielded the same measurement records at other times (in blue).

have efficiencies η_ν. Note that a heterodyne detection of a jump operator L_ν, with efficiency η, can be modeled as 2 simultaneous homodyne detections with the same efficiency, say labelled ν_1 and ν_2, of the jumps $L_{\nu_1} = \frac{1}{\sqrt{2}} L_\nu$ and $L_{\nu_2} = \frac{i}{\sqrt{2}} L_\nu$.

We let $s_{t,\nu} = \mathrm{d}y_{t,\nu}/\sqrt{\mathrm{d}t}$[3], where $y_{t,\nu}$, the measurement record associated with detection ν, is defined as in Eq. (129) as

$$\mathrm{d}y_{t,\nu} = \sqrt{\eta_\nu}\langle L_\nu + L_\nu^\dagger \rangle \mathrm{d}t + \mathrm{d}W_{\nu,t}. \tag{174}$$

Then, as in the previous section, we define

$$K_{s_t} : \rho(t) \mapsto M_{s_t} \rho(t) M_{s_t}^\dagger + \sum_\nu (1-\eta_\nu) L_\nu \rho(t) L_\nu^\dagger \mathrm{d}t, \tag{175}$$

with

$$M_s = \mathbb{1} - (iH + \frac{1}{2}\sum_\nu (L_\nu^\dagger L_\nu + L_\nu L_\nu^\dagger))\mathrm{d}t + \sum_\nu \sqrt{\eta_\nu} L_\nu s_{t,\nu} \sqrt{\mathrm{d}t}. \tag{176}$$

This operator is used to map $\rho(t)$ to $\rho(t+\mathrm{d}t)$ as in Eq. (152) as

$$\rho(t+\mathrm{d}t) = \frac{K_{s_t}[\rho(t)]}{\mathrm{Tr}[K_{s_t}[\rho(t)]]}. \tag{177}$$

Then, integrating from 0 to t,

$$\rho(t) = \frac{K_{s_{t-\mathrm{d}t}} \circ \ldots \circ K_{s_0}[\rho_0]}{\mathrm{Tr}[K_{s_{t-\mathrm{d}t}} \circ \ldots \circ K_{s_0}[\rho_0]}, \tag{178}$$

3 We consider $\mathrm{d}t$ to be finite, which is the case for experimental data or numerical simulation

We now assume that the measurement of interest at time t is itself a homodyne detection[4] and we suppose, without loss of generality, that it corresponds to one of the L_ν's jump operators, which we label μ, with efficiency $\tilde{\eta}_\mu$[5]. Our goal is thus to predict the statistics of the random output ξ of the μ detection at time t conditioned on a given value of the measurement records from 0 to t and from $t+\mathrm{d}t$ to T. This means computing, for all values of $s_{t,\mu}$, $p(\xi \in [s_{t,\mu}, s_{t,\mu}+\mathrm{d}\xi]|s_{[0,t]} \cap s_{[t+\mathrm{d}t,T]}])$ up to the dominant order in $\mathrm{d}t$, which is $\sqrt{\mathrm{d}t}$ as we can check at the end of the calculation.

We then model this detection at time t, as in the previous section, as an interaction with a meter initially in a pure state $|\psi_0\rangle$ followed by a projective measurement of this meter, and the interaction reads, similarly to Eq. (165),

$$\rho(t) \otimes |\psi_0\rangle \mapsto \int\int \mathrm{d}\xi \mathrm{d}\xi' \; \tilde{\Omega}_\xi \rho(t) \tilde{\Omega}_{\xi'}^\dagger \otimes |\xi\rangle\langle\xi'|, \tag{179}$$

where $\{|\xi\rangle\}$ is a continuous orthogonal basis of the meter verifying $\langle\xi|\xi'\rangle = \delta(\xi-\xi')$, and $\{\tilde{\Omega}_\xi\}$ is a set of Kraus operators. We show here that

$$\tilde{\Omega}_\xi = (2\pi)^{-1/4} \exp -\frac{\xi^2}{4} \Omega_\xi, \tag{180}$$

where Ω_ξ reads

$$\Omega_\xi = \mathbb{1} - \frac{1}{2} L_\mu^\dagger L_\mu \mathrm{d}t + L_\mu \sqrt{\tilde{\eta}_\mu} \xi \sqrt{\mathrm{d}t}. \tag{181}$$

Indeed, in order to determine Eq. (180), one can expand Eq. (152) at order $\sqrt{\mathrm{d}t}$. Thus, if the output ξ of the μ detection integrated over the time step $\mathrm{d}t$ is $\mathrm{d}y_{\mu,t} = s_{t,\mu}\sqrt{\mathrm{d}t}$, the density matrix at time $t+\mathrm{d}t$ has to read $\tilde{\rho}(t+\mathrm{d}t) = \dfrac{\Omega_{s_{t,\mu}} \rho(t) \Omega_{s_{t,\mu}}^\dagger}{\mathrm{Tr}[\Omega_{s_{t,\mu}} \rho(t) \Omega_{s_{t,\mu}}^\dagger]}$, which leads directly to Eq. (181). Now, in order to get the proper prefactor in Eq. (180), one requests that $\mathrm{Tr}[\tilde{\Omega}_\xi \rho(t) \tilde{\Omega}_\xi^\dagger]$ is consistent with the distribution of outputs for detection μ conditioned on past measurements only. In our model, the output $\mathrm{d}y_{\mu,t}/\sqrt{\mathrm{d}t}$ is Gaussian distributed with variance 1 and mean $\sqrt{\tilde{\eta}_\mu}\mathrm{Tr}[\rho_t(L_\mu + L_\mu^\dagger)]\sqrt{\mathrm{d}t}$. For any value of $s_{t,\mu}$, the probability that ξ is found between $s_{t,\mu}$ and $s_{t,\mu}+\mathrm{d}\xi$ reads

$$\begin{aligned}
p(\xi \in [s_{t,\mu}, s_{t,\mu}+\mathrm{d}\xi]) &= \mathrm{Tr}[\tilde{\Omega}_{s_{t,\mu}} \rho(t) \tilde{\Omega}_{s_{t,\mu}}^\dagger] \mathrm{d}\xi \\
&= \tfrac{1}{\sqrt{2\pi}} \exp \tfrac{-(s_{t,\mu} - \sqrt{\tilde{\eta}_\mu}\langle L_\mu + L_\mu^\dagger\rangle \sqrt{\mathrm{d}t})^2}{2} \mathrm{d}\xi \\
&= \tfrac{1}{\sqrt{2\pi}} \exp[-\tfrac{s_{t,\mu}^2}{2}] \exp[\sqrt{\tilde{\eta}_\mu} s_{t,\mu} \langle L_\mu + L_\mu^\dagger\rangle \sqrt{\mathrm{d}t} + O(\mathrm{d}t)] \mathrm{d}\xi \\
&= \tfrac{1}{\sqrt{2\pi}} \exp[-\tfrac{s_{t,\mu}^2}{2}] (1 + \sqrt{\tilde{\eta}_\mu} s_{t,\mu} \langle L_\mu + L_\mu^\dagger\rangle \sqrt{\mathrm{d}t}) \mathrm{d}\xi \\
&= \tfrac{1}{\sqrt{2\pi}} \exp\left[-\tfrac{s_{t,\mu}^2}{2}\right] \mathrm{Tr}[\Omega_{s_{t,\mu}} \rho(t) \Omega_{s_{t,\mu}}^\dagger] \mathrm{d}\xi.
\end{aligned} \tag{182}$$

4 To model a strong measurement taking place during a weak monitoring, we use the equations of this section to propagate ρ and E until time t and then use Eq. (172)

5 This efficiency can be differ from η_μ. For example when one does not condition the outcome of the μ detection at time t on the measurement record of the same detection at other times, $\eta_\mu = 0$ but $\tilde{\eta}_\mu \neq 0$.

This final relation terminates the proof.

The combined evolution of the system and meter at t outlined in Eq. (179) thus reads

$$\rho(t)\otimes|\psi_0\rangle \mapsto \int\int \frac{1}{\sqrt{2\pi}}\exp-\frac{\xi^2+\xi'^2}{4}\mathrm{d}\xi\mathrm{d}\xi'\ \Omega_\xi\rho(t)\Omega_{\xi'}^\dagger\otimes|\xi\rangle\langle\xi'|. \tag{183}$$

We now follow the same line of reasoning as in the previous section. After interaction with the meter and further monitoring until T, the full density matrix reads [153]

$$\rho_{tot}(T)=\frac{\int\int \frac{1}{\sqrt{2\pi}}\exp-\frac{\xi^2+\xi'^2}{4}\mathrm{d}\xi\mathrm{d}\xi'\ K_{s_T}\circ...\circ K_{s_{t+\mathrm{d}t}}[\Omega_\xi\rho(t)\Omega_{\xi'}^\dagger]\otimes|\xi\rangle\langle\xi'|}{D}, \tag{184}$$

where

$$\begin{aligned} D &= \mathrm{Tr}[\textstyle\int\int \frac{1}{\sqrt{2\pi}}\exp-\frac{\xi^2+\xi'^2}{4}\mathrm{d}\xi\mathrm{d}\xi'\ K_{s_T}\circ...\circ K_{s_{t+\mathrm{d}t}}[\Omega_\xi\rho(t)\Omega_{\xi'}^\dagger]\otimes|\xi\rangle\langle\xi'|] \\ &= \textstyle\int \frac{1}{\sqrt{2\pi}}\exp-\frac{\xi^2}{2}\mathrm{d}\xi\ \mathrm{Tr}[K_{s_T}\circ...\circ K_{s_{t+\mathrm{d}t}}[\Omega_\xi\rho(t)\Omega_\xi^\dagger]. \end{aligned} \tag{185}$$

We can then write the probability to find a value $s_{t,\mu}$ when measuring the meter conditioned on the measurement records at other times as

$$\begin{aligned} &p(\xi\in[s_{t,\mu},s_{t,\mu}+\mathrm{d}\xi]|s_{[0,t]}\cap s_{[t+\mathrm{d}t,T]}) \\ &= \textstyle\frac{1}{\sqrt{2\pi}}\exp-\frac{s_{t,\mu}^2}{2}\mathrm{d}\xi\mathrm{Tr}[\mathbb{1}\ K_{s_T}\circ...\circ K_{s_{t+\mathrm{d}t}}[\Omega_{s_{t,\mu}}\rho(t)\Omega_{s_{t,\mu}}^\dagger]]/D \\ &= \textstyle\frac{1}{\sqrt{2\pi}}\exp-\frac{s_{t,\mu}^2}{2}\mathrm{d}\xi\mathrm{Tr}[K_{s_{t+\mathrm{d}t}}^*\circ...\circ K_{s_T}^*[\mathbb{1}]\ \Omega_{s_{t,\mu}}\rho(t)\Omega_{s_{t,\mu}}^\dagger]/D, \end{aligned} \tag{186}$$

where $K_{s_t}^*$ is the adjoint map of K_{s_t} defined by its action on a matrix E as

$$K_{s_t}^*[E]=M_{s_t}^\dagger EM_{s_t}+\sum_\nu(1-\eta_\nu)L_\nu^\dagger EL_\nu\mathrm{d}t. \tag{187}$$

Defining the effect matrix $E(t)=K_{s_t}^*\circ K_{s_{t+\mathrm{d}t}}^*\circ...\circ K_{s_T}^*[\mathbb{1}]$, we get

$$p(\xi\in[s_{t,\mu},s_{t,\mu}+\mathrm{d}\xi]|s_{[0,t]}|s_{[t+\mathrm{d}t,T]})=\frac{\frac{1}{\sqrt{2\pi}}\exp-\frac{s_{t,\mu}^2}{2}\mathrm{Tr}[E(t+\mathrm{d}t)\Omega_{s_{t,\mu}}\rho(t)\Omega_{s_{t,\mu}}^\dagger]}{\frac{1}{\sqrt{2\pi}}\int\exp-\frac{\xi'^2}{2}\mathrm{Tr}[E(t+\mathrm{d}t)\Omega_{\xi'}\rho(t)\Omega_{\xi'}^\dagger]\mathrm{d}\xi'}\mathrm{d}\xi. \tag{188}$$

This expression allows us to compute the statistics of the measurement record of the homodyne detection μ at time t, conditioned on a given value of all measurement records from 0 to t and from $t+\mathrm{d}t$ to T. In practice, in the 2 cases described in the following sections, we are interested only in the mean value of this measurement. Then, considering that $\Omega_\xi=\mathbb{1}-\frac{1}{2}L_\mu^\dagger L_\mu\mathrm{d}t+\xi\sqrt{\tilde{\eta}_\mu}L_\mu\sqrt{\mathrm{d}t}$, the expressions simplify due to the parity of the gaussian distribution and we find that the average measurement record of the μ detection, conditioned on all the other records that we dispose of, reads

$$\begin{aligned} \overline{\frac{\mathrm{d}y_\mu}{\mathrm{d}t}} &= \frac{\overline{s_{t,\mu}}}{\sqrt{\mathrm{d}t}}=\frac{\mathrm{Tr}[E(t)\sqrt{\tilde{\eta}_\mu}(L_\mu\rho(t)+\rho(t)L_\mu^\dagger)]}{\mathrm{Tr}[E(t)\rho(t)]}=2\mathrm{Re}[\frac{\mathrm{Tr}[\rho(t)E(t)\sqrt{\tilde{\eta}_\mu}L_\mu]}{\mathrm{Tr}[\rho(t)E(t)]}] \\ &\overset{\mathrm{def}}{=} 2\sqrt{\tilde{\eta}_\mu}\mathrm{Re}[\langle L_\mu\rangle_w(t)]. \end{aligned}$$

(189)

For simplicity, we replace here $E(t+\mathrm{d}t)$ by $E(t)$ in this final expression. Indeed, if the outcome of the μ detection at the time of interest t is not conditioned on the record of the same detection at other times ($\eta_\mu = 0$), these two matrices differ only at the order $\sqrt{\mathrm{d}t}$ and can thus be identified. When $\eta_\mu \neq 0$, one does not include the value of $s_{\mu,t}$ in the post-selection criterion so that the identification still holds.
In the last equality of Eq. (189), we have defined the so-called *weak value* of the L_μ operator at time t. Historically, the term weak value was used to describe the mean-value of a weak measurement when preparing and post-selecting the system [144]. In this sense, ρ and E are rather the states resulting of a preparation and post-selection by strong measurements. However, when integrated over time, a weak continuous measurement can effectively be seen as a strong one. Recently, observation of weak values out of the accessible range for unconditional average has been reported in superconducting qubits when post-selecting trajectories according to the measurement record of the continuous weak monitoring itself [154] .

In this section, we saw how to actuate the density and effect matrices using all the measurement records. This allows one to predict the statistics of an intermediate weak measurement. The weak value can be computed from this probability density. When combining this continuous version formalism with the discrete version described in Sec. 4.1.1, one can can take into account final post-selection as we will see in the next section.

4.2 WEAK VALUES OF THE FLUORESCENCE SIGNAL

4.2.1 *Master equation*

We now want to describe the same experiment [82] as the one described in 3.4.1 except that a final projective measurement takes place at time T (see Fig. 33a). The same qubit (Qubit 2 in Tab 3) is driven resonantly through the *in* port, and while it undergoes Rabi oscillations, its fluorescence signal is collected at the *out* port. Note that the contribution of the transmitted drive field is subtracted, and only the quadrature I containing information about the qubit state is recorded.

We average the signal conditionally to the final projective measurement outcome, implementing the situation described in 4.1.1. This projective readout follows the high-power readout protocol described in 3.3. Thus, it has two possible outcomes denoted 1 and 0 for two possible Kraus operators $M_e = |e\rangle\langle e|$ and $M_g = |g\rangle\langle g|$. Its efficiencies have been independently calibrated to be

$$\begin{cases} \eta_{0,g} = \eta_{1,e} \overset{\text{def}}{=} F = 0.96 \\ \eta_{1,g} = \eta_{0,e} = 1-F \end{cases} . \tag{190}$$

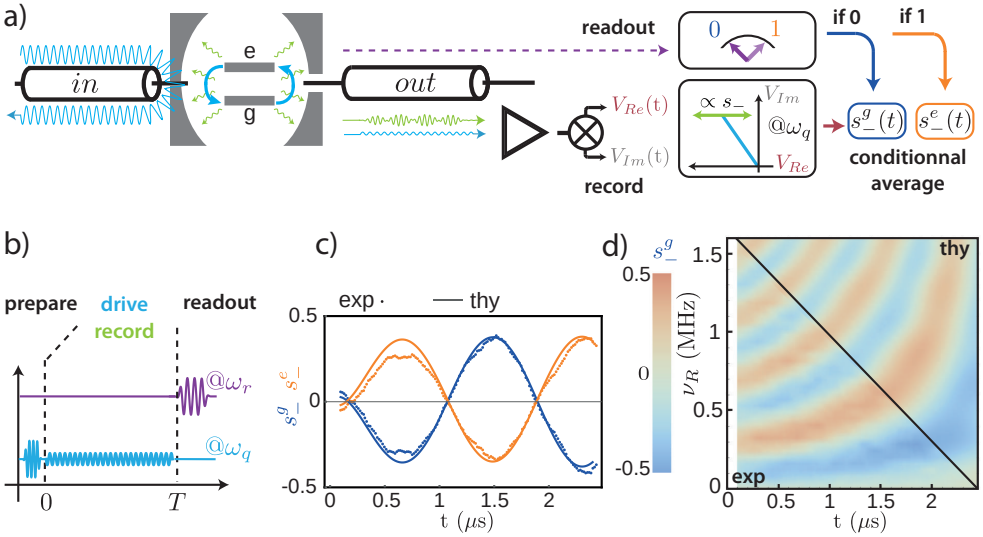

Figure 33: a) Simplified schematic of the experiment (full wiring can be found on Fig. 65). The qubit is prepared near $|g\rangle$ by active cooling (see Sec. 6.1) or near $|e\rangle$ by applying a fast π-pulse afterward. It is then driven for $T = 2.5$ μs through a weakly coupled line *in* and the fluorescence signal (in green) is collected on the strongly coupled line *out*, down converted and digitized. The constant transmitted field (in blue) is subtracted. Drive phase is chosen so that the signal develops on the real quadrature only. At the end of the experiment, a strong measurement of the σ_Z operator of the qubit is performed. Signal is averaged conditionally to this outcome to give 2 mean traces $s^g_-(t)$ (resp. $s^e_-(t)$) when the qubit is post-selected (with finite fidelity) in $|g\rangle$ (resp. $|e\rangle$). b) Pulse sequence representation. c) Mean fluorescence traces for a qubit initially in $\rho_0 = \frac{1}{2}\mathbb{1}$, driven at Rabi frequency $\nu_R = 1$ MHz and post-selected in $|g\rangle$ (in blue) or $|e\rangle$ (orange). Theoretically predicted traces are numerically filtered to mimic JPC finite bandwidth. d) Mean fluorescence signal encoded in color for a qubit initially in $\rho_0 = \frac{1}{2}\mathbb{1}$ and post-selected in $|g\rangle$, and for drive amplitudes from 0 to 1.6 MHz. Lower left corner: experimental data. Upper right: theoretical prediction.

Thus, at time T and considering the experiments which yielded the result y for the final readout with $y \in \{0, 1\}$, the effect matrix reads

$$E_y(T) = K_y^*[\mathbb{1}] = \begin{cases} F|g\rangle\langle g| + (1-F)|e\rangle\langle e| & \text{if } y = 0 \\ (1-F)|g\rangle\langle g| + F|e\rangle\langle e| & \text{if } y = 1 \end{cases}. \tag{191}$$

Our aim is to predict the mean value of the post-selected trajectories. Thus we need to compute the value of the PQS $(\rho(t), E(t))$ at any time $t \in [0, T]$. This state evolves due to the hamiltonian

$$H = -\hbar\frac{\Omega}{2}\sigma_y \tag{192}$$

that accounts for the resonant drive in the frame rotating at ω_q, but also due to the action of the relaxation operators [6]

$$\begin{cases} L &= \sqrt{\frac{\gamma_1}{2}}\sigma_- \\ iL &= i\sqrt{\frac{\gamma_1}{2}}\sigma_- \end{cases} . \tag{193}$$

Note that pure dephasing and thermal excitations during the drive are neglected.

In this experiment, the fluorescence signal is recorded but is not used to post-select the trajectories. Thus we do not actuate the PQS according to the measurement record of the signal s. The evolution of ρ and E is then modeled by a weak continuous monitoring with 0 efficiency. Time evolution of ρ is governed by the Lindblad master equation

$$\frac{\mathrm{d}\rho}{\mathrm{d}t} = -\frac{i}{\hbar}[H,\rho] + \gamma_1(\sigma_-\rho\sigma_+ - \frac{1}{2}(\sigma_+\sigma_-\rho + \rho\sigma_+\sigma_-)) \tag{194}$$

and, defining K^* as in Eq. (187), the evolution of E reads

$$\begin{aligned} E(t) &= K^*_{\eta=0}[E(t+\mathrm{d}t)] \\ &= E(t+\mathrm{d}t) + \tfrac{i}{\hbar}[H, E(t+\mathrm{d}t)]dt \\ &\quad + \textstyle\sum_\nu (L_\nu^\dagger E(t+\mathrm{d}t)L_\nu - \frac{1}{2}L_\nu^\dagger L_\nu E(t+\mathrm{d}t) - \frac{1}{2}E(t+\mathrm{d}t)L_\nu L_\nu^\dagger)\mathrm{d}t \\ &= E(t+\mathrm{d}t) + \tfrac{i}{\hbar}[H, E(t+\mathrm{d}t)]dt \\ &\quad + \gamma_1(\sigma_+ E(t+\mathrm{d}t)\sigma_- - \tfrac{1}{2}\sigma_+\sigma_- E(t+\mathrm{d}t) - \tfrac{1}{2}E(t+\mathrm{d}t)\sigma_-\sigma_+)\mathrm{d}t, \end{aligned} \tag{195}$$

so that, at first order,

$$\boxed{\frac{\mathrm{d}E}{\mathrm{d}t} = -\frac{i}{\hbar}[H,E] - \gamma_1(\sigma_+ E\sigma_- - \frac{1}{2}(\sigma_+\sigma_- E + E\sigma_+\sigma_-))}. \tag{196}$$

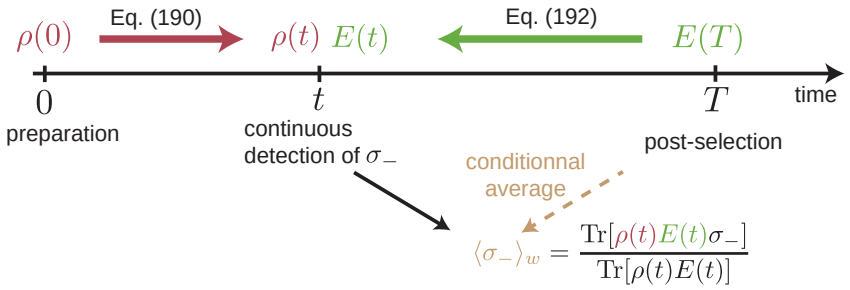

Figure 34: The density matrix ρ and effect matrix E are propagated respectively forward and backward from initial state (resp. final post selection) toward t. They allow to predict the average value of the detected signal at time t for the post-selected experiments.

6 these 2 operators play the same role in the Lindblad form of the master equation (194) and can be seen as one damping operator $\sqrt{\gamma_1}\sigma_-$, but in the actuation term of the SME (128), they correspond to 2 different homodyne detections. Only the measurement record associated with the first one is used in this experiment.

Thus, we obtain for E a master equation which looks similar to the Lindblad form (194) for ρ, but with some major differences. Indeed, the damping term only cancels for $E = \frac{1}{2}\mathbb{1}$, contrary to the damping term in Eq. (194) which cancels for $\rho = |g\rangle\langle g|$. The evolution of E is then not the time-symmetric of the one of ρ, as described in Sec. 4.2.4.
Another important difference is that the trace of E is not preserved and we have to renormalize $E(t)$ to make predictions about a measurement at time t. A trace-preserving version of this equation would no longer be linear. However, we can show that $\mathrm{Tr}[\rho(t)E(t)]$ is constant. Since $\mathrm{Tr}[\rho(T)E_{y=0}(T)]]$ represents the probability of the outcome $y = 0$ for the final measurement, the denominator appearing in the weak-value of an operator $\langle A\rangle_w = \dfrac{\mathrm{Tr}[\rho(t)E(t)\sigma_-]}{\mathrm{Tr}[\rho(t)E(t)]}$ corresponds to the fraction of selected experiments out of the whole. When post-selection becomes unlikely, the weak value can diverge.

4.2.2 *Post-selected fluorescence traces*

As a first step to test these equations, we consider a qubit for which we have no information about the past so that it is prepared in $\rho_0 = \frac{1}{2}\mathbb{1}$. It then undergoes Rabi oscillations at frequency $\nu_R = 1$ MHz for $T = 2.5$ μs, and is measured projectively along σ_Z at T. We then average the fluorescence traces only for experiments that yielded the outcome 0 during the final readout so that the qubit is mainly in $|g\rangle$ at time T. After subtraction of the constant contribution of the transmitted field, the mean fluorescence trace $s^g_-(t)$ is plotted on Fig. 33c (blue dots). Note that up to a scaling factor, it corresponds to the average measurement record associated with the homodyne detection of the jump operator $L = \sqrt{\gamma_1/2}\sigma_-$. The other quadrature detecting iL is dismissed in this experiment. Alternatively, we choose here to set the scaling factor at the same value as in 3.4.1, so that without post-selection, the experimental signal $s_-(t)$ would match the numerically filtered value[7] of $\mathrm{Re}[\langle\sigma_-(t)\rangle]$ (see Sec. 3.4.1). A consequence of this filtering is that the recorded signal in Fig. 33c-d is delayed compared to the fluorescence field dynamics so that it does not cancel at $t = T$.

Using Eq. (189), we compute the expected signal at time t with this scaling factor. It reads $\mathrm{Re}[\langle\sigma_-\rangle_w] = \mathrm{Re}\left[\dfrac{\mathrm{Tr}[\rho(t)E(t)\sigma_-]}{\mathrm{Tr}[\rho(t)E(t)]}\right]$. ρ is propagated forward in time following Eq. (194) starting from ρ_0 at $t = 0$, and E is propagated backward using Eq. (196) starting from $E_{y=0}(T)$. With no new fit parameter the agreement is good between experimental data (dotted line) and theoretical prediction (solid line). This stays true for a qubit post-selected in $|e\rangle$ (orange curves), and when varying the drive field amplitude (Fig. 35d).

Let us comment on this experiment.

7 from now on, every theoretically predicted value will be numerically filtered to mimic the finite bandwidth of the JPC

- The overall number of averaged experiments varies according to the probability of the chosen outcome at time T and for a drive frequency ν_R, but every point of the plots correspond to a minimum of 3×10^5 averages. This leads to a maximal standard deviation of 0.05 on s_-.

- The post-selected traces have a slightly larger contrast than the pre-selected ones (see Sec. 3.4.1) because of the better fidelities F_g and F_e of the final readout than of the ones of the initial preparation f_g and f_e.

- Except for this slightly larger contrast, the color plot on Fig. 35d is the near time-symmetric version of the one presented on Fig. 24c. The phase of the Rabi oscillation, instead of being set by the initial preparation, is set by the final post-selection. Thus, post-selection plays a symmetric role to preparation [27]. The evolution of E here appears to be the time-symmetric of the one of ρ because, on the time-scale of the traces $T \ll T_1$, relaxation is negligible.

- Experimentally, the preparation of $\rho_0 = \frac{1}{2}\mathbb{1}$ is an active task since thermal equilibrium is not described by $\frac{1}{2}\mathbb{1}$. It is done by averaging with the appropriate coefficients the mean traces for a qubit prepared near $|g\rangle$, that is $\rho_0^g = f_g|g\rangle\langle g| + (1-f_g)|e\rangle\langle e|$, and the traces for a qubit prepared near $|e\rangle$, that is $\rho_0^e = (1-f_e)|g\rangle\langle g| + f_e|e\rangle\langle e|$. The finite preparation fidelities $f_g = 91\%$ and $f_e = 85\%$ are due to spurious thermal excitations despite the active cooling preceding every experiment (6.1), and to inefficient preparation π-pulse. Then, the resulting traces are summed up with weights $a_g = \frac{1/2-(1-f_e)}{f_g+f_e-1}$ and $a_e\frac{1/2-(1-f_g)}{f_g+f_e-1}$ chosen so that $a_g\rho_0^g + a_e\rho_0^e = \rho_0$.
  This active preparation of $\rho = \frac{1}{2}\mathbb{1}$ contrasts with the non post-selected experiment in Sec. 3.4.1, for which $E = \frac{1}{2}\mathbb{1}$ is naturally the final effect matrix in absence of post-selection. This comes from the asymmetry between ρ and E in presence of dissipation toward a non zero-temperature environment, as described in Sec. 4.2.4.

- The absolute value of s_- remains well bellow 0.5, which is the allowed range for an unconditional measurement of σ_-. Thus, in this experiment, the weak value $\langle\sigma_-\rangle_w$ does not have new features compared to a regular average. Indeed, since ρ is nearly $\frac{1}{2}\mathbb{1}$, we can write $\mathrm{Re}[\langle\sigma_-\rangle_w] \simeq \mathrm{Re}[\mathrm{Tr}[\rho_E(t)\sigma_-]] = \mathrm{Tr}[\rho_E(t)\frac{\sigma_x}{2}]$, where $\rho_E = \frac{E}{\mathrm{Tr}[E]}$ has all the properties of a density matrix.

4.2.3 *Pre and post-selected fluorescence traces*

We now consider the case where the qubit is initially prepared near $|e\rangle$, that is $\rho(0) = \rho_0^g = f_g|g\rangle\langle g| + (1-f_g)|e\rangle\langle e|$, and post-selected near $|g\rangle$, that is an effect matrix $E_{y=0}(T) = F|g\rangle\langle g| + (1-F)|e\rangle\langle e|$ at time T.
Average fluorescence traces for drive amplitudes corresponding to Rabi frequencies from 0 to 1.6 MHz are represented with the same scaling factor as on Fig. 33 on the color plot of Fig. 35a. The theoretical counterpart, which is the weak value $\langle\sigma_-(t)\rangle_w$ with the PQS $(\rho(t), E(t))$ propagated in time using equations (194) and (196), is presented

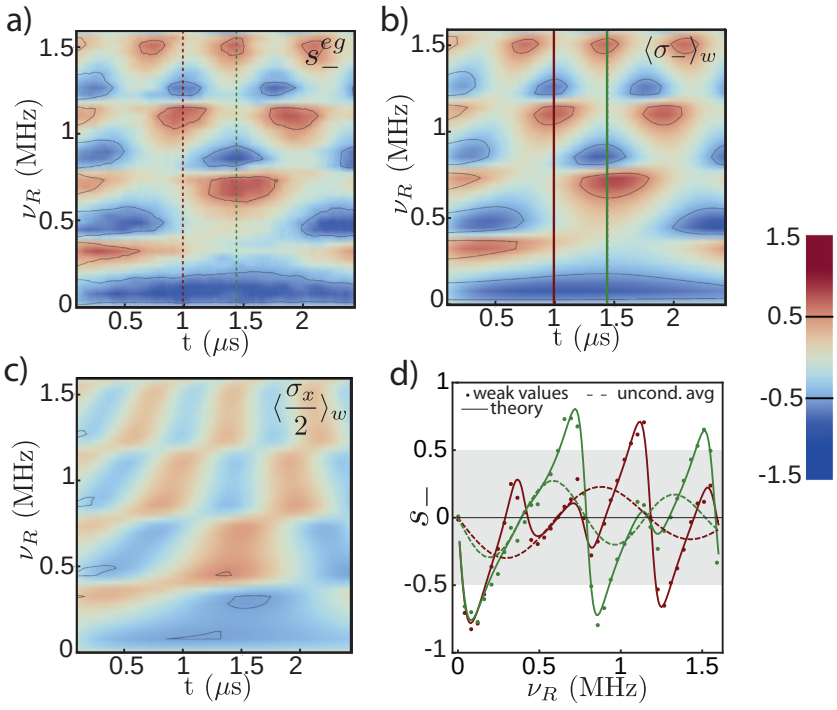

Figure 35: a) Mean fluorescence signal s_-^{eg} as a function of both time and Rabi frequency, for a qubit prepared in $|e\rangle$ and post-selected in $|g\rangle$. Plain lines surround regions with weak values beyond the range allowed by macro realism. b) Predicted value of $\langle\sigma_-\rangle_w$ for the same range of parameters as a. c) Same plot for the predicted value of $\langle\sigma_x\rangle_w$. d) Dots: cuts of a as a function of ν_R for times $t = 0.99$ μs (green) and $t = 1.44$ μs (red). Plain lines: prediction for $\langle\sigma_-\rangle_w$ for the same curves. Dashed lines: cuts of Fig. 24c at the same times. The gray region delimits the range of possible unconditional average values, like the contours in a.

on Fig. 35b. Once again, agreement between experimental data and theory is excellent.

On the other hand, the computed weak value of $\sigma_x/2 = \mathrm{Re}[\sigma_-]$, represented on Fig. 35c, obviously does not match with the measured mean fluorescence signal. In Eq. (134), for non post selected trajectories, the mean heterodyne fluorescence signal verified $\mathrm{Re}[J(t)] = \mathrm{Re}[\langle\sigma_-\rangle] = \frac{1}{2}\langle\sigma_x\rangle$[8]. So far, we could thus identify the averaged outcome of the measurement record associated with the $L = \sqrt{\gamma_1/2}\sigma_-$ (resp. iL) jump operator with a measurement of the σ_x (resp. σ_y) observable. This identification does not hold anymore for weak values. Indeed, the pseudo density matrix $\rho_p = \frac{\rho E}{\mathrm{Tr}[\rho E]}$ is not hermitian, so that

$$\begin{aligned}\mathrm{Re}[\langle\sigma_-\rangle_w] &= \mathrm{Re}[\mathrm{Tr}[\rho_p\sigma_-]] \\ &= \mathrm{Tr}[\mathrm{Re}[\rho_p]\mathrm{Re}[\sigma_-] - \mathrm{Im}[\rho_p]\mathrm{Im}[\sigma_-]] \\ &= \tfrac{1}{2}\mathrm{Tr}[\mathrm{Re}[\rho_p]\sigma_x - \mathrm{Im}[\rho_p]\sigma_y] \\ &\neq \tfrac{1}{2}\mathrm{Re}[\mathrm{Tr}[\rho_p\sigma_x]].\end{aligned} \tag{197}$$

8 We denote $\mathrm{Re}[A]$ the hermitian part of an operator A so that $\mathrm{Re}[\sigma_-] = \frac{1}{2}(\sigma_- + \sigma_-^\dagger) = \frac{\sigma_x}{2}$

Thus, by averaging the real measurement record associated with jump L only, one can access properties of the imaginary part of L. This property of the weak value is at the base of protocols for direct tomography of a wave function [147].

Another characteristic feature of these plots is that there are regions in which the fluorescence signal is much stronger (dark blue or dark red on the same color scale) than for only pre-selected or only post-selected traces. In the regions with a black contour, the signal even goes beyond eigenvalues of $\mathrm{Re}[\langle\sigma_-\rangle]$, corresponding to $-0.5 \leq s_- \leq 0.5$. The observation of this quantum feature predicted by Aharonov *et al.* [28] has been shown to contradict macro-realism when using a non-invasive detector, equivalently to the violation of a Leggett-Garg inequality [140]. Considering the isolation by circulators placed between the cavity output port and the amplifier (see Sec. A.2), the measurement here is indeed non-invasive. It has only recently been observed with superconducting qubits [141, 142].

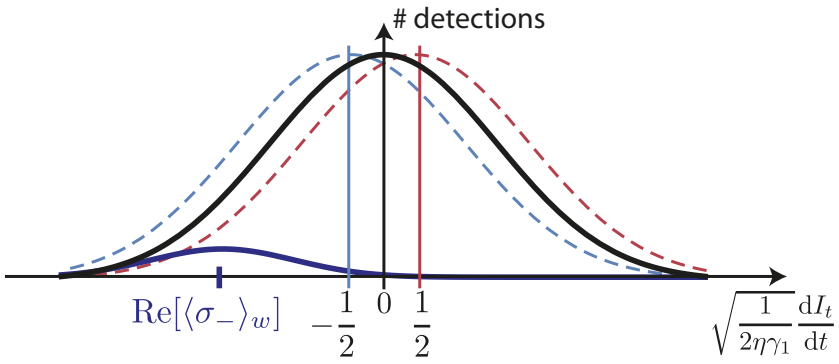

Figure 36: Schematic representation of the rescaled detector output distribution at time t, over a great number of experiments, for a non driven qubit. Black: preparation in $|e\rangle$, no post-selection. Dark blue: preparation in $|e\rangle$, post-selection in $|g\rangle$. The average value for the post-selected experiments goes beyond the largest average values accessible for the non post-selected cases, reached when the qubit is prepared in $|+x\rangle$ (red) and $|-x\rangle$ (light blue).

It can seem paradoxical: the average value of an operator on a sub ensemble of trajectories goes beyond the reachable values with no post-selection. However, this is possible when the measurement on the considered time-step is weak. Thus, the variance of its possible outcomes goes well beyond its mean value. For a single trajectory, such a large value of the fluorescence signal is not forbidden. As represented schematically on Fig. 36, when post-selecting trajectories far out-centered in the outcomes probability distribution, one can get an average beyond the reachable mean-value for non post-selected trajectories.
Here, we considered the situation corresponding to the bottom part of Fig. 35a: the qubit is prepared at time $t = 0$ in $|e\rangle$, and after a time $T \ll T_1 = 16$ μs, we select only the experiments during which it has decayed down to $|g\rangle$. For a weak Rabi drive ($\Omega_R = 0$), the only process that allows for such a final state is the maps K_{s_t} defined in Eq. (175) for $t \in [0, T]$, which can have a particularly strong effect. This happens

only if the fluorescence signal $s_t\sqrt{\mathrm{d}t}$ is itself very strong.

More generally, in absolute value, the largest fluorescence signal is detected when the probability of post-selection is low. Indeed, we can write

$$\mathrm{Tr}[\rho E] = \frac{1}{2}\mathrm{Tr}[\rho E + E\rho] = \mathrm{Tr}[\mathrm{Re}[\rho E]], \tag{198}$$

so that Eq. (197) reads

$$\mathrm{Re}[\langle\sigma_-\rangle_w] = \mathrm{Tr}\Big[\frac{\mathrm{Re}[\rho E]}{\mathrm{Tr}[\mathrm{Re}[\rho E]]}\frac{\sigma_x}{2}\Big] + \mathrm{Tr}\Big[\frac{\mathrm{Im}[\rho E]}{\mathrm{Tr}[\mathrm{Re}[\rho E]]}\frac{\sigma_y}{2}\Big]. \tag{199}$$

The first term in this sum looks like a usual average value whereas the second can diverge. This is often interpreted as amplification [145, 146] since the corresponding quantum noise is the same as for a usual average. Indeed, in Eq. (186), the variance of the distribution for ξ remains of order 1. However, taking into account the post-selection probability, the number of repetition of the experiment needed to get a given signal to noise ratio is at least as large as with conventional methods [150]. This property may still be useful in some quantum information protocols [155].

An illustration of this amplifying property of the weak values can be seen on Fig. 35d. In this plot, dots represent the experimental value of the fluorescence signal as a function of Rabi frequency at times $t = 0.99$ μs (green) and $t = 1.44$ μs (red). Plain lines represent the corresponding computed weak value, and dotted lines the unconditional average, corresponding to cuts of Fig. 24c at the same time. At a fixed time, when varying the Rabi drive amplitude Ω_R, there are some values for which the slope of the detected signal is much stiffer than for non post-selected traces. Thus, in these regions, the sensitivity of our detection to a small variation of a parameter is increased. It could be infinitely large if not for the finite preparation and post-selection fidelities.

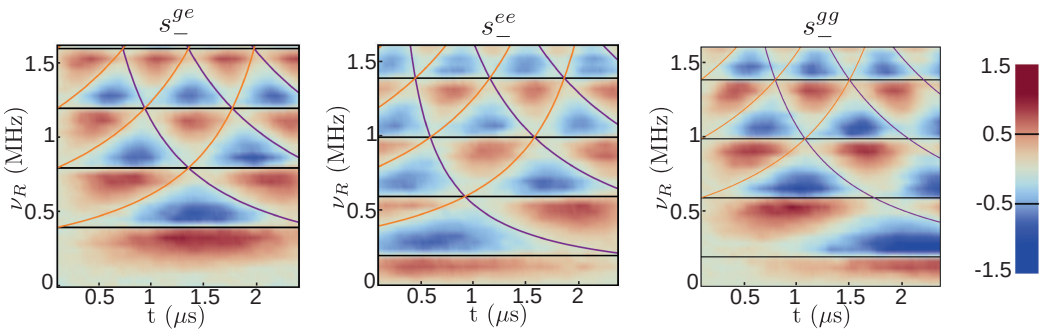

Figure 37: Mean fluorescence signal for trajectories from $|g\rangle$ to $|e\rangle$ (to the left), from $|e\rangle$ to $|e\rangle$ (center) and from $|g\rangle$ to $|g\rangle$ (to the right). Horizontal black lines materialize regions in which preparation and post-selection disagree (lowest probability of post-selection). Purple (resp. orange) lines materialize times for which $\rho(t) = |g\rangle\langle g|$ (resp. $E(t)|e\rangle\langle e|$

On Fig. 37, we present the average fluorescence signal for trajectories from $|g\rangle$ to $|e\rangle$ (to the left), from $|g\rangle$ to $|g\rangle$ (center) and from $|e\rangle$ to $|e\rangle$ (to the right). Horizontal black

lines materialize Rabi drive values for which preparation and post-selection disagree ($\mathrm{Tr}[\rho E] \to 0$). It corresponds to an integer number of oscillations for s_-^{ge} and an integer plus one half oscillations for s_-^{gg} and s_-^{ee}. In every case, it corresponds to the lowest probability of post selection and to the highest sensitivity to the Rabi frequency value. Indeed, bellow a line, we rather select trajectories for which the relaxation has accelerated the rotation of the qubit, so that it was strong when the qubit state was rotating down to the south pole of the Bloch sphere, which happens when $\langle\sigma_x\rangle > 0$. Thus, in these regions, we get a strong positive signal (dark red regions). On the other hand, above these lines, we rather select trajectories for which the relaxation has slowed down the rotation of the qubit, so that it was strong when the qubit state was rotating up from the south pole of the Bloch sphere, which happens when $\langle\sigma_x\rangle < 0$. We then get a strong negative signal (dark blue).

A last interesting feature is materialized by the curved lines. They represent times for which ρ indicates a qubit near $|g\rangle$ (purple lines) or times for which E indicates a qubit near $|e\rangle$ (orange lines). In both cases, the fluorescence signal goes down to zero. Indeed,

$$\mathrm{Tr}[|g\rangle\langle g|E\sigma_-] = \mathrm{Tr}[\rho|e\rangle\langle e|\sigma_-] = 0. \tag{200}$$

In this section we have described an experiment in which the resonance fluorescence of the qubit was recorded during $t = 2.5$ μs and then averaged conditionally to a final projective measurement of σ_Z. The information from the final readout is encoded in the effect matrix E, propagated backward in time using Eq. (196). It is similar to the Lindblad master equation (194) but not time symmetric. This asymmetry between preparation and post-selection was not visible here because $T \ll T_1$ so that the dynamics was dominated by the hamiltonian evolution induced by the Rabi drive, which is reversible. Thus in Fig. 35a and Fig. 37, the color plots are invariant under the transformation

$$\begin{cases} t & \leftrightarrow & -t \\ |e\rangle & \leftrightarrow & |g\rangle \end{cases}, \tag{201}$$

the second substitution compensating for the minus sign introduced by the first in the hamiltonian. However, on longer timescales and when not driving the qubit ($\Omega_R = 0$) ρ converges to $\rho_e q \simeq |g\rangle\langle g|$ at $t \to +\infty$ when E converges to $\frac{1}{2}\mathbb{1}$ at $t \to -\infty$, breaking the symmetry. To highlight this property, we briefly describe a similar experiment but corresponding to longer trajectories with a shorter lived qubit.

4.2.4 *Time asymmetry for a dissipative system*

The qubit used here corresponds to Qubit 4 in Tab. 3. The experiment is similar to the one described in the previous sections, but after preparation, the fluorescence signal is averaged for 10 μs $> T_1 = 4$ μs. Moreover, as in Sec. 3.4.2, the final projective readout conditioning the average is done along σ_X, σ_Y or σ_Z, each on one third of the experiments. We also let the possibility to prepare the qubit in $|\pm x\rangle$ and $|\pm y\rangle$,

which respectively denote the eigenstates of σ_X and σ_Y. Finally, the occupation of the excited state at thermal equilibrium is $P_{eq}(|e\rangle) \leq 1$ %, so that errors in preparation can be neglected. On the other hand, the final readout leads to 15 % errors (for both false positives and false negatives) for the 3 types of measurements[9].

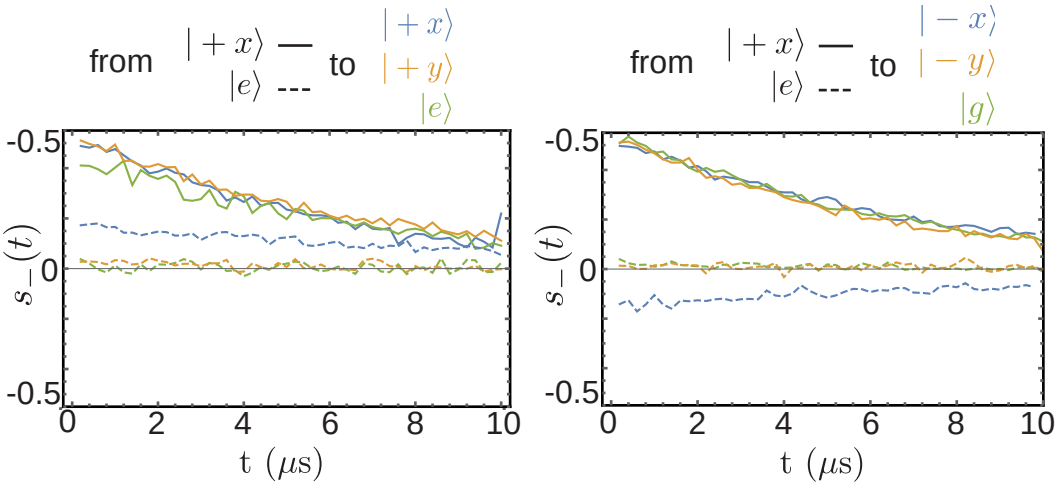

Figure 38: Fluorescence traces for a qubit initially in $|+x\rangle$ (plain lines) or $|e\rangle$ (dashed lines), averaged conditionally to the outcome of a final projective readout along σ_X (blue), σ_Y (yellow) and σ_Z (green) at $T = 10$ μs. The traces are grouped in 2 panels according to the pos-selected outcome of the projective measurement for clarity.

As stated previously, the asymmetry between E and ρ is not visible when the dynamics is dominated by a fast hamiltonian evolution such as a high frequency Rabi oscillations. Therefore, no drive is applied in order to highlight the asymmetry. On Fig. 38, we plot the average fluorescence signal for a qubit initially in $|+x\rangle$ (plain lines) or $|e\rangle$ (dashed lines) and post-selected according to the outcome of the final readout along σ_X (blue), σ_Y (yellow) or σ_Z (green). Each panel corresponds to a different post-selection.

A first striking feature of these plots is that *all average signals* decrease to 0 after a few T_1's. This reflects that $\rho(t) \overset{t\to\infty}{\to} \rho_{eq} \simeq |g\rangle\langle g|$, so that $\mathrm{Tr}[\rho(t)E(t)\sigma_-] \to 0$. This is in contrast with the evolution of the effect matrix that verifies $E(t) \overset{t\to-\infty}{\to} \frac{1}{2}\mathbb{1}$. This asymmetry is characteristic of a dissipative system: predictions can be made about a measurement in the far future, since the entropy of the system eventually decreases down to 0. On the other hand, a final measurement does not bring information about the far past, and knowing only measurement outcomes after a few T_1's, all initial preparations are equally probable.

Note that, had we considered only a non-dissipative decoherence process such as dephasing, the corresponding jump operator would have been hermitian ($\sqrt{\frac{\Gamma_d}{2}}\sigma_z$ in the

9 In this particular experiment, the microwave pulses used during the high power readout protocol (see Sec. 3.3) degraded the coherence time of the qubit for tens of milliseconds after the readout, limiting the repetition rate of the experiment. We chose to decrease the amplitude of these pulses in order to limit this effect, at the expense of the readout fidelity.

case of dephasing), and the master equations (194) for ρ and (196) for E would have been symmetric.

Let us comment further on the traces of Fig. 38.

- When the qubit is prepared in $|+x\rangle$ and for a final readout along σ_x (plain blue lines), the conditional average depends on the preparation (positive signal), but *not* on the final detection outcome. This surprising feature, predicted by the past quantum state formalism even for perfect readout fidelity, illustrates further the asymmetry between preparation and post-selection when monitoring σ_-.
- The post-selection using a final readout along σ_Y (yellow lines) does not affect the fluorescence signal either. This can be understood considering that, up to now, only the signal from the detection of the I quadrature of the fluorescence field, corresponding to the $\sqrt{\gamma_1/2\sigma_-}$ jump, was recorded (see Fig. 33 and Eq. (193)). In Sec. 3.4.2.4, we have shown that, in terms of Bloch sphere representation, the record of this detection only influences the x and z coordinates of the qubit (see Eq. (160)). Thus, the signal is not correlated to the outcome of the final measurement along σ_Y. Both conditionally averaged traces are equal to the unconditional one.
- Were there no readout errors, an experiment where the qubit is post-selected in $|e\rangle$ (green lines on the left panel) would yield no signal. This can be understood considering that if the qubit is detected in $|e\rangle$ at T, it cannot have leaked energy prior to T. However, for the trace $s_-^{ee}(t)$ (plain line) the signal is only slightly lower than on the right panel, when the qubit is post-selected in $|g\rangle$. This is because at $T \simeq 2.5\ T_1$, most detections of a qubit in $|e\rangle$ are in fact false positives.

In this experiment, we also record the signal corresponding to the detection of the Q quadrature of the fluorescence field. As expected, the two averaged traces conditioned on the outcome of a final measurement along σ_Y differ. On Fig. 39, are represented in red (resp. in blue) these conditionally averaged traces when the qubit is driven at $\Omega_R/2\pi = 0.5$ MHz around σ_Y, for a qubit in $|g\rangle$ at $t = 0$ and detected in $|+y\rangle$ (resp. $|-y\rangle$) at $T = 10\ \mu$s. On Fig. 39a, we plot the rescaled average signal on the I quadrature. It is reproduced by the weak value of σ_-, which reads $\mathrm{Re}\left[\frac{\mathrm{Tr}[\rho(t)E(t)\sigma_-]}{\mathrm{Tr}[\rho(t)E(t)]}\right]$. The conditionally averaged signal on the Q quadrature is plotted on Fig. 39b and, according to Eq. (189), is reproduced by the weak value of $i\sigma_-$ which reads,

$$\begin{aligned} \langle i\sigma_-\rangle_w &= \mathrm{Re}\left[\frac{\mathrm{Tr}[\rho(t)E(t)i\sigma_-]}{\mathrm{Tr}[\rho(t)E(t)]}\right] \\ &= -\mathrm{Im}\left[\frac{\mathrm{Tr}[\rho(t)E(t)\sigma_-]}{\mathrm{Tr}[\rho(t)E(t)]}\right]. \end{aligned} \tag{202}$$

The predictions using the past quantum states formalism match quantitatively the experimental curves. The signal on I is not affected by the post-selection, similarly to the signal on Q when post-selecting with a measurement along σ_X (see Fig. 38). The conditionally averaged traces on Q, resulting from the combined effects of both the post-selection, which forces the selected trajectories toward $y = \pm 1$ in the Bloch

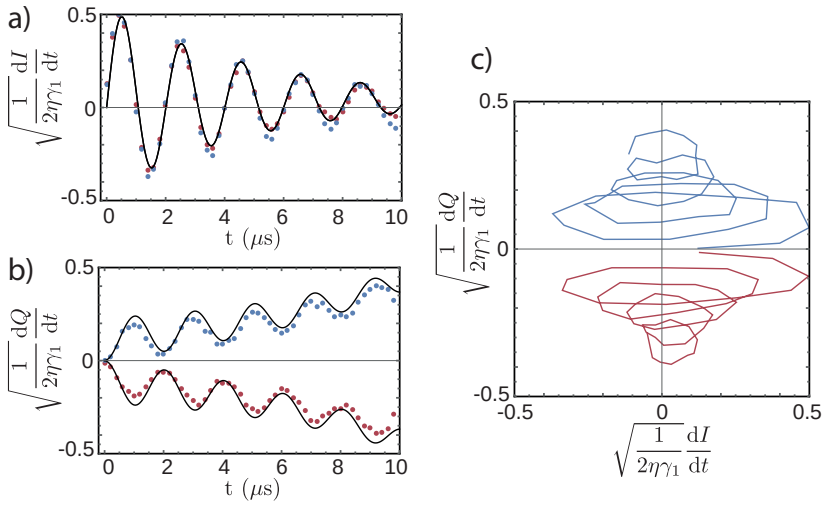

Figure 39: Fluorescence traces for a qubit initially in $|g\rangle$, undergoing Rabi oscillations around σ_Y at $\Omega_R/2\pi = 0.5$ MHz, and post-selected in $|+y\rangle$ (in red) or $|-y\rangle$ (in blue) at $T = 10$ μs. **a** Signal on the I quadrature detection, corresponding to the $\sqrt{\frac{\gamma_1}{2}}\sigma_-$ jump operator. **b** Signal on the Q quadrature detection, corresponding to the $\sqrt{\frac{\gamma_1}{2}}i\sigma_-$ jump operator. **c** Same traces represented in the IQ plane.

sphere, and the drive around the y-axis, are non-trivial.

In this chapter, we have described an experiment in which the fluorescence signal of the qubit is averaged conditionally to a final projective measurement outcome. The average value is predicted using both ρ and E, which are propagated in time deterministically from 0 (resp. T) to the time of interest t. This contrasts with the stochastic master equation formalism which makes use of all the measurement record before t (see Sec. 3.1) and after t (See Sec. 4.1.2).
In the present case of a weak monitoring via the fluorescence detection, a single trajectory unravelled using the measurement record from both past and future would not differ much from the one we would get using the measurement record from the past only[10]. This contrasts with the situation in which past quantum states are used to *smooth* trajectories [30, 157]. Smoothing is used when monitoring the system with a strong measurement of low efficiency. Calling dt the integration time step and Γ_d the dephasing rate associated with the measurement backaction, it requires the hierarchy

$$\eta\Gamma_d dt < 1 < \Gamma_d dt. \tag{203}$$

In this essentially classical situation, the system state is always projected by the measurement, but the knowledge of the observer is imperfect. By combining information both from past and future measurements, one can, for instance, better resolve quantum jumps of the system [157].
In our case where $\gamma_1 dt \ll 1$, the trajectories are continuous, and knowing the value of the record at $t + dt$ only slightly changes our estimation of the measurement outcome

10 We call here measurement record only the outcomes of the weak detection of σ_-, and not the final projective readout, which influences dramatically the trajectories [156]

at t.
In the experiment, the past quantum state can describe the statistics of a particular measurement, but not the state of the qubit. In an ideal weak value experiment, both knowledge from the past and from the future are perfect, but different. It thus highlights the backaction of the weak measurement at t, which is strongly correlated to the choice of post-selection.

4.3 CONCLUSION

In this part, we have described the design and constraints on the parameters of a superconducting qubit, the 3D transmon. This system implements the simplest open quantum system one can think of, which is a two-level system in presence of a single relaxation channel. Its long coherence time combined with fast electronics allows for coherent manipulations and, using the interaction of the qubit with the cavity mode, one can realize a QND measurement of its σ_Z operator. This measurement effectively opens a dephasing channel for the qubit.
These two decoherence channels (relaxation and dephasing) can be monitored efficiently to limit information loss in the environment, and thus to access the quantum trajectory of the qubit on a single experiment.

The main results of this part are

- Demonstration of high efficiency ($\eta = 67$ %) detection of a microwave mode dispersively coupled to a superconducting qubit. This detection is used to implement a high fidelity, QND readout of the σ_Z operator of the qubit in a single-shot. Observation of quantum jumps.
- Efficient collection and heterodyne measurement of the fluorescence of a qubit. The overall detection efficiency is $\eta = 24$ %. The signal is filtered using a Stochastic Master Equation to follow in time the state of the qubit during relaxation. Predictions are validated by independent tomographic reconstruction.
- Conditional averaging of the fluorescence traces according to the outcome of a final projective measurement to measure weak values of the σ_- operator of the qubit. Observation of weak values out of the accessible range for unconditional average.

Future uses of the fluorescence detection may include parameter estimation using the past quantum states formalism [158]. For instance, with a sideband detector, one could reconstruct the texture of non-gaussian noise on the qubit resonance frequency from low frequency up to a few GHz . The statistics of fluorescence trajectories may also prove a useful tool to study heat and entropy exchange in simple quantum systems, which are the relevant quantities to the new field of quantum thermodynamics [159].

Up to now, we have described how to monitor the state of the qubit. In the next part, we describe active control schemes that make use of the information extracted via dispersive measurement or fluorescence detection.

Part II

QUANTUM CONTROL

Hideo Mabuchi [160] distinguishes three modes of quantum control.

- *Open loop* control in which a quantum system is driven by a time-dependent control hamiltonian in a predetermined way. As we have seen in Sec. 2.1.2, hamiltonian evolution preserves the entropy of a system. Thus, it cannot be used by itself to prepare a given target state starting from an unknown state. However, it can de done in an open system by taking advantage of the dissipation into a cold environment. For an open qubit, the simplest scheme is as follows. For a sufficiently cold environment, starting from any state, we wait for a few T_1's. This brings the qubit close to its ground state. We then apply a fast control pulse to bring it to the desired state.
  Defining the preparation fidelity as the average distance between the qubit state $\rho(t)$ and the target state $\sigma(t)$ as $F = \int_0^\infty \mathrm{Tr}[\rho(t)\sigma(t)]\mathrm{d}t$, we can show that this open loop control scheme results in a low preparation fidelity for a target state far from the ground state. Indeed, the error rate and the dissipation rate used to evacuate entropy are the same since they are both set by the dissipation of the qubit on a time scale T_1.

- *Measurement based feedback* in which a discrete or continuous measurement record as defined in Chap. 3 is processed classically and used to adjust the system state in real time. In Sec. 5.1, we describe an experiment implementing a stroboscopic feedback that takes advantage of the high measurement rate and the non demolition nature of the dispersive readout to stabilize an arbitrary state or trajectory of the qubit. In Sec. 5.2, we describe another experiment in which the measurement record associated with the relaxation channel of the qubit is fedback continuously to the qubit through a Markovian controller in order to stabilize an arbitrary state.

- *Autonomous feedback*, also referred to as *coherent feedback*, in which a quantized field scattered by the system is processed coherently (without measurement) and then redirected to the system as a control input. It makes use of an auxiliary system whose dissipation rate is much larger than the qubit decay rate. By engineering the coupling between the qubit and the auxiliary system, dissipation then brings the qubit to the desired state on a rate much larger than the error rates associated with uncontrolled decoherence channels. In Chap. 6, we show a simple implementation of autonomous feedback using the high decay rate of the cavity to reset the qubit state.

Closely related to these feedback based schemes, Facchi *et al.* define a fourth control scheme. [36, 161] consisting in tailoring dynamically the Hilbert space of a system in time.

- *Quantum Zeno dynamics* occurs when the evolution of a system of large Hilbert space dimension is restricted to a given subspace either through repeated measurement or by a unitary coupling to an auxiliary system. In Chap.7, we describe an experiment in which a qubit is used to induce such dynamics for a cavity mode.

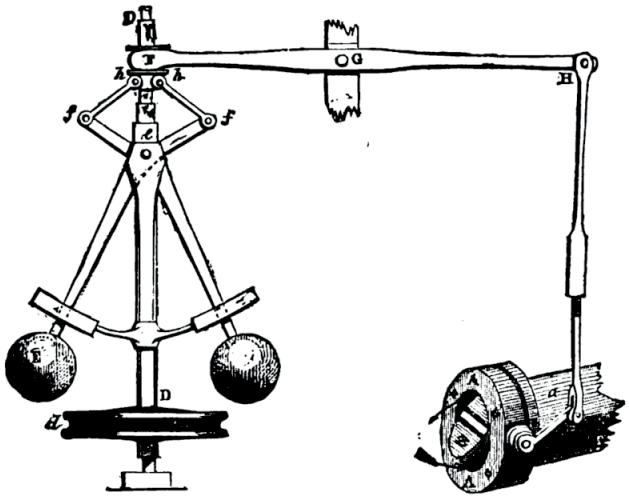

Figure 40: The centrifugal governor for steam engines designed by Boulton and Watt in 1788 is inspired by previous governors used to regulate the distance and pressure between millstones in windmills. The output of the engine is connected to the governor and causes it to rotate. When the output power increases, the centrifugal force draws the balls away from the rotation axis. This causes the valve admitting the steam flow to the engine to close, decreasing its power. This auxiliary system can be seen as implementing a coherent feedback in the sense that no further information comes out of the system. However, in a classical system, coherent and measurement based feedback are equivalent since the steam flow could be measured without perturbing the system.

5

MEASUREMENT BASED FEEDBACK

Feedback loops are ubiquitous in complex systems, from automatics to biology or economics. They stabilize a system subjected to uncontrolled stochastic noise from its environment or prepare a given state starting from an unknown initial state. A feedback loop can be decomposed in three components. A *sensor* that monitors a given observable (temperature, blood-glucose level...) sends this signal to a *controller* (electronic integrated circuit, insulin activation enzymes...) that analyzes it and uses an *actuator* (heater power, insulin amount...) to react on the system.

In the quantum domain, there is a change of paradigm in feedback since measurements modify the state of the system. However, using the stochastic master equation formalism described in Chap. 3, the controller can be designed to take into account the measurement backaction when estimating the state of the system. Thus, results from classical control theory can be more or less transposed to quantum systems [33, 24].

The first implementation of measurement-based quantum feedback was performed by Sayrin *et al.* in 2011 [40, 41]. Using Rydberg atoms, they managed to measure the state of a microwave field inside a high finesse cavity and to use the information to steer this state towards a target Fock state by applying coherent drive pulses or photon transfer on a time scale much shorter than photons lifetime inside the cavity. Several demonstrations of MBF have since been performed using superconducting qubits [42, 48, 81].

In this chapter, we describe two experiments implementing measurement based feedback on a superconducting qubit. First, a stroboscopic digital feedback based on a dispersive measurement, and then a continuous analog feedback based on the fluorescence signal of the qubit.

5.1 STROBOSCOPIC DIGITAL FEEDBACK USING DISPERSIVE MEASUREMENT

5.1.1 *Feedback loop*

The principle of this digital feedback is as follows. Given a target state or trajectory, at arbitrary times,

- A fast control pulse is applied to map the target state to $|g\rangle$.
- The qubit is measured using the QND dispersive readout described in Sec. 3.2.3.1[1].

1 Note that in the experiment, the JPC is turned on only during this measurement. Due to imperfect isolation from the cavity, it would otherwise induce extra dephasing of the qubit, which would lower the feedback efficiency when stabilizing states that are not $|g\rangle$ or $|e\rangle$

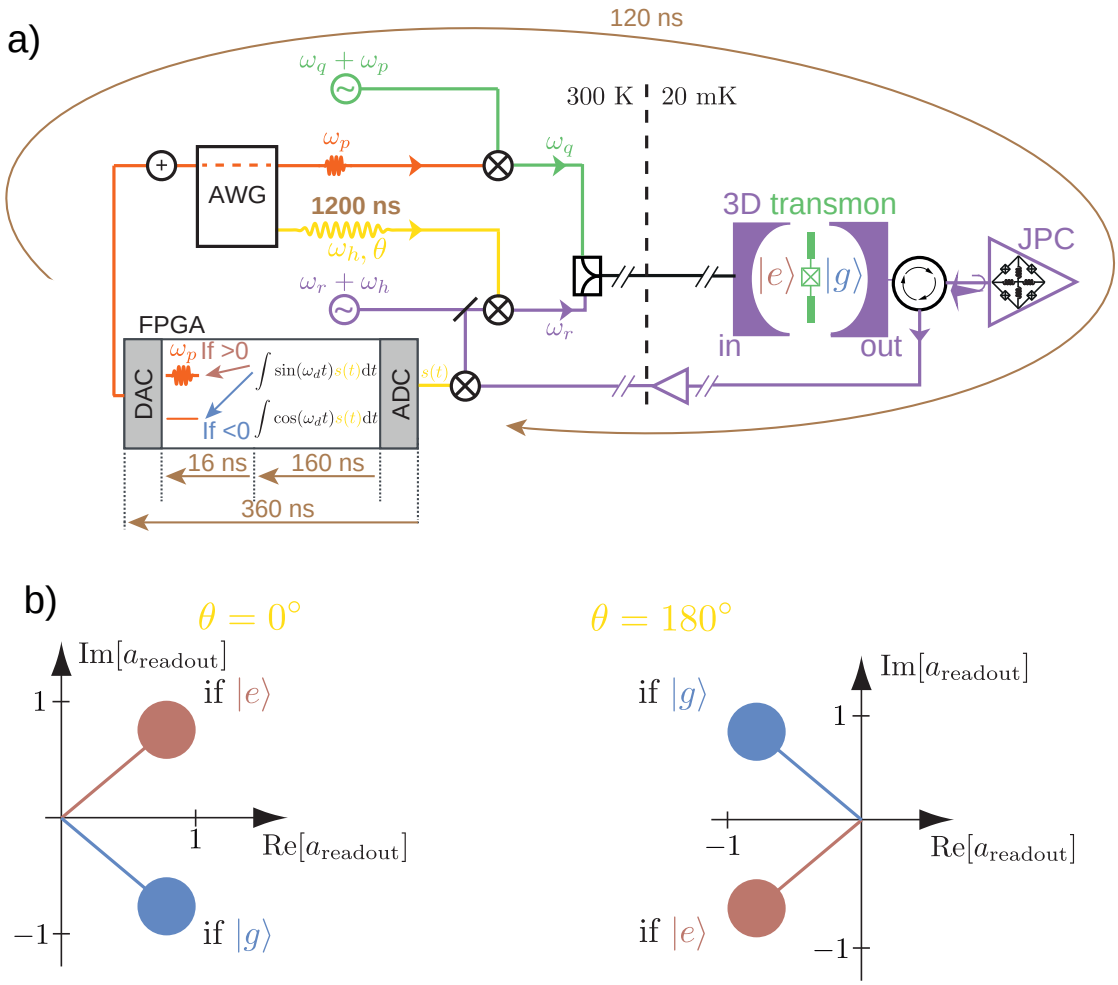

Figure 41: a) Schematic of the feedback loop to stabilize $|g\rangle$ or $|e\rangle$. A square readout pulse (in yellow) at $\omega_h/2\pi = 62.5$ MHz and with phase θ is generated by an arbitrary waveform generator (AWG) and then up-converted to ω_r by mixing with a local oscillator (LO) at $\omega_r + \omega_h$ (in purple). It is sent to the input port of the cavity and the transmitted signal is amplified and down-converted using the same LO. The resulting signal $s(t)$ is then digitized by the FPGA board, demodulated and integrated over its 960 ns long stationary regime. If its imaginary part is positive, a short square pulse at $\omega_p/2\pi = 125$ MHz is generated (in orange). This pulse is added up to other control pulses of the qubit with the same phase, and up-converted to ω_q by mixing with a LO at $\omega_q + \omega_p$ (in green) before being sent to the qubit. Full schematic of the wiring can be found on Fig. 64. b-c) a_{readout} is the integrated and rescaled readout signal as defined in Eq. (204). The disks represent the fluctuations. By setting the phase θ of the readout pulse, one can choose to trigger a feedback pulse if the qubit is detected in $|e\rangle$ ($\theta = 0°$) or in $|g\rangle$ ($\theta = 180°$).

- If the qubit is measured in $|e\rangle$, a fast π pulse is applied in order to bring it back to $|g\rangle$.
- The qubit is sent back to the target state by applying a control pulse opposed to the initial one.

To be efficient, the repetition rate of this feedback loop must be much higher than the error rate γ_1 that needs to be corrected for. The two intermediate steps use the same reset by digital feedback as described by Ristè *et al.* [42]

The experiment [81] uses the same setup and measurement pulse as depicted in Sec. 3.2.3.1 (Qubit 1 in Tab. 3). The feedback loop is represented on Fig. 41a. After mapping the target state to $|g\rangle$, a 1.2 μs long pulse at cavity frequency, corresponding to an average photon number in the stationary regime calibrated to be 1.4 photons, is sent through the cavity. We set the phase[2] of the readout pulse to be $\theta = 0°$ so as to get the configuration described on Fig. 41b. In that case, the imaginary part of the detected signal, found integrating the measurement record of Eq. (118) and rescaled as for Fig. 20, reads

$$\begin{aligned} a_{\text{readout}} &= \frac{1}{T_{\text{meas}}\sqrt{2\eta\kappa}} \int_{t_{\text{coll}}}^{t_{\text{coll}}+T_{\text{meas}}} J(t)\mathrm{d}t \\ &= \cos\tfrac{\theta}{2} + \langle\sigma_Z\rangle i \sin\tfrac{\theta}{2} + \frac{1}{T_{\text{meas}}\sqrt{2\eta\kappa}}\Big(W_1(T_{\text{meas}}) + iW_2(T_{\text{meas}})\Big) \end{aligned} \tag{204}$$

Here, as in Sec. 3.2.3.1, the signal integration is performed a time $t_{\text{coll}} > 1/\Gamma_d$ after the beginning of the readout pulse so that the state of the qubit has been collapsed to $|e\rangle$ or $|g\rangle$, and $\langle\sigma_Z\rangle = \pm 1$. T_{meas} is long enough so that the fluctuations encoded by the Wiener processes W_1 and W_2 are small compared to the mean signal. Therefore, $\mathrm{Im}[a_{\text{readout}}] > 0$ only if the qubit is in $|e\rangle$ (the readout fidelity beyond relaxation errors is 99.6 %), and this criterion can be used to apply a correction pulse.

The high fidelity of the readout performed on a short time scale compared to T_1 is enabled by the high efficiency detection setup ($\eta = 67$ %), in which the JPC is used as a pre amplifier. After further amplification, the detected signal is down-converted and sent to a Tekmicro Triton-V5 board. The board then triggers a square pulse modulated at $\omega_2 = \pi \times 125$ MHz conditioned on the measurement outcome. The overall feedback delay is 480 ns and can be decomposed as follows.

- The electrical delay between the cavity output and the board ADC is 60 ns, including the down-conversion to $\omega_h = 2\pi \times 62.5$ MHz.
- The board ADC digitizes the signal by sampling it at a rate 500 MSample/s and sends it to the FPGA core itself. The board is clocked using the same 10 MHz reference as the AWG.
- The FPGA numerically demodulates this signal and averages it over its 960 ns long stationary regime. This demodulation consists in averaging the product of the down-converted signal $s(t)$ and the pre-recorded values of $\sin\omega_h t$ (resp. $\cos\omega_h t$) on an integer number of periods so as to get, up to a scaling factor, the values of $\mathrm{Im}[a_{\text{readout}}]$ (resp. $\mathrm{Re}[a_{\text{readout}}]$). Note that only the imaginary part contains information about the qubit state, but it is convenient to get both values in order to adjust the phase of the readout pulse. The integration is triggered by

2 a constant offset is chosen so that $|\overline{\mathrm{Im}[a_{\text{readout}}]}|$ does not depend on the qubit state and $\overline{\mathrm{Re}[a_{\text{readout}}]} > 0$.

the AWG. If the imaginary part is positive, a control bit is then set to 1 and sent to the DAC that generates a 104 ns long pulse modulated at $\omega_p = 2\pi \times 125$ MHz. The phase of this pulse is the reference phase for the qubit drive (rotation around the y-axis). Note that the overall processing by the board lasts 360 ns, out of which 160 ns are used for demodulation and integration. The remaining 200 ns are needed to generate and send the control bit (16 ns) and to allow reliable synchronization of the ADC/DAC and FPGA clocks (180 ns).

- The output of the board is then added up by an AWG to other control pulses of the qubit. The resulting signal is up-converted to ω_q by mixing with a LO and sent to the qubit. The overall attenuation of the input lines is such that the FPGA generated pulse corresponds to a π rotation of the qubit around the y-axis of the Bloch sphere.

Including the duration of the readout pulse and the correction pulse, the overall feedback loop duration is $T_{\text{loop}} = 1.8$ μs, much smaller than the qubit decay time $T_1 = 28$ μs and than pure dephasing time $T_\phi = 14.5$ μs. Moreover, the protocol can in principle be repeated as fast as the readout pulse is short. Indeed, as long as the qubit remains in the (x, z) plane of the Bloch sphere, one can implement any control sequence while the board is processing the readout signal. At each detection event, if the readout outcome turns out to be the one expected, the measurement back action itself projects the qubit on the target state and the entropy that had appeared since the previous measurement is evacuated. This is a difference with classical feedback where measurement does not produce stabilization alone. If, on the contrary, the readout outcome is not the one expected, the qubit state is orthogonal to the target state during the 420 ns needed for the correction pulse to reach the qubit. Whatever the evolution of the qubit state during this lapse, as long as it is in the (x, z) plane when the correction pulse is applied, the trajectory is then refocused to the target state. However, the cavity readout time $1/\kappa = 90$ ns being finite, following a measurement, one should wait until the photons leak out of the cavity before driving the qubit in order to avoid dephasing due to photon noise.

Note that another possibility consists in setting the readout pulse phase at $\theta = 180°$. In that case, $\text{Im}[a_{\text{readout}}] > 0$ if the qubit is in $|g\rangle$ as represented on Fig. 41c. Then, otherwise using the same pulse sequence and criterion to trigger the correction pulse, one stabilizes the orthogonal state. However, this configuration is less efficient. Indeed, since the qubit is more frequently measured in $|e\rangle$, there is a higher rate of relaxation induced bit flip errors between the readout and the correction pulse. These errors are not corrected for until the following feedback loop.

5.1.2 *Qubit reset*

As a first implementation of this protocol, we choose the ground state itself as the target state. The feedback loop is then used to reset the qubit starting from any undetermined state, similarly to what was demonstrated by Ristè *et al.* [42]. Quantum

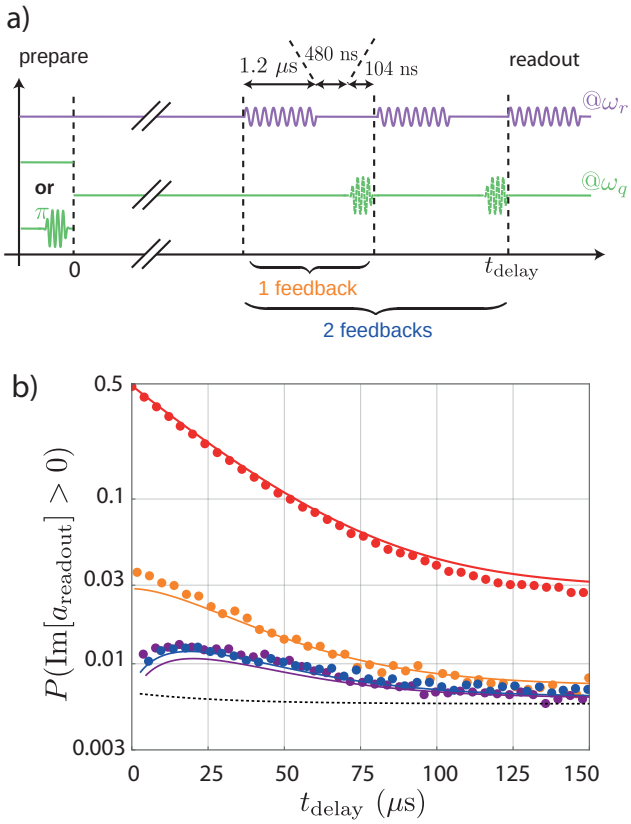

Figure 42: a) Schematic of the reset pulse sequence. The qubit is effectively prepared in $\rho = \frac{1}{2}(|g\rangle\langle g| + |e\rangle\langle e|)$ by averaging over experiments in which it is left at thermal equilibrium and others in which its population is inverted by applying a fast π pulse. For a time t_{delay}, the qubit is left to relax toward thermal equilibrium or actively cooled down by applying between 1 and 4 feedback loops before being measured. b) Measured occupation of the $|e\rangle$ level as a function of t_{delay} with no feedback (in red) or after applying 1 (orange), 2 (blue) or 3 (purple) feedback loops. Dots: experimental data. Lines: theoretical prediction including thermal excitations toward higher energy levels of the transmon. Black dotted line: same prediction for 2 feedback loops neglecting the higher excited states of the transmon.

information processing requires such removal of entropy during initialization or when correcting for errors [43]. This method allows to do so without fast frequency tuning [162, 163, 16, 164], post-selection [165, 166] or limited coupling rate $\kappa < \chi$ [44].

As an illustration, the qubit is first prepared in the most entropic mixed state $\rho = (|g\rangle\langle g| + |e\rangle\langle e|)/2$ by either applying a π-pulse or not (the outcomes are averaged over these two possibilities). After a time t_{delay}, we measure the occupation of the $|e\rangle$ level following zero, one or more resets by feedback. On Fig. 42b, we plot the probability to detect a positive value of the imaginary part of the readout field as a function of t_{delay} for these various situations. Note that due to finite fidelity of the measurement, this is not directly $P(|e\rangle)$. We found that starting from $P_{|e\rangle} = 50$ %, a single reset brings this probability down to $P(\text{Im}[a_{\text{readout}}] > 0) = 3.6$ %, which, without feedback, would require to thermalize during 110 μs. Yet, events where the

qubit relaxes between the middle of the measurement pulse and the feedback pulse limit the efficiency of a single reset. Doing a second reset immediately after the first brings the qubit much closer to the ground state with $P(\mathrm{Im}[a_{\mathrm{readout}}] > 0) = 1.1$ %. Further feedback loops do note improve this figure, but for long delay, that is applying feedback loops from thermal equilibrium, it gets as low as 0.6 %.

This can be understood considering a finite thermal excitation rate to higher energy levels of the transmon. We model it considering a three-level system. The decay time of the third energy level, noted $|f\rangle$, has been measured independently to be $T_{1,ef} = 15$ μs. This is possible using a detection scheme described in the supplementary material of [81] and similar to the method used in Sec. 6.1.2. Assuming a Boltzmann distribution for the occupation of the levels at thermal equilibrium we can compute the transition rates between these levels using

$$\begin{cases} \frac{\Gamma_{e\to f}}{\Gamma_{f\to e}+\Gamma_{e\to f}} &=& \frac{\Gamma_{g\to e}}{\Gamma_{e\to g}+\Gamma_{g\to e}} &=& 1 - P_{\mathrm{th}}(|g\rangle) = 2.4\% \\ \frac{1}{\Gamma_{f\to e}+\Gamma_{e\to f}} &=& T_{1,ef} & & \\ \frac{1}{\Gamma_{e\to g}+\Gamma_{g\to e}} &=& T_1 & & \end{cases} . \tag{205}$$

Considering no further errors but the thermally induced transitions, and perfectly QND readout pulses, we can reproduce quantitatively the feedback results (plain lines in Fig.42b). Note that, with the present readout scheme at $\omega_{\mathrm{readout}} = \frac{\omega_{r,g}+\omega_{r,e}}{2}$, a qubit in $|f\rangle$ yields a result $\mathrm{Im}[a_{\mathrm{readout}}] > 0$ so that it is not distinguishable from $|e\rangle$. Moreover, denoting F the fidelity of the measurement[3], we suppose that

$$P(\mathrm{Im}[\mathrm{a_{readout}}] > 0) = F \times (P_{\mathrm{mid}}(|e\rangle) + P_{\mathrm{mid}}(|f\rangle)) + (1-F) \times P_{\mathrm{mid}}(|g\rangle), \tag{206}$$

where $P_{\mathrm{mid}}(g, e, f)$ is the occupation of the levels in the middle of the integration interval by the board. Finally, the correction pulse is supposed not to affect a qubit in $|f\rangle$ and to flip a qubit in $|g\rangle$ and $|e\rangle$ only 99% of the time[4].

In Sec. 3.2.3.1, F had been calibrated to be 99.7%. However, this value fails to reproduce faithfully the data, and the agreement between data and theoretical prediction is far better with $F = 99.6\%$. This more precise value is well within the error bar associated with the estimation made in Sec. 3.2.3.1.

Correcting for these final readout errors, we get better results for the reset than presented in [81]. These results are summarized in Table 1. Note that this reset could prepare any state with similar purity by applying fast rotation pulses once the qubit is in state $|g\rangle$. In practice, the fidelity is limited by the fidelity of the rotation pulses.

5.1.3 *Rabi oscillations*

We now aim at stabilizing a dynamical state of the qubit, namely Rabi oscillations. This was first performed by Vijay *et al.* [48] using a continuous and weak measurement

3 we make the approximation that F is also the fidelity for the detection of $|f\rangle$

4 This value corresponds the decoherence during a 104 ns long Rabi oscillation.

Table 1: Occupation of $|e\rangle$ using zero, one or two resets by feedback when starting in the most entropic state or in the thermalized state (effectively at 46 mK). Finite fidelity of the final readout has been corrected for.

reset number	0	1	2
from $(\|g\rangle\langle g\| + \|e\rangle\langle e\|)/2$	50 %	3.2 %	0.8 %
from thermalized state	2.4 %	0.4 %	0.2 %

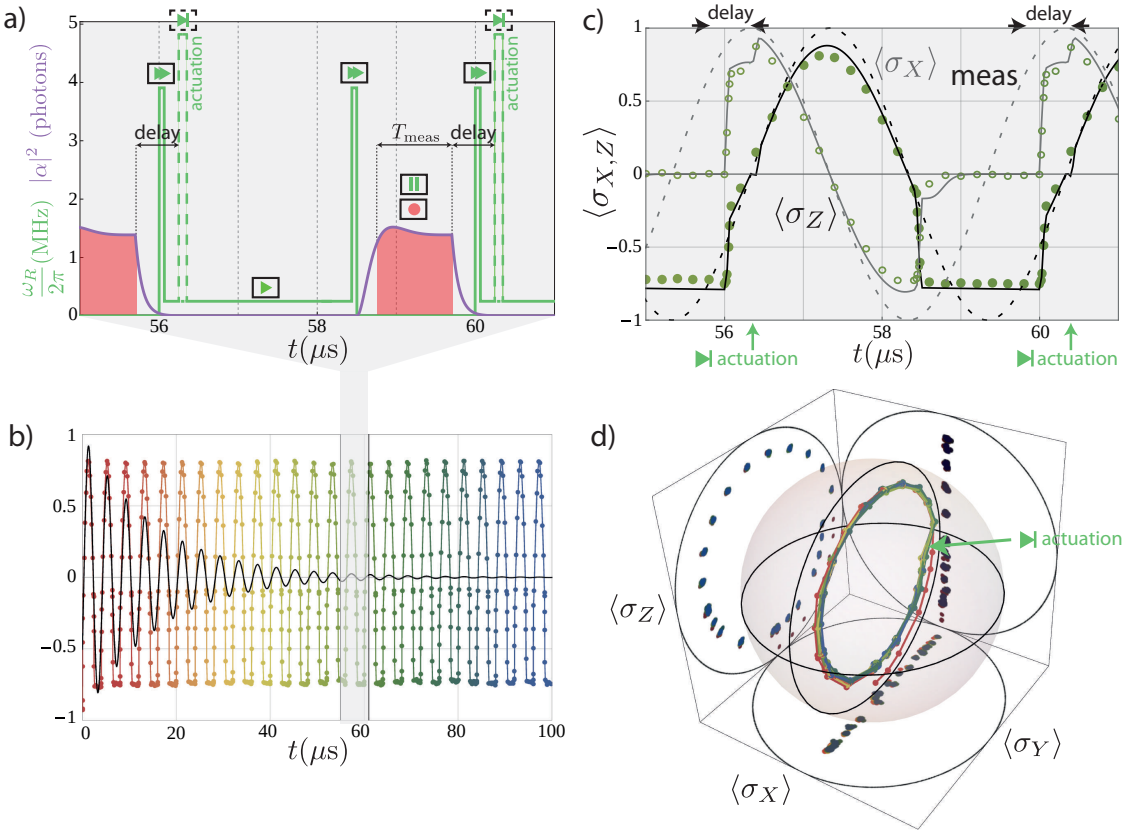

Figure 43: a) Pulse sequence for stabilizing Rabi oscillations. For a typical period of 4 μs, the lines represents the drive amplitude (green) and expected occupation of the cavity (purple). The complex amplitude a of the measurement field is recorded only during the steady part of the occupation (red area). When $\mathrm{Im}[a_{\mathrm{readout}}] > 0$, a fast π pulse is applied after a total delay of 480 ns (actuation). These steps are illustrated with usual symbols for media player. b) Black line: decaying Rabi oscillation around σ_Y with frequency $\omega_R = 2\pi \times 250$ kHz and measured decay time $T_R = 15.5$ μs. Dots on line: persistent Rabi oscillations measured using the pulse sequence described in (a). c) Same measurement as in (b) shown on a smaller span for $\langle\sigma_Z\rangle$ (dots) and $\langle\sigma_X\rangle$ (circles). The targeted Rabi trajectory is shown as two dashed lines, black for $\langle\sigma_Z\rangle$ and gray for $\langle\sigma_X\rangle$. Predictions using Bloch equations are represented as solid lines with the same color convention. d) Bloch sphere representation of the full tomography of the qubit for persistent Rabi oscillations during 100 μs. Time is encoded in color as in (b).

of the qubit state and analog feedback. Here, we make use of the fact that a qubit undergoing such oscillations passes periodically by the state $|g\rangle$, which we know how to stabilize from the previous section. The new feedback protocol is a simple adaptation of the loop presented in that section and is inspired by the stroboscopic measurement scheme proposed in [167].

A constant microwave signal at ω_q induces a Rabi oscillation of the qubit around σ_Y at a frequency chosen to be $\omega_R/2\pi = 250$ kHz. Without feedback, these oscillations decay on a timescale $T_R = 15.5$ μs (Fig. 43b). In order to make the Rabi oscillations persistent, a measurement is performed each time the qubit is supposed to be in state $|g\rangle$ (Fig. 43a). The FPGA controller then sends a fast correcting π-pulse (actuation) each time the measurement reveals that the qubit is in the excited state. In order to optimize the fidelity of the feedback controlled trajectory to the targeted Rabi oscillation, the precession angle which is left idle during the measurement – Zeno effect freezing the trajectory anyway [168] – is briefly accelerated before and after the measurement to compensate exactly for that pause (see Fig. 43a). Moreover, since the qubit remains in the (y, z) plane during the whole experiment, the correction pulse performs a bit flip, whatever its state. Thus, it is not needed to wait for the FPGA board to finish its computation before driving again the qubit. However, to avoid extra dephasing, we leave the qubit in the ground state as long as the measurement field has not leaked out of the cavity. Quantitatively, we impose that the measurement induced dephasing rate $\Gamma_d(t)$ associated with this field be of the same order as the qubit decoherence rate γ_2. The criterion we use is $\Gamma_d < 5\ \gamma_2$, which corresponds to a ringdown time of ~ 300 ns. $\Gamma_d(t)$ is estimated as in Sec. 2.2.4 using Eq. (85)

$$\Gamma_d(t) = \chi \mathrm{Im}[\alpha_g(t)\alpha_e^*(t)], \tag{207}$$

where $\alpha_g(t)$ and $\alpha_e(t)$ are computed numerically.

As can be seen in Fig. 43b, the Rabi oscillations are indeed stabilized permanently with this protocol. Their average fidelity to the targeted Rabi oscillation is $F = 85\%$ and their average purity 80%. The discrete correction events lead to visible discontinuities in the trajectories restoring the purity lost during the last Rabi period due to decoherence (see Fig. 43c). Although it is possible to perform this stabilization using analog feedback on a weak, continuous measurement [48], we demonstrate here that, for limited detection efficiency, discrete feedback events are more efficient [169]. This is simply explained by the added flexibility to vary the measurement strength in time so as to avoid extra dephasing when the qubit is not in $|g\rangle$ or $|e\rangle$.

We can quantitatively reproduce the measured average trajectory (see Fig. 43c) by simulating the evolution of the density matrix ρ[5] using Bloch's equations. These equations are equivalent to the Lindblad form of the master equation (27) derived in

5 Occupation of the higher energy levels of the transmon and thermal excitations are here neglected

Sec. 2.1.3.1 [67]. Letting $\omega_R(t)$ the Rabi pulsation that varies during the various steps of the feedback loop, they read

$$\frac{d}{dt}\begin{pmatrix}\rho_{ee}\\ \rho_{ge}\end{pmatrix} = \begin{pmatrix}-\Gamma_1 & \omega_R(t)\\ -\omega_R(t) & -\Gamma_2-\Gamma_d(t)\end{pmatrix}\cdot\begin{pmatrix}\rho_{ee}\\ \rho_{ge}\end{pmatrix} + \begin{pmatrix}0\\ \omega_R(t)/2\end{pmatrix} \tag{208}$$

We can divide a period of the Rabi oscillations of duration $T_{\text{osc}} = 4000$ ns in 4 steps (see Fig. 43a) according to the values of the Rabi pulsation and of the field amplitude in the cavity.

- step A : measurement and pause from 0 to $T_{\text{p}} = 1500$ ns
  During this step, the qubit is left idle ($\omega_R = 0$). When turning on the readout tone, coherences collapse nearly instantaneously. After 240 ns, the cavity field amplitude has reached its steady state and the FPGA board starts its acquisition. For the simulation, at half the acquisition time by the FPGA board (middle of the red time interval in Fig. 43a), we record the population $\rho_{ee,\text{mid}}$ in $|e\rangle$ and afterwards simulate separately two trajectories with $\rho_{ee,\text{mid}} = 0$ or $\rho_{ee,\text{mid}} = 1$ according to the measurement outcome. To get the average trajectory plotted on Fig. 43c, we add up those with the actual weights $\rho_{ee,\text{mid}}$ and $1-\rho_{ee,\text{mid}}$.

- step B: fast forward from $T_{\text{p}} = 1500$ ns to $T_{\text{p}} + T_{\text{ff}} = 1564$ ns.
  In order to compensate for half the precession lost during the pause, the drive is performed beyond the targeted Rabi frequency during a short period of time, hence $\omega_R = \frac{2\pi}{T_{\text{ff}}}\frac{T_{\text{p}}}{2T_{\text{osc}}}$ (the other half is compensated in step D). The field amplitude remaining in the cavity after step A decreases exponentially from a mean photon number 0.05 ($\Gamma_d \simeq 5\,\Gamma_2$) to 0.025 ($\Gamma_d \simeq 2.5\,\Gamma_2$). In fact, the JPC is turned off after the measurement and there may be a change in the effective cavity exit rate κ_{tot}[6]. A slight modification of these parameters lead to a better fit to the measured trajectory.

- step C : nominal Rabi drive from $T_{\text{p}} + T_{\text{ff}} = 1564$ ns to $T_{\text{osc}} - T_{\text{ff}} = 3936$ ns.
  Rabi oscillation is here nominally driven at the target frequency $\omega_R = \frac{2\pi}{T_{\text{osc}}}$. Average photon number in the cavity keeps decreasing down to 0. At $t = 1850$ ns, a correcting π-pulse occurs in case the measurement outcome is $|e\rangle$ in step A. In the simulation, the Rabi pulsation is briefly increased for the corresponding trajectory and the two parallel trajectories are averaged into a single one with weights $\rho_{ee,\text{mid}}$ and $1-\rho_{ee,\text{mid}}$.

- step D : fast forward from $T_{\text{osc}} - T_{\text{ff}} = 3936$ ns to $T_{\text{osc}} = 4000$ ns.
  Same purpose as step B with $\omega_R == \frac{2\pi}{T_{\text{ff}}}\frac{T_{\text{p}}}{2T_{\text{osc}}}$. There is no readout field inside the cavity at this step.

For any initial value of ρ, the simulated trajectory converges in about 3 or 4 periods toward the steady state represented in Fig. 43c.

6 Due to finite isolation, the cavity mode hybridizes weakly with the amplified mode of the JPC with which it is in resonance.

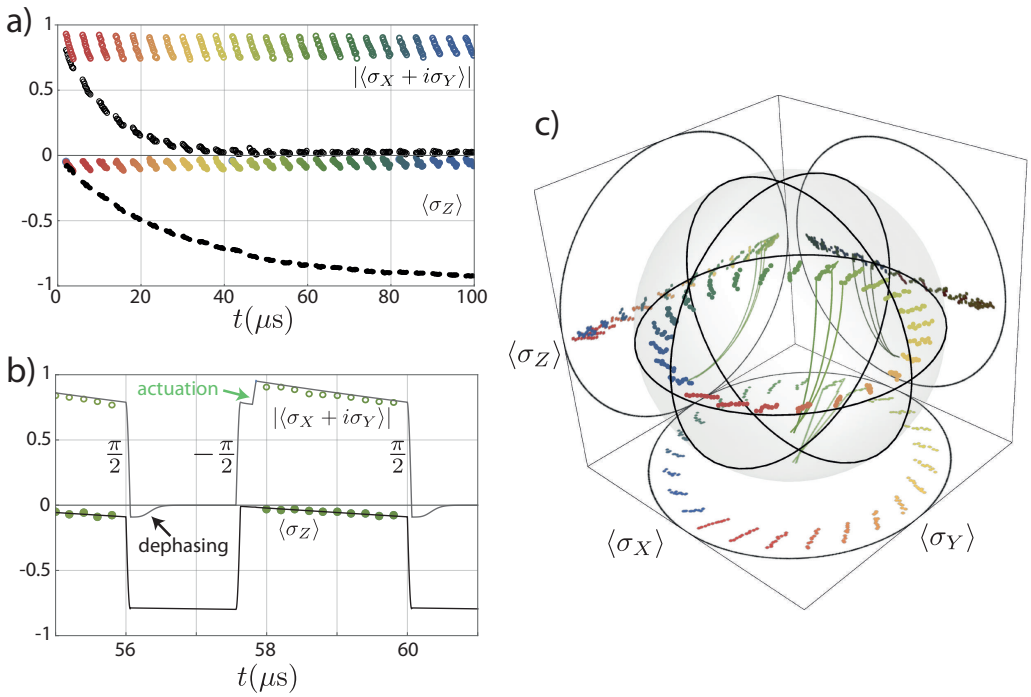

Figure 44: a) Evolution of $\langle\sigma_Z\rangle$ (dots) and of the coherence $|\langle\sigma_X + i\sigma_Y\rangle|$ (circles) when the qubit is prepared in state $(|g\rangle + |e\rangle)/\sqrt{2}$ at time 0. State tomography is only performed outside of the sensing and actuation periods. In color: feedback on. In black: without feedback. b) Same evolution shown on a shorter span. Lines: simulation of $\langle\sigma_Z\rangle$ (black) and $|\langle\sigma_X + i\sigma_Y\rangle|$ (gray) using Bloch equations. Due to relaxation, the qubit does not stay on the equator between sensing periods, so that coherences remain when rotating it by $\pi/2$ toward the pole. These coherences are quickly suppressed by the measurement induced dephasing. c) Same evolution represented in the Bloch sphere with a Ramsey frequency $\omega_{Ry}/2\pi = 10$ kHz. The color encodes the time as in (a). The simulated trajectory is only represented as a line during sensing and actuation periods for clarity.

We now show that this feedback protocol can also be used to stabilize a state of the qubit that does not pass by $|g\rangle$. As an example, the target state is now $(|g\rangle + |e\rangle)/\sqrt{2}$. The feedback loop is simply adapted from the one described in Sec. 5.1.2. Every 4 μs, a fast $\pi/2$ pulse is applied to rotate the qubit around σ_Y before measuring its state and sending it back to the equator with a $-\pi/2$ pulse. This operation maps the x-axis on the z-axis, so that we effectively perform a measurement of the σ_X operator. In order to maximize average fidelity to $(|g\rangle + |e\rangle)/\sqrt{2}$, the qubit is rotated back to the equator before the correction pulse is applied by the FPGA board.

Without measurement based feedback, the Bloch vector of the qubit decays exponentially both in Z with rate $1/T_1$ and in the X, Y plane with rate $1/T_2$ (Fig. 44a). With the feedback on, it follows the same evolution in between sensing periods, but the lost purity is recovered when the correction pulse takes place. From these simulations,the

average purity $\mathrm{Tr}(\rho^2)$ of the density matrix ρ is calculated to be 85%, the time averaged fidelity $F = \overline{\langle\psi_{\mathrm{targ}}|\rho(t)|\psi_{\mathrm{targ}}\rangle}$ to the target trajectory $|\psi_{\mathrm{targ}}\rangle = (|g\rangle + |e\rangle)/\sqrt{2}$ is $F = 76\%$ and the average information quantity $1 - \mathrm{Tr}(-\rho\log_2\rho) = 0.60$ bit.

We simulate the evolution of the qubit state as in Sec. 5.1.3. The only difference is the value of $\omega_R(t)$ which is 0 except during the $\pi/2$ rotations. Simulated average trajectory on a feedback period is represented on Fig. 44b and fits quantitatively the data.
In order to connect to the usual representation of Ramsey fringes at a given frequency ω_{Ry}, we can rotate linearly in time the measurement axis so that $\langle\sigma_X\rangle$ maps onto $\langle\cos(\omega_{Ry}t)\sigma_X + \sin(\omega_{Ry}t)\sigma_Y\rangle$ and $\langle\sigma_Y\rangle$ onto $\langle-\sin(\omega_{Ry}t)\sigma_X + \cos(\omega_{Ry}t)\sigma_Y\rangle$. The Bloch sphere representation of the corresponding tomography is represented on Fig. 44c.

In this experiment, we showed the versatility of stroboscopic measurement based feedback to stabilize any state or trajectory of a single qubit. Efficient QND measurement associated with fast electronics allow to detect and correct for errors on a timescale much faster than qubit lifetime. Even though for a single qubit, this feedback loop can essentially be understood as a fast reset and preparation of the target state, if combined with parity measurement in a multi qubit architecture, it could pave the way for full error correction of a logical qubit [18].

5.2 CONTINUOUS ANALOG FEEDBACK USING THE FLUORESCENCE SIGNAL

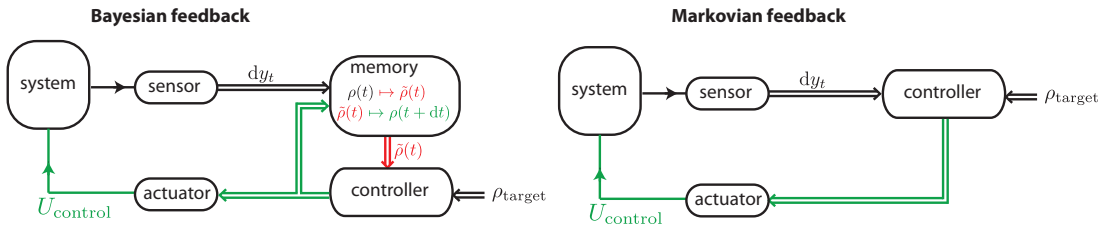

Figure 45: Bayesian versus Markovian feedback. In Bayesian feedback, the measured signal from the sensor at time t is used to update the density matrix $\rho(t)$. The controller then compares the new matrix $\tilde{\rho}(t)$ and the target state ρ_{target}, and then use the actuator to steer the system towards this state. The correction applied to the system needs to be taken into account to compute the new density matrix $\rho(t + dt)$. In Markovian feedback, the control signal is sent to a static controller that processes it and reacts on the system independently of its history. Double line arrows represent classical communication channels.

In Sec. 3.4, we showed that we were able to detect with high-efficiency ($\eta = 25\%$) the fluorescence signal of our qubit by heterodyne measurement of the field leaking out of the cavity at ω_q. This measurement corresponds to a weak continuous measurement

of the σ_- operator and we have shown that the two output signals from the heterodyne detection read at time t[7]

$$\begin{cases} \mathrm{d}I_t &= \sqrt{\frac{\eta\gamma_1}{2}}\langle\sigma_x\rangle\mathrm{d}t + \mathrm{d}W_{t,I} \\ \mathrm{d}Q_t &= \sqrt{\frac{\eta\gamma_1}{2}}\langle\sigma_y\rangle\mathrm{d}t + \mathrm{d}W_{t,Q} \end{cases}, \tag{209}$$

where $W_{t,I}$ and $W_{t,Q}$ are two independent Wiener processes. We want to use this signal and feed it back to the system in order to change its dissipation. The most general control hamiltonian for our qubit is

$$H_{\mathrm{cont}} = \hbar\Big(u(t)\sigma_X + v(t)\sigma_Y + w(t)\sigma_Z\Big), \tag{210}$$

where u, v and w are functions of the measurement records from 0 to t. We now limit ourselves to *Markovian feedback* [24], in which these controls only depend on the values of $\mathrm{d}I_t$ and $\mathrm{d}Q_t$ at time t. Less general than *Bayesian feedback* in which the state of the system is estimated to react optimally given a cost function for the controls and a target state (see Fig. 45), it still yields similar results for a single qubit [170] and is much simpler to implement experimentally. Assuming a linear dependence of the controls on the output signals, we write

$$\begin{pmatrix} u(t) \\ v(t) \\ w(t) \end{pmatrix} = \breve{\mathrm{G}} \times \begin{pmatrix} \frac{\mathrm{d}I_t}{\mathrm{d}t} \\ \frac{\mathrm{d}Q_t}{\mathrm{d}t} \end{pmatrix} + \begin{pmatrix} \overline{u} \\ \overline{v} \\ \overline{w} \end{pmatrix}, \tag{211}$$

where $\breve{\mathrm{G}}$ is a constant 3×2 constant gain matrix. We now derive an effective master equation for the qubit when turning on this feedback.

5.2.1 *Effective master equation in presence of feedback*

5.2.1.1 *SISO Markovian feedback with diffusive measurements*

For simplicity, we first consider the case of a Single Input Single Output (SISO) Markovian feedback following [23, 171, 172]. We thus neglect the pure dephasing of the qubit so that the only decoherence channel is a relaxation channel monitored by homodyne detection with efficiency η. In the absence of feedback, the SME (128) simplifies into

$$\rho(t+\mathrm{d}t) = -\frac{i}{\hbar}\mathrm{d}t[H,\rho(t)] + \sqrt{\gamma_1}\mathrm{d}t\mathcal{D}[\sigma_-]\rho(t) + 2\sqrt{\eta\gamma_1}\mathrm{d}W_t\mathcal{M}[\sigma_-]\rho(t), \tag{212}$$

where damping and measurement super operators $\mathcal{D}$ and $\mathcal{M}$ defined as in Sec.2.1.3.1 and Sec. 3.2.2 by

$$\begin{cases} \mathcal{D}[L]\rho &= L\rho L^\dagger - \frac{1}{2}L^\dagger L\rho - \frac{1}{2}\rho L^\dagger L \\ \mathcal{M}[c]\rho &= \frac{1}{2}\Big((c-\langle c\rangle)\rho + \rho(c^\dagger - \langle c^\dagger\rangle)\Big) \end{cases}. \tag{213}$$

7 These signals are filtered by the finite amplification bandwidth δf_{JPC} (see Eq. (147)), but it will not affect the feedback performances as long as this bandwidth is much larger than the characteristic evolution rate of the system. In the present case, this condition reads $\delta f_{\mathrm{JPC}} \gg \gamma_1$.

The output signal y_t verifies

$$y_t \mathrm{d}t = \sqrt{\eta\gamma_1}\langle\sigma_x\rangle \mathrm{d}t + \mathrm{d}W_t. \tag{214}$$

The controller condition (211) simplifies into

$$u(t) = g \times y_t + \overline{u}, \tag{215}$$

where g is a constant scalar gain and $\overline{u}$ a constant as defined in Eqs. (210, 211). We call σ_1 the control operator (typically σ_X, σ_Y or σ_Z for rotations around the axes of the Bloch sphere). We group the constant drive with the hamiltonian H in absence of feedback so that the full time-dependent hamiltonian reads

$$H_{\mathrm{cont}} + H = \hbar(g y_t \sigma_1 + \overline{u}\sigma_1) + H = H_1(t) + H_0, \tag{216}$$

Due to the singular nature of W_t which is not a bounded time function, we cannot simply take $H \mapsto H_1(t) + H_0$ in Eq. (212) to get the closed-loop evolution. In order to preserve causality, we need to first apply the open-loop evolution from t to $t + \mathrm{d}t$ and then use the measurement record y_t to apply the unitary $e^{-\frac{i}{\hbar}H_1(t)}$ on the system. The closed-loop evolution of ρ thus reads

$$\begin{aligned}\rho(t+\mathrm{d}t) = \\ e^{-\frac{i}{\hbar}H_1(t)\mathrm{d}t}\Big\{ -\tfrac{i}{\hbar}\mathrm{d}t[H_0,\rho] + \sqrt{\gamma_1}\mathrm{d}t\mathcal{D}[\sigma_-]\rho + 2\sqrt{\eta\gamma_1}\mathrm{d}W_t\mathcal{M}[\sigma_-]\rho(t)\Big\}e^{+\frac{i}{\hbar}H_1(t)\mathrm{d}t}.\end{aligned} \tag{217}$$

We now simplify this formula using Itô rules, which state that $\overline{\mathrm{d}W_t} = 0$ and $\mathrm{d}W_t^2 = 1$. Via the Baker-Campbell-Hausdorff formula

$$e^A B e^{-A} = B + [A,B] + [A,[A,B]]/2 + O(||A||^3) \tag{218}$$

with

$$\left\{\begin{array}{rcl} A &=& -ig\sigma_1(\sqrt{\eta\gamma_1}\langle\sigma_x\rangle\mathrm{d}t + \mathrm{d}W_t) \\ B &=& -\frac{i}{\hbar}\mathrm{d}t[H_0,\rho] + \sqrt{\gamma_1}\mathrm{d}t\mathcal{D}[\sigma_-]\rho + 2\sqrt{\eta\gamma_1}\mathrm{d}W_t\mathcal{M}[\sigma_-]\rho \end{array}\right. \tag{219}$$

and neglecting terms of order $O(\mathrm{d}t^{3/2})$ we get the effective master equation

$$\begin{array}{rcl} \rho(t+\mathrm{d}t) &=& -i\mathrm{d}t[\frac{H_0}{\hbar} + \frac{g\sqrt{\eta\gamma_1}}{2}(\sigma_-\sigma_1 + \sigma_1\sigma_+), \rho(t)] \\ && +\mathrm{d}t\mathcal{D}[L_1]\rho(t) + 2\sqrt{\eta}\mathrm{d}W_t\mathcal{M}[L_1]\rho(t) \\ && +\mathrm{d}t\mathcal{D}[L_2]\rho(t) + 2\sqrt{1-\eta}\mathrm{d}W_t\mathcal{M}[L_2]\rho(t), \end{array} \tag{220}$$

with

$$\left\{\begin{array}{rcl} L_1 &=& \sqrt{\gamma_1}\sigma_- - ig\sqrt{\eta}\sigma_1 \\ L_2 &=& -i\sqrt{1-\eta}g\sigma_1 \end{array}\right. . \tag{221}$$

Note that a constant drift $H_{\mathrm{drift}} = \frac{g\sqrt{\eta\gamma_1}}{2}(\sigma_-\sigma_1 + \sigma_1\sigma_+)$ has appeared in the effective hamiltonian. It can be compensated for, or adjusted to a given value, by changing H,

which means adding more constant drives than $\overline{u}\sigma_1$. Such constant drives are necessary to stabilize an arbitrary state of the Bloch sphere (see Eq. (225)).

Otherwise, for efficiency $\eta = 1$, the effect of the feedback is thus to modify the damping operator $\sqrt{\gamma_1}\sigma_- \to \sqrt{\gamma_1}\sigma_- - ig\sigma_1$. Note that the choice of $g\sigma_1$ modifies at will the imaginary part of the damping operator. This has the same effect as dissipation engineering for the qubit (see Sec. 6.2.2). In general, the new stable state under the SME (220) is not $|g\rangle$. In the next section, we show that we can choose arbitrarily the stabilized state in the MIMO case.
However, the real part of the jump operator cannot be modified. In practice, this implies that with the homodyne detection considered here, a state on the x-axis of the Bloch sphere cannot be stabilized with this feedback loop[8]. Intuitively, information is extracted only along $\sigma_X = \mathrm{Re}[\sigma_-]$, so that when some spurious noise pulls the state away from the target state, say $|+x\rangle$, the fluorescence detection does not yield any information about the angle of the displaced state around to the x-axis. Then, the controller does not get the necessary information to restore the target state with a coherent drive.

Let us comment on two particular cases.

- $\sigma_1 = \sigma_Y$ and $g = -\sqrt{\gamma_1}$. The new damping operator is then $L_1 = \sqrt{\gamma_1}\sigma_X$ so that relaxation transforms into a weak non destructive measurement of the σ_X operator with rate $2\gamma_1$. As stated above, even though the measurement collapses the state on $|\pm x\rangle$ on a time scale larger than $1/2\gamma_1$, spurious noise can trigger jumps between $|+x\rangle$ and $|-x\rangle$. Neither state is stabilized.
- $\sigma_1 = \sigma_Y$ and $g = -2\sqrt{\gamma_1}$ so that $L_1 = \sqrt{\gamma_1}\sigma_+$. Dissipation now causes the qubit to relax toward the $|e\rangle$ state.

For finite efficiency, a new damping operator $L_2 = -i\sqrt{1-\eta}g\sigma_1$ appears, limiting the fidelity of the stabilized state to the target state.

In this section, we have described a continuous, markovian, feedback loop in the SISO (single-input, single-output) regime. In practice, it describes a continuous feedback based on a homodyne detection. In the next section, we generalize the results to MIMO, which can model feedback using heterodyne detection.

5.2.1.2 *MIMO Markovian feedback and arbitrary state stabilization*

The derivation of the closed-loop master equation for Multi Intput Multi Output (MIMO) systems is derived by Chia and Wiseman in [46]. For concreteness, we now consider the case of the heterodyne detection, with efficiency η, of the fluorescence field of the qubit as in Sec. 3.4. The 2 outputs correspond to the 2 measurement records $\frac{\mathrm{d}I}{\mathrm{d}t}$ and $\frac{\mathrm{d}Q}{\mathrm{d}t}$, and we consider 3 inputs which are rotations around the x, y and z axes as

8 However, $|\pm y\rangle$ can be stabilized. Thus, here, this is not a limitation in practice since $|+x\rangle$ and $|+y\rangle$ are equivalent. It however limits the feedback protocol based on the dispersive detection presented in Sec. 6.2.2.

in Eq. (210). The form of the effective master equation in presence of feedback can be understood as a generalization of the SISO case.

The drift in the effective hamiltonian now reads[9]

$$H_{\text{drift}} = \frac{\hbar}{2}\sqrt{\frac{\eta\gamma_1}{2}} \sum_{\alpha\in\{X,Y,Z\}} G_{\alpha,I}(\sigma_\alpha\sigma_- + \sigma_+\sigma_\alpha) + G_{\alpha,Q}(i\sigma_\alpha\sigma_- - i\sigma_+\sigma_\alpha) \tag{222}$$

where G is the gain matrix defined in Eq. (211), and the two damping operators $\sqrt{\frac{\gamma_1}{2}}\sigma_-$ and $\sqrt{\frac{\gamma_1}{2}}i\sigma_-$ lead to four effective damping operators

$$\begin{cases} L_{I,1} &= \sqrt{\frac{\gamma_1}{2}}\sigma_- - i\sqrt{\eta} \sum\limits_{\alpha\in\{X,Y,Z\}} G_{\alpha,I}\sigma_\alpha \\ L_{Q,1} &= i\sqrt{\frac{\gamma_1}{2}}\sigma_- - i\sqrt{\eta} \sum\limits_{\alpha\in\{X,Y,Z\}} G_{\alpha,Q}\sigma_\alpha \\ L_{I,2} &= -i\sqrt{1-\eta} \sum\limits_{\alpha\in\{X,Y,Z\}} G_{\alpha,I}\sigma_\alpha \\ L_{Q,2} &= -i\sqrt{1-\eta} \sum\limits_{\alpha\in\{X,Y,Z\}} G_{\alpha,Q}\sigma_\alpha \end{cases} . \tag{223}$$

With these notations, the master equation becomes

$$\begin{aligned} \rho(t+\mathrm{d}t) \;=\; & -\tfrac{i}{\hbar}\mathrm{d}t[H_0 + H_{\text{drift}}, \rho(t)] \\ & +\mathrm{d}t\mathcal{D}[L_{I,1}]\rho(t) + \mathrm{d}t\mathcal{D}[L_{I,2}]\rho(t) \\ & +\mathrm{d}t\mathcal{D}[L_{Q,1}]\rho(t) + \mathrm{d}t\mathcal{D}[L_{Q,2}]\rho(t) \\ & +\mathrm{d}t\mathcal{D}[\sqrt{\tfrac{\gamma_\phi}{2}}\sigma_z]\rho(t) \end{aligned} \tag{224}$$

where we have dropped the actuation terms, which will not be used in the experiment since we record only average traces, and added the dephasing term.

We now want to stabilize the pure state $\rho_{\text{target}} = \frac{1}{2}(\mathbb{1} + \cos\theta\sigma_y + \sin\theta\sigma_z)$ (see Fig. 47c). Let us consider the control matrix

$$\begin{pmatrix} u(t) \\ v(t) \\ w(t) \end{pmatrix} = \begin{pmatrix} 0 & \sqrt{\frac{\gamma_1}{8\eta}}(1+\sin\theta) \\ -\sqrt{\frac{\gamma_1}{8\eta}}(1+\sin\theta) & 0 \\ \sqrt{\frac{\gamma_1}{8\eta}}\cos\theta & 0 \end{pmatrix} \times \begin{pmatrix} \frac{\mathrm{d}I_t}{\mathrm{d}t} \\ \frac{\mathrm{d}Q_t}{\mathrm{d}t} \end{pmatrix} + \begin{pmatrix} \frac{\gamma_1}{8}(1-\sin\theta/\eta)\cos\theta \\ 0 \\ 0 \end{pmatrix} . \tag{225}$$

With this choice we find that

$$\begin{cases} H_{\text{drift}} &= -\hbar\frac{\gamma_1\cos\theta}{8}\,\sigma_X \\ L_{I,1} &= \sqrt{\frac{\gamma_1}{8}}(\sigma_X + i\sin\theta\,\sigma_Y - i\cos\theta\,\sigma_Z) \\ L_{Q,1} &= -i\sqrt{\frac{\gamma_1}{8}}(\sin\theta\,\sigma_X + i\sigma_Y) \end{cases} . \tag{226}$$

If $\eta = 1$, $L_{I,2} = L_{Q,2} = 0$ and we can then check that, when neglecting pure dephasing, ρ_{target} is indeed a stable state under the master equation (224). Note that H_0 does not

9 for compactness, we call G_α the rows of G, with the correspondence $1 \leftrightarrow X$, $2 \leftrightarrow Y$ and $3 \leftrightarrow Z$.

compensate exactly for H_{drift}. This constant drive, detuned by $w(t)$ from the qubit resonance frequency, is necessary to stabilize a state different from $|e\rangle$.

For $\eta < 1$, $L_{I,2}$ and $L_{Q,2}$ limit the preparation fidelity of ρ_{target}. Pure dephasing and finite feedback delay also limit this fidelity. All these effects will be taken into account in the simulations which results are shown in the following section. In that case, the markovian controller defined in Eq. (225) is not optimized to get as high a preparation fidelity to ρ_{target} as possible.

5.2.2 *Experimental implementation*

The qubit used for this experiment is the same as in Sec. 3.4.2 (Qubit 4 in Tab. 3). However, this experiment corresponds to a different cool down of the sample so that the qubit parameters are slightly different. The characteristic times of the qubit were measured to be $T_1 = 5.23$ μs, $T_2 = 6.83$ μs, and the cavity pull $\chi = 9$ MHz. Moreover, the parametric amplifier (JPC) at the head of the detection setup was changed so that the new amplifier was optimized for a detection at the new qubit frequency $\omega_q/2\pi = 6.26$ GHz, and the connectors between the cavity and the amplifier were changed. As a result, the detection efficiency was improved to $\eta = 30\%$.

5.2.2.1 *Stabilization of* $|e\rangle$

As a first step, we implement the feedback loop with $\theta = \frac{\pi}{2}$ so that $|e\rangle$ is the target state. The control w is not used and the control matrix boils down to

$$\begin{pmatrix} u(t) \\ v(t) \end{pmatrix} = \sqrt{\frac{\gamma_1}{2\eta}} \begin{pmatrix} 0 & 1 \\ -1 & 0 \end{pmatrix} \times \begin{pmatrix} \frac{\mathrm{d}I_t}{\mathrm{d}t} \\ \frac{\mathrm{d}Q_t}{\mathrm{d}t} \end{pmatrix}. \tag{227}$$

The form of the off-diagonal matrix can be qualitatively understood by acknowledging that the value of $\frac{\mathrm{d}I_t}{\mathrm{d}t}$ gives information about the x-coordinate of the qubit in the Bloch sphere. This information can then be used to send the qubit toward $|e\rangle$ by applying a rotation with the appropriate sign around σ_Y.

A rotation of the qubit around σ_Y corresponding to the v control is performed by applying a tone at ω_q with phase[10] $\phi = 0$ through the input port of the cavity (see Eq. (130)). Rotations around σ_X are performed by applying a tone with phase $\phi = \frac{\pi}{2}$. Since in the laboratory frame, the fluorescence signal reads $\frac{\mathrm{d}I_t}{\mathrm{d}t}\cos(\omega_q t) + \frac{\mathrm{d}Q_t}{\mathrm{d}t}\sin(\omega_q t)$, the feedback loop can simply be implemented by shifting its phase by $\frac{\pi}{2}$ and re directing it toward the input port. It also needs to be amplified by an *a priori* unknown factor accounting for the target gain of the loop $\sqrt{\frac{\gamma_1}{2\eta}}$, the filtering by the cavity and the losses in the lines. However, it can be calibrated with the following steps.

- In open loop, the qubit is driven resonantly and the average fluorescence signal is recorded. The amplitude of the oscillations when starting from $\rho = |g\rangle\langle g|$ can

10 In the present experiment, the phase reference for the qubit is set by the source used to apply the $\pi/2$ pulses of the final tomography used to characterize the stabilized state.

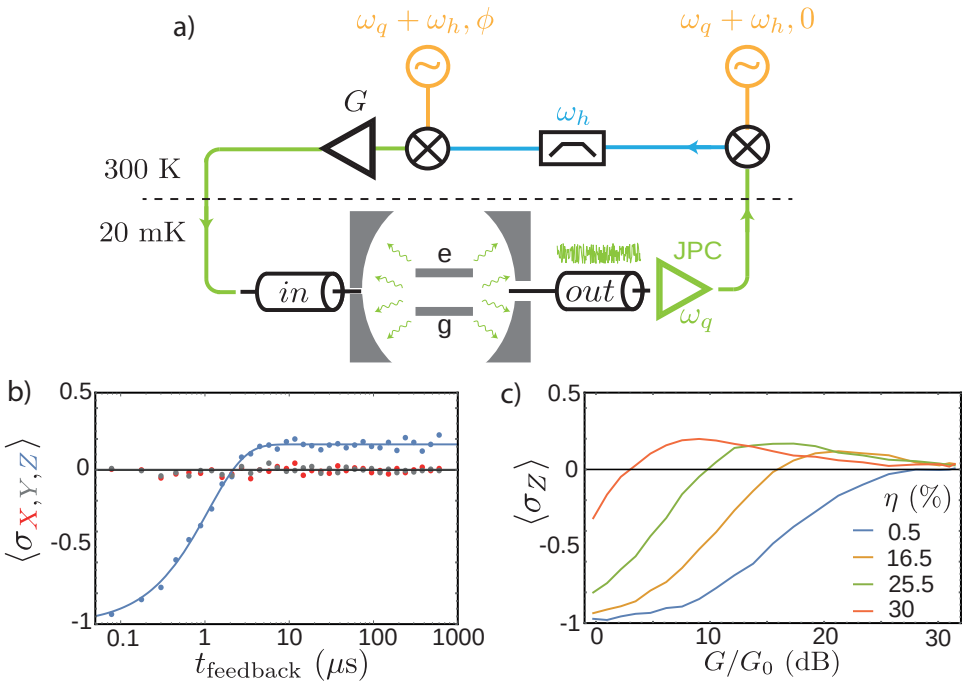

Figure 46: a) Simplified schematic of the experimental setup. The fluorescence field is collected on the output line and amplified by the JPC at 20 mK. After further amplification, the signal is down-converted to $\omega_h/2\pi = 40$ MHz at room temperature to be finely filtered (bandpass $25 - 50$ MHz) before being up converted back to ω_q with a different LO, which phase is shifted by ϕ from the one used for down-conversion. After amplification (tunable gain G), the signal is fed back to the qubit via the input line. Full schematic of the wiring can be found in Sec. A.2.2. b) Dots: measured tomography of the qubit after a time t_{feedback} of MBF designed to prepare $|e\rangle$. The Bloch coordinates are shown as a function of time (on logarithmic scale) starting from thermal equilibrium at $t = 0$. Blue line: exponential fit with characteristic time $T = 1.1$ μs. c) Mean value of σ_Z in the stationary regime when varying the total gain of the loop, scaled by an unknown factor accounting for the losses of the lines. The efficiency of the detection setup is varied by adjusting the gain of the JPC. When turned off ($\eta = 0.5\%$), the occupation of $|e\rangle$ can reach 50% by heating but the population is never inverted. Best performance: $\langle \sigma_Z \rangle = 0.17$ corresponding to $\eta = 28\%$.

be used to calibrate the scale of the detected signal. The signal reads $\overline{\frac{\mathrm{d}I_t}{\mathrm{d}t}} = \sqrt{\frac{\eta\gamma_1}{2}} \sin \Omega_r t \overset{\text{def}}{=} i_1 \sin \Omega_r t$.

- A constant signal with amplitude i_1 is amplified by a gain G and sent through the input line. It induces Rabi oscillations of the qubit that can be detected in the fluorescence or by dispersive measurement.
- The gain G is tuned until the period of these oscillations is $4\pi/\gamma_1$[11]. Note that here, G designates a *gain in amplitude*.

11 In practice, since $T_{\text{Rabi}} = \frac{4\pi}{\gamma_1} > T_1$, no oscillations can be observed. It is easier to tune G in order to get oscillations with period, say $T_{\text{Rabi}}/100$, and then divide G by 100.

In practice, this amplifier is situated at room temperature (see Fig. 46a). To avoid heating the qubit with an important noise power over a large frequency span and in particular at the $|e\rangle \to |f\rangle$ transition frequency, the amplified signal needs to be filtered around ω_q[12]. For fine filtering, the signal is first down-converted to $\omega_h/2\pi = 40$ MHz at room temperature. At this low frequency, the resulting signal can be accurately filtered using commercial low and high pass filters. Note that the bandwidth of this filter, centered on ω_h needs to verify $\delta f_{\text{filter}} \gg \gamma_1$. The signal is then converted back to ω_q. Down-conversion and up-conversion are performed by mixing with 2 different LO, phase-shifted by ϕ. This tunable phase-shift is set to satisfy the closed-loop locking condition of Eq. (227) as $\phi = \frac{\pi}{2} - \omega_q t_{\text{delay}}$, the second term compensating for the electrical delay of loop.

Starting from thermal equilibrium, we turn on the feedback and after a time t_{feedback}, full tomography of the qubit state is performed. The tomography can here be implemented either by the usual dispersive measurement at cavity frequency or by fluorescence measurement. Both methods were demonstrated to be equivalent for all relevant gains. Note that the feedback needs to be turned off during the tomography in both cases in order not to disturb the readout. The results are presented on Fig. 46b. The mean value of σ_Z converges exponentially toward its stationary value $\langle\sigma_Z\rangle_{\text{stat}} = 0.17$. The convergence time $T = 1.1$ μs can be reproduced by performing discrete time quantum Monte Carlo simulations (solid blue line) but $\langle\sigma_Z\rangle_{\text{stat}}$ is underestimated by these simulations for detection efficiency $\eta = 30\%$.

We can vary the detection setup efficiency from close to 0 up to this optimal value by varying the gain of the JPC. Indeed the gain of the setup is determined by

$$\eta^{-1} = \eta_{\text{JPC}}^{-1} + \frac{\eta_H^{-1}}{G_{\text{JPC}}}, \tag{228}$$

where η_H is the efficiency of the following chain of amplifiers. When turning off the JPC ($G_{\text{JPC}} = 1$), we measured $\eta_1 = 0.005$. When increasing G_{JPC}, this value improves until it reaches its maximal value (measured for $G_{\text{JPC}} = 27$ dB). With these two conditions, we can compute the efficiencies for intermediate gains, summarized in Table 2. The feedback performances when varying η are presented on Fig. 46c. When the JPC is off ($\eta \sim 0$), one can excite the qubit by increasing the gain of the loop but the population is never inverted. This situation corresponds to an increased effective temperature of the qubit induced by a large noise power at ω_q. When η is increased, larger values of $\langle\sigma_Z\rangle$ are reached. The optimal loop gain is shifted to larger gains, but $G_{\text{opt}}/G_{\text{JPC}}$ is not exactly constant. This could be due to the fact that the estimation of G_{opt} from the previous section does not take into account the damping operators $L_{I,2}$ and $L_{Q,2} = 0$ appearing at finite efficiency.

Table 2

G_{JPC}	0 (dB)	18 (dB)	23 (dB)	27 (dB)
η	0.5 %	16.5 %	25.5 %	30 %
$P_{\max}(\|e\rangle)$	50 %	56 %	58 %	60 %

5.2.2.2 *Arbitrary state stabilization*

We now set as the target an arbitrary[13] pure state $\rho_{\mathrm{target}} = \frac{1}{2}(\mathbb{1} + \cos\theta\ \sigma_y + \sin\theta\ \sigma_z)$. In the controller of Eq. (225), $w(t)$ is now proportional to $\frac{\mathrm{d}I}{\mathrm{d}t}$. In order to implement this frequency modulation of the qubit, we use the Stark shift induced when driving coherently the cavity mode nearby its resonance frequency [173]. In Eq. (85), we found that the Stark shift and the measurement induced dephasing rate read

$$\begin{cases} \Omega_{\mathrm{Stark}}(t) &= \chi \mathrm{Re}[\alpha_g(t)\alpha_e^*(t)] \\ \Gamma_d(t) &= \chi \mathrm{Im}[\alpha_g(t)\alpha_e^*(t)] \end{cases}, \tag{229}$$

where $\alpha_g(t)$ and $\alpha_e(t)$ are the complex amplitudes of the cavity field when the qubit is in $|g\rangle$ or $|e\rangle$. We can show that, in the stationary regime and for a large detuning δ of the drive field from the cavity frequency (see Fig. 15),

$$\frac{\Gamma_d}{\Omega_{\mathrm{Stark}}} \to 0. \tag{230}$$

Thus, by driving sufficiently far from the cavity frequency, the qubit frequency can be shifted with negligible extra dephasing. Moreover, for $\delta \gg \kappa$ where κ is the cavity linewidth, the stationary regime is reached on a time-scale $1/\delta$. By choosing $\delta \gg \kappa \gg \gamma_1$, the frequency modulator as a sufficient dynamical bandwidth to implement the w control.

In the experiment, we set $\delta = 2\pi \times 100$ MHz. Note that Ω_{Stark} is proportional to the power of the field at $\omega_s = \omega_c + \delta$, so that we cannot simply modulate the amplitude of a continuous wave at ω_s with $\frac{\mathrm{d}I}{\mathrm{d}t}$. The experimental setup is represented on Fig. 47a. To get the proper linear dependence of the wave power on $\frac{\mathrm{d}I}{\mathrm{d}t}$, we up-convert the fluorescence signal to ω_s (in purple) and amplify it with gain G_2 so that it reads[14] $G_2\left(\frac{\mathrm{d}I}{\mathrm{d}t}\cos\omega_s t + \frac{\mathrm{d}Q}{\mathrm{d}t}\sin\omega_s t\right)$, and combine it with a constant tone of large amplitude $A_0\cos\omega_s t$. We then get

$$\Omega_{\mathrm{Stark}}(t) \propto |A_0 + G_2\frac{\mathrm{d}I}{\mathrm{d}t} + iG_2\frac{\mathrm{d}Q}{\mathrm{d}t}|^2 \simeq A_0^2 + 2G_2A_0\frac{\mathrm{d}I}{\mathrm{d}t}. \tag{231}$$

We then tune the gain G_2 in order to get $\Omega_{\mathrm{Stark}}(t) = w(t) + \Omega_0$. The offset $\Omega_0/2\pi = 700$ kHz shifts slightly the qubit frequency.

12 The JPC finite bandwidth acts as a first filter.

13 contrary to the homodyne case, here both $\sigma_- = \sigma_X - i\sigma_Y$ and $i\sigma_- = \sigma_- Y + i\sigma_X$ are detected, so that one can stabilize $|\pm x\rangle$ and $|\pm y\rangle$. In practice, the stabilization of $|\pm x\rangle$ is performed by changing the phase reference of the drive.

14 The phase of the signal is chosen as the reference at ω_s to simplify the expressions.

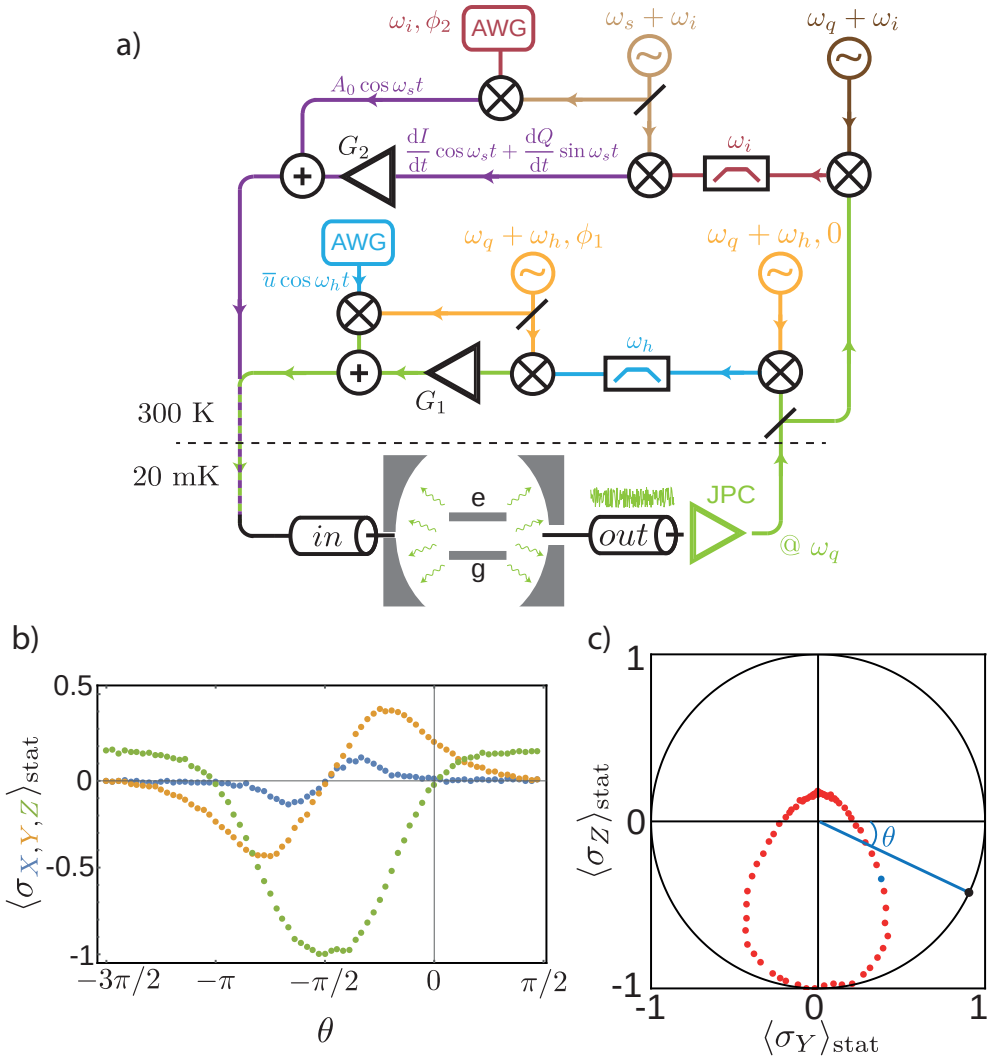

Figure 47: **a**) Schematic of the experiment. After detection and amplification, the fluorescence signal (in green) is split. One part is down-converted to ω_h (in blue), filtered, and up-converted back to ω_q before being fed back to the system (same scheme as on Fig. 46). A constant drive around σ_X, corresponding to a Rabi pulsation $\overline{u}$, is implemented by mixing a sine form at $\omega_h = 2\pi \times 40$ MHz with a L0 at $\omega_q + \omega_h$ (in orange). This wave is used as phase reference in the setup. Another part of the fluorescence signal is down-converted to $\omega_i = 2\pi \times 70$ MHz (in red), filtered and up-converted to $\omega_s = \omega_c + 2\pi \times 100$ MHz (in purple). In order to get a linear dependence of the total power of the field at ω_s sent through the input line, with respect to $\frac{dI}{dt}$, it is combined with a wave of same frequency, large constant amplitude A_0, and phase ϕ_2 adjusted to compensate for electrical delays in the circuit. Full schematic of the wiring can be found in Sec. A.2.2 **b**) Measured tomography of the stabilized states in the stationary regime of the feedback when varying $\theta \in [0, 2\pi]$. **c**) Same states represented in the (y,z) plane. For $\theta = -25°$ (in blue), the stabilized state is highlighted in blue, the target state in black.

Let us detail further these steps and the whole feedback setup as represented on Fig. 47a.

- The conversion from ω_q (in green) to ω_s (in purple) is performed by first down-converting the signal to $\omega_i = 2\pi \times 70$ kHz (in red) for fine filtering, before up converting it to ω_s.

- The large amplitude wave is phase shifted by ϕ_2 with respect to the signal wave. This is done by mixing the same LO that is used for up-conversion of the fluorescence signal with a sine waveform of controlled phase at ω_i. This allows us to adjust the quadrature for $\Omega_{\text{Stark}}(t)$, so as to compensate for the phase $\phi_{\text{delay,w}}$, determined by the electrical delays in the circuit. Indeed, taking these delays into account, the frequency modulation given in Eq. (231) becomes $\Omega_{\text{Stark}}(t) = \sqrt{\frac{\gamma_1}{8\eta}} \cos\theta \Big(\cos\left(\phi_2 + \phi_{\text{delay,w}}\right) \frac{\mathrm{d}I}{\mathrm{d}t} + \sin\left(\phi_2 + \phi_{\text{delay,w}}\right) \frac{\mathrm{d}Q}{\mathrm{d}t} \Big)$, and we set $\phi_2 = -\phi_{\text{delay,w}}$ to stabilize a state of the yz plane of the Bloch sphere, as prescribed by the controller (225).

- Here, the phase reference for this state is set by the microwave at ω_q implementing the constant drive $\overline{u}\hbar\sigma_X$ in the controller (225) (L0 at $\omega_q + \omega_h$ in orange, mixed with a sine waveform at ω_h in blue).

- The controls on σ_X and σ_Y are the same as for the stabilization of $|e\rangle\langle e|$, but for a lower loop gain $\sqrt{\frac{\gamma_1}{8\eta}}(1 + \sin\theta)$, which is adjusted via the gain G_1 of a different amplifier.

On Fig. 47c, we plot the ensemble of states that we have managed to stabilize in the (y, z) plane of the Bloch sphere (red dots), when applying the feedback with optimal gains G_1 and G_2. Note that since the controller is not optimized for the finite detection efficiency, the best fidelity to a given target state $\rho_{\text{target}} = \frac{1}{2}(\mathbb{1} + \cos\theta\ \sigma_y + \sin\theta\ \sigma_z)$ is not given by the corresponding value in of the controller (225). For example, the maximum value for $\langle\sigma_Y\rangle_{\text{stat}}$ is found to be 0.42 and is reached for $\theta \sim \pi/3$. Note, though, that we demonstrated here that it is possible to stabilize a state of the (x, y) plane with markovian feedback on the fluorescence signal, contrary to what was predicted in [170].

In this chapter, we demonstrated the use of quantum feedback to prepare an arbitrary state of a single qubit. It was performed using either a projective measurement result and reacting much faster than the qubit lifetime, or feedbacking continuously a weak measurement signal to the system. These two types of feedback loops are different in nature and use different measurement schemes but are both measurement based feedback. Indeed, in both cases, information is extracted from the system and processed classically to react on the system via drive controls. In the following chapter, we show an example of autonomous feedback, in which the system of interest is coupled coherently to an ancillary quantum system of high dissipation. It allows one to engineer the dissipation of the first system so that it relaxes toward a desired state or subspace. In the example that we give, the feedback is a simple scheme used to cool down a thermally excited qubit before starting an experiment.

6

RESERVOIR ENGINEERING

In the definition given by Seth Lloyd [174], *coherent quantum feedback* consists in bringing a quantum system to a desired state by processing the information leaking out from it via another quantum system, with no classical information channel involved. He thus distinguishes the reset of a qubit realized by a measurement based feedback loop such as the one described in Sec. 5.1.2 from a reset based on quantum gates only. The idea of this coherent reset is to swap the state of the controlled qubit with an ancillary qubit starting in its ground state. Therefore, this feedback loop relies on the use of a cold auxiliary degree of freedom. If one wants to repeat this loop, other degrees of freedom forming a cold bath, need to be used. Thus, this coherent feedback actually relies on dissipation toward a controlled environment.

In Sec. 6.1, we describe such a *reservoir engineering* [34] scheme that can be used to cool down a thermally excited qubit before an experiment. This cooling procedure is applied continuously during a time depending on the cooling rate involved. We give an analysis of this rate depending on the system characteristic timescales. In Sec. 6.2.1, we describe an implementation of a discrete version of this feedback loop, which corresponds to the one originally described by Lloyd [174].

6.1 DOUBLE DRIVE RESET OF POPULATION

6.1.1 *Principle and limits*

Despite careful filtering of the refrigerator microwave lines (see Sec. A.2), it is common with superconducting qubits, and particularly with 3D transmons, that spurious thermal excitations at equilibrium become an issue for the experiments. In 2013, Geerlings *et al.* [44] demonstrated an instrumental reset protocol, the *Double Drive Reset of Population* (DDROP), which can be easily implemented to initialize the qubit in the ground state before an experiment, without resorting to post-selection [165, 166] or more elaborate schemes such as frequency tuning [162, 163, 16, 164] or feedback [42, 81]. In particular, it was used in the experiment reported in [82] and Sec. 3.4.1.
In this section, we analyze the DDROP performances in terms of induced relaxation rates between the transmon energy levels. We show, that, as expected, the DDROP efficiently cools down the transmon, emptying all of its energy levels toward $|g\rangle$. Extracting quantitatively the induced relaxation rate from excited to ground state, we show that, within a certain range of parameters[1], this rate is limited by the Quantum Zeno effect.

1 This range is not explored in operational regime.

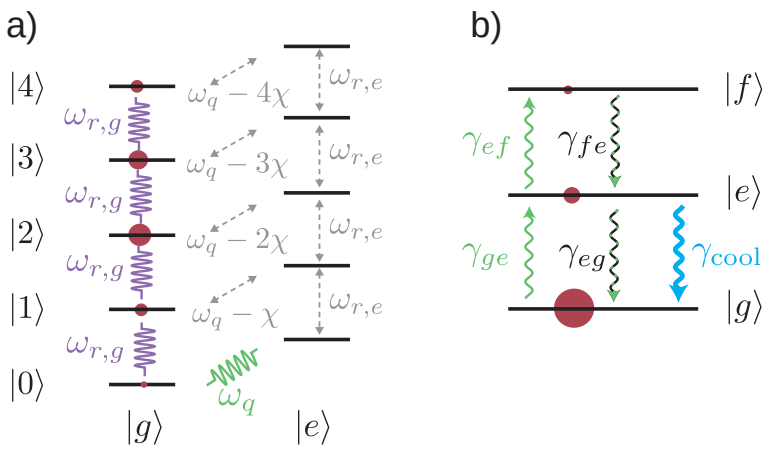

Figure 48: **a**) Principle of the DDROP scheme. On the combined energy level diagram for the cavity and qubit, the drive at $\omega_{r,g}$ (in purple) generates a large coherent state $|\alpha\rangle$ with negligible overlap with $|0\rangle$ if the qubit is in $|g\rangle$ (state occupation represented by red circles). The Rabi drive at ω_q (in green) is then ineffective and $|g,\alpha\rangle$ is stabilized. In case of thermal excitation, the state jumps to the right ladder where the cavity drive is off resonant. It rapidly decays down to $|e,0\rangle$, and the Rabi drive can send it to the left ladder, where it climbs back to $|g,\alpha\rangle$. **b**) 3-level model for the heated transmon. Excitations are induced by the Johnson-Nyquist noise (in green). This noise increases the relaxation rates due to dissipation into cold lines (dotted black and green arrows). The DDROP adds a supplementary relaxation process (in blue) that offsets the equilibrium population toward $|g\rangle$.

The DDROP implementation requires for the qubit to be in the *resolved photon number* regime [45], defined by $\chi \gg \kappa, \gamma_1, \gamma_2$. In that case, one can address the qubit transition conditioned on the number of photons hosted in the cavity mode (see Fig. 53b). The qubit pulsation dressed by n photons reads $\omega_q - n\chi$. In particular, if the cavity is continuously driven so that the generated coherent state $|\alpha\rangle$ verifies $\langle 0|\alpha\rangle \simeq 0$ (negligible overlap with Fock state $|0\rangle$), a microwave tone at ω_q does not excite the qubit. Conversely, if the cavity damping rate κ verifies $\kappa \ll \chi$, one can address the cavity resonance conditioned on the qubit state. For instance, a drive tone at $\omega_{r,g} = \omega_r + \frac{\chi}{2}$ populates the cavity mode only if the qubit is in $|g\rangle$.

When these conditions are met, one can use the DDROP as schematized on Fig. 48a. The principle consists in driving the system continuously and simultaneously with a tone at $\omega_{r,g}$ and a Rabi drive at ω_q. If the qubit is in the ground state $|g\rangle$, the drive at $\omega_{r,g}$ combined with the relaxation rate κ excites the cavity in the steady state $|\alpha\rangle$. On the other hand, if the qubit is excited, both drives are off resonance and relaxation brings the cavity mode towards the vacuum state. When in the vacuum state, the Rabi drive at ω_q tends to equilibrate the populations $|g\rangle \otimes |0\rangle$ and $|e\rangle \otimes |0\rangle$[2], which cools

2 In the limit where the transition rate induced by the Rabi drive is much lower than the displacement rate associated with the cavity drive, this equilibrium is never reached since the cavity gets excited as soon as the qubit jumps to $|g\rangle$

down the qubit in the ground state before exciting the cavity at $\omega_{r,g}$. In the end, the process prepares the steady state $|g\rangle \otimes |\alpha\rangle$ at a rate which is limited by κ.

We can identify a limit to the rate at which this method resets the qubit in the ground state. When a thermal excitation takes place, the cavity drive becomes off resonant. The ring down time of the cavity is then an incompressible delay before the Rabi drive comes in resonance and resets the qubit.

Note than even though the higher excited states of the transmon are not directly affected by the DDROP scheme, by emptying the $|e\rangle$ state, the detailed balance condition with the higher states implies that their population eventually leaks down toward $|e\rangle$, and thus to $|g\rangle$. A simple model considering three levels for the transmon is depicted on Fig. 48b. We consider transitions between $|g\rangle$, $|e\rangle$ and $|f\rangle$, which is the second excited state. The excitation and relaxation rates are linked to the thermal equilibrium occupation of each level by

$$\begin{cases} P_{eq,g}\gamma_{ge} &= P_{eq,e}\gamma_{eg} \\ P_{eq,e}(\gamma_{eg}+\gamma_{ef}) &= P_{eq,g}\gamma_{ge} + P_{eq,f}\gamma_{fe} \end{cases} . \tag{232}$$

When turning on the DDROP, a supplementary relaxation process from $|e\rangle$ to $|g\rangle$ appears at rate γ_{cool} (in blue), offsetting the equilibrium toward $|g\rangle$. In the next sections, we measure and give an interpretation of this cooling rate in the limit of weak Rabi drive.

6.1.2 *Heating up the transmon*

We consider the qubit that corresponds to Qubit 4 in Tab. 3. It has a very low occupation of the excited states at thermal equilibrium ($P^0_{eq,e} \leq 1$ %). We heat it in a controlled way using the Johnson-Nyquist noise [175] emitted by a hot load. In practice, a resistor at room temperature is loaded at the input of a high power amplifier. The output noise power spectrum is measured at the input of the refrigerator[3] and displays variations below 1.5 dB over a large bandwidth covering the qubit $g \leftrightarrow e$ and $e \leftrightarrow f$ transitions. It is then sent to the the input port of the cavity via the input lines, along which it is attenuated. This results in larger transition rates γ_{ge}, γ_{eg}, γ_{ef} and γ_{fe} [11].

For a given thermal noise power, we measure the transmission of the cavity around its resonance frequency. Three peaks appear, corresponding to the cavity resonance frequencies when the qubit is in $|g\rangle$, $|e\rangle$ and $|f\rangle$ (see Fig. 49a). A fourth peak corresponding to a higher excited state is barely visible. Fitting the cavity transmission and assuming a Boltzmann distribution for the level occupations (see Fig. 16), we get a first estimate of the effective temperature of the qubit $T_{\text{eff}} = 260$ mK. The probability for the qubit to be in a state higher than $|f\rangle$ is then below 2 %, justifying the 3-level model presented in the previous section. We also extract from this curve the damping rate of the cavity $\kappa = 2\pi \times 3.45$ MHz.

3 The noise power spectrum is not calibrated at the input port of the cavity.

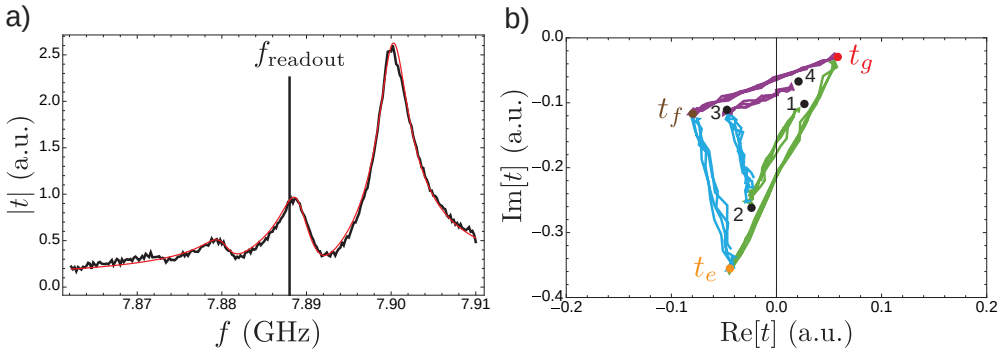

Figure 49: **a** Measured transmission of the cavity in amplitude (black dots) as a function of the probe frequency, for a qubit at thermal equilibrium in presence of the added Johnson-Nyquist noise. Red line: fit assuming a Boltzmann occupation of the qubit levels corresponding to a temperature $T_{\text{eff}} = 260$ mK. The cavity damping rate is adjusted at $\kappa = 2\pi \times 3.45$ MHz. **b**) Measured transmission of the cavity (probe frequency at f_{readout} on **a**) in the Fresnel plane, after driving the qubit with a variable length pulse to induce Rabi oscillations between $|g\rangle$, $|e\rangle$ and $|f\rangle$ (details in the main text). Large triangle: heating noise off. Small triangle: heating noise on. t_g is the transmission when the qubit is in $|g\rangle$ (negligible thermal excitations when the heating noise is off), t_e (resp. t_f) when prepared $|e\rangle$ with a π-pulse on $g \leftrightarrow e$ (resp. $|f\rangle$ with a π-pulse on $g \leftrightarrow e$ and a π-pulse on $e \leftrightarrow f$).

In order to measure more finely the occupation of each level, we detect the transmitted field by the cavity when sending through the input port a 2μs-long pulse at f_{readout}, chosen to be nearby $\omega_{r,e}/2\pi$ (see Fig. 49a). This frequency was chosen in order to maximize the distance in the Fresnel plane between the transmission of the cavity when the qubit is in each of the 3 possible states. On Fig. 49b, the summits of the larger triangle materialize these 3 amplitudes, called t_g, t_e and t_f, when the qubit is in the pure state $|g\rangle$, $|e\rangle$ or $|f\rangle$. For this measurement, we turn the heating noise off, so that the qubit is in $|g\rangle$ at equilibrium. Each side of the triangle corresponds to a measured Rabi oscillation of the qubit between $|g\rangle$ and $|e\rangle$ (in green, by applying a variable length Rabi drive on $e \leftrightarrow g$), between $|g\rangle$ and $|f\rangle$ (in purple, by applying Rabi drive on $e \leftrightarrow g$ followed by a π-pulse on $e \leftrightarrow f$) and between $|e\rangle$ and $|f\rangle$ (in blue, by applying Rabi drive on $e \leftrightarrow g$ followed by a π-pulse on $e \leftrightarrow f$ and another on $g \leftrightarrow e$). Now that these 3 possible transmissions are known, one can determine the occupation of each level by measuring the average transmission t of the cavity for a given qubit state. Indeed, t then verifies

$$t = P_g t_g + P_e t_e + P_f t_f. \tag{233}$$

This equation is solvable assuming that $P_g + P_e + P_f = 1$.

As a first test of this method, we again measure the transmission of the cavity when performing the three Rabi oscillations described above, but with the heating noise on[4]. The four summits can be understood as follows Fig. 49b.

4 note that the heating power needs to be turned off during the dispersive measurement in order not to distort the transmission

- 1. Transmission at equilibrium
  $t_1 = P_{eq,g}t_g + P_{eq,e}t_e + P_{eq,f}t_f$
- 2. Transmission when applying a π-pulse on $e \leftrightarrow g$ from equilibrium
  $t_2 = P_{eq,e}t_g + P_{eq,g}t_e + P_{eq,f}t_f$
- 3. Transmission when applying a π-pulse on $e \leftrightarrow g$ followed by a π-pulse on $e \leftrightarrow f$ from equilibrium
  $t_3 = P_{eq,f}t_g + P_{eq,g}t_e + P_{eq,g}t_f$
- 4. Transmission when applying a π-pulse on $e \leftrightarrow f$ from equilibrium
  $t_4 = P_{eq,g}t_g + P_{eq,f}t_e + P_{eq,e}t_f$

The black dots are predicted transmissions assuming a Boltzmann distribution with $T_{\text{eff}} = 260$ mK. Qualitatively, the measured transmissions match these predictions. Quantitatively, the measured distribution from the dispersive readout does not follow exactly the Boltzmann law. In particular, $P_{eq,f} = 12$ % is 5 % larger than predicted. This could originate from a textured heating noise once filtered by the refrigerator lines, or imprecisions when neglecting higher excited states.

We now use this readout method to follow the occupation of each of the levels of the qubit when turning on the DDROP. This will allow us to extract the value of γ_{cool} for various relative amplitudes of each drive.

6.1.3 *Cooling performances*

To optimize the amplitude of the drive at cavity frequency used in the DDROP, we first measure the occupation of $|g\rangle$ in the steady state when varying this amplitude and for various qubit drive amplitudes at ω_q (expressed in terms of Rabi pulsation Ω_R).
It is represented on Fig. 50a. The horizontal axis corresponding to the amplitude of the drive at $\omega_{r,g}$ has been calibrated in terms of coherent state amplitude α inside the cavity, for a qubit in $|g\rangle$. This calibration follows the same method that is described in details on Fig. 54d. It consists, for a given α, in measuring the occupation of each Fock state $|n\rangle$ by applying a π-pulse on the qubit that operates only if there are exactly n photons in the cavity mode (excitation at $\omega_q - n\chi$). The probability to measure the qubit in the excited state afterwards reads $|\langle n|\alpha\rangle|^2$. Note that here, we consider the steady state of the cavity mode in presence of a constant drive, and not after a fast displacement pulse. It is slightly distorted by the small cavity anharmonicity induced by its hybridization with the qubit, so that it is not a coherent state at large drive amplitudes (for $\alpha > 2$). On this scale, α thus represents the square root of the mean photon number in the field, rather than the amplitude of a coherent state.
When $\alpha = 0$, the Rabi drive equalizes the occupation of $|e\rangle$ and $|g\rangle$ as a mean. Linked by the detailed balance of Eq. (232), this leads to $P_g = 0.4$. When increasing α, the qubit is effectively cooled down to $|g\rangle$. The corresponding cooling rate saturates for a coherent field containing about 5 photons as a mean, corresponding to an overlap with state $|0\rangle$ of less than 1 %. From now on, we set $\alpha = \sqrt{6}$, for which we measure the best cooling performances. Note that when increasing α from this value, P_g decreases since

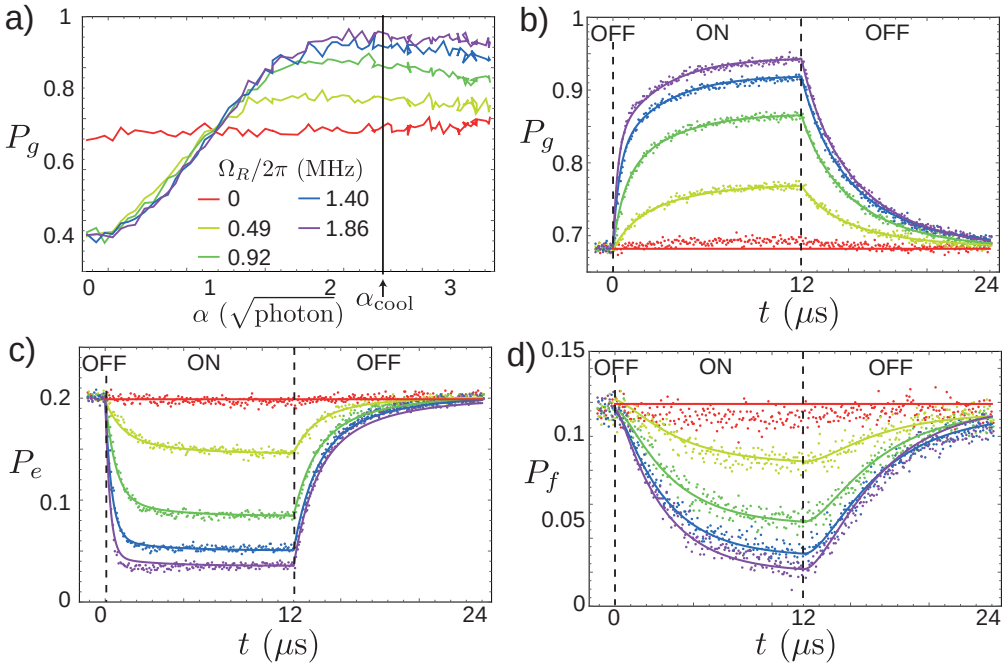

Figure 50: **a**) Measured occupation of $|g\rangle$ in the steady state of DDROP as a function of the amplitude of the coherent state generated when the qubit is in $|g\rangle$. The amplitude of the Rabi drive at ω_q is encoded in color. **b-d**) Occupation of each level as a function of time when turning on the DDROP at $t = 0$ and off at $t = 12$ μs. The amplitude of the field at $\omega_{r,g}$ is set to $\alpha_{\text{cool}} = \sqrt{6}$ (black line on **a**), and the same color code is used for Rabi drive amplitude. Dots: experimental data. Lines: fit with 2 global fit parameters (γ_{eg} and γ_{fe}). The value of γ_{cool} is a supplementary fit parameter for each Rabi drive amplitude when the DDROP is on.

it takes more time for the photons to leak out of the cavity when the qubit gets excited.

The cooling performances also depend on the Rabi drive amplitude. When increasing Ω_R, the steady state occupation of $|g\rangle$ increases until it saturates at $P_{max,g} = 0.95$, for $\Omega_R \simeq 2\pi \times 2$ MHz (for $\kappa = 2\pi \times 3.45$ MHz). We want to extract the cooling rate γ_{cool} associated with each value of Ω_R. In order to do so, we measure the occupation of the qubit levels in time when turning on or off the DDROP. The results are presented as dots on Fig. 50b-d, when turning on the cooling drives at $t = 0$ and turning them off at $t = 12\mu$s (same color code as in a) .

The transition rates between the 3 qubit levels are then fit parameters in a differential equation which should match the measured traces

$$\begin{cases} \dot{P}_g &= -P_g(t)\gamma_{ge} + P_e(t)\gamma_{tot}(t) \\ \dot{P}_e &= -P_e(t)(\gamma_{tot}(t) + \gamma_{ef}) + P_g(t)\gamma_{ge} + P_f(t)\gamma_{fe} \\ \dot{P}_f &= -P_f(t)\gamma_{fe} + P_e(t)\gamma_{ef} \end{cases} , \tag{234}$$

with

$$\gamma_{tot} = \begin{cases} \gamma_{eg} & \text{for the cooling off} \\ \gamma_{eg} + \gamma_{\text{cool}} & \text{for the cooling on} \end{cases} . \tag{235}$$

Note that the 4 transition rates when the cooling is off are linked by the detailed balance condition at equilibrium (see Eq. (232)). In practice, we fit for the last two free parameters when the drives are off, and then fit for γ_{cool} when the drives are on. The corresponding fitted curves of $P_g(t)$, $P_e(t)$ and $P_f(t)$ are also represented on Fig. 50b-d (lines).

The extracted values of γ_{cool} are presented on Fig. 51 (red dots). They follow a quadratic law for small Ω_R and then should saturate around $\gamma_{\text{max}} = 2.6\ \mu\text{s}^{-1} \simeq \kappa/8$ (saturated regime not shown). The quadratic law for $\Omega_R \ll \kappa$ results from a Zeno blockade [115] of the transition from $|e\rangle$ to $|g\rangle$ induced by the drive at $\omega_{r,g}$ acting as a continuous measurement of the σ_Z operator of the qubit. Indeed, the dephasing rate associated with this drive is $\Gamma_d = 63\ \mu\text{s}^{-1} \gg \Omega_R$ (computed from the cavity parameters following Eq. (85)). In this regime, coherent Rabi oscillations are inhibited, but the Zeno blockade is incomplete so that the qubit state jumps randomly from $|e\rangle$ to $|g\rangle$.

However, the jump rate computed from a reduced master equation model by Gambetta *et al.* in [115], which reads

$$\gamma_{\text{jump}} = \frac{\Omega_R^2}{2(\gamma_2 + \Gamma_d)} \tag{236}$$

(black line on Fig. 51), is not sufficient to account for the measured transition rates. This underestimated jump rate for a large drive at cavity frequency was also observed by Gambetta *et al.* when comparing the reduced master equation model with the results of a full simulation of the cavity-qubit system [115].

We reproduced this experiment with a smaller value of the Johnson-Nyquist noise. The extracted cooling rates are slightly larger (blue dots on Fig. 51), in qualitative agreement with Eq. (236) since the qubit coherence time $1/\gamma_2$ was measured to be slightly longer for this weaker heating power.

In this section, we presented a practical scheme used to reset the qubit to the ground state. In practice, it is used to get rid of spurious thermal excitations before starting an experiment. The performances depend on the cooling rate, ultimately limited by the ring down time of the cavity. This time depends on the amplitude of the driving field at $\omega_{r,g}$. In the next section, we present the discrete time version of this scheme, and analyze the dependence of the reset fidelity on the amplitude of this field.

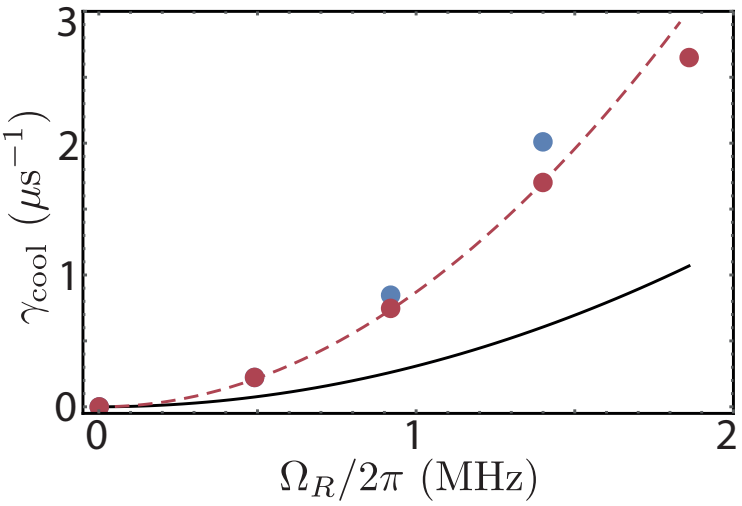

Figure 51: Extracted values of the DDROP-induced relaxation rate $\gamma_{\rm cool}$ from $|e\rangle$ to $|g\rangle$ as a function of the Rabi drive amplitude. Red dots: values extracted from the fits in Fig. 50b-d. Blue dots: values extracted for a similar experiment with a weaker Johnson-Nyquist noise. Black line: jump rate under Zeno blockade computed from Eq. (236). Dotted red line: best quadratic fit to the extracted rates.

6.2 AUTONOMOUS FEEDBACK VERSUS MBF

6.2.1 *Swap reset*

The pulsed version of the DDROP that we present here also relies on the possibility to address a transition of the qubit conditioned on the cavity hosting a given number of photons. More specifically it requires to apply a *controlled* π-rotation on the qubit that operates only if the cavity mode is in the vacuum [125]. The reset is performed on Qubit 3 in Tab. 3 that verifies $\chi \gg \kappa, \gamma_{1,2}$. The data is the same as presented on Fig. 54, and we give here an interpretation in terms of autonomous cooling of what is described as a spurious effect when measuring the cavity Fock states occupation in Chap. 7[5]. The reset sequence is as follows.

- The qubit is initially at thermal equilibrium in the state $\rho_{th} = p_e|e\rangle\langle e| + (1-p_e)|g\rangle\langle g|$ and the cavity mode in the vacuum.
- We apply a displacement pulse at $\omega_{r,g} = \omega_r + \frac{\chi}{2}$ so that a coherent field of amplitude $\alpha \in \mathbb{R}$ develops in the cavity if the qubit is in $|g\rangle$. The total system state is then $\rho_1 = p_e|e\rangle\langle e| \otimes |0\rangle\langle 0| + (1-p_e)|g\rangle\langle g| \otimes |\alpha\rangle\langle\alpha|$.

  We define a cavity state $|0^\perp\rangle = \frac{(\mathbb{1}-|0\rangle\langle 0|)|\alpha\rangle}{\sqrt{1-|\langle\alpha|0\rangle|^2}}$, and an angle θ as $\sin\frac{\theta}{2} = \langle 0^\perp|\alpha\rangle = \sqrt{1-e^{-\alpha^2}}$ so that the state of the system reads

$$\begin{aligned}\rho_1 \;=\; & p_e|e\rangle\langle e| \otimes |0\rangle\langle 0| + \\ & (1-p_e)|g\rangle\langle g| \otimes \Big(\cos\tfrac{\theta}{2}|0\rangle + \sin\tfrac{\theta}{2}|0^\perp\rangle\Big)\Big(\cos\tfrac{\theta}{2}\langle 0| + \sin\tfrac{\theta}{2}\langle 0^\perp|\Big).\end{aligned}$$

5 see Sec. 7.2.1 for pulse shaping details and thermal occupation calibration

(237)

Considering the effective two-level system $\{|0\rangle, |0^{\perp}\rangle\}$, this controlled displacement of the cavity field is thus a rotation $R^q|_\theta$ *controlled* by the transmon and whose target is the cavity two-level system (see Fig. 52a).

- A π-pulse at ω_q is applied on the qubit. In the resolved photon number regime, which is enforced here, it affects the qubit only if the cavity is in the vacuum. This is a C-NOT gate on the qubit controlled by the cavity. The system state now reads

$$\begin{aligned}\rho_2 \;=\; & p_e|g\rangle\langle g|\otimes|0\rangle\langle 0|+ \\ & (1-p_e)\Big(\cos\tfrac{\theta}{2}|e\rangle\otimes|0\rangle+\sin\tfrac{\theta}{2}|g\rangle\otimes|0^{\perp}\rangle\Big)\Big(\cos\tfrac{\theta}{2}\langle e|\otimes\langle 0|+\sin\tfrac{\theta}{2}\langle g|\otimes\langle 0^{\perp}|\Big).\end{aligned} \tag{238}$$

- Up to now, every operation was coherent and reversible. In general, the cavity mode and the qubit are entangled. We now trace out the cavity, which is not a unitary operation. The qubit density matrix then reads

$$\rho_f = \Big(\sin^2\frac{\theta}{2}+p_e\cos^2\frac{\theta}{2}\Big)|g\rangle\langle g|+(1-p_e)\cos^2\frac{\theta}{2}|e\rangle\langle e|. \tag{239}$$

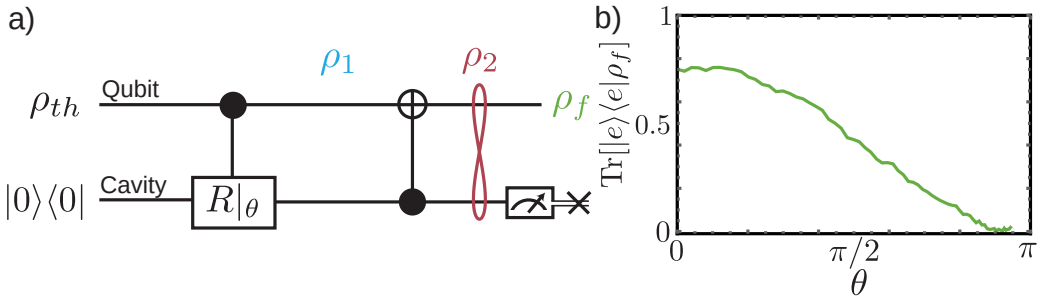

Figure 52: **a**) Quantum logic representation of the autonomous feedback loop. The displacement corresponds to a rotation by angle θ of a qubit formed by two orthogonal states of the cavity mode. A C-NOT gate controlled by this qubit is then applied and the cavity mode is traced out. **b**) Measured occupation of $|e\rangle$ after one feedback loop as a function of θ.

Unsurprisingly, the reset is perfectly efficient only for $\theta = \pi$. This means that $|\alpha\rangle$ needs to a have a sufficiently large amplitude to be perfectly distinguishable from $|0\rangle$. In that case, in terms of operations on the effective "double qubit" system, this scheme implements a double C-NOT gate that swaps the qubit and the cavity state. Even though this operation is coherent, the cavity needs to be reset to the vacuum to perform another cycle. It is essential to take into account this step to avoid a paradox similar to the Maxwell's demon thought experiment [176]. Indeed, this essentially classical reset scheme requires to evacuate entropy either by a measurement based reset of the cavity, or more simply by dissipation into the cold probe lines. In that sense, this scheme is equivalent to the measurement based reset of the qubit described in

Sec. 5.1.2, where a bit of memory of the FPGA board plays the role of the ancillary system absorbing the original entropy of the qubit.

We plot on Fig. 52b the measured occupation of $|e\rangle$ after one feedback loop and starting from thermal equilibrium. Note that the calibration of the qubit readout protocol, presented in Sec. 7.2.1, does not allow a precision better than a few percents. Quantitative comparison with the performances of the measurement based scheme presented in Sec. 5.1.2 is thus impossible. However, the performances of both protocols are qualitatively comparable, since they are both based on the entanglement of the qubit state with the intra cavity field, acting as an ancilla. The reset is efficient if the 2 states of the ancilla corresponding to a qubit in $|g\rangle$ or $|e\rangle$ are perfectly distinguishable. In that case, for perfect detection efficiency, the MBF scheme also corresponds to a double C-NOT classical gate.

6.2.2 *Engineering dissipation with continuous feedback*

In the previous section, we have seen that an autonomous reset of the qubit based on a double C-NOT gate with a cold ancilla was equivalent, for perfect detection efficiency, to the stroboscopic feedback protocol presented in Sec. 5.1.2. One may wonder if this equivalence between the measurement based and autonomous protocols can be generalized to reservoir engineering techniques.

In Sec. 5.2.1, we showed that a continuous feedback based on the fluorescence detection could be used to effectively engineer dissipation. However, the dissipation rate is limited, for perfect detection efficiency, by the measurement rate γ_1[6]. Thus, it cannot be used to *increase* dissipation, but rather to redirect it. Therefore, it cannot be used to cool down the qubit as the DDROP protocol, which essentially increases the relaxation rate of the qubit using the stronger dissipation of the cavity.

This limitation does not arise for a continuous feedback protocol based on the dispersive measurement of the σ_Z operator (see Sec. 3.2), whose strength can be varied via the amplitude of the drive at cavity frequency. We now roughly sketch a feedback protocol based on this dispersive measurement that, for perfect detection efficiency, stabilizes $|+x\rangle = \frac{1}{\sqrt{2}}(|g\rangle + |e\rangle)$.

We consider a constant drive at cavity frequency that leads to a dephasing rate Γ_d of the qubit (see Eq.(85)) and, for simplicity, a perfect homodyne detection of the Q quadrature of the transmitted field. It corresponds to the case of a single jump

6 In general, the total dissipation rate in Eq. (224) is larger due to the spurious jump operators denoted $L_{I,2}$ and $L_{Q,2}$.

operator $L = \sqrt{\frac{\Gamma_d}{2}}\sigma_Z$, and the detection yields the signal $\mathrm{d}J_t = \sqrt{2\Gamma_d}\langle\sigma_Z\rangle\mathrm{d}t + \mathrm{d}W_t$ (see Eq. (114)). Feeding back this signal to the qubit via the control hamiltonian

$$H_{\mathrm{cont}} = \sqrt{\frac{\Gamma_d}{2}}\frac{\mathrm{d}J_t}{\mathrm{d}t}\sigma_Y, \tag{240}$$

a similar calculation to the one made in Sec. 5.2.1.1 leads to the effective master equation for the qubit[7] [23]

$$\frac{\mathrm{d}\rho}{\mathrm{d}t} = \frac{\Gamma_d}{2}\Big(L_1\rho L_1^\dagger - \frac{1}{2}(L_1^\dagger L_1\rho + \rho L_1^\dagger L_1)\Big), \tag{241}$$

where the new jump operator L_1 reads

$$L_1 = \sqrt{\frac{\Gamma_d}{2}}(\sigma_Z - i\sigma_Y). \tag{242}$$

The stable point of this equation is $\rho = |+x\rangle\langle+x|$.

Thus, the QND measurement of the σ_Z operator combined with a simple markovian feedback loop creates an effective dissipation toward $|+x\rangle$. In its effects, this protocol is similar to a reservoir engineering method demonstrated by Murch *et al.* [47]. It can simply be adapted to stabilize any state of the Bloch sphere. Surprisingly though, the dissipation rate drops to 0 when the target state is on the z-axis. It thus cannot be used to stabilize $|g\rangle$ or $|e\rangle$. This can be understood considering that, in these cases, when spurious noise draws the state away from the z-axis, the σ_Z measurement does not provide any information about its new phase. Thus, no coherent control can be applied in order to restore the target state. For the same reason, the feedback protocol based on the fluorescence signal cannot, using homodyne detection of σ_-, stabilize $|\pm x\rangle$ because information is then extracted along $\mathrm{Re}[\sigma_-] = \frac{1}{2}\sigma_X$[8]. Note that $|g\rangle$ and $|e\rangle$ are precisely the states naturally stabilized by the stroboscopic protocol described in Sec. 5.1.2. More sophisticated, non markovian, feedback protocols need further investigation.
Using heterodyne detection does not seem to offer more controllability since the detection of $i\sigma_z$ only shifts randomly the phase of the state. However, De Lange *et al.* have shown recently that this back action could be compensated for by feedback [116]. Thus, it should be possible to reach the same performances as with homodyne detection.

The question of whether a MBF with equivalent performances to coherent protocols can be found for any stabilization problem remains open to date. In the particular case of stabilizing the vacuum state of a resonant cavity mode in presence of photon shot noise, Hamerly *et al.* have shown that coherent feedback was superior to MBF

7 Other decoherence channels, and in particular relaxation, are neglected here.

8 Using heterodyne detection though, one detects both $\sigma_- = \frac{1}{2}(\sigma_X - i\sigma_Y)$ and $i\sigma_- = \frac{1}{2}(\sigma_Y + i\sigma_X)$ so that any state can be stabilized. Moreover, there is no phase reference but the one of the source used both for detecting the fluorescence field and driving the qubit, so that $|\pm x\rangle$ and $|\pm y\rangle$ are equivalent. On the other hand, heterodyne detection does not help for the dispersive measurement since neither the detection of σ_Z or $i\sigma_Z$ is sensitive to the phase of the state so that it cannot be used to stabilize $|\pm z\rangle$.

using homodyne or heterodyne detection, even for perfect detection efficiency [177]. In particular, the MBF scheme they consider does not lower the occupation of the cavity when in the quantum regime, which they define by a low occupation of the cavity mode at thermal equilibrium $\langle a^\dagger a \rangle_{th} \ll 1$. In that case, the cavity mode can be considered as an effective qubit, so that the problem is equivalent to stabilizing $|g\rangle$ with a MBF using the fluorescence signal. We have shown that the feedback loop was ineffective in that case. On the other hand, they propose a coherent protocol that lowers the cavity mode occupation, even in the quantum regime. This protocol leads to an enhancement of the dissipation similar to a Purcell enhanced spontaneous emission. However, it is not shown that another type of measurement based feedback could not achieve similar performances.

Recently, generation of Bell pairs [178, 179, 180] and stabilization of a particular manifold of a cavity mode [181] through reservoir engineering have been demonstrated. Engineered dissipation is thus an important resource for quantum information. Feedback protocols based on specific measurements [182, 183, 184] may prove to be an alternative or complementary tool to efficiently engineer dissipation.

In this chapter, we have described protocols stabilizing a particular target state of the qubit by autonomous feedback, which consists in engineering the dissipation so that the target state becomes stable under continuous monitoring by the environment. In the next chapter, we describe an experiment in which Zeno dynamics of the cavity mode is enforced by coherent coupling to an ancillary system, which is the qubit. Zeno dynamics can be seen as restricting the evolution of a system to a stabilized subspace of its Hilbert space. In that sense, it implements coherent, dissipationless feedback. Thus, such a protocol cannot be used to correct for errors induced by the decoherence channels, which lead to an increase of entropy of the system.

7

QUANTUM ZENO DYNAMICS

7.1 ZENO DYNAMICS OF A MICROWAVE MODE

7.1.1 *Zeno dynamics by repeated measurements*

In the original sense of Quantum Zeno Effect (QZE) [35, 36], one inhibits the departure from a given state of a system due to a coherent evolution by measuring strongly and repeatedly whether the system is in that state. Indeed, a general unitary operator acting from time t_1 to t_2 corresponds to the evolution of the system under a hamiltonian H and it can be written $U(t_2 - t_1) = e^{-i\frac{H}{\hbar}(t_2-t_1)}$. The projective measurement observable $\mathcal{O}$ is modeled as

$$\mathcal{O} = \sum_i \lambda_i \Pi_i, \tag{243}$$

where the Π_i's are projectors on orthogonal states $|\alpha_i\rangle$ of the system. Then, if the system is measured in $|\alpha_1\rangle$ at time t, the following measurement at time $t + \delta t$ yields the same outcome with probability

$$p(\delta t) = |\langle\alpha_1|U(\delta t)|\alpha_1\rangle|^2 = |\langle\alpha_1|\mathbb{1} - i\frac{H_m}{\hbar}\delta t - O(\delta t^2)|\alpha_1\rangle|^2 = 1 + O(\delta t^2). \tag{244}$$

Then, if one measures regularly the system N times from 0 to a given time T, and if its initial state is $|\alpha_1\rangle$, it is found in the same state at T with probability

$$p(N) = \left(1 + O\Big(\frac{\Delta t}{N}\Big)^2\right)^N = 1 + O\Big(\frac{\Delta t^2}{N}\Big) \overset{N\to\infty}{\to} 1. \tag{245}$$

Thus, by measuring repeatedly a system, one can freeze its dynamics. QZE was first demonstrated for transitions of a trapped ion [185, 186]. Zeno blockade of a coherent field growth was observed in 2008 by Bernu *et al.* with Rydberg atoms [187], and with superconducting qubits, inhibition of transitions induced by a Rabi drive was reported in 2010 [141]. In Sec. 6.1.3, we showed that limited cooling performances of the DDROP protocol for a weak Rabi drive were also due to QZE.

Interestingly, if the measurement projects the system not on orthogonal states but on multidimensional manifolds, evolution is possible inside of each stabilized subspace. Thus, the dynamics of the system is dramatically modified but not frozen. The resulting constrained dynamics are then called *Quantum Zeno Dynamics* (QZD) [37, 38, 39]. Naming $\mathcal{H}_\mu$ each subspace stable under the action of the projector Π_μ the system now evolves under the Zeno modified hamiltonian

$$H_\mu = \Pi_\mu H \Pi_\mu. \tag{246}$$

If its state is initially in one the $\mathcal{H}_\mu$'s, the evolution is constrained within that subspace. Note that the Zeno effect can also appear under continuous detection. Expressed in the

Lindblad formalism, if a system dynamics described by a master equation (27) reading

$$\frac{\mathrm{d}\rho(t)}{\mathrm{d}t} = -\frac{i}{\hbar}[H,\rho] + \mathcal{D}[\sqrt{\Gamma}L]\rho, \tag{247}$$

with L a jump operator of order 1, the evolution is confined to subspaces of the system Hilbert space stable under the action of L when $\hbar\Gamma$ is much larger than the eigenenergies of H [115]. Thus, an actual measurement by an observer does not need to take place. A strong engineered dissipation can also entail QZD [181].

7.1.2 *Zeno dynamics by strong coherent driving*

7.1.2.1 *Phase randomization*

In 2004, Facchi *et al.* [37] proposed an alternative scheme, with no measurement involved, to enforce the same dynamics. Applying repeated unitary "kicks", which are instantaneous coherent evolutions encoded by a unitary operator U_Z, effectively confines a slow, continuous evolution governed by the hamiltonian H to orthogonal subspaces $\mathcal{H}_\mu$, whose states are stable under the action of U_Z[1]. Following [37, 38], QZD thus refers to this general class of dynamics constrained within a chosen subspace, even when the Zeno effect is not involved.

The coherently induced QZD can be understood as an effect of *dynamical decoupling* or *phase randomization*. Indeed, if the system is initially in the pure state $|\psi_0\rangle$[2] and N kicks take place between 0 and t, its state at time t reads

$$|\psi(t)\rangle = (U_Z e^{-i\frac{H}{\hbar}\frac{t}{N}})^N|\psi_0\rangle \overset{\text{def}}{=} \tilde{U}^N(t)|\psi_0\rangle. \tag{248}$$

Deriving this expression with respect to time leads to

$$\frac{\mathrm{d}|\psi(t)\rangle}{\mathrm{d}t} = -\frac{i}{\hbar}\frac{1}{N}\sum_{k=0}^{N-1}\tilde{U}^k(t)U_Z H\tilde{U}^{N-k-1}(t)|\psi_0\rangle. \tag{249}$$

The proper dynamics appear by then neglecting the slow evolution $e^{-i\frac{H}{\hbar}\frac{t}{N}}$ compared to U_Z. In the limit $N\to\infty$, we get

$$\begin{aligned}\tfrac{\mathrm{d}|\psi(t)\rangle}{\mathrm{d}t} &= -\tfrac{i}{\hbar}\tfrac{1}{N}\sum_{k=0}^{N-1}U_Z^k U_Z H U_Z^{N-k-1}|\psi_0\rangle \\ &= -\tfrac{i}{\hbar}\Big(\tfrac{1}{N}\sum_{k=0}^{N-1}U_Z^{k+1}HU_Z^{\dagger k+1}\Big)U_Z^N|\psi_0\rangle.\end{aligned} \tag{250}$$

By diagonalizing U_Z as

$$U_Z = \sum_\mu e^{-i\lambda_\mu}\Pi_\mu, \tag{251}$$

1 Up to a global phase for each subspace as described below.

2 the system is supposed in a pure state for simplicity, but the result can be directly generalized to mixed states.

where the Π_μ's are projectors on the orthogonal eigenspaces $\mathcal{H}_\mu$ and $\lambda_\mu \neq \lambda_\nu$ for $\mu \neq \nu$, we can then rewrite the central term in Eq. (250) as

$$\frac{1}{N}\sum_{k=0}^{N-1} U_Z^{k+1} H U_Z^{\dagger k+1} = \sum_{\mu,\nu} \Pi_\mu H \Pi_\nu \frac{1}{N}\sum_{k=0}^{N-1} e^{-i(k+1)(\lambda_\mu-\lambda_\nu)}. \tag{252}$$

In that sum, the terms for which $\mu \neq \nu$ cancel for $N \to \infty$, so that we can write Eq. (250) as

$$\frac{\mathrm{d}|\psi(t)\rangle}{\mathrm{d}t} = -\frac{i}{\hbar}\Big(\sum_\mu \Pi_\mu H \Pi_\mu\Big) U_Z^N |\psi_0\rangle. \tag{253}$$

Thus, if $|\psi_0\rangle$ is initially in one of the $\mathcal{H}_\mu$'s, it remains in that subspace, and up to a constant phase $N\lambda_\mu$ depending on the number of kicks, its dynamics is governed by the same Zeno hamiltonian as in Eq. (246).

7.1.2.2 *Zeno dynamics using an ancillary system*

Zeno dynamics can thus be entailed by unitary kicks, and adapting this scheme, Schäfer *et al.* have demonstrated experimentally with Rb condensates that a chosen level of a system could be disabled by coupling it to an ancillary degree of freedom and driving continuously a transition of the hybrid system. This method was also successfully implemented with Rydberg atoms [50]. To be more concrete, we now describe the experiment[83] that we performed with a transmon dispersively coupled to the first resonant mode of a cavity. The qubit is used to induce Zeno dynamics on the microwave mode. Note that, in opposition to the experiments described up to now in this thesis, the system of interest is thus the cavity mode, the qubit being used as an ancillary system.

The qubit corresponds to Qubit 3 in Tab. 3. Full wiring schematic can be found on Fig. 66. Its coherence and decay times $1/\gamma_1 = 11.5$ μs and $1/\gamma_2 = 8.9$ μs are of the same order of magnitude as the photon lifetime in the cavity mode[3] $1/(2\pi\kappa) = 1.3$ μs. The cavity mode resonates at $\omega_r/2\pi = 7.804$ GHz and the qubit at $\omega_r/2\pi = 5.622$ GHz. Including drives for the qubit and the cavity mode, the hamiltonian in the dispersive limit reads (see Eq. 80)

$$\begin{aligned} H \;=\; & \hbar\omega_r a^\dagger a + \hbar\tfrac{\omega_q}{2}\sigma_z - \hbar\tfrac{\chi}{2} a^\dagger a \sigma_z \\ & + \hbar(\epsilon_c e^{-i\omega_c t} a^\dagger + \epsilon_c^* e^{+i\omega_c t} a) + \hbar(\epsilon_d e^{-i\omega_d t}\sigma_+ + \epsilon_d^* e^{+i\omega_d t}\sigma_-), \end{aligned} \tag{254}$$

where the dispersive shift $\chi/2\pi = 4.63$ MHz is much larger than the decay rates $\chi \gg \gamma_1, \kappa$. The system is thus in the *resolved photon number* regime [45] as shown on Fig. 53b. In color is represented the transmission of the cavity when probed in continuous wave at $\omega_c = \omega_{r,g} = \omega_r + \frac{\omega_q}{2}$. Transmission thus gets lower as the probability for the qubit to be excited increases. We then sweep the frequency of a second continuous wave at ω_d nearby ω_q (horizontal axis). At low probing power for the cavity, the qubit is excited only when $\omega_d = \omega_q$. When cranking up the power (vertical axis), other

3 determined spectroscopically by the method described in Sec. 2.2.2.3

resonances appear for the qubit at $\omega_q - k\chi$, each corresponding to different photon numbers k in the cavity.

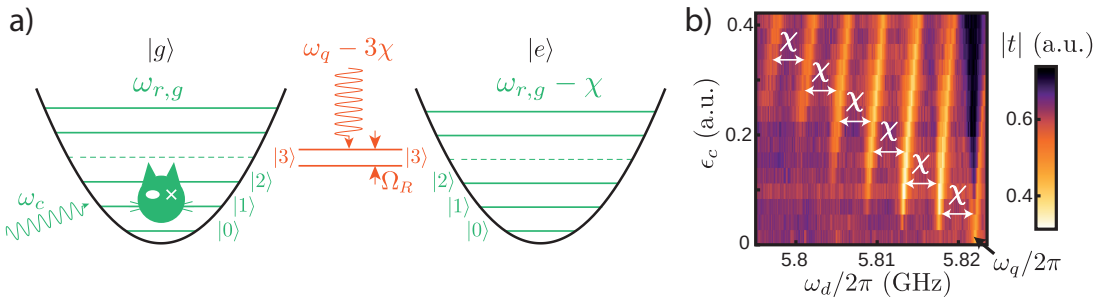

Figure 53: **a)** Combined energy level diagram for the cavity and qubit. When driving specifically the $|g, N\rangle \leftrightarrow |e, N\rangle$ transition, these levels repel each other. The $|N-1\rangle \leftrightarrow |N\rangle$ transition of the cavity mode is no longer resonant with a drive at $\omega_c = \omega_{r,g}$. When starting from $|0\rangle$ and applying a drive at this frequency, the evolution of the cavity state is confined to N levels. **b)** Spectroscopy of the qubit *dressed* states. When increasing the amplitude of a wave at cavity frequency (vertical axis) the qubit resonates at several frequencies (horizontal axis) separated by χ. When reaching a resonance, the qubit gets excited, which lowers the cavity transmission (encoded in color).

By applying microwaves at $\omega_q - N\chi$, we can thus address specifically the transition $|g, N\rangle \leftrightarrow |e, N\rangle$ of the total system. A continuous, strong drive (corresponding to a Rabi oscillation around σ_Y with frequency $\Omega_R/2\pi = 6.24$ MHz if the level were occupied) on this transition thus implements the repeated kicks of Sec. 7.1.2.1. Indeed, the subspaces unaffected by this coherent drive are $\mathcal{H}_+ = \text{span}(|+y, N\rangle)$[4], $\mathcal{H}_- = \text{span}(|-y, N\rangle)$, and most importantly, $\mathcal{H}_0 = \text{span}(|g, k\rangle, |e, k\rangle_{k\neq N})$. Tracing out the qubit state, and for a cavity mode initially empty of photons, the level $|N\rangle$ is disabled and the cavity mode is described by the Zeno hamiltonian (246)

$$H_Z = \Pi H \Pi, \tag{255}$$

where $H = \hbar\omega_r a^\dagger a$ and

$$\Pi = \sum_{k\neq N} |k\rangle\langle k|. \tag{256}$$

In practice, since the cavity is initially empty of photons and the 2-photon transitions are forbidden, when driving at $\omega_{r,g}$, the cavity state is confined to the N first levels (from $|0\rangle$ to $|N-1\rangle$). Another way of understanding the experiment is depicted on Fig. 53a. When driving the transition $|g, N\rangle \leftrightarrow |e, N\rangle$ ($N = 3$ on the figure), these levels are hybridized and repel each over by Ω_R. The level $|N\rangle$ is thus removed from the cavity mode harmonic ladder, and the $|N-1\rangle \leftrightarrow |N\rangle$ transition is no longer resonant with the drive at $\omega_{r,g}$.

We can already identify some constraints in this setup.

4 $|\pm y\rangle = |g\rangle \pm i|e\rangle$

- To be able to manipulate coherently the effective N-level system, we need to address it on a timescale shorter than its decay time $1/(k2\pi\kappa)$ ($k < N$). The displacement rate ϵ_c associated with the cavity drive thus needs to verify $\epsilon_c \gg N\kappa$. In practice, it was chosen to be $\epsilon_c = 3\ \mu\text{s}^{-1}$. The calibration of this rate is described below.

- In order for the blockade of the level n to be effective, the shift $\Omega_R/2$ needs to be much larger than the transition rate induced by the cavity drive from $|N-1\rangle$ to $|N\rangle$. We then have to choose $\Omega_R \gg \epsilon_c$.

- In order for the blockade tone at $\omega_q - N\chi$ not to affect the other levels, we need to have $\chi \gg \Omega_R$.

- Due to its hybridization with the qubit, the cavity inherits some anharmonicity λ (see Eq. (61)), even in the absence of a blockade tone. This limits intrinsically the number of accessible levels in the harmonic ladder of the cavity for a drive resonant at 0 photon. In order to create an N-level system as large as possible, we then must have $\kappa > N\lambda$. Note that, even if it limits the number of accessible levels without Zeno blockade, anharmonicity in the cavity mode yields dynamics that are different from the QZD (see Sec. 7.3.3).

  Surprisingly, this self-Kerr term has been measured to be negative in our experiment ($\lambda/2\pi = -70$ kHz), both from the behavior of the cavity mode in presence of the Zeno blockade (λ is a global fit parameter in the simulations in Eq. (271)) and from independent spectroscopic measurements (see Fig. 55b). Note that during the first cool-down of the sample, the Kerr term was initially positive and of similar amplitude. It became negative after an unwanted warm-up (around 270 K) and cool-down of the fridge that barely modified the other parameters. This in contradiction with the model presented in Sec. 2.2.3.2 and in [62, 72, 73], which predicts that the self-Kerr of the cavity inherited from its hybridization with the transmon mode has the same sign as the transmon anharmonicity, no matter whether the qubit is detuned above or below the cavity[5]. A possible explanation for this anomalous self-Kerr is a defect or trapped vortex that has a transition frequency near the cavity resonance frequency.

Summarizing these constraints, an ideal Zeno experiment would verify the hierarchy

$$\boxed{\lambda \ll \kappa \ll \epsilon_c \ll \Omega_R \ll \chi}. \tag{257}$$

This situation is hard to reach with a transmon since λ and χ are linked by $\chi = 2\sqrt{\chi\alpha}$, where α is the transmon anharmonicity (see Eq. (61)). This anharmonicity needs to remain small ($\alpha \leq 400$ MHz) in order to retain transmon high coherence properties (see Sec. 2.2.3.1).

In our experiment, we had to release the constraint $\Omega_R \ll \chi$. The value Ω_R/χ was adjusted empirically to maximize the Zeno barrier efficiency. As a result, the blockade

5 except in the straddling regime when the cavity resonance frequency lies in between two transmon transitions.

tone constitutes a Rabi drive at finite detuning for the transitions $|g,k\rangle \leftrightarrow |e,k\rangle$ with $k < N$. This has two effects. First, the levels $|k\rangle$ are slightly shifted by an amount that depends on k. To take this into account when simulating the system (see Eq. (271)), we model it as a global shift of the cavity resonance frequency so that the drive at ω_c is effectively slightly detuned, and a spurious negative non-linearity appears. Second, the qubit can actually get excited from one of the $|g,k\rangle$ levels to $|e,k\rangle$. In that case, the cavity resonance shifts to $\omega_{r,e} = \omega_r - \frac{\chi}{2}$ and the drive at ω_c is far detuned so that the cavity state decays down to $|0\rangle$ as long as the qubit stays in $|e\rangle$. This effect depends on the blocked level $|N\rangle$ and has been measured to always remain below 18 % of the experiments (see Fig. 55a).

At this point, let us insist that, as predicted in [37], no measurement or dissipation needs to be involved in our experiment. In our experiment, the only leak of information on the system originates in the decay of the field under QZD itself, which relaxes at rate κ. In principle, the QZD would work even better if the escape rate κ were as small as possible, in which case the measurement rate would be negligible. In practice, even dismissing the limitation on the field amplitude due to the Zeno barrier and the saturation induced by the Kerr effect, there would be at most $\langle n_{\max}\rangle = \frac{4\epsilon_c^2}{\kappa} = 21$ cavity photons on average in the steady state. The measurement induced dephasing associated with such a coherent field (see Eq. (85)) would be $\Gamma_d = 14\ \mu\text{s}^{-1}$. It corresponds to the measurement rate of the qubit by the whole environment, and thus to the maximum measurement rate of the occupation of the blocked level $|N\rangle$ (to compare with the Zeno barrier "width" $\Omega_R = 40\ \mu\text{s}^{-1}$). This rate, far overestimated as is the average number of photons, could not inhibit the transitions induced by the displacement rate $\epsilon_c = 3\ \mu\text{s}^{-1}$ since the corresponding jump rate from $|N-1\rangle$ to $|N\rangle$ for $N = 3 \ll \langle n_{\max}\rangle$ would be [115] $\gamma_{\text{jump}} \approx \epsilon_c^2/(2\Gamma_d) = 0.35\ \mu\text{s}^{-1}$.

Note also that on Fig. 53b, each resonance of the qubit is shifted toward higher frequencies when increasing ϵ_c. It results from a combined effect of AC-Stark shift and cavity mode anharmonicity. Following Gambetta *et al.* [188], for a detuned drive at $\omega_c = \omega_{r,g} - \delta$ and in the limit $\delta, \kappa \ll \chi$, all the resonance peaks are shifted depending on the mean photon number $\overline{n}$ in the cavity when the qubit is in $|g\rangle$ as $\omega_q - k\chi \leftarrow \omega_q - k\chi + B$ with

$$B = \frac{\chi}{2}\overline{n}\Big(1 - \frac{2\chi^2}{\kappa^2 + \chi^2 + (\chi + 2\delta)^2}\Big) \simeq \overline{n}(\delta + \frac{\kappa^2}{4\chi}). \tag{258}$$

In the experiment, δ is pushed toward positive values when increasing ϵ_c due to the anomalous Kerr effect (see Eq. (271)). Qualitatively, the resonances are thus shifted toward positive frequencies proportionally to $\overline{n}^2$.

Up to now, we have described the qubit as an auxiliary degree of freedom used to enforce QZD through coherent driving. In the next section, we show that this qubit, which is not excited during the Zeno blockade, can also be used as a photon number detector.

7.2 OSCILLATIONS IN LEVELS OCCUPATION FOR A DRIVEN N-LEVEL SYSTEM

The possibility to address specifically a transition of the qubit dressed by a given number of photons is used to characterize the field developing in the cavity under Zeno blockade. A first enlightening measurement consists in measuring the probability $P_m = \mathrm{Tr}(\rho_r|m\rangle\langle m|)$ for the field to host m photons. To do so, we perform a CNOT operation on the qubit, conditioned on the cavity hosting exactly m photons [125]. The qubit is then measured using dispersive readout (see Sec. 3.2.3), and the probability to find it excited allows us to access the P_m's. Some spurious excitation processes of the qubit need to be corrected for. In order to calibrate this method, we first measure the P_m's for a coherent state (see Sec. 7.2.1), before measuring those for the field under QZD (see Sec. 7.2.2).

7.2.1 *Fock states occupation for a coherent field*

In order to put the cavity mode in a coherent state $|\alpha\rangle$, starting from the vacuum, we apply a fast displacement $D(\alpha)$, on a time scale much shorter than $1/\lambda$. This is needed to avoid the distortion of the coherent field due to the Kerr effect [125]. The displacement is performed by sending a 240 ns pulse at $\omega_c = \omega_{r,g}$. The pulse is shaped using the DRAG technique [189, 190], which consists in a gaussian envelop $\mathcal{G}(t)$ on the I quadrature and derivative of gaussian on Q so as to get $\mathcal{A}(t) = \mathcal{G}(t)\cos\omega_c t - \frac{\partial_t \mathcal{G}}{\Delta}\sin\omega_c t$. The proportionality factor Δ is chosen such that the overall Fourier transform cancels at $\omega_c \pm \Delta$. With $\Delta = \chi$, it prevents the field to enter in the cavity when the qubit is in its excited state (at $\omega_{r,e}$). In practice we have used a Gaussian envelop with a 67 ns full width at half maximum.

Right after the displacement, a 0.4 μs π-pulse at $\omega_q - m\chi$ is applied to the qubit. Its duration is much longer than χ^{-1} to ensure its selectivity in photon number, and shorter than κ^{-1} to minimize cavity relaxation. The pulse is shaped with a gaussian envelope of characteristic spectral bandwidth $\sigma = 2.1$ MHz. This results in a pulse selectivity $1 - e^{-\frac{\chi^2}{2\sigma^2}} > 0.9$. This operation corresponds to the CNOT gate on Fig. 54a. At this point, the average occupation of the $|e\rangle$ level of the qubit should correspond to the probability P_m for the field to host m photons. However 2 spurious effects need to be taken into account to infer this probability.

The first effect is the dependence of the qubit readout exact calibration on the intra cavity field. The qubit is measured dispersively by sending a 6 μs pulse at $\omega_{r,g}$ and then integrating the transmitted field amplitude. A JPC is used as a pre-amplifier on the detection setup to maximize the measurement SNR. Note that the frequency and power of the readout pulse have been finely tuned for the same purpose. In particular, the readout frequency is slightly detuned from ω_c ($\omega_{\mathrm{readout}} - \omega_c \simeq 2\pi \times 0.5$ MHz). As a result, any contribution from the first displacement pulse in the transmitted field is cancelled out when averaging the readout outcome. However, due to the Kerr induced resonance frequency shift by the photons at ω_c, the cavity transmission at $\omega_{\mathrm{readout}}$

depends on the photon number in this field. To reduce this effect, the readout of the qubit is delayed for 2 μs so as to let the pre-existing field leak out of the cavity.

The average transmitted signal S_m is shown in Fig. 54b as a function of the amplitude of the initial displacement pulse, for m ranging from 0 to 6. The cavity transmission still displays a slight dependence on α, even when no π-pulse is applied to the qubit (see Fig. 54c). To model this, we consider an average value for the integrated readout amplitude dependent on both the qubit state and the pre existing field state. We call $t_{k,\alpha}$[6] this average value corresponding to a qubit in state α and the field in the Fock state $|k\rangle$.

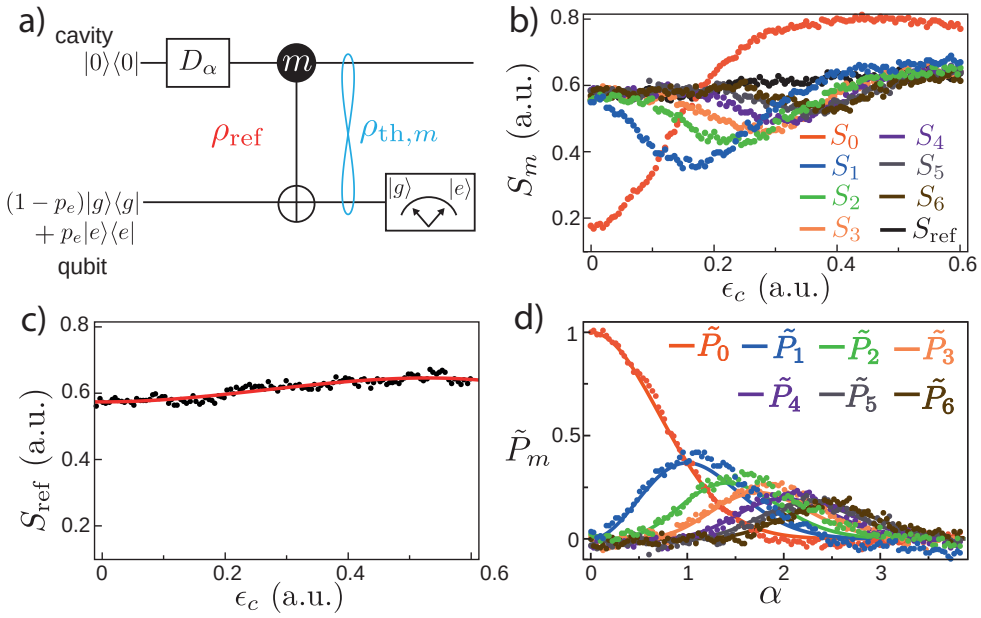

Figure 54: **a**) Circuit diagram for detecting the Fock state probability P_m as a function of the coherent displacement α. After a 240 ns displacement pulse at $\omega_c = \omega_{r,g}$ and displacement rate ϵ_c, a conditional qubit rotation is applied to the qubit so that it is flipped if and only if m photons are in the cavity. After a 2 μs waiting time to empty the cavity, the qubit state is measured using the qubit-state dependent transmission of the cavity. **b**) Shown is the corresponding integrated readout signal S_m at $\omega_{\rm readout}$ as a function the displacement rate ϵ_c for different values of m. The black curve $S_{\rm ref}$, which corresponds to the case without any qubit rotation, depends slightly on the drive amplitude due to the self-Kerr effect of the cavity. **c**) $S_{\rm ref}$ (black dots) and its third order polynomial fit (red line). **d**) Measured (dots) and theoretical (solid lines) Fock state probabilities $\tilde{P}_m$ as a function of the coherent displacement α. The axes were scaled to fit a Poisson distribution $P_m(\alpha) = e^{-|\alpha|^2}\frac{|\alpha|^{2m}}{m!}$ (solid lines) with the same fit parameters for all seven Fock state populations simultaneously. This allows one to calibrate the drive amplitude in term of coherent displacement α.

6 In principle, $t_{k,\alpha}$ is complex. However, for simplicity, we consider only its modulus since $t_{\alpha,k}$ is measured to have a constant phase for all α and k.

A second spurious effect that needs to be taken into account is that the qubit has a residual thermal population. Thus, about $p_e = 22\ \%$[7] of the experiments start with a qubit in the excited state. In these cases, the displacement $D(\alpha)$ is not effective and the system remains in $|0, e\rangle$. This affects the signal for $m = 0$ (red-dotted curve in Fig. 54b) which is above all the other curves at large drive amplitude. At such a large displacement amplitude, the probability of being in state $|g, 0\rangle$ is very small and the selective π-pulse is efficient only when the qubit was initially thermally excited. In this case, it empties state $|e, 0\rangle$ in state $|g, 0\rangle$. This phenomenon can actually be used as a procedure to cool the qubit (see Sec. 6.2.1). In contrast, state $|e, 0\rangle$ stays occupied for $m \geq 1$.

Beside the offset on the measurement of P_m for $m = 0$, the experiments that start with a qubit in $|e\rangle$ yield no signal since the cavity mode remains empty. We now present a model used to infer the probabilities $\tilde{P}_m$ for the field to host m photons *knowing* that the qubit was initially in $|g\rangle$. Note that there is no post-selection here. For a qubit at zero temperature, we would have $\tilde{P}_m = P_m$.

Starting from thermal equilibrium and under a resonant drive at $\omega_c = \omega_{r,g}$, a field develops only if the qubit is in $|g\rangle$ since the cavity is out of resonance when the qubit is in $|e\rangle$. The system is then in the state

$$\rho_{\text{ref}} = (1 - p_e)|\psi\rangle\langle\psi| \otimes |g\rangle\langle g| + p_e|0\rangle\langle 0| \otimes |e\rangle\langle e|, \tag{259}$$

with $|\psi\rangle = \sum_k c_k|k\rangle$ the cavity state corresponding to the qubit initially in $|g\rangle$. The corresponding reference signal is

$$S_{\text{ref}} = (1 - p_e) \sum_k \tilde{P}_k t_{k,g} + p_e t_{0,e} \tag{260}$$

with $t_{k,g}$ the average value of the integrated readout signal for a system in $|k\rangle \otimes |g\rangle$ as defined above, $\tilde{P}_k = |\langle k|\psi\rangle|^2 = |c_k|^2$ the probability of finding k photons knowing that the qubit is initially in $|g\rangle$. These probabilities are precisely what we want to extract. To extract a given $\tilde{P}_m$, one needs to apply a π-pulse at $\omega_q - m\chi$.

After this π-pulse conditioned to Fock state m, the system is in the state

$$\rho_{\text{th},m} = (1 - p_e)|\psi_{m,g}\rangle\langle\psi_{m,g}| + p_e|\psi_{m,e}\rangle\langle\psi_{m,e}| \tag{261}$$

with

$$\begin{cases} |\psi_{m,g}\rangle = \sum_{k\neq m} c_k|k\rangle \otimes |g\rangle + c_m|m\rangle \otimes |e\rangle \\ |\psi_{0,e}\rangle = |0\rangle \otimes |g\rangle \\ |\psi_{m\neq 0,e}\rangle = |0\rangle \otimes |e\rangle \end{cases} \tag{262}$$

Then, the measured signal is

$$S_m = (1 - p_e)\left[\tilde{P}_m t_{m,e} + \sum_{k\neq m} \tilde{P}_k t_{k,g}\right] + \begin{cases} p_e t_{0,g}, & \text{if } m = 0 \\ p_e t_{0,e}, & \text{if } m \neq 0 \end{cases}. \tag{263}$$

7 The value is slightly different from the one given in Fig. 16d since here, the occupation of the higher excited states of the transmon is neglected. These are occupied less than 4% of the experiments, and unless the transmon decays down to $|e\rangle$ during the experiment, they yield no signal on the final readout so that their effect can be assimilated to a global scaling factor.

By subtracting the two signals, it is possible to isolate the contribution of the m-th level from all the other levels. Indeed,

$$\tilde{S}_m = S_{\text{ref}} - S_m = \tilde{P}_m \times (1 - p_e)\,(t_{m,g} - t_{m,e}) - \delta_{m,0} p_e\,(t_{0,g} - t_{0,e}) \tag{264}$$

with δ the Kronecker delta. At this point we have to make an extra assumption. We suppose that, since we wait 2 μs for the cavity to empty after the qubit encode the presence of m photons, the differential signal $t_{k,g} - t_{k,e}$ is independent of k (see Supplementary Information in Ref [125]). We have measured this value for $k = 0$ so that, in the units of Fig. 54b,

$$t_{k,g} - t_{k,e} = t_{\text{diff}} = t_{0,g} - t_{0,e} = 0.3955. \tag{265}$$

Therefore, the occupation of Fock state $|m\rangle$ is given by

$$\tilde{P}_m = \frac{\tilde{S}_m}{(1 - p_e) t_{\text{diff}}} + \delta_{m,0} \frac{p_e}{1 - p_e}. \tag{266}$$

The nonzero thermal population p_e of the qubit only induces an offset in the probability of measuring 0 photon (second term). With no prior knowledge of the qubit state (apart from its statistical population) and without performing any post-selection, one thus accesses the conditional probability of occupying level m on the condition that the qubit is initially in the ground state.

In order not to add extra noise, we do not subtract directly S_{ref} but rather its third order polynomial fit (red line in Fig. 54c). The inferred Fock state probabilities are shown as dotted lines in Fig. 54d. The solid lines correspond to the standard Poisson distribution of a coherent state

$$\tilde{P}_m(\alpha) = e^{-|\alpha|^2} \frac{|\alpha|^{2m}}{m!}. \tag{267}$$

This measurement and comparison with theory also allows us to calibrate the drive amplitude of the displacement rate ϵ_c. This independent calibration was used to scale the axes of the Wigner tomographies shown in Sec. 7.3. Besides, this measurement also demonstrates that the fast displacement pulse shaped with DRAG technique indeed produces a coherent state only when the qubit is in the ground state, and that one can safely ignore any Kerr distortion with so short pulses.

7.2.2 *Fock state occupation for a field under QZD*

Now that this method to measure the occupation of the Fock states of a field has been validated, we apply it to the field developing under the Zeno blockade as described in Sec. 7.1.2.2. While blocking the level $|N\rangle$, a square pulse at ω_c and with length varying from 0 to 3 μs is sent to the cavity. Its amplitude corresponds to a displacement rate $\epsilon_c = 3\ \mu\text{s}^{-1}$ were there no blockade or damping of the cavity. This rate is calibrated as the horizontal axis of Fig. 54d.

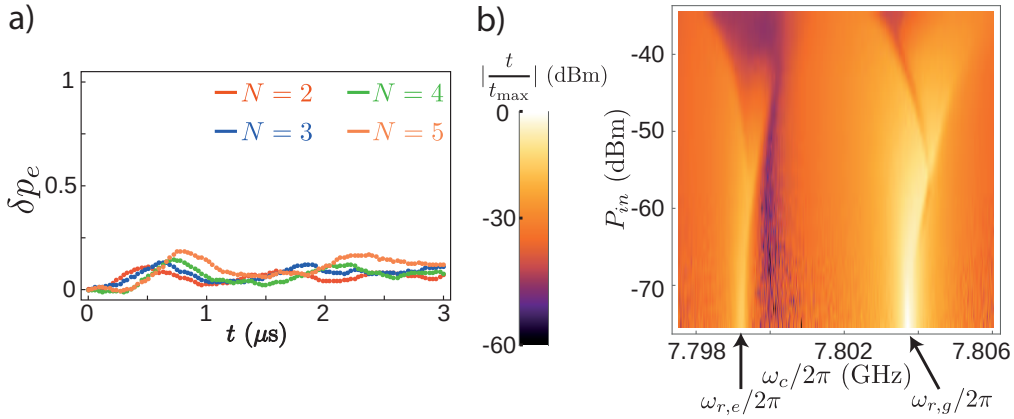

Figure 55: **a**) Measured probability δp_e for spurious excitation of the qubit as a function of time and in presence of a blockade of level $|N\rangle$ (N from 2 to 5). Maximum measured probability: $\delta p_{e,\max} = 18$ %. **b**) When the qubit is at thermal equilibrium, transmission of the cavity (encoded in color) as a function of the probing frequency (horizontal axis) and power (vertical axis). Starting from low power, the resonance frequency shifts toward higher frequencies when increasing probe power, indicating a negative self Kerr λ. This is in opposition to the behavior of other transmons (see Fig. 22). Behavior is canonical for higher probe powers.

Spurious excitation of the qubit as mentioned in Sec. 7.1.2.2 needs to be corrected for to access the $\tilde{P}_m$'s. On Fig. 55a, we present the measured extra probability δp_e of finding the qubit in $|e\rangle$ as a function of time and in absence of any π-pulse, for a blocked level N from 2 to 5. It is inferred from the integrated readout signal that reads

$$S_{N,\mathrm{ref}}(t) = (1 - p_e - \delta p_e(t)) \sum_k \tilde{P}_k t_{k,g} + (p_e + \delta p_{e,N}(t))\, t_{0,e}. \tag{268}$$

The leak into the excited state is therefore given by

$$\delta p_{e,N}(t) = \frac{S_{\mathrm{N,ref}}(0) - S_{\mathrm{N,ref}}(t)}{\sum_k \tilde{P}_k (t_{k,g} - t_{0,e})} \simeq \frac{S_{\mathrm{N,ref}}(0) - S_{\mathrm{N,ref}}(t)}{t_{0,g} - t_{0,e}}. \tag{269}$$

Note that the origin of this leak from ladder $|g\rangle$ to ladder $|e\rangle$ is not fully understood. It is assumed to be a consequence of the finite detuning between the blocking tone at $\omega_q - N\chi$ and the transitions $|g,k\rangle \leftrightarrow |e,k\rangle$ for $k < N$. Yet, a simple model where $p_{k,e}$ comes from detuned Rabi oscillations fails to reproduce our results quantitatively. Moreover, this measurement corresponds to the total extra excitation in state $|e\rangle$ and $\delta p_{e,N}(t)$ is not resolved in Fock state. Assuming all levels $|k\rangle \otimes |e\rangle$ to be equally excited for $0 \leq k < N$ (on top of the thermal excitation), one can infer the effective probability to be in Fock state $|m\rangle$ as in Eq. (266) and making the substitution

$$\tilde{P}_m \leftarrow \tilde{P}_m + \frac{2\delta p_e}{N(1 - p_{N,e})}, \text{ for } 0 \leq m < N. \tag{270}$$

The corresponding probabilities are shown in Fig. 56 as a function of time for several photon numbers m and for a blocked level N from 2 to 5. Levels with more than N

photons are unoccupied, as expected from the Zeno blockade. At small times, the occupation of the levels rise in order starting with level 1, similarly to a coherent state of increasing amplitude (see Fig. 54d). At longer times, the level distribution bounces on a wall at $m = N$, so that the probabilities start to oscillate. The period of the oscillations increases with N as expected, since it takes more time to reach $N-1$ photons with a constant drive as N increases. The case $N = 2$ is straightforward since it implements an effective qubit [49]. The time traces of Fig. 56 correspond to Rabi oscillations of a two-level system that is driven off resonance. For larger N, the evolution is similar to that of a resonantly driven N-level system, as seen in Rydberg atoms [50]. In particular, at half period, $\tilde{P}_0$ displays a plateau all the more pronounced as N gets larger. Finally, the $N-1$ level occupation evolves in opposition to level 0, with a maximum at half period.

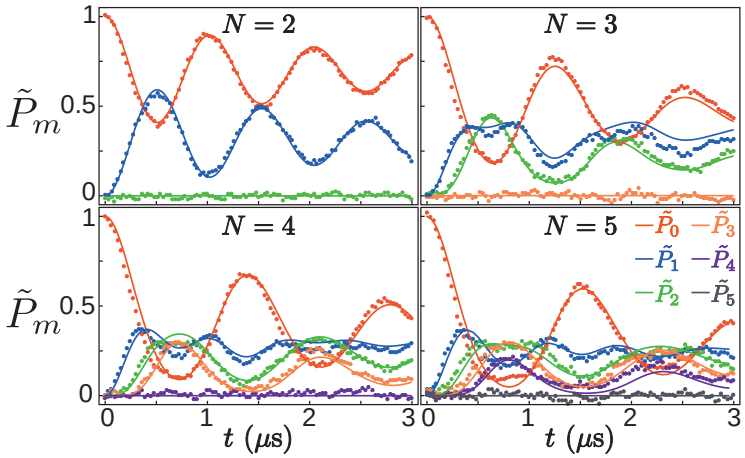

Figure 56: Measured (dots) and theoretical (solid lines) photon number state probabilities $\tilde{P}_m$ for a field under QZD and as a function of time t. The blocked level N ranges from 2 to 5 and is indicated on each panel.

In the frame rotating at ω_c, the evolution of the field can be modeled with the Hamiltonian

$$H_Z = \hbar(\omega_c - \omega_{r,g}) + \hbar\lambda a_N^{\dagger 2} a_N^2 + i\hbar\epsilon_c(a_N^\dagger - a_N), \tag{271}$$

where the annihilation operator a_N has been modified as

$$a_N = a - \sqrt{N}|N-1\rangle\langle N| - \sqrt{N-1}|N\rangle\langle N+1|, \tag{272}$$

so that H_Z is equivalent to the form given in Eq. (255). This hamiltonian takes into account the coherent drive, its detuning, and the nonlinearity of the cavity. The damping of the photons is taken into account in the master equation as (see Eq. (42))

$$\frac{\mathrm{d}\rho(t)}{\mathrm{d}t} = -\frac{i}{\hbar}[H_Z, \rho] + \kappa\mathcal{D}[a]\rho. \tag{273}$$

Note that the annihilation operator a appearing in the damping term is not affected by the Zeno blockade since QZE only inhibits *coherent* transitions between levels (see

Sec. 7.1.1).

Using this model, one can reproduce with a good agreement the photon number probabilities P_m's as shown in solid lines on Fig. 56. All the theoretical results presented here are obtained by numerical resolution of Eq. (273) in a 15-dimensional truncated Hilbert space. This is done by using *QuTip, a Quantum toolbox for Python* [191]. The parameters are chosen as follows to optimally match the measurements.

- The amplitude of the drive ϵ_c, which directly determines the period of the oscillations in the occupation is finely tuned between 2.83 and 3.05 μs for each blocked level N.
- We attribute the origin of the detuning $\omega_c - \omega_{r,g}$ to an energy shift of the levels due to the blocking tone. It was found to be 0.1 MHz for $N > 2$ and 0.4 MHz for $N = 2$. These values are consistent with the levels being more strongly disturbed by the blocking field when closer to N.
- The anharmonicity $\lambda/2\pi = -70$ kHz is slightly modified by the Zeno blockade tone compared to the value that can be inferred from the map on Fig. 55b.

These first measurements demonstrate how the cavity is transformed into an N-level system by inducing dynamically a Zeno blockade at an arbitrary level N. Yet only the photon number probabilities have been investigated so far. A full characterization of the field state is presented in the next section. It is done by directly measuring the Wigner function of the field, which is a representation of a quantum state in continuous variables.

7.3 WIGNER TOMOGRAPHY

Full characterization of the cavity field requires one to measure all the coefficients of its density matrix and not just the diagonal coefficients corresponding to the occupation of the Fock states. An equivalent representation is the *Wigner function* [192, 51]. It is possible to measure directly the value of the Wigner function at a given point α in phase space through a parity measurement of the field. Indeed, a possible expression for $W(\alpha)$ is [51]

$$W(\alpha) = \langle D_\alpha \mathcal{P} D_\alpha^\dagger \rangle, \tag{274}$$

where $D_\alpha = e^{\alpha a^\dagger - \alpha^* a}$ is a displacement under the action of a coherent drive such as the one calibrated in Sec. 7.2.1, and $\mathcal{P} = e^{i\pi a^\dagger a}$ is the photon parity operator. We now describe the parity measurement in Sec. 7.3.1 and use it to measure the Wigner function of a field under QZD in Sec. 7.3.2 following Lutterbach and Davidovich protocol [193, 194, 195].

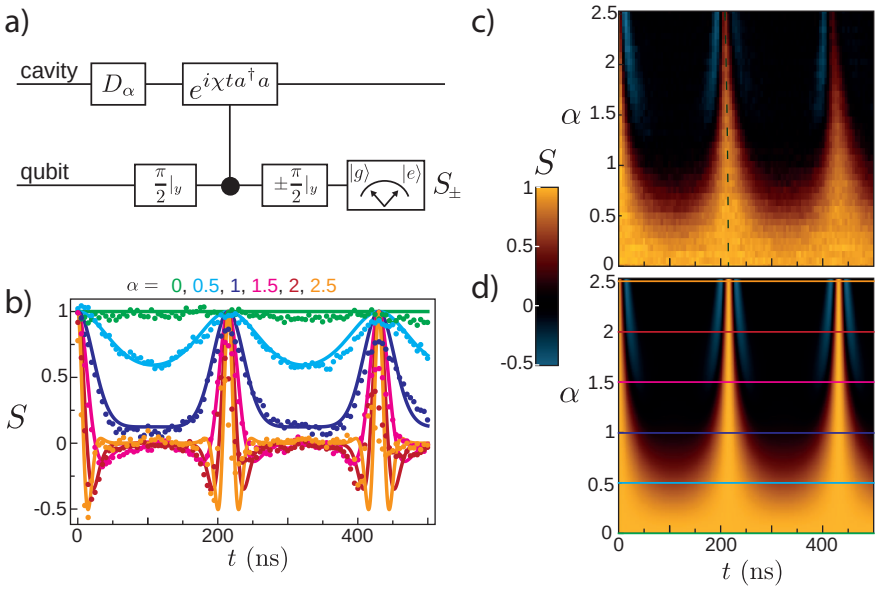

Figure 57: **a**) Circuit diagram for Ramsey interferometry of a coherent state under dispersive interaction. After a 240 ns displacement pulse at the cavity frequency, an unconditional $\pi/2$ rotation is applied to the qubit so that it gets in state $(|g\rangle + |e\rangle)/\sqrt{2}$ whatever the cavity state is. Then, one lets the qubit evolve during a time t and performs a second unconditional $\pm\pi/2$ rotation. Finally, after a 2 μs waiting time to empty the cavity, one measures the qubit state dispersively. **b**) Measured (dots) and predicted (lines) signal S as a function of delay time t for various displacement amplitudes α. Qubit state revival occurs at a waiting time $t_{\text{revival}} = 1/(2\pi\chi)$. **c**) Measured signal S as a function of both delay time t and displacement amplitude α. At larger amplitude, the revival time shifts to smaller values. The dashed line corresponds to a theory including a higher order interaction term $\beta a^\dagger a^\dagger a a |e\rangle\langle e|$ in the Hamiltonian, with $\beta = -23$ kHz. **d**) Predicted signal S as a function of both delay time t and displacement amplitude α. It is obtained using a simple theory without higher order interaction term (Eq. 282). Lines show cuts from **b**.

7.3.1 *Photon parity measurement*

The procedure to measure the parity of a field is schematized in Fig. 57a. It is calibrated on a coherent field $|\alpha\rangle$. Starting from the vacuum[8], we apply a fast displacement $D(\alpha)$. We then perform a Ramsey interferometry experiment such as the one described on Fig. 16, consisting in applying two $\pi/2$ pulses on the qubit, independent of the cavity state, separated by a time t. Since the qubit frequency depends on the photon number in the cavity, the phase accumulated during t depends on this number. For a well chosen time, this phase is 0 (mod 2π) for any even number of photons, and π (mod 2π) for any odd number of photons. The second $\pi/2$ pulse then maps the photon parity onto the qubit states $|\pm z\rangle$. By measuring the qubit and correcting for the imperfections described in Sec. 7.2.1, we thus directly measure the parity of the field.

8 if starting from an arbitrary field state, this sequence corresponds to the measurement of $W(\alpha)$

A key point here is to be able to perform broadband qubit rotation so as to succeed independently of the photon number in the cavity. It is performed by shining a 50 ns broadband pulse at ω_q. We have used a "sinc" shape and a gaussian envelope to design a pulse bandwidth larger than 10χ. At the photon level considered in the experiment ($k < 10$), this $\pi/2$-rotation of the qubit can be regarded as unconditional.

We model the dressed interferometry experiment as follows. After the displacement $D(\alpha)$ and taking into account the $p_e = 22$ % spurious excitations of the qubit at thermal equilibrium, the total density matrix describing the cavity-qubit system is

$$\rho_{\text{th}}(0) = (1-p_e)|\alpha\rangle\langle\alpha| \otimes |g\rangle\langle g| + p_e|0\rangle\langle 0| \otimes |e\rangle\langle e|, \tag{275}$$

with $|\alpha\rangle = e^{-\frac{|\alpha|^2}{2}} \sum_{k=0}^{\infty} \alpha^k |k\rangle/\sqrt{k!}$ the coherent state of amplitude α. The displacement is fast enough so that the state is coherent despite Kerr terms.

Then, one applies a broadband $\pi/2$ pulse, lets the qubit evolve during a time t and applies another broadband $\pm\pi/2$ pulse (see Fig. 57a). In practice, two types of experiments are performed with a final pulse either $+\pi/2$ or $-\pi/2$. At the end of this Ramsey sequence, the density matrix is

$$\rho_{\text{th},\pm}(t) = (1-p_e)|\psi_{g,\pm}\rangle\langle\psi_{g,\pm}| + p_e|\psi_{e,\pm}\rangle\langle\psi_{e,\pm}|, \tag{276}$$

with

$$\begin{cases} |\psi_{g,\pm}\rangle &= R|_{\pm\frac{\pi}{2}} e^{i\chi t a^\dagger a|e\rangle\langle e|} R|_{\frac{\pi}{2}} |\alpha\rangle \otimes |g\rangle \\ |\psi_{e,\pm}\rangle &= R|_{\pm\frac{\pi}{2}} e^{i\chi t a^\dagger a|e\rangle\langle e|} R|_{\frac{\pi}{2}} |0\rangle \otimes |e\rangle \end{cases} \tag{277}$$

and $R|_\theta = \exp(-i\frac{\theta}{2}\sigma_y)$. One finds

$$\begin{cases} |\psi_{g,\pm}\rangle &= \frac{1}{2}\left(|\alpha\rangle \mp |\alpha e^{i\chi t}\rangle\right) \otimes |g\rangle + \left(\pm|\alpha\rangle + |\alpha e^{i\chi t}\rangle\right) \otimes |e\rangle \\ |\psi_{e,+}\rangle &= -|0\rangle \otimes |g\rangle \\ |\psi_{e,-}\rangle &= |0\rangle \otimes |e\rangle \end{cases} . \tag{278}$$

After this Ramsey sequence, the integrated transmitted signal, measured at readout frequency is (see Sec. 7.2.1)

$$\begin{cases} S_+ = & \frac{1}{4}(1-p_e)e^{-|\alpha|^2} \sum_k \frac{|\alpha|^{2k}}{k!} \left[\left(2 - e^{ik\chi t} - e^{-ik\chi t}\right) t_{k,g} + \left(2 + e^{ik\chi t} + e^{-ik\chi t}\right) t_{k,e}\right] \\ & + p_e t_{0,g} \\ S_- = & \frac{1}{4}(1-p_e)e^{-|\alpha|^2} \sum_k \frac{|\alpha|^{2k}}{k!} \left[\left(2 + e^{ik\chi t} + e^{-ik\chi t}\right) t_{k,g} + \left(2 - e^{ik\chi t} - e^{-ik\chi t}\right) t_{k,e}\right] \\ & + p_e t_{0,e}. \end{cases} \tag{279}$$

Therefore, the differential signal is

$$S_- - S_+ = \frac{1}{2}(1-p_e)e^{-|\alpha|^2} \sum_k \frac{|\alpha|^{2k}}{k!} \left[\left(e^{ik\chi t} + e^{-ik\chi t}\right)(t_{k,g} - t_{k,e})\right] - p_e\left(t_{0,g} - t_{0,e}\right). \tag{280}$$

Assuming a linear readout $t_{k,g} - t_{k,e} = t_{0,g} - t_{0,e}$ as in Sec. 7.2.1, the reduced signal, defined similarly to Eq. (266), is

$$S(\alpha, t) = \frac{S_- - S_+}{(t_{0,g} - t_{0,e})(1 - p_e)} + \frac{p_e}{1 - p_e} = \exp\left[|\alpha|^2 \left(\cos(\chi t) - 1\right)\right] \cos\left[|\alpha|^2 \sin(\chi t)\right]. \tag{281}$$

This measurement is performed differentially in order to avoid spurious effects due to the cavity anharmonicity (see Supplementary Information in Ref [125]).

Fig. 57 displays the corresponding measurements (b and c) and theory (d), similarly to the experiment of Vlastakis *et al.* [195]. After a time $t_{\text{revival}} = 2\pi/\chi = 216$ ns, there is a revival in the Ramsey signal. This is in agreement with the spectroscopic measurement $\chi/2\pi = 4.63$ MHz (see Fig. 53b). As time increases, there is a reduction in revival visibility partly due to qubit dephasing and to cavity relaxation at large displacements.

At last, one can notice a shift of the revival time as a function of displacement amplitude in the experiment (Fig. 57c), not visible in theory (Fig. 57d). Following Ref. [195], we model this effect by a supplementary higher order interaction term in the hamiltonian, which reads $\beta a^\dagger a^\dagger a a |e\rangle\langle e|$. To first order, this non-linearity results in a small change in the revival time

$$\begin{aligned} t_{\text{revival}} &= \tfrac{2\pi}{\chi}(1 + \langle a^\dagger a \rangle \tfrac{\beta}{\chi}) \\ &= \tfrac{2\pi}{\chi}(1 + |\alpha|^2 \tfrac{\beta}{\chi}) \text{ for a coherent state.} \end{aligned} \tag{282}$$

Fitting the experimental revival time (dashed line in Fig. 57c), one finds a non-linear frequency $\beta/2\pi = -23$ kHz. Like the cavity self-Kerr anharmonicity λ, this term is opposite to what has been previously observed [195].

7.3.2 *Wigner function of a field under QZD*

In the experiment, the state of the cavity is unknown and one wants to perform its tomography. To measure the photon parity, we chose a waiting time $t_{\text{wait}} = \pi/\chi = 108$ ns such that the evolution operator of Fig. 57a is $\exp(i\pi a^\dagger a |e\rangle\langle e|)$. The experimental Wigner function can therefore be defined as $W(\alpha) = S(\alpha, t_{\text{wait}})$. Note that the thermal population of the qubit has been corrected for, but the spurious thermal excitation are not taken into account in the model presented in the previous section. It changes the value of p_e so that there is an offset in the Wigner distributions (see Eq. (281)). Moreover, the uncalibrated attenuation of the lines and cavity transmission induce a scaling factor in the Wigner distributions. In practice, for each Wigner distribution, the zero was defined as the integral far outside the exclusion circle and a scaling factor was applied to normalize the integral of the distribution.

On Fig. 58, we plot the measured Wigner distributions (encoded in color) as a function of time, for a Zeno blockade of level 3 (top panel) and 4 (bottom panel). For each distribution, we also plot (lower panels) the theoretical prediction using the same model and numerical simulation as on Fig. 56 (see Eq. 273). The barrier is materialized by a white dotted circle (radius $\sqrt{N}$). As expected, $W(\alpha) = 0$ outside of these

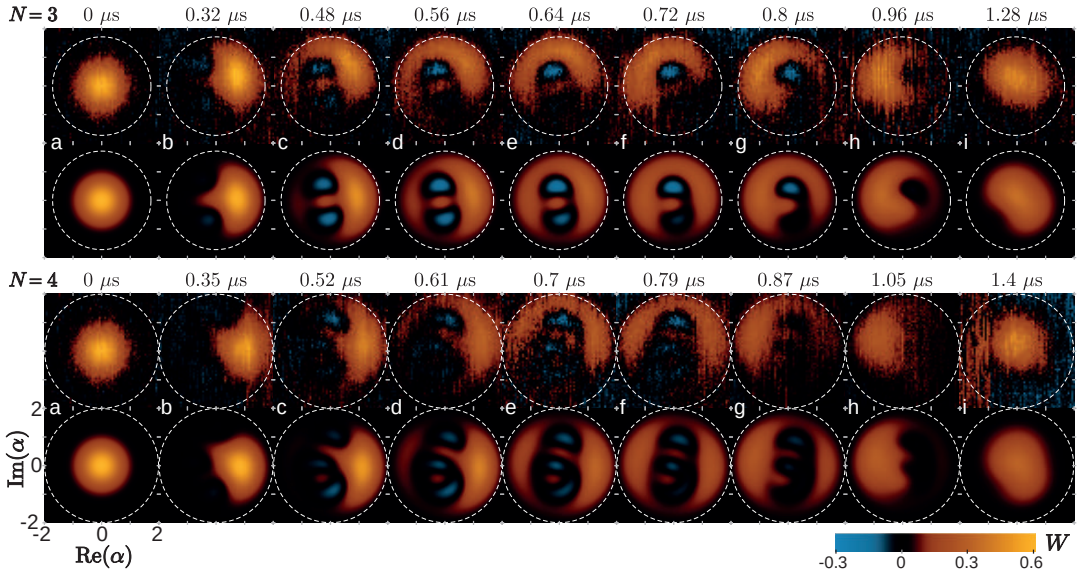

Figure 58: Shown are measured (top rows) and predicted (bottom rows) Wigner functions $W(\alpha)$ as a function of the displacement amplitude α, for a blockade at N = 3 (top panel) and N = 4 (bottom panel). The time t (nonlinear scale) for the frames shown in a-i is given above each panel. The field is confined in phase space by a Zeno barrier at amplitude $\alpha = \sqrt{N}$ (white dashed circle). Negative values of the Wigner function, in blue, demonstrate the non-classical nature of the field produced under QZD. The model used is the same as for Fig. 56. Note that Wigner functions are here directly measured and not reconstructed.

circles. At t=0 (panel a), the field is in the vacuum state, corresponding to a gaussian centered in 0 and of standard deviation $\frac{1}{2}$. When the cavity is driven, at small times, a nearly coherent state $|\beta\rangle$ develops inside the cavity so that the Wigner distribution is the same gaussian shifted by β (panel b). For longer times (panels c-h), the distribution "bounces" off the wall and reappears at negative Re[α]. In between, it displays interference fringes with some negative parts (in blue). These negativities of the Wigner function are characteristic of *non gaussian* states and are a purely quantum feature [51]. After a full period that depends on N, the field is again in a state close to the vacuum (panel i). The broader distribution compared to (a) is explained by the decoherence of the field due to the damping of the cavity. The asymmetry of the distributions comes from the self-Kerr of the cavity and is captured by the theoretical model.

The strongest negativities appear at half period of the oscillation. On Fig. 59, we show the Wigner distributions for blocked levels from 2 to 5. The color scale is rescaled compared to Fig. 58. Near 0, these distributions all exhibit fringes with negative parts. The photon parity of the non displaced field $W(0)$ is that of the highest allowed level N-1, which is also the number of negative fringes. These properties are reminiscent from a quantum superposition between the two coherent states of amplitude $\sqrt{N-1}$, so called "Schrödinger cat states" [51]. However, here the distribution is confined within

the Zeno barrier in opposition to cat states distributions, which are infinite.

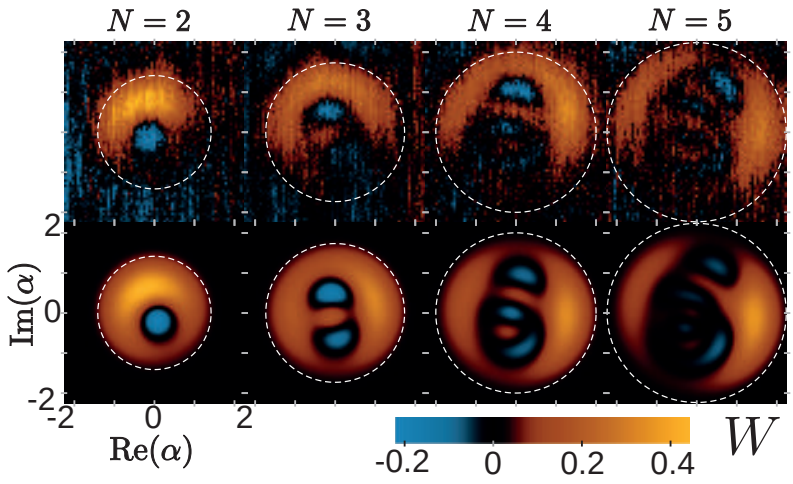

Figure 59: Wigner tomography at half period. Measured (top row) and calculated (bottom row) Wigner functions of the cavity field for various blockade levels N from 2 to 5, taken at half period ($t = 0.51$ μs, $t = 0.64$ μs, $t = 0.7$ μs and $t = 0.75$ μs). The color scale is rescaled compared to Fig. 58 by A=0.7. Similarly to "Schrödinger cat states", these states exhibit fringes with alternating positive and negative values.

We have thus demonstrated that, coupling an electromagnetic mode dispersively to an ancillary qubit and driving coherently a transition of the hybrid system, we could inhibit coherent transitions to or from a given Fock state $|N\rangle$. When starting from a state with no overlap with the levels $|k\rangle$ for $k > N-1$, the evolution of the mode state is confined in phase-space. An electromagnetic mode having an infinite Hilbert space, we could in principle choose N as large as we want. However two parameters limit this choice. First, the decay rate of level $|k\rangle$ is $k\kappa$. Thus, coherent oscillations of the induced N-level system can only be observed if the oscillation period is shorter than $1/(N\kappa)$. Since the displacement rate ϵ_c is qualitatively limited by the Zeno barrier "height" ϵ_d, in the case of the experiment presented here, coherence after one oscillation is hardly retained for $N > 5$. However, for a cavity and qubit with sufficiently long decay and coherence times, one could in principle choose an arbitrarily large N-level system. A second limitation is the anharmonicity induced on the cavity mode by its hybridization with the qubit (see Eq. (61)). In the next section, we show that, when driven at $\omega_{r,g}$, oscillations appear in the level occupations even in the absence of any Zeno blockade. However, the Wigner tomography reveals a qualitatively different dynamics from QZD.

7.3.3 *A tailorable infinite Hilbert space?*

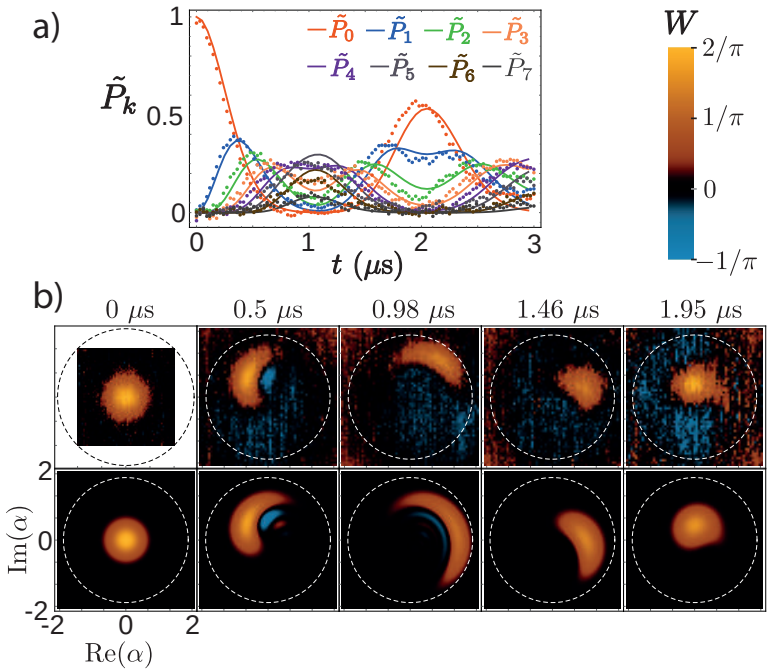

Figure 60: **a**) Measured occupation of the cavity Fock states as a function of time in absence of Zeno blockade. The strong Kerr effect induces oscillations in the level occupation which are qualitatively different from Zeno oscillations: at half period, the occupation $P(k)$ decreases smoothly to 0 as a function of k. **b**) Snapshots of the measured Wigner function of the same field. Negativities are clearly visible, indicating that the system is nearly in the single-photon Kerr regime [125]. However, no fine interference pattern is visible as on Fig. 59.

We now characterize the field that develops in the cavity in the same conditions[9] as the experiment presented on Fig. 54 or Fig. 58, but without Zeno blockade. With the same displacement rate $\epsilon \simeq 3\ \mu s^{-1}$, we detect oscillations of the Fock state occupation probability with a period $T_{\text{Kerr}} = 2\ \mu$s (see Fig. 60a). These oscillations look qualitatively very similar to the ones appearing under QZD (see Fig. 56). However, the amplitude of these oscillations decrease smoothly to 0 when considering Fock states of higher energy. On Fig. 60a, the probability of occupation of level $N = 7$ (in black) is small, but clearly visible. On the other hand, for a field under QZD, in all considered cases, no population can be detected in the blocked level N, but the probability of occupation of all the levels within the Zeno barrier clearly oscillates.

Further differences appear when comparing the Wigner functions for a field distorted by the cavity non linearity [125] (Fig. 60b) and a field under QZD (Fig. 58). In the first case, even though some negativities are observed, the interference pattern does

9 Note that the situation is different from Sec. 7.2.1 when the displacement after which the P_m's were measured was performed by a short and intense pulse. This was precisely done to avoid Kerr induced distortions of the coherent state.

not include a large number of fringes as one would expect for such a large field under QZD (the white circle has radius $\alpha = \sqrt{8}$, which would be the position of the Zeno barrier needed to get such an extended distribution.

The observed negativities show however that our system is nearly in the *single photon Kerr regime* [125] and are consistent with $\lambda \simeq \kappa$. For a large enough non linearity, a non driven coherent state should collapse quickly, but is expected to exhibit revivals at integer submultiples of $1/\lambda$. At these times, Schrödinger cat states are formed [196]. In our experiment, the fast decay of coherences due to photons damping prevents us from observing such revivals.

In this chapter, we described a scheme for quantum control consisting in tailoring dynamically the Hilbert space of a system in time. Combined with multi qubit operations or detection, QZD can be used to generate and protect entanglement [197, 198, 199]. It can also be used to implement logic gates [200]. Considering evolutions outside of the exclusion circle, where the barrier acts as a peculiar scatterer in phase space[39], other cat-like states and squeezed states could be produced. Finally, combined with fast displacement pulses so as to effectively move the position of the Zeno barrier, one could realize phase space tweezers of light in a high-Q cavity [38].

7.4 CONCLUSION

In this part, we have described three modes of quantum control on the qubit. Measurement based feedback allows us to stabilize a state by extracting information, via dispersive measurement or fluorescence detection, and to react on the system accordingly, on a time scale much shorter than the qubit lifetime. In autonomous feedback, the qubit is coupled to a highly dissipative system, which is the cavity, to effectively engineer its dissipation. This allows us, for instance, to cool down a thermally excited qubit. Finally, we used the qubit to stabilize coherently a subspace of the cavity mode Hilbert space. Departure from this subspace due to coherent processes is inhibited.

The main results of this part are

- Demonstration of a stroboscopic feedback protocol to stabilize an arbitrary state or trajectory of the qubit. This scheme benefits from a high fidelity, single-shot, QND readout of the qubit.
- Implementation of a continuous analog feedback protocol using the detection of the fluorescence of the qubit. It effectively engineers the system dissipation so as to stabilize an arbitrary state.
- Observation of Quantum Zeno Dynamics of a microwave mode. The qubit is used as an ancillary system to enforce QZD via coherent controls.

Evacuation of entropy is essential for a quantum machine to be used in information processing. Strong engineered dissipation can also be used to implement error

correction[178, 201], which is a crucial step toward fault-tolerant quantum computation, or to generate entanglement [178, 179, 180]. Measurement based feedback, effectively engineering dissipation in the continuous case, may prove to be a complementary tool to autonomous techniques. Stroboscopic feedback based on parity measurements of several physical qubits [182, 183, 184] can also be used to implement error correction on a collective logical qubit. Recent experimental developments towards this aim show great promise [202, 203, 204, 205].

Part III

APPENDIX

A

EXPERIMENTAL TECHNIQUES

A.1 QUBITS FABRICATION AND CHARACTERIZATION

The transmons used in the experiments described throughout this thesis follow the design developed at Yale by Paik *et al.* [13]. In this section, we describe in details the fabrication process that was developed in our experiments and the attempts that were made to improve thermalization and coherence times of the qubits. Table 3 summarizes the fabrication parameters and measured characteristics of the qubits used in the experiments.

Table 3: **List of characterized qubits.**
Gray: aluminum cavity in Cu box covered with Eccosorb and SiC powder. Red: copper cavity in Cryoperm shield and aluminum foil.
Green cells indicate HCl surface etching of the cavity prior to cool down.
Brown: 0.05 mm × 1.5 mm antennas. Yellow: 0.4 mm × 1 mm antennas
Blue: silicon chip instead of sapphire chip.
Cavity surface state appears to be the dominant factor to determine qubit thermal anchoring and coherence time.

	ref	$\frac{\omega_c}{2\pi}$ (GHz)	$\frac{\kappa}{2\pi}$ (MHz)	$\frac{\omega_q}{2\pi}$ (GHz)	$\frac{\chi}{2\pi}$ (MHz)	$\frac{\alpha}{2\pi}$ (MHz)	T_1 (μs)	T_2 (μs)	$P_{eq}(\|g\rangle)$	$\Gamma_\uparrow$ (ms^{-1})	Γ_ϕ (ms^{-1})
1	T3D32	7.75	1.85	3.73	1.6	198	28	11.5	97.6 %	10	69
2	T3D40	7.76	0.254	5.19	5.2	160	16	10.5	71.5 %	18	64
3	T3D51	7.80	0.123	5.62	4.63	172	11.5	8.9	58 %	37	69
4	T3D59	7.89	3.45	6.3	11.5	158	4.1	6.2	$\geq$ 99 %	2.5	40
5	T3D59	7.89	1.1	6.41	11.5	157	5	2	93 %	14	400
6	T3D22	7.83	6.0	6.11		180	4	1.5	89 %	28	541
7	T3D25	7.63	1.8	4.08	2.9	196	17	14	85 %	9	42
8	QMD02	8.13	0.135	4.58	2.7	160	10	6.2	77 %	23	111

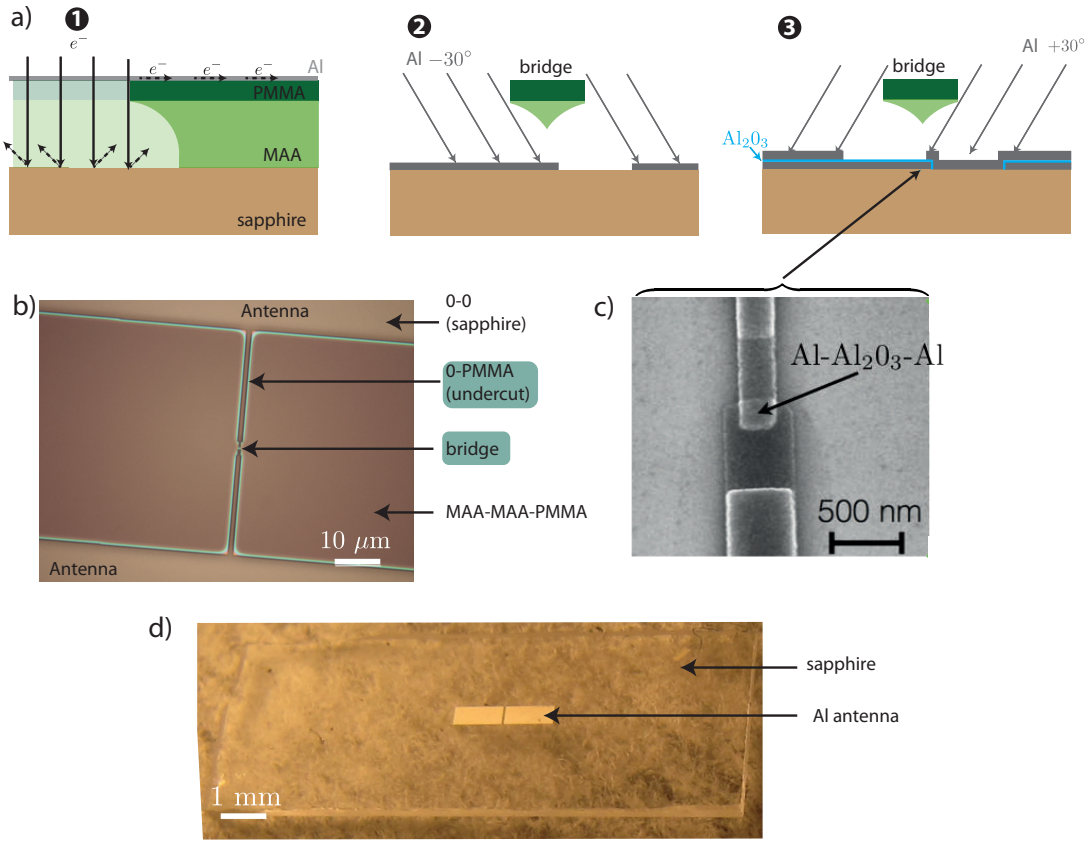

Figure 61: Sample fabrication. **a**) Schematic representation of the double-angle evaporation process used for Josephson Junction fabrication. A bi-layer MAA/PMMA of electro-sensitive resist is spin-coated on the substrate. A thin layer (10 nm) of aluminum is deposited on top of the resist in order to evacuate charges during lithographhy. During e-beam lithography, the resist polymers are cracked on the exposed areas (step 1). Note that the cracked polymers are not removed until development (not represented here for clarity). The MAA being more sensitive, an undercut is formed by backscattered electrons on the substrate. After development, a PMMA bridge is formed (step 2). A first layer of aluminum is then evaporated at an angle $-30°$. Static oxidation then forms an insulating barrier (in blue) before that a new layer is evaporated at $+30°$ (step 3). **b**) Optical microscope picture of the resist mask after development. The undercut appears in green. **c**) E-beam microscope picture of a Josephson junction (completed fabrication process). **d**) Picture of the sample ready to be placed in a cavity.

The transmon circuits are fabricated by double angle evaporation (see Fig. 61) of aluminum (Al 5N) on 10×7 mm chips. The size of the chips was progressively changed to 11×4 mm. The height of the 3D cavities used in the experiments being set to 9.6 mm, the longer height aimed at better thermalizing.
The first samples used high resistivity silicon substrate (500 μm thickness). Indeed, silicon is easier of use during e-beam lithography, the charges being more easily evacuated,

which avoid drifts during the e-beam exposure. Once the fabrication process better characterized, the following samples were fabricated on C-plane oriented, 430 μm thick sapphire substrate. Note that fabrication is made on diced chips, and not on entire wafers. The fabrication recipe steps are as follows.

Substrate cleaning. Once diced, the chip surface needs to be cleaned.

- Acetone sonicate for 1 min. IPA rinsing.
- Plasma 0_2 for 10 min.

Spin coating. Double-layer spin coating and thin layer aluminum deposition is performed in Paris 7 Diderot clean room facility.

- Bake at 180°C for 1min on a hot plate.
- One drop of MAA. Spinning for 1 min at a speed of 4000 rpm and 400 rmp/s acceleration.
- Bake at 180°C for 4min (2 min is sufficient for silicon due to higher thermal conductivity) on a hot plate.
- One drop of PMMA. Spinning for 1 min at a speed of 4000 rpm and 400 rmp/s acceleration.
- Bake at 180°C for 4 min on a hot plate.
- For a sapphire chip, evaporate a 10 nm layer of aluminum to avoid charge accumulation during lithography.

E-beam lithography. Lithography is performed on a Raith e-beam masker in the ENS clean room facility. The whole pattern is done in a single step-lithography.

- For the junction and the aluminum fingers that link it to the antennas (see Fig. 61b), aperture 7.5 μm, insolating dose 450 μC.cm^{-2} for sapphire (300 μC.cm^{-2} for silicon).
- For the antennas (see Fig. 61d), aperture 120 μm, insulating dose 450 μC.cm^{-2} for sapphire

Developement

- Remove the aluminum layer by plunging the chip in a KOH solution. Necessary duration and concentration of the solution can vary, wait until the film is no more visible with bare eyes.
- 42 s in a MIBK 1:3 IPA solution at room temperature.
- Stop development by plunging the chip for 20 s in IPA.

Aluminum deposition High purity aluminum deposition is performed in Paris 7 Diderot clean room facility in a Plassys e-beam evaporator.

- Pump chamber for at least 45 min ($P < 3 \times 10^{-6}$ mbar).
- Evaporation of 40 nm of titanium, with shutter still on, in order to lower further the chamber pressure and remove water residue.
- 4s ion milling (parameters 500V, -100V, 50 mA, 12sccn $Ar0_2$) at $-30°$ and $+30°$.
- First Al layer deposition: 35 nm, $-30°$, 1 nm.s^{-1}.
- Static oxidation. $Ar0_2$ (80 %Ar-20 %0_2), 20 mbar for 7 min.
- Second Al layer deposition: 100 nm, $+30°$, 1 nm.s^{-1}.

Note that the evaporator is time-shared and also used for nickel evaporation. This may explain limited qubit coherence times. The chip edges are protected with kapton tape to avoid Al deposition.

Lift-off

- At least 15 min in acetone at 55°C.
- *No sonicate*
- Remove Al foil. Stir the solution with pressurized acetone using a syringe if necessary.
- Rinse in IPA.

A.1.2 *Wafer probing*

Since the wafers are diced prior to lithography, sample fabrication is made chip by chip. More than 60 samples were fabricated, but only 8 were actually cooled down for complete characterization. Indeed, as a first step after fabrication, the resistance R_N^T of the transmon junction in the normal state is measured on a wafer probe station at room temperature. The probe setup is schematized on Fig. 62 and includes a large resistor R in series with the junction to avoid large current flowing through the junction, and a variable resistor $0 - R$ to avoid abrupt voltage variations across the junction when contacting the electrodes. The junctions that we fabricate range from 2 to 8 kΩ, so that we set $R = 100$ kΩ.

About 50 % of the samples were measured to be shorted ($R_N \leq 1\ \Omega$) or open ($R_N = \infty$). On the samples successfully fabricated, we observed a variation of the resistance within a batch of fabrication (aluminum deposition at the same time) of about 10 %. The wafer probe step is thus essential to post-select the sample that displays the closest resistance to the targeted one. The target resistance depends on the desired junction critical current I_0 in the superconducting state, which sets the qubit resonance frequency (see Sec. 2.2.3).

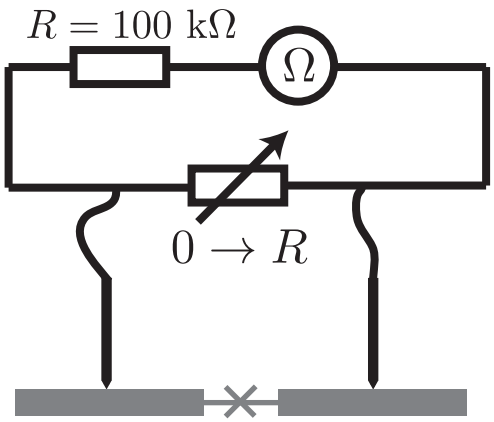

Figure 62: Wafer probing. A large resistor R is placed in series with the junction to avoid large currents flowing through it. In order to avoid abrupt release of the charges accumulated on the points through the junction, contacting is made while the points are short-circuited by the variable resistor set to 0. Its value is then slowly increased to $R = 100$ kΩ $\gg R_N$. The measured resistance then reads $R_m = R + (R_N||R) \simeq R + R_N$.

One can deduce I_0 from R_N via the Ambegaokar-Baratoff formula

$$I_0 = \frac{E_J}{\varphi_0} = \frac{1}{R_N^0}\frac{\pi\Delta}{2e}, \tag{283}$$

where e is the electron charge, $\varphi_0 = \frac{\hbar}{2e}$ is the flux quantum, and $\Delta = 180\ \mu eV$ is the aluminum superconducting gap. Note that R_N^0 is the resistance of the junction in the normal state at zero temperature, which is typically 10 % lower than the measured resistance R_N^T at room temperature. In practice, the target resistance is rather computed from a previously measured qubit making the approximation $\omega_q = \sqrt{8E_J E_C} \propto \frac{1}{R_N^{1/2}}$.

A.1.3 *Cavity machining and surface treatment*

The 3D cavities used in the experiments were fabricated in the ENS machine shop from high purity (4N) Aluminum or OFHC copper. The cavity two halves are symmetric (see Fig. 8a and Fig. 10a) except that a gutter is carved on one half only to host an Indium thread used to seal the cavity, and a notch to place the transmon chip. The part of the chip that is slid in that notch (out of the resonant cavity) is covered with a 100μm-thick indium foil folded over. Indium is chosen for its plasticity, in order to apply a uniform pressure on the chip for thermalization.
The cavities are then anchored by copper braids to the refrigerator base plate (see Fig. 63). Aluminum cavities are enclosed in a copper box covered with Eccosorb CRS 117 PTA mixed with SiC beads to scatter and absorb infrared radiations [206]. Copper cavities are wrapped in an aluminum foil and placed in a cryoperm box to provide magnetic shielding.
Note from Tab. 3 that the dominant factor for qubit thermalization appears to be the cavity surface finish. In green are highlighted the transmons for which the cavity

surface was etched in highly concentrated (37 %) HCl acid[1]. These samples display lower thermal excitation rates for the qubit, and longer coherence times. In particular, qubits 4 and 5 use the same chip and cavity, but the cavity was properly etched in acid for qubit 4. When not etched, the properties of the cavity seem to degrade with each opening of the refrigerator (qubits 1, 2 and 3 use the same cavity in chronological order).

A.2 WIRING AND CRYOGENICS

A.2.1 *Wiring the dilution refrigerator*

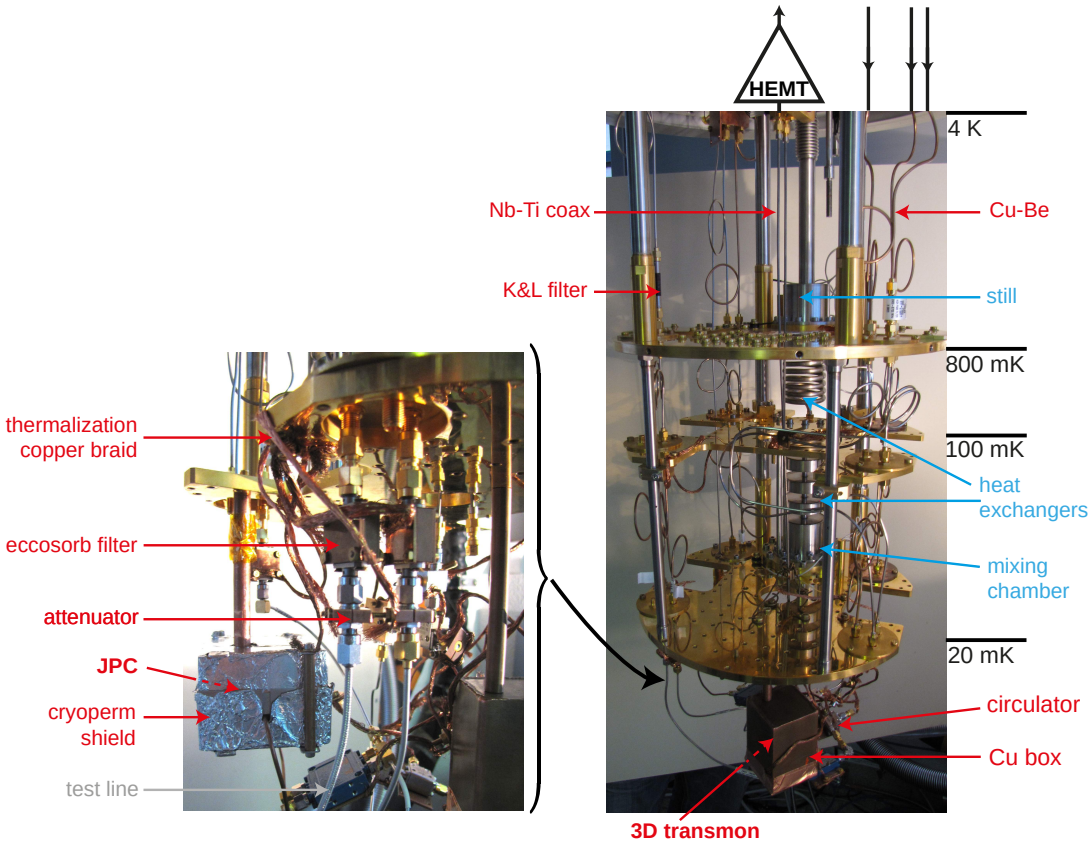

Figure 63: Pictures of the Bluefors dilution refrigerator and various RF components. The conformable cables labelled *test lines*, not present for the actual experiment, are used to calibrate the transmission of the lines before closing the refrigerator.

The experiments described in this thesis have been performed in a *Bluefors* dry dilution refrigerator with a base temperature of 20 mK (see Fig. 63). Wiring of the input and output lines needs to limit thermal conductance between stages. Circulators at base temperature allow us to decouple input and output lines. Note that all RF lines (except Nb-Ti) are commercially connectorized, which may result in a better impedance

1 beware that the reaction with aluminum becomes explosive once the oxide layer has been removed. Use of aluminum etchant is recommended

matching with 50 Ohms components compared to home-made connectors, and may thus explain partly the high detection efficiency reported in [81]. Full schematic of the wiring for the experiment implementing stroboscopic feedback (see Sec. 5.1 and [207]) is represented on Fig. 64. Schematic for the experiment witnessing Zeno dynamics of a microwave mode (See Chap. 7 and [83]) is presented on Fig. 66. The low temperature setup is the same for the experiments in which the fluorescence signal is averaged on post-selected ensembles (see Chap. 4 and [82]), used to reconstruct quantum trajectories (see Sec. 3.4), and to implement continuous analog feedback (see Sec. 5.2).

Input lines are strongly attenuated and filtered to progressively thermalize the electromagnetic field down to the base temperature. Note that the attenuators are thermally anchored at each stage using copper clamps. Furthermore, Cu-Be, CuNi and stainless steel semi-rigid coaxial cables are used on the way down as a tradeoff between the heat exchange between the stages and the dissipation of microwaves frequencies. At base temperature, mostly copper coaxial cables are used to minimize the losses between the cryogenic microwave components. Home-made Eccosorb filters (copper microstrip embedded in Eccosorb), and commercial K&L 12GHz lowpass filters are also inserted on the lines for infrared radiations filtering. This is needed to avoid quasi particle creation in the superconducting aluminum that would limit the qubit coherence and relaxation times [88].

High detection efficiency is achieved by pre-amplifying the signal with a JPC, the following amplifier being a commercial, low-noise High Electron Mobility Transistor (HEMT) amplifier from Caltech university, anchored at 4 K. Superconducting NbTi coaxial cables are used for the output lines between the base temperature and the HEMT in order to minimize the losses as well as the heat exchange between these stages. A bias-tee anchored at base temperature is inserted on the line. It allows to thermalize the coaxial cable core at 20 mK while transmitting with negligible losses the microwave signal.

A DC line is also used in order to current bias the coil which provides the magnetic flux threading the JPC loop. This DC line is twisted to avoid flux noise and is strongly filtered using homemade Ecosorb filter that dissipates out infrared frequencies. Below 4K, the twisted pair is made in NbTi to avoid Joule dissipation and above 4K in manganin to minimize heat exchange.

A.2.2 *Room temperature pulse generation and measurement setup*

Microwave pulses at a given pulsation ω (typically ω_r or ω_q) are generated at room temperature by mixing a local oscillator (LO) at $\omega + \omega_h$ with a sine waveform at ω_h windowed by a gaussian or square envelop. This waveform is generated by an Arbitrary Waveform Generator AWG4014x from *Tektronix*. The AWG has a sampling frequency of 1.2 GSample.s^{-1} with a bandwidth of 450 MHz, and we thus we choose ω_h in the 40-125 MHz range. Finite frequency modulation is chosen so that the leaking LO signal is detuned from the system resonance frequency.

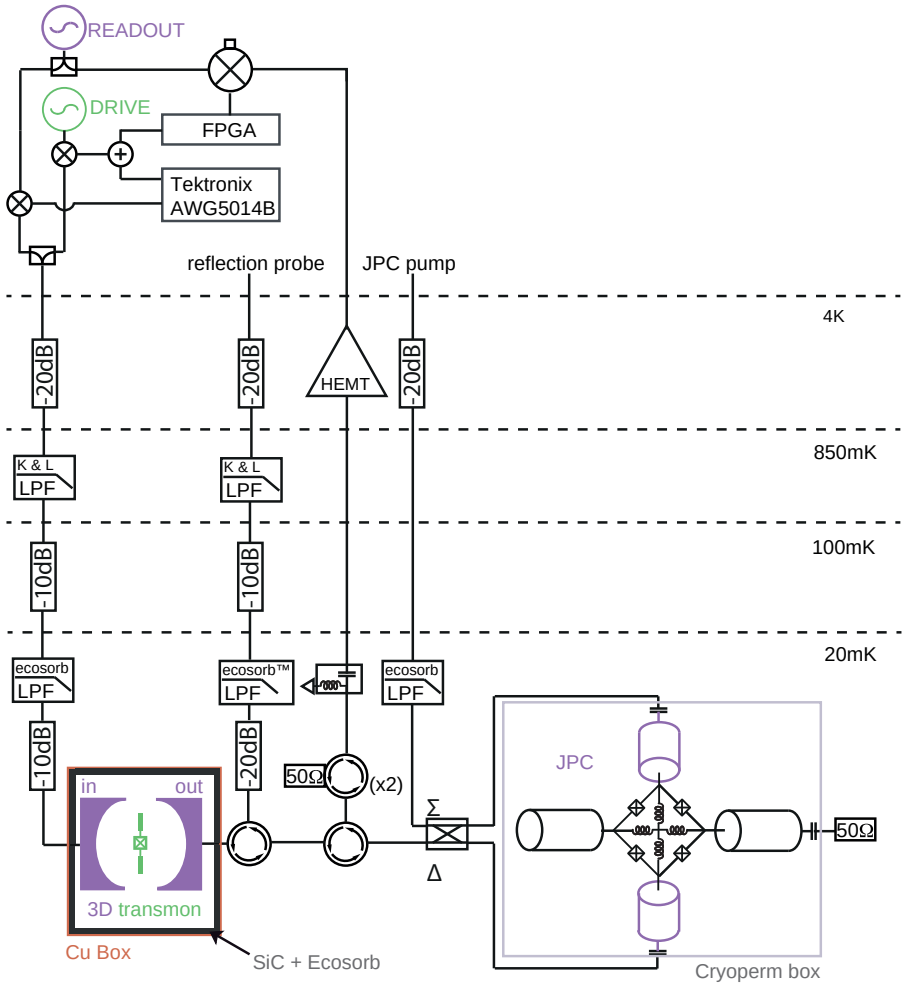

Figure 64: Full schematic of the wiring for the stroboscopic feedback experiment described in Sec. 5.1. Input lines are attenuated and filtered with home-made Eccosorb filters and commercial K&L 12GHz lowpass filter. The reflection probe is used to characterize the cavity ports coupling rates and to facilitate the adjustment of the JPC amplification gain and bandwidth. The amplification is performed in reflection using circulators. A 180° hybrid coupler allows to address on different lines the signal and pump modes of the JPC [120]. Circulators are also used for insulation from the HEMT amplifier noise, and a bias-tee ensures the coaxial cable core thermalization.

The AWG is used in *triggered* mode. The trigger signal is generated by frequency division of a 10 MHz reference provided by a SRS FS725 atomic clock, which is also used to clock all the instruments. The trigger signal is generated by an integer division of the 10 MHz using a AD9517/PCBZ board from *Analog Device*. Note that in order to avoid a 2 ns jitter on the waveforms, it is necessary to trig the AWG at a period that is a multiple of 32/10 MHz.

We preferably use for modulation commercial Single Side Band mixers (SSB) from *Polyphase Microwave*. The left[2] side band is used to effect control, and the rejection

2 This choice is relevant when driving the qubit to avoid exciting transitions between the excited states of the transmon.

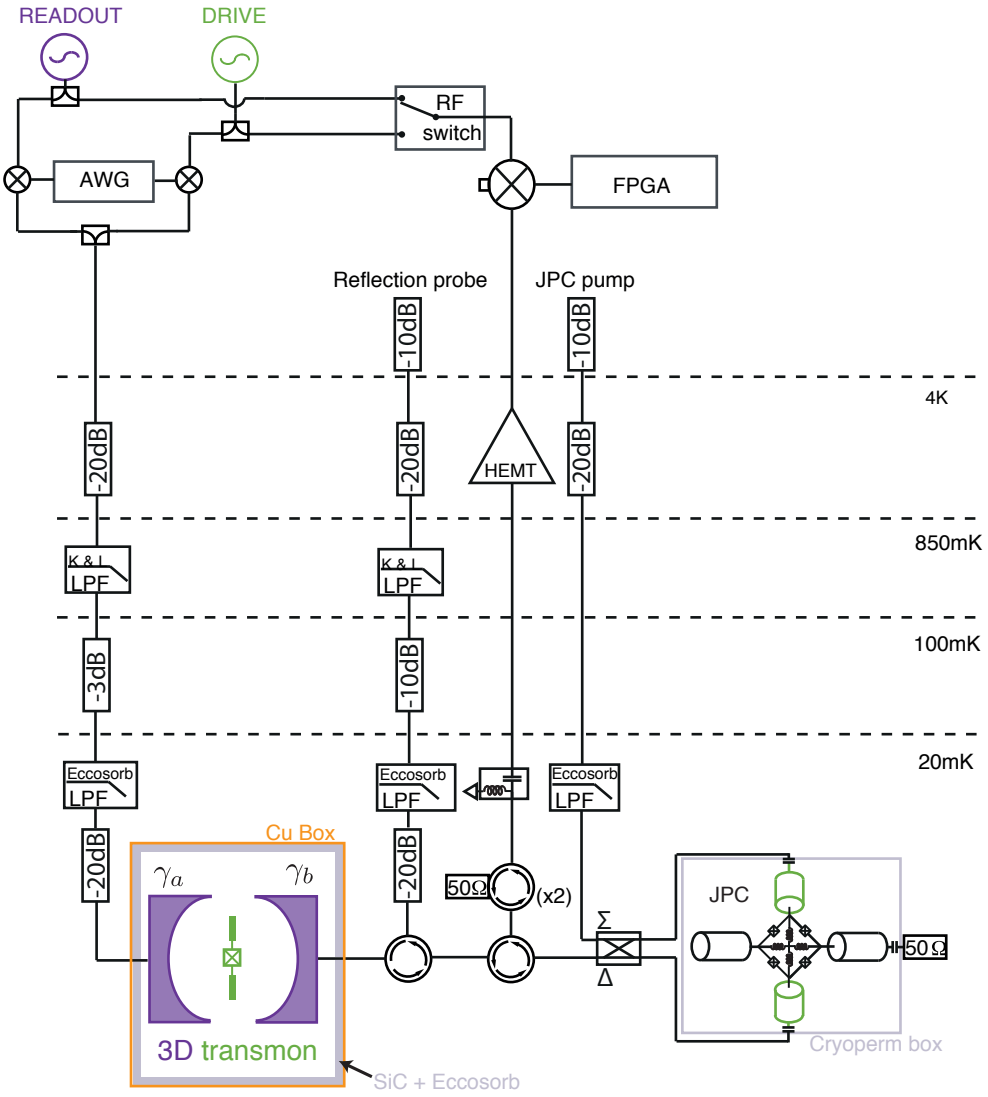

Figure 65: Full schematic of the wiring for the weak value experiment described in Chap. 4. Wiring inside the refrigerator is similar to the one presented on Fig. 64, but for minor changes in attenuators, and the reflection line which is now connected to the cavity via a directional coupler. This was done to improve the impedance matching between the cavity ports and the circulators, which should allow for a better isolation from the JPC.

of the right side-band and the LO is typically 20-30 dB. This allows for a better control of the power spectrum at the system input while using only one channel of the AWG. Indeed, an alternative scheme consists in using an IQ mixer with two signals in quadrature on I and Q. Fine tuning of the relative phase and amplitude of the signals on I and Q is usually required to achieve similar rejection performances.
The microwave sources used as LO are Keysight E8257D, Anritsu MGC369X and Vaunix LabBrick LMS. Note that this last source has a lower phase stability and is only

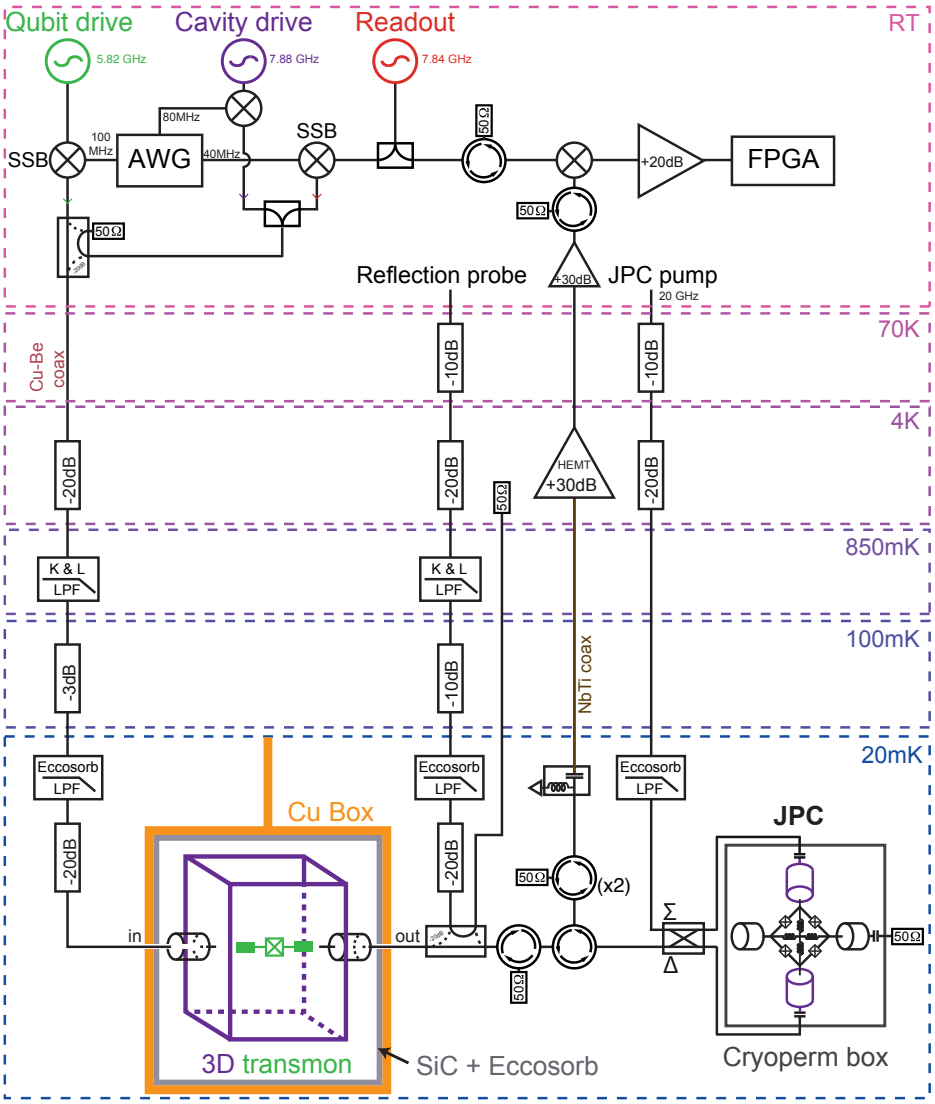

Figure 66: Full schematic of the wiring for the Zeno dynamics experiment described in Chap. 7. Wiring inside the refrigerator is similar to the one presented on Fig. 65, except that the JPC is now tuned at cavity resonance frequency.

used to pump the JPC.

Detection of the output signal from the refrigerator is performed by amplifying further the signal at room temperature with RF amplifiers by *Miteq*, and down converting the amplified signal to ω_h by mixing with the same LO that was used for the pulse generation. The conversion is here performed by an IQ mixer by *Marki microwaves*. When signals at different frequencies are involved, the signal is first divided by a low reflection power splitter or a hybrid coupler whose Δ port is loaded with a 50-Ω impedance. Circulators from *Aerotek* are inserted before and after the mixers and splitters to avoid cross talks.
The low frequency signal is then digitized by an acquisition board. For the experiments reported in Sec. 5.1.3 and Chap. 4, the board is a Triton-V5 FPGA by *Tekmicro*. For

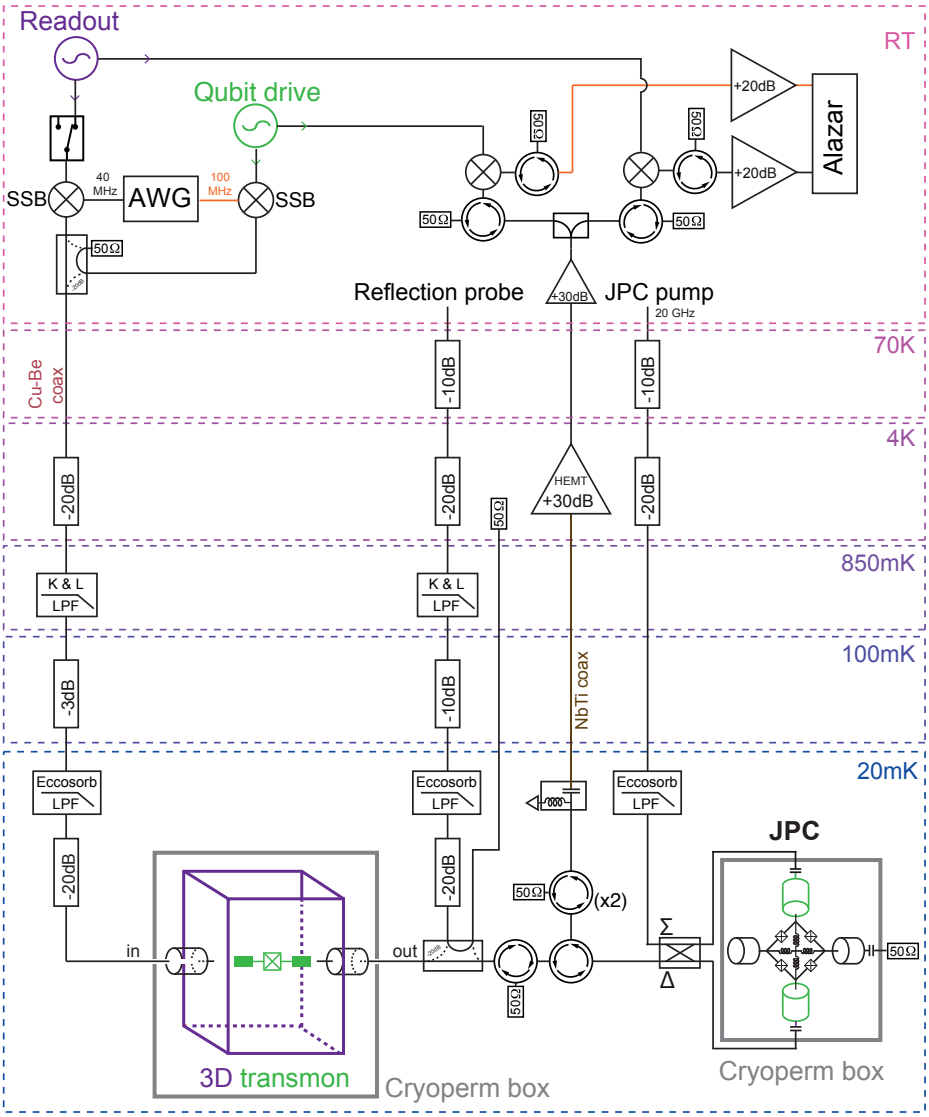

Figure 67: Full schematic of the wiring for the fluorescence trajectories experiment described in Sec. 3.4.2. The fluorescence field from the qubit on the output line is amplified by a JPC tuned at ω_q. The same source used to generate preparation pulses of the qubit is used to down convert the resulting signal to 100 MHz (in orange) before digitization and numerical demodulation.

the experiment of Chap. 7, the board is a X6RX FPGA by *Innovative Integration*. For the experiments of Sec. 3.4 and the analog feedback presented on Sec. 5.2, the board is an ATS9351 by *Alazar*. The full room temperature wiring schematic of the latest experiment is presented on Fig. 68. The wiring inside the refrigerator is the same as in Fig. 67, and is not represented for simplicity.

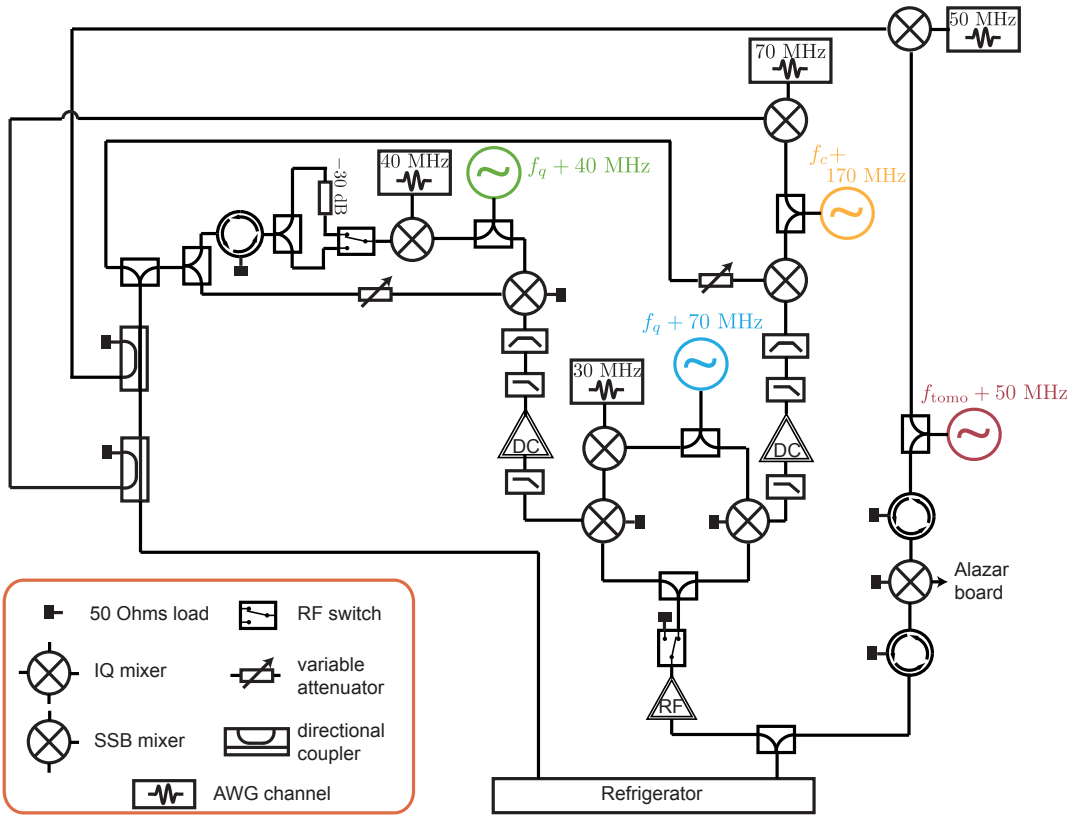

Figure 68: Full wiring schematic at room temperature for the continuous feedback experiment presented in Sec. 5.2. Note that the RF switches are controlled by the AWG markers. The one at the fridge output is used to turn on or off the feedback. The other one is used to switch from low power signal generation (to implement the constant drive at around σ_X in the controller (225)) to high power (for tomography fast $\frac{\pi}{2}$ rotations). Some attenuators, used to finely tune to nominal value the LO power on the mixers are not represented.

A.3 ELECTROMAGNETIC SIMULATIONS

An advantage of the 3D transmon compared to 2D architectures for superconducting qubits is that the electromagnetic environment of the Josephson Junction is better controlled and can be simulated. Prior to experiments, we perform full 3D electromagnetic simulations of the system using the *Ansys HFSS* software, which uses finite elements method. This allows us, following the theoretical description given in Sec. 2.2.3, to test a given design (dimensions of the cavity, of the antennas, length of the connector pins dipping in the cavity, critical current of the Josephson Junction) to compute the effective parameters of the qubit (cavity and qubit resonance frequencies, transmon anharmonicity, cavity pull, coupling of to the microwave lines through the cavity ports). This software can be run in two modes.

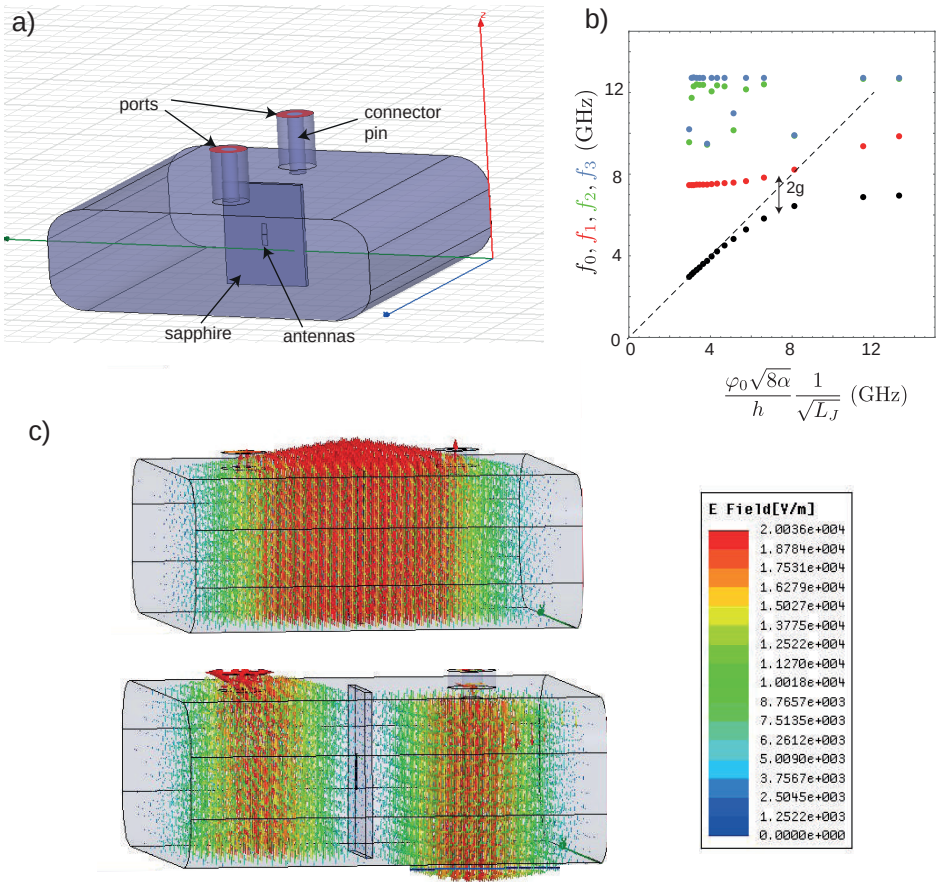

Figure 69: **a**) Simulated geometry for the cavity and qubit system. All metallic surfaces are modeled as perfect conductors. The sapphire chip is simulated as a rectangular volume of relative dielectric constant $\epsilon_r = 10$. The port connector pins are subtracted from the cavity volume. Wave ports are represented in red. **b**) First four resonance frequencies of the system (no wave ports) as a function of $\sqrt{1/L_J}$. For small values of $\sqrt{1/L_J}$, black dots correspond to the qubit mode and red dots to the cavity mode. The scale of the horizontal axis is adjusted so that the black dotted line has a slope 1. This allows us to extract $\alpha/h = 200$ MHz with this geometry. **c**) Simulated field direction and amplitude when exciting through the left port at cavity first (top) and second (bottom) resonance frequencies.

In the *driven modal mode*, the software is fed with the system geometry, which includes the cavity walls, the transmon antennas[3] and the port connector lengths (all considered as perfect conductors), and the sapphire chip which relative dielectric constant is $\epsilon_r \simeq 10$.

To estimate the coupling rate to the coaxial lines through the ports, the Josephson Junction can be approximated by a lumped element inductor $L_J = \frac{\hbar}{2e} I_0$, where I_0 is the critical current of the junction. *Wave ports* are then placed in between the port connector pins and the tunnel drilled into the cavity bulk (see Fig. 69a). Sweeping the

3 Note that the antennas thickness need to be increased compared to the actual 135 nm of the aluminum layer in order for the simulation mesh to remain coarse enough to be handled by the computer in a reasonable time.

excitation frequency, and computing the reflection and transmission coefficients for the two ports, one can extract the coupling rate of the cavity mode through each port, as described in Sec. 2.2.2.3. This also allows us to determine the cavity resonance frequencies, and to verify the electric field configuration at resonance. On Fig. 69c, we plot the amplitude and direction of the electric field for the two first cavity resonance modes. As expected, for the first mode, the field direction is parallel to the antennas, and the amplitude is maximal around them. For the second mode, the field direction is orthogonal and the chip is at a node. The coupling to the junction is thus expected to be negligible.

To predict the qubit parameters, the Josephson Junction is replaced by a lumped port with inductance L_J. Simulating the system response to an excitation through that port and computing the impedance seen by the Junction around the resonance frequency allows us to access the qubit anharmonicity, the cavity pull to the cavity modes, and, in principle, the Purcell decay rate of the qubit following the Black Box Quantization method (see Sec. 2.2.3.2 and [62, 72, 73]).

One can also use the HFSS software in the *eigen mode*, in which the ports are replaced by perfect conductors, and the junction by a lumped element inductor L_J. The software then determines the resonances of the system. The four first resonant mode frequencies as a function of $\sqrt{\frac{1}{L_J}}$ are represented on Fig. 69b. We clearly see an anti crossing between the first mode, which is the qubit mode and whose resonance frequency depends linearly on $\sqrt{\frac{1}{L_J}}$, and the first cavity mode. The size of the anti crossing is $2g$ in the two-mode model presented in Sec. 2.2.3.3. For large values of L_J (low qubit resonance frequency), according to Eq. (64), the first mode resonance frequency is the qubit frequency which reads $\frac{1}{h}\sqrt{8E_J\alpha} = \frac{\varphi_0\sqrt{8\alpha}}{h}\sqrt{\frac{1}{L_J}}$. The slope of the black dotted line on Fig. 69c thus allows us to extract the value of the transmon anharmonicity α.
Note that beside parasitic resonances, the cavity second and third modes do not depend on L_J which confirms that they are not coupled to the qubit mode. However, for small values of L_J, the qubit resonance frequency is no longer proportional to $\sqrt{1/L_J}$, which is not predicted by the 2-mode model. Hybridization to higher modes is thus likely.

B

QUANTUM CIRCUITS

In this appendix, we derive 2 results used in Sec. 2.2.2.1, which are the equivalence between a capacitive coupling to a transmission line and a galvanic coupling to a line with higher characteristic impedance, and the quantization of a semi-infinite line.

B.1 CAPACITIVELY COUPLED TRANSMISSION LINE

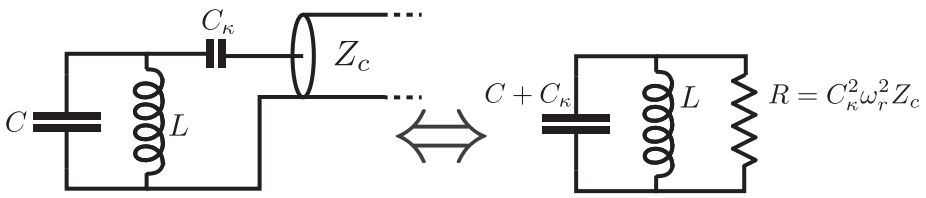

Figure 70: LC circuit capacitively coupled to a coaxial transmission line: equivalence to a galvanic coupling to a high-impedance line.

Let us consider the situation represented on Fig. 70. A transmission line is capacitively coupled to the LC resonator. We suppose that the coupling capacitance C_κ is much smaller than $1/Z_c\omega_r$, where $\omega_r = \frac{1}{\sqrt{LC}}$ is the circuit resonance frequency and Z_c the line characteristic impedance. The semi-infinite line being equivalent to a resistor of resistance Z_c, around ω_r, the impedance seen from the resonator is:

$$\begin{aligned} Z_0 &= \frac{1}{jC_\kappa\omega} + Z_c \\ &= \frac{1}{jC_\kappa\omega}(1 + jC_\kappa\omega_r Z_c + jC_\kappa(\omega - \omega_r)Z_c) \\ &\underset{\substack{|\omega-\omega_r|\ll\omega_r \\ C_\kappa \ll 1/Z_c\omega_r}}{\approx} \frac{1}{jC_\kappa\omega}\frac{1}{1 - jC_\kappa\omega_r Z_c} \\ &\approx \frac{1}{jC_\kappa\omega + C_\kappa^2\omega_r^2 Z_c} \\ &\approx \frac{1}{jC_\kappa\omega} || \frac{1}{C_\kappa^2\omega_r^2 Z_c}, \end{aligned} \tag{284}$$

which is the impedance of the coupling capacitance in parallel with a resistor $R = \frac{1}{C_\kappa^2\omega_r^2 Z_c} \gg Z_c$. Thus, a capacitive coupling to a line of characteristic impedance Z_c is equivalent to a galvanic coupling to a resistor of high resistance, or equivalently to a semi-infinite line of high characteristic impedance $Z_0 = R$. Note that the coupling capacitance slightly increases the resonator capacitance.

Physically, the hypothesis of small capacitance means that we can neglect the low-pass filter formed by this capacitance in series with the line of real impedance Z_c.

Probing the cavity on a small bandwidth around its resonant frequency, we can neglect the dependance on ω of the impedance seen from the cavity. In the following section, this translates in a constant density of states for the cavity environment on the probed bandwidth.

B.2 INPUT OUTPUT FORMALISM

In this section, we define the input and output field operators of a semi-infinite transmission line and derive the form of the interaction hamiltonian with the cavity mode. This derivation follows the one by Clerk *et al.* in the appendices of [11], but we place ourselves in the Schrödinger picture.

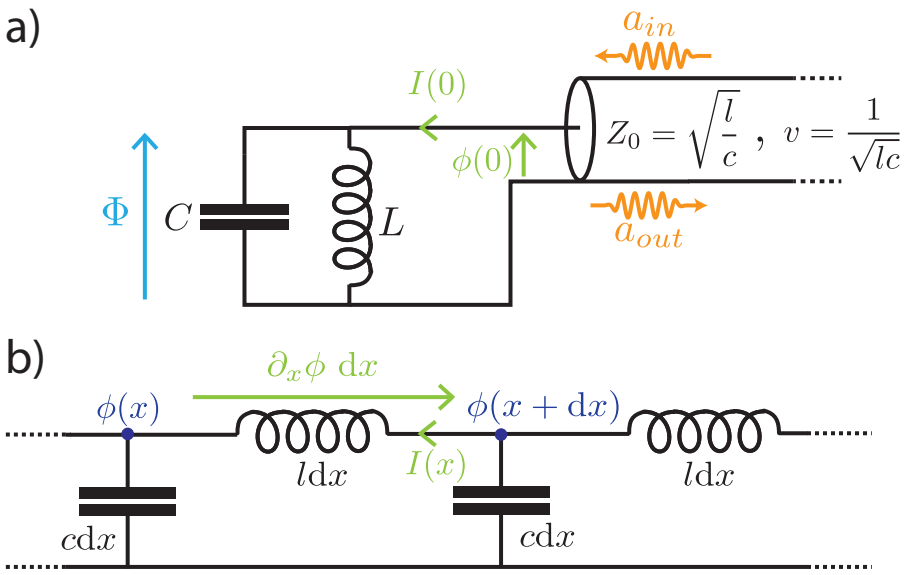

Figure 71

We consider the situation represented on Fig. 71 a. A LC resonator is connected to a coaxial line which has an inductance per unit length l and a capacitance to the ground per unit length c. We define the characteristic impedance of the line $Z_0 = \sqrt{\frac{l}{c}}$ and the traveling waves velocity $v = \frac{1}{\sqrt{lc}}$.

On the telegraph model for the line represented on Fig. 71 b, the charge $q(x)\mathrm{d}x$ on the node at position x and its phase defined in Eq. (31) are canonically conjugated so that

$$[\phi(x), q(x')] = i\hbar\delta(x - x'). \tag{285}$$

The electrostatic energy stored in a portion of length $\mathrm{d}x$ reads $\frac{q^2}{2c}\mathrm{d}x$ and the magnetic energy is $\frac{(\partial_x\phi)^2}{2l}\mathrm{d}x$

To simplify calculations, we suppose that the line has a finite length λ and we impose a periodic boundary condition between $x = 0$, where the line is connected to the resonator, and $x = \lambda$. We will take $\lambda \to \infty$ at the end of the calculation. The hamiltonian of the line reads

$$H_{\text{line}} = \int_0^\lambda (\frac{q^2}{2c} + \frac{(\partial_x \phi)^2}{2l}) \mathrm{d}x. \tag{286}$$

We now define the left and right traveling waves amplitudes at position x as

$$A^{\rightleftarrows}(x) = \frac{1}{2\sqrt{vc}} q(x) \mp \frac{1}{2\sqrt{vl}} \partial_x \phi. \tag{287}$$

From Eq. (285), we find the commutation relations

$$\left\{ \begin{array}{rcl} [A^{\rightleftarrows}(x), A^{\rightleftarrows}(x')] &=& \pm \frac{i\hbar}{2} \partial_x \delta(x - x') \\ [A^{\rightleftarrows}(x), A^{\leftrightarrows}(x')] &=& 0 \end{array} \right. , \tag{288}$$

so that left and right propagating waves are independent. We then write the hamiltonian

$$H_{\text{line}} = v \int_0^\lambda (A^{\leftarrow}(x)^2 + A^{\rightarrow}(x)^2) \mathrm{d}x. \tag{289}$$

We now define the wave amplitudes A_k in the wave vectors domain as, for $k = \frac{2\pi n}{\lambda}$ and n an integer,

$$\left\{ \begin{array}{rcll} A_k &=& \sqrt{\frac{2v}{\lambda}} \int_0^\lambda A^{\rightarrow}(x) e^{-ikx} \mathrm{d}x & \text{if } k > 0 \text{ (right propagating modes)} \\ A_k &=& \sqrt{\frac{2v}{\lambda}} \int_0^\lambda A^{\leftarrow}(x) e^{-ikx} \mathrm{d}x & \text{if } k < 0 \text{ (left propagating modes)} \end{array} \right. , \tag{290}$$

and using Parseval relation,

$$H_{\text{line}} = \frac{1}{2} \sum_{k=-\infty}^{+\infty} (A_k^\dagger A_k + A_k A_k^\dagger). \tag{291}$$

Let us now find the commutation relation for the A_k's. For $k, k' > 0$,

$$\begin{array}{rcll} [A_k, A_{k'}^\dagger] &=& \frac{2v}{\lambda} \int_0^\lambda \int_0^\lambda [A^{\rightarrow}(x), A^{\rightarrow}(x')] e^{i(k'x' - kx)} \mathrm{d}x \mathrm{d}x' \\ &=& -\frac{i\hbar v}{\lambda} \int_0^\lambda \int_0^\lambda \partial_x \delta(x - x') e^{i(k'x' - kx)} \mathrm{d}x \mathrm{d}x' \\ \left\{ \begin{array}{l} s = (x+x')/2 \\ u = x - x' \end{array} \right. & & \\ &=& \int_0^\lambda \int_{-2s}^{2s} \partial_u \delta(u) e^{-i\frac{k+k'}{2}u} \mathrm{d}u e^{i(k'-k)s} \mathrm{d}s \\ &=& \hbar \frac{v}{2} (k + k') \delta_{kk'}. \end{array} \tag{292}$$

Similarly, we find that

$$\begin{array}{rcll} [A_k, A_{k'}^\dagger] &=& -\hbar \frac{v}{2} (k + k') \delta_{kk'} & \text{if } k, k' < 0 \\ [A_k, A_{k'}^\dagger] &=& 0 & \text{if } \mathrm{sgn}(kk') < 0 \end{array} , \tag{293}$$

and we check that $[A_k, A_{k'}] = 0$. We can now define the annihilation operators a_k as

$$a_k = \frac{1}{\sqrt{\hbar\omega_k}} A_k, \tag{294}$$

where $\omega_k = v|k|$. These operators obey the canonical commutation relation $[a_k, a_{k'}^\dagger] = \delta_{kk'}$, and the hamiltonian reads

$$H_{\text{line}} = \sum_{k=-\infty}^{+\infty} \hbar\omega_k (a_k a_k^\dagger + \frac{1}{2}). \tag{295}$$

Thus, the line is assimilated to a bath of harmonic oscillators of frequencies ω_k.

We now consider the interaction hamiltonian H_{int} between the line and the LC resonator. It corresponds to the work performed by a current source $I(x = 0)$ over a tension $V = \partial_t \Phi$ from $t' = -\infty$ to t (see Fig. 71). It thus reads

$$\begin{aligned} H_{\text{int}} &= \Phi.I(x=0) \\ &= \sqrt{\tfrac{\hbar Z_r}{2}}(a + a^\dagger)\sqrt{\tfrac{v}{l}}(A^{\leftarrow}(0) - A^{\rightarrow}(0)) \\ &= \sqrt{\tfrac{\hbar Z_r}{2}}(a + a^\dagger)\sqrt{\tfrac{\hbar v}{2Z_0\lambda}} \sum_{k=0}^{+\infty} \sqrt{\omega_k}(a_{-k} - a_k + a_{-k}^\dagger - a_k^\dagger), \end{aligned} \tag{296}$$

where $Z_r = \sqrt{\frac{L}{C}}$ is the characteristic impedance of the LC resonator.

We now make the Rotating Wave Approximation (RWA) [67]. In the hamiltonian (296), we only keep the oscillators whose frequency ω_k are around the LC resonator frequency ω_r, within a given span $\Delta\omega \ll \omega_r$. The other terms in the hamiltonian result in fast oscillating contributions that are neglected. Making the approximation $\omega_k \simeq \omega_r$ for $\omega_k \in [\omega_r - \frac{\Delta\omega}{2}, \omega_r + \frac{\Delta\omega}{2}] \overset{\text{def}}{=} \text{RBW}$, the hamiltonian becomes

$$H_{\text{int}} = \frac{\hbar}{2}\sqrt{\frac{\omega_r Z_r}{Z_0}}(a + a^\dagger)\sqrt{\frac{v}{\lambda}} \sum_{k=0}^{+\infty} (a_{-k} - a_k + a_{-k}^\dagger - a_k^\dagger). \tag{297}$$

We can now define the input and output annihilation operators as

$$\begin{cases} a_{in} = \frac{1}{\sqrt{2\pi D}} \sum_{\omega_k \in \text{RBW}} a_{-k} \\ a_{out} = \frac{1}{\sqrt{2\pi D}} \sum_{\omega_k \in \text{RBW}} a_k \end{cases}, \tag{298}$$

where $D = \frac{\lambda}{2\pi v}$ is the density of states around ω_r. D is supposed constant within the probed bandwidth $\Delta\omega$. It is exactly true for a galvanically connected line, and valid for a capacitively coupled line in the limit of a small coupling capacitance.

Introducing the coupling rate $\kappa = \omega_r \frac{Z_r}{Z_0}$, the interaction hamiltonian finally reads

$$\begin{aligned} H_{\text{int}} &= \tfrac{\hbar\sqrt{\kappa}}{2}(a + a^\dagger)(a_{in} + a_{in}^\dagger - a_{out} + a_{out}^\dagger) \\ &\overset{\text{RWA}}{=} \tfrac{\hbar\sqrt{\kappa}}{2}(a^\dagger(a_{in} - a_{out}) + (a(a_{in}^\dagger - a_{out}^\dagger)). \end{aligned} \tag{299}$$

In the Heisenberg picture, the equation of motion for Let us comment on these results.

- In the limit $\lambda \to \infty$, we have $[a_{in}, a_{in}^\dagger] = [a_{out}, a_{out}^\dagger] = \frac{\Delta\omega}{2\pi} = \Delta f$. Therefore, the photon flux, and thus the power detected at the line output depends on the bandwidth on which it is probed. This bandwidth corresponds to the resolution bandwidth of a commercial Power Spectrum Analyzer.

- If we turn off the interaction between the resonator and the line, in the Heisenberg picture, we find that the equation of motion for the a_k's read

$$\begin{aligned} i\hbar\partial_t a_k &= [a_k, H_{\text{line}}] \\ &= \hbar\omega_k a_k, \end{aligned} \tag{300}$$

so that $a_k(t+\tau) = a_k(t)e^{-i\omega_k\tau}$, and we have

$$\begin{cases} a_{in}(t+\tau) &= \frac{1}{\sqrt{2\pi D}} \sum\limits_{\omega_k \in \text{RBW}} a_{-k}(t)e^{-i\omega_k\tau} \\ a_{out}(t+\tau) &= \frac{1}{\sqrt{2\pi D}} \sum\limits_{\omega_k \in \text{RBW}} a_k(t)e^{-i\omega_k\tau} \end{cases}. \tag{301}$$

Therefore, in the limit $\lambda \to \infty$, the correlation time for a_{in} and a_{out} is $\tau_c = \frac{1}{\Delta f}$. It is the correlation time that appears in Eq. (23). This sets the limit of the hypothesis of a Markovian environment when we derive a master equation for the resonator mode. The coarse-grained description imply that the time step $\mathrm{d}t$ on which we probe the cavity is chosen to obey the hierarchy

$$\frac{1}{\omega_r} \ll \frac{1}{\Delta\omega} \ll \mathrm{d}t \ll \frac{1}{\kappa}. \tag{302}$$

- On Fig. 71, the boundary condition at $x = 0$ is $\Phi = \phi(x = 0)$. Thus, in the Heisenberg picture,

$$\begin{aligned} \sqrt{\tfrac{\hbar Z_r}{2}}(a(t) + a^\dagger(t)) &= \int_{-\infty}^{t} \tfrac{1}{c} q(0,t')\ \mathrm{d}t' \\ &= \sqrt{\tfrac{v}{c}} \int_{-\infty}^{t} (A^{\rightarrow}(0,t') + A^{\leftarrow}(0,t'))\ \mathrm{d}t' \\ &\overset{\text{Eq. (300)}}{\underset{\omega_k \simeq \omega_r}{\simeq}} i\sqrt{\tfrac{\hbar Z_0}{2\omega_r}}(a_{in}(t) - a_{in}^\dagger(t) + a_{out}(t) - a_{out}^\dagger(t)). \end{aligned} \tag{303}$$

Then, separating the contributions of the oscillating and the counter-oscillating terms, we get the input/output relation

$$\sqrt{\kappa}a(t) = a_{in}(t) + a_{out}(t), \tag{304}$$

where we have redefined the phase of a_{in} and a_{out}

$$\begin{cases} a_{in} &\leftarrow ia_{in} \\ a_{out} &\leftarrow ia_{out} \end{cases}. \tag{305}$$

- In the Heisenberg picture, the equation of motion for the annihilation operator of the LC resonator reads

$$i\hbar\partial_t a = [a, \hbar\omega_r(a^\dagger a + 1/2)] + [a, H_{\text{int}}], \tag{306}$$

and using Eq. (299) and Eq. (304), we get the so-called Langevin equation

$$\boxed{\partial_t a = -i\omega_r a - \frac{\kappa}{2}a + \sqrt{\kappa}a_{in}}. \tag{307}$$

C

STOCHASTIC MASTER EQUATIONS FOR DISPERSIVE MEASUREMENT

In Sec. 3.1.2, we derive the Stochastic Master Equation associated with a *jump detector* for the jump operator $L = \sqrt{\frac{\gamma_\phi}{2}}\sigma_Z$. In Sec. 3.2.2, we give the Stochastic Master Equation associated with a homodyne detection of the transmitted field at the *out* port when driving the cavity at ω_r through the *in* port[1]. In [115], Gambetta *et al.* derive this equation starting from the SME for the cavity mode coupled to a qubit (Jaynes-Cummings model).
In this appendix, we propose jump operators associated with the detection of the same field with a photo-counter. Note that high efficiency photo-counters do not exist in the microwave range yet. We then retrieve the SME for homodyne detection from a model borrowed from quantum optics, in which this detection is performed by mixing the signal with a strong LO on a balanced beam-splitter, and then detecting the splitter outputs with photo counters. Retrieving the same SME as the one given in [115] justifies the jump operators found for the photo-counter.

C.1 JUMP OPERATORS FOR DETECTION WITH A PHOTOCOUNTER

We suppose that we probe the cavity in transmission with an input field a_{in} at ω_r. Due to the dispersive term $-\frac{\chi}{2}a^\dagger a\sigma_Z$ in the hamiltonian (80), the output field is entangled with the qubit. Following Eq.(83), in the stationary regime, the mean number of photons in the cavity mode is $n = \dfrac{4\kappa_{in}|a_{in}|^2}{\kappa^2+\chi^2}$, where κ_{in} is the coupling rate through the input port. Detection of the transmitted photons with a perfect efficiency photo counter[2] leads to abrupt jumps for the qubit state.

To respect the QNDness of the dispersive measurement, we suppose that these jumps only change the phase of the qubit state. Moreover, assuming a markovian environment, the phase shift $-\theta$ associated with a photon detection does not depend on the history of the qubit and is thus constant. Finally, on average, photons need to be detected at rate $\kappa n t$. We thus write the jump operator associated with the detection of a photon as

$$L = \sqrt{\kappa n}\begin{pmatrix} e^{-i\theta/2} & 0 \\ 0 & e^{i\theta/2}\end{pmatrix}. \tag{308}$$

1 neglecting pure dephasing, the dephasing is then induced by the measurement so that $L = \sqrt{\frac{\Gamma_d}{2}}\sigma_Z$

2 and a coupling rate through the output port far larger than the input and the losses of the cavity $\kappa_{out} \simeq \kappa = \kappa_{out} + \kappa_{in} + \kappa_l$, so that all photons are collected and directed to the photo-counter

We can check that this operator effectively shifts the phase of the qubit by an angle $-\theta$ when the photocounter clicks, which happens, as a mean, at a rate κn. Indeed, from Eq.(90), when a jump occurs,

$$\rho(t+\mathrm{d}t) = \frac{L\rho(t)L^\dagger}{\langle L^\dagger L\rangle} - \rho(t) = \begin{pmatrix} \rho_{ee}(t) & \rho_{eg}(t)e^{-i\theta} \\ \rho_{ge}(t)e^{i\theta} & \rho_{gg}(t) \end{pmatrix}. \tag{309}$$

We saw in Sec. 2.1.3.2 that the choice of the no-jump operator modifies the qubit hamiltonian. To respect the QNDness of the measurement, we suppose that it leads to the modification $H \leftarrow H - \omega_{NJ}\frac{\sigma_Z}{2}$, where ω_{NJ} will be chosen so that the AC Stark-shift found from this model matches the value given in Eq. (85).

Since the number k of detected photons after a time t follows a Poisson law of parameter $\kappa n t$ (photon shot-noise), as a mean, the coherence of the qubit at time t reads

$$\begin{aligned} \rho_{eg}(t) &= e^{-i(\omega_q+\omega_{NJ})t}\sum_k P(k)e^{-ik\theta}\rho_{eg}(0) \\ &= e^{-i(\omega_q+\omega_{NJ})t}e^{-\kappa n t}\sum_k \frac{(\kappa n t)^k}{k!}e^{-ik\theta}\rho_{eg}(0) \\ &= e^{-\kappa n t(1-\cos\theta)}e^{-i(\omega_q+\omega_{NJ}+n\kappa\sin\theta)t}\rho_{eg}(0). \end{aligned} \tag{310}$$

We then require that the AC Stark shift and the coherence decay rate match the values given in Eq. (85) and in [21] in the stationary regime so that

$$\left\{ \begin{array}{ccccccc} n\kappa(1-\cos\theta) & = & \Gamma_d & = & \mathrm{Im}[\alpha_e^s\alpha_g^{s*}] & = & n\chi\sin\left(2\arctan(\frac{\chi}{\kappa})\right) \\ \omega_{NJ}+n\kappa\sin\theta & = & \omega_{Stark} & = & \mathrm{Re}[\alpha_e^s\alpha_g^{s*}] & = & n\chi\cos\left(2\arctan(\frac{\chi}{\kappa})\right) \end{array} \right. . \tag{311}$$

We find that these conditions are respected for

$$\left\{ \begin{array}{ccc} \theta & = & 2\arctan(\frac{\chi}{\kappa}) \\ \omega_{NJ} & = & -n\chi \end{array} \right. . \tag{312}$$

The phase-shift $-\theta$ on the qubit state associated with a photon detection is thus equal to the phase shift on the field transmitted at ω_r when the qubit is excited. When no photon is detected, the qubit frequency is simply shifted by $-n\chi$, where n is the mean photon number in the cavity.

C.2 DERIVATION OF THE SME FOR HOMODYNE DETECTION

We now derive the SME associated with homodyne detection, using a model inherited from quantum optics. In this model, homodyne detection is performed by mixing the output field from the cavity with a strong local oscillator (LO) b_{in} at ω_r on a balanced beam-splitter. This traveling field is in a coherent state $|\beta_{in}\rangle$ with a large number of photons per time unit. Thus, in the natural time scale of the cavity, $|\beta_{in}|^2 \gg \kappa$. An acceptable scattering matrix for this beam-splitter reads $S = \frac{1}{\sqrt{2}}\begin{pmatrix} 1 & i \\ 1 & -i \end{pmatrix}$. The two

output beams are then sent to photocounters. Considering the photocounter on one output of the beam splitter, the jump operator associated with the detection of a photon acts on the composite system formed by the LO and the qubit and reads

$$L_{tot} = \frac{1}{\sqrt{2}}(L + ib_{in}), \tag{313}$$

where L is the jump operator found in Eq. (308).
Defining the phase δ by $\beta_{in} = -i|\beta_{in}|e^{i\delta}$, when a photon is detected and tracing out the LO degree of freedom, the evolution of the qubit density matrix is, up to the first order in $\kappa/|\beta_{in}|$:

$$\begin{aligned} \mathrm{d}\rho_{\text{click}} &= \mathrm{Tr}_{\text{LO}}[\frac{L_{tot}\rho_{tot}L_{tot}^\dagger}{\langle L_{tot}^\dagger L_{tot}\rangle} - \rho_{tot}] \\ &= \frac{1}{|\beta_{in}|}((L_\delta - \langle L_\delta\rangle)\rho_{tot} + \rho_{tot}(L_\delta^\dagger - \langle L_\delta^\dagger\rangle)) \\ &= \frac{2}{|\beta_{in}|}\mathcal{M}[L_\delta]\rho_{tot}, \end{aligned} \tag{314}$$

where we have defined the operator

$$L_\delta = e^{-i\delta}L, \tag{315}$$

and the measurement super operator $\mathcal{M}$ as

$$\mathcal{M}[c]\rho = \frac{1}{2}((c - \langle c\rangle)\rho + \rho(c^\dagger - \langle c^\dagger\rangle)). \tag{316}$$

Integrated over a time step $\mathrm{d}t$ such that $1/|\beta_{in}|^2 \ll \mathrm{d}t \ll 1/\kappa n$, the photon shot-noise in the field b_{in} leads to a number of clicks $\mathrm{d}N_{\text{click}} = \langle L_{tot}^\dagger L_{tot}\rangle \mathrm{d}t + \frac{|\beta_{in}|}{2}\mathrm{d}W_t$, with W_t a Wiener process representing an ideal random walk [94]. Following Itô rules,

$$\begin{cases} \overline{\mathrm{d}W_t} &= 0 \\ \mathrm{d}W_t^2 &= \mathrm{d}t \end{cases}. \tag{317}$$

Then, equation (92) becomes

$$\mathrm{d}\rho_{tot} = -\frac{i}{\hbar}\mathrm{d}t[H_{tot}, \rho_{tot}] + \mathrm{d}t\mathcal{D}[L_{tot}]\rho_{tot} + \frac{|\beta_{in}|}{2}\mathrm{d}W_t\Big(\frac{L_{tot}\rho_{tot}L_{tot}^\dagger}{\langle L_{tot}^\dagger L_{tot}\rangle} - \rho_{tot}\Big), \tag{318}$$

with

$$\mathcal{D}[L_{tot}]\rho_{tot} = \frac{1}{2}(\mathcal{D}[b_{in}]\rho_{tot} + \mathcal{D}[L]\rho_{tot} + |\beta_{in}|\Big(L_\delta\rho_{tot} + \rho_{tot}L_\delta^\dagger - \frac{1}{2}\{L_\delta + L_\delta^\dagger, \rho_{tot}\}\Big)\Big). \tag{319}$$

On the other output of the beam splitter, the jump operator reads $L_{tot,2} = \frac{1}{\sqrt{2}}(L - ib_{in})$, so that the Wiener process associated to the photon shot noise on this second detector is $-W_t$ and the effect on ρ_{tot} is the same as in Eq.(318) with the substitution $L_\delta \to -L_\delta$. Then, summing up the contributions of both diodes at the outputs of the beam splitter and tracing other the b_{in} degree of freedom, we get

$$\mathrm{d}\rho = -\frac{i}{\hbar}\mathrm{d}t[H, \rho] + \mathrm{d}t\mathcal{D}[L]\rho + 2\mathrm{d}W_t\mathcal{M}[L_\delta]\rho, \tag{320}$$

where we have used the fact that b_{in} is in a stationary regime so that the effects of $\mathcal{D}[a_{in}]$ and its hamiltonian evolution compensate.

Let us now consider two cases for the phase δ.

If $\boxed{\delta = \frac{\pi}{2}}$, we have

$$\begin{aligned}\mathcal{M}[L_\delta]\rho &= \sin\tfrac{\theta}{2}\sqrt{\kappa n}\begin{pmatrix} 2\rho_{gg}\rho_{ee} & \rho_{eg}(\rho_{gg}-\rho_{ee}) \\ \rho_{ge}(\rho_{gg}-\rho_{ee}) & -2\rho_{gg}\rho_{ee}\end{pmatrix} \\ &= \sqrt{\Gamma_d/2}\mathcal{M}[\sigma_Z]\rho.\end{aligned} \tag{321}$$

From Eq. (320), we then find the SME

$$\mathrm{d}\rho = -\frac{i}{\hbar}\mathrm{d}t[H,\rho] + \mathrm{d}t\mathcal{D}[L]\rho + \mathrm{d}W_t\sqrt{\eta 2\Gamma_d}\mathcal{M}[\sigma_Z]\rho, \tag{322}$$

which is the same as in Eq. (322) since, with $\theta = 2\arctan\frac{\chi}{\kappa}$, we showed in Sec. C.1 that the unconditioned evolution $\mathrm{d}\rho = -\frac{i}{\hbar}\mathrm{d}t[H,\rho] + \mathrm{d}t\mathcal{D}[L]\rho$ reproduces the dephasing rate and AC-Stark shift found in Eq. (85).
The measurement record, which is the normalized signal at the output of one of the photocounters is $J_{\frac{\pi}{2}}(t)$ with

$$\begin{aligned}J_{\frac{\pi}{2}}(t)\mathrm{d}t &= \tfrac{2}{|\beta_{in}|}(\mathrm{d}N_{\text{click}} - (|\beta_{in}|^2+1)/2) \\ &= \tfrac{2}{|\beta_{in}|}(\langle L_{tot}^\dagger L_{tot}\rangle + \tfrac{|\beta_{in}|}{2}\mathrm{d}W_t - (|\beta_{in}|^2+1)/2) \\ &= 2\sqrt{\kappa n}\sin\tfrac{\theta}{2}\langle\sigma_Z(t)\rangle + \mathrm{d}W_t \\ &= \sqrt{2\Gamma_d}\langle\sigma_Z(t)\rangle + \mathrm{d}W_t,\end{aligned} \tag{323}$$

where we have removed the constant part $(|\beta_{in}|^2+1)/2$ and normalized the signal by $|\beta_{in}|/2$. This is in agreement with the expression given in Eq. (114).

If $\boxed{\delta = 0}$, we have

$$\begin{aligned}\mathcal{M}[L_\delta]\rho &= -i\sin\tfrac{\theta}{2}\sqrt{\kappa n}\begin{pmatrix} 0 & \rho_{ge} \\ -\rho_{eg} & 0\end{pmatrix} \\ &= -i\sqrt{\tfrac{\Gamma_d}{2}}[\sigma_Z,\rho].\end{aligned} \tag{324}$$

Then, Eq. (320) reads

$$\mathrm{d}\rho = -\frac{i}{\hbar}\mathrm{d}t[H,\rho] + \mathrm{d}t\mathcal{D}[L]\rho - i\frac{\mathrm{d}W_t}{2}\sqrt{2\Gamma_d}[\sigma_Z,\rho], \tag{325}$$

in agreement with Eq. (322).
In this case, and with the same offset and normalization as in Eq. (323), the measurement record is $J_0(t)$ with

$$J_0(t)\mathrm{d}t = 2\sqrt{\kappa n}\cos\frac{\theta}{2}\mathrm{d}t + \mathrm{d}W_t, \tag{326}$$

also in agreement with the expression given in Eq. (116).

In conclusion, starting from the jump operators acting on the qubit that we proposed in Sec. C.1 to describe the detection of the field at ω_r by a photocounter, we derived in this section the SME associated with homodyne detection of the same field. For both considered phases of the homodyne detection, we find the same SME and the same expressions for the measurement records as derived by Gambetta *et al.* [21] and recalled in Sec. 3.2.2. This validates a posteriori the values of the jump operators associated with a photon detection guessed in Sec. C.1.

Part IV

BIBLIOGRAPHY

BIBLIOGRAPHY

[1] B. S. DeWitt, N. Graham, H. Everett, and J. A. Wheeler, *The many-worlds interpretation of quantum mechanics*, vol. 3. Princeton University Press Princeton, 1973. (Cited on page 1.)

[2] W. H. Zurek, "Quantum darwinism," *Nature Physics*, vol. 5, no. 3, pp. 181–188, 2009. (Cited on page 1.)

[3] A. Daneri, A. Loinger, and G. M. Prosperi, "Quantum theory of measurement and ergodicity conditions," *Nuclear physics*, vol. 33, pp. 297–319, 1962. (Cited on page 1.)

[4] A. Daneri, A. Loinger, and G. Prosperi, "Further remarks on the relations between statistical mechanics and quantum theory of measurement," *Il Nuovo Cimento B Series 10*, vol. 44, no. 1, pp. 119–128, 1966. (Cited on page 1.)

[5] W. H. Zurek, "Quantum darwinism, classical reality, and the randomness of quantum jumps," *arXiv preprint arXiv:1412.5206*, 2014. (Cited on page 1.)

[6] M. Brune, E. Hagley, J. Dreyer, X. Maitre, A. Maali, C. Wunderlich, J. Raimond, and S. Haroche, "Observing the progressive decoherence of the "meter" in a quantum measurement," *Physical Review Letters*, vol. 77, no. 24, p. 4887, 1996. (Cited on page 1.)

[7] C. Monroe, D. Meekhof, B. King, and D. Wineland, "A "Schrödinger cat" superposition state of an atom," *Science*, vol. 272, no. 5265, pp. 1131–1136, 1996. (Cited on page 1.)

[8] N. Katz, M. Neeley, M. Ansmann, R. C. Bialczak, M. Hofheinz, E. Lucero, A. O'Connell, H. Wang, A. Cleland, J. M. Martinis, *et al.*, "Reversal of the weak measurement of a quantum state in a superconducting phase qubit," *Physical review letters*, vol. 101, no. 20, p. 200401, 2008. (Cited on pages 1 and 47.)

[9] G. ChiriBella, G. M. D'Ariano, and P. Perinotti, "Quantum Theory, Namely the Pure and Reversible Theory of Information," *Entropy*, vol. 14, pp. 1877–1893, Oct. 2012. (Cited on pages 1 and 17.)

[10] M. Devoret and R. Schoelkopf, "Superconducting circuits for quantum information: an outlook," *Science*, vol. 339, no. 6124, pp. 1169–1174, 2013. (Cited on pages 1 and 21.)

[11] a. a. Clerk, M. H. Devoret, S. M. Girvin, F. Marquardt, and R. J. Schoelkopf, "Introduction to quantum noise, measurement, and amplification," *Reviews of Modern Physics*, vol. 82, pp. 1155–1208, Apr. 2010. (Cited on pages 1, 3, 4, 18, 45, 46, 50, 51, 52, 55, 131, and 182.)

[12] J. Koch, T. Yu, J. Gambetta, a. Houck, D. Schuster, J. Majer, A. Blais, M. Devoret, S. Girvin, and R. Schoelkopf, "Charge-insensitive qubit design derived from the Cooper pair box," *Physical Review A*, vol. 76, pp. 1–19, Oct. 2007. (Cited on pages 1, 2, 28, and 32.)

[13] H. Paik, D. I. Schuster, L. S. Bishop, G. Kirchmair, G. Catelani, a. P. Sears, B. R. Johnson, M. J. Reagor, L. Frunzio, L. I. Glazman, S. M. Girvin, M. H. Devoret, and R. J. Schoelkopf, "Observation of High Coherence in Josephson Junction Qubits Measured in a Three-Dimensional Circuit QED Architecture," *Physical Review Letters*, vol. 107, p. 240501, Dec. 2011. (Cited on pages 1, 2, 21, and 165.)

[14] D. M. Pozar, *Microwave engineering*. John Wiley & Sons, 2009. (Cited on page 3.)

[15] E. M. Purcell, "Proceedings of the american physical society," *Phys. Rev.*, vol. 69, pp. 674–674, Jun 1946. (Cited on pages 3 and 32.)

[16] M. Reed, B. Johnson, A. Houck, L. DiCarlo, J. Chow, D. Schuster, L. Frunzio, and R. Schoelkopf, "Fast reset and suppressing spontaneous emission of a superconducting qubit," *Applied Physics Letters*, vol. 96, no. 20, p. 203110, 2010. (Cited on pages 3, 8, 32, 111, and 129.)

[17] E. A. Sete, A. Galiautdinov, E. Mlinar, J. M. Martinis, and A. N. Korotkov, "Catch-disperse-release readout for superconducting qubits," *Phys. Rev. Lett.*, vol. 110, p. 210501, May 2013. (Cited on pages 3, 8, and 32.)

[18] M. A. Nielsen and I. L. Chuang, *Quantum computation and quantum information*. Cambridge university press, 2010. (Cited on pages 3, 4, 17, 82, 83, and 117.)

[19] N. Bergeal, F. Schackert, M. Metcalfe, R. Vijay, V. Manucharyan, L. Frunzio, D. Prober, R. Schoelkopf, S. Girvin, and M. Devoret, "Phase-preserving amplification near the quantum limit with a Josephson ring modulator," *Nature*, vol. 465, no. 7294, pp. 64–68, 2010. (Cited on pages 4 and 55.)

[20] N. Roch, E. Flurin, F. Nguyen, P. Morfin, P. Campagne-Ibarcq, M. H. Devoret, and B. Huard, "Widely tunable, nondegenerate three-wave mixing microwave device operating near the quantum limit," *Physical review letters*, vol. 108, no. 14, p. 147701, 2012. (Cited on pages 4 and 55.)

[21] J. Gambetta, A. Blais, M. Boissonneault, A. Houck, D. Schuster, and S. Girvin, "Quantum trajectory approach to circuit QED: Quantum jumps and the Zeno effect," *Physical Review A*, vol. 77, no. 1, p. 012112, 2008. (Cited on pages 4, 38, 54, 188, and 191.)

[22] R. Vijay, D. H. Slichter, and I. Siddiqi, "Observation of Quantum Jumps in a Superconducting Artificial Atom," *Physical Review Letters*, vol. 106, p. 110502, Mar. 2011. (Cited on pages 5, 47, and 59.)

[23] H. M. Wiseman, *Quantum trajectories and feedback*. PhD thesis, University of Queensland, 1994. (Cited on pages 5, 10, 63, 118, and 139.)

[24] H. M. Wiseman and G. J. Milburn, *Quantum measurement and control*. Cambridge University Press, 2009. (Cited on pages 5, 6, 8, 10, 25, 52, 63, 75, 107, and 118.)

[25] A. A. Houck, D. I. Schuster, J. M. Gambetta, J. A. Schreier, B. R. Johnson, J. M. Chow, L. Frunzio, J. Majer, M. H. Devoret, S. M. Girvin, and R. J. Schoelkopf, "Generating single microwave photons in a circuit," *Nature*, vol. 449, pp. 328–331, Jan. 2007. (Cited on pages 6 and 64.)

[26] O. Astafiev, A. M. Zagoskin, A. Abdumalikov, Y. A. Pashkin, T. Yamamoto, K. Inomata, Y. Nakamura, and J. Tsai, "Resonance fluorescence of a single artificial atom," *Science*, vol. 327, no. 5967, pp. 840–843, 2010. (Cited on pages 6 and 64.)

[27] Y. Aharonov, P. G. Bergmann, and J. L. Lebowitz, "Time symmetry in the quantum process of measurement," *Phys. Rev.*, vol. 134, pp. B1410–B1416, Jun 1964. (Cited on pages 6, 81, and 92.)

[28] Y. Aharonov, D. Albert, and L. Vaidman, "How the result of a measurement of a component of the spin of a spin-1/2 particle can turn out to be 100," *Physical Review Letters*, vol. 60, pp. 1351–1354, Apr. 1988. (Cited on pages 6, 81, and 94.)

[29] H. Wiseman, "Weak values, quantum trajectories, and the cavity-QED experiment on wave-particle correlation," *Physical Review A*, vol. 65, p. 032111, Feb. 2002. (Cited on pages 6, 81, and 84.)

[30] M. Tsang, "Optimal waveform estimation for classical and quantum systems via time-symmetric smoothing," *Physical Review A*, vol. 80, no. 3, p. 033840, 2009. (Cited on pages 6, 81, and 99.)

[31] S. r. Gammelmark, B. Julsgaard, and K. Mølmer, "Past quantum states," p. 5, May 2013. (Cited on pages 6 and 81.)

[32] Y. Aharonov, S. Popescu, and J. Tollaksen, "A time-symmetric formulation of quantum mechanics," *Phys. Today*, vol. 63, no. 11, pp. 27–32, 2010. (Cited on pages 7 and 81.)

[33] A. C. Doherty, S. Habib, K. Jacobs, H. Mabuchi, and S. M. Tan, "Quantum feedback control and classical control theory," *Physical Review A*, vol. 62, no. 1, p. 012105, 2000. (Cited on pages 8 and 107.)

[34] J. Poyatos, J. Cirac, and P. Zoller, "Quantum reservoir engineering with laser cooled trapped ions," *Physical review letters*, vol. 77, no. 23, p. 4728, 1996. (Cited on pages 8 and 129.)

[35] B. Misra and E. C. G. Sudarshan, "The Zeno's paradox in quantum theory," *Journal of Mathematical Physics*, vol. 18, no. 4, pp. 756–763, 1977. (Cited on pages 8 and 141.)

[36] P. Facchi, V. Gorini, G. Marmo, S. Pascazio, and E. Sudarshan, "Quantum Zeno dynamics," *Physics Letters A*, vol. 275, no. 1, pp. 12–19, 2000. (Cited on pages 8, 105, and 141.)

[37] P. Facchi, D. Lidar, and S. Pascazio, "Unification of dynamical decoupling and the quantum Zeno effect," *Physical Review A*, vol. 69, no. 3, p. 032314, 2004. (Cited on pages 8, 11, 141, 142, and 146.)

[38] J.-M. Raimond, C. Sayrin, S. Gleyzes, I. Dotsenko, M. Brune, S. Haroche, P. Facchi, and S. Pascazio, "Phase space tweezers for tailoring cavity fields by quantum Zeno dynamics," *Physical review letters*, vol. 105, no. 21, p. 213601, 2010. (Cited on pages 8, 11, 141, 142, and 160.)

[39] J.-M. Raimond, P. Facchi, B. Peaudecerf, S. Pascazio, C. Sayrin, I. Dotsenko, S. Gleyzes, M. Brune, and S. Haroche, "Quantum Zeno dynamics of a field in a cavity," *Physical Review A*, vol. 86, no. 3, p. 032120, 2012. (Cited on pages 8, 141, and 160.)

[40] C. Sayrin, I. Dotsenko, X. Zhou, B. Peaudecerf, T. Rybarczyk, S. Gleyzes, P. Rouchon, M. Mirrahimi, H. Amini, M. Brune, *et al.*, "Real-time quantum feedback prepares and stabilizes photon number states," *Nature*, vol. 477, no. 7362, pp. 73–77, 2011. (Cited on pages 10 and 107.)

[41] X. Zhou, I. Dotsenko, B. Peaudecerf, T. Rybarczyk, C. Sayrin, S. Gleyzes, J. Raimond, M. Brune, and S. Haroche, "Field locked to a fock state by quantum feedback with single photon corrections," *Physical review letters*, vol. 108, no. 24, p. 243602, 2012. (Cited on pages 10 and 107.)

[42] D. Ristè, C. Bultink, K. Lehnert, and L. DiCarlo, "Feedback control of a solid-state qubit using high-fidelity projective measurement," *Physical review letters*, vol. 109, no. 24, p. 240502, 2012. (Cited on pages 10, 107, 109, 110, and 129.)

[43] D. P. DiVincenzo *et al.*, "The physical implementation of quantum computation," *arXiv preprint quant-ph/0002077*, 2000. (Cited on pages 10 and 111.)

[44] K. Geerlings, Z. Leghtas, I. Pop, S. Shankar, L. Frunzio, R. J. Schoelkopf, M. Mirrahimi, and M. H. Devoret, "Demonstrating a driven reset protocol for a superconducting qubit," *Physical review letters*, vol. 110, no. 12, p. 120501, 2013. (Cited on pages 10, 42, 111, and 129.)

[45] D. Schuster, A. Houck, J. Schreier, A. Wallraff, J. Gambetta, A. Blais, L. Frunzio, J. Majer, B. Johnson, M. Devoret, *et al.*, "Resolving photon number states in a superconducting circuit," *Nature*, vol. 445, no. 7127, pp. 515–518, 2007. (Cited on pages 10, 11, 130, and 143.)

[46] A. Chia and H. M. Wiseman, "Quantum theory of multiple-input–multiple-output markovian feedback with diffusive measurements," *Physical Review A*, vol. 84, no. 1, p. 012120, 2011. (Cited on pages 10 and 120.)

[47] K. Murch, U. Vool, D. Zhou, S. Weber, S. Girvin, and I. Siddiqi, "Cavity-assisted quantum bath engineering," *Physical review letters*, vol. 109, no. 18, p. 183602, 2012. (Cited on pages 11 and 139.)

[48] R. Vijay, C. Macklin, D. Slichter, S. Weber, K. Murch, R. Naik, A. N. Korotkov, and I. Siddiqi, "Stabilizing rabi oscillations in a superconducting qubit using quantum feedback," *Nature*, vol. 490, no. 7418, pp. 77–80, 2012. (Cited on pages 11, 107, 112, and 114.)

[49] F. Schäfer, I. Herrera, S. Cherukattil, C. Lovecchio, F. S. Cataliotti, F. Caruso, and A. Smerzi, "Experimental realization of quantum Zeno dynamics," *Nature communications*, vol. 5, 2014. (Cited on pages 11 and 152.)

[50] A. Signoles, A. Facon, D. Grosso, I. Dotsenko, S. Haroche, J.-M. Raimond, M. Brune, and S. Gleyzes, "Confined quantum Zeno dynamics of a watched atomic arrow," *Nature Physics*, vol. 10, no. 10, pp. 715–719, 2014. (Cited on pages 11, 143, and 152.)

[51] S. Haroche and J.-M. Raimond, *Exploring the quantum: atoms, cavities, and photons (Oxford graduate texts)*. Oxford University Press, USA, 2013. (Cited on pages 12, 21, 153, and 157.)

[52] J. Preskill, "Lecture notes for physics 229: Quantum information and computation," *California Institute of Technology*, 1998. (Cited on pages 16 and 17.)

[53] P. Cappellaro *et al.*, "Quantum theory of radiation interactions (pdf)," 2011. (Cited on page 20.)

[54] G. Lindblad, "On the generators of quantum dynamical semigroups," *Communications in Mathematical Physics*, vol. 48, no. 2, pp. 119–130, 1976. (Cited on page 20.)

[55] S. Haroche, "Nobel lecture: Controlling photons in a box and exploring the quantum to classical boundary," *Reviews of Modern Physics*, vol. 85, no. 3, p. 1083, 2013. (Cited on page 21.)

[56] D. J. Wineland, "Nobel lecture: Superposition, entanglement, and raising Schrödinger's cat," *Reviews of Modern Physics*, vol. 85, no. 3, p. 1103, 2013. (Cited on page 21.)

[57] A. Wallraff, D. I. Schuster, A. Blais, L. Frunzio, R.-S. Huang, J. Majer, S. Kumar, S. M. Girvin, and R. J. Schoelkopf, "Strong coupling of a single photon to a superconducting qubit using circuit quantum electrodynamics," *Nature*, vol. 431, no. 7005, pp. 162–167, 2004. (Cited on page 21.)

[58] J. You and F. Nori, "Quantum information processing with superconducting qubits in a microwave field," *Physical Review B*, vol. 68, no. 6, p. 064509, 2003. (Cited on page 21.)

[59] M. H. Devoret and J. M. Martinis, "Implementing qubits with superconducting integrated circuits," in *Experimental Aspects of Quantum Computing*, pp. 163–203, Springer, 2005. (Cited on page 21.)

[60] R. Schoelkopf and S. Girvin, "Wiring up quantum systems," *Nature*, vol. 451, no. 7179, pp. 664–669, 2008. (Cited on page 21.)

[61] J. Clarke and F. K. Wilhelm, "Superconducting quantum bits," *Nature*, vol. 453, no. 7198, pp. 1031–1042, 2008. (Cited on page 21.)

[62] S. E. Nigg, H. Paik, B. Vlastakis, G. Kirchmair, S. Shankar, L. Frunzio, M. H. Devoret, R. J. Schoelkopf, and S. M. Girvin, "Black-Box Superconducting Circuit Quantization," *Physical Review Letters*, vol. 108, p. 240502, June 2012. (Cited on pages 22, 30, 31, 32, 145, and 179.)

[63] Y. Kagan and A. J. Leggett, *Quantum tunnelling in condensed media*. Elsevier, 2012. (Cited on page 22.)

[64] M. H. Devoret, "Quantum fluctuations in electrical circuits," *Les Houches, Session LXIII*, 1995. (Cited on page 22.)

[65] S. M. Girvin, "Circuit QED: superconducting qubits coupled to microwave photons," *Les Houches, Session XCVI*, 2011. (Cited on page 22.)

[66] M. Devoret, "QUANTUM SIGNALS AND CIRCUITS Lecture III : The "atoms" of signal," *Lectures at the College de France (physinfo.fr)*, pp. 1–24, 2008. (Cited on page 23.)

[67] C. Cohen-Tannoudji, J. Dupont-Roc, G. Grynberg, and P. Thickstun, *Atom-photon interactions: basic processes and applications*. Wiley Online Library, 1992. (Cited on pages 25, 115, and 184.)

[68] M. H. Devoret and J. M. Martinis, "Course 12 superconducting qubits," *Les Houches*, vol. 79, pp. 443–485, 2004. (Cited on page 28.)

[69] J. Schreier, A. A. Houck, J. Koch, D. I. Schuster, B. Johnson, J. Chow, J. M. Gambetta, J. Majer, L. Frunzio, M. H. Devoret, *et al.*, "Suppressing charge noise decoherence in superconducting charge qubits," *Physical Review B*, vol. 77, no. 18, p. 180502, 2008. (Cited on page 28.)

[70] A. Houck, J. Koch, M. Devoret, S. Girvin, and R. Schoelkopf, "Life after charge noise: recent results with transmon qubits," *Quantum Information Processing*, vol. 8, no. 2-3, pp. 105–115, 2009. (Cited on page 28.)

[71] V. Manucharyan, E. Boaknin, M. Metcalfe, R. Vijay, I. Siddiqi, and M. Devoret, "Microwave bifurcation of a Josephson junction: Embedding-circuit requirements," *Physical Review B*, vol. 76, p. 014524, July 2007. (Cited on page 28.)

[72] J. Bourassa, F. Beaudoin, J. M. Gambetta, and A. Blais, "Josephson-junction-embedded transmission-line resonators: From Kerr medium to in-line transmon," *Physical Review A*, vol. 86, no. 1, p. 013814, 2012. (Cited on pages 30, 145, and 179.)

[73] F. Solgun, D. W. Abraham, and D. P. DiVincenzo, "Blackbox quantization of superconducting circuits using exact impedance synthesis," *Physical Review B*, vol. 90, no. 13, p. 134504, 2014. (Cited on pages 30, 32, 145, and 179.)

[74] M. Boissonneault, J. Gambetta, and A. Blais, "Improved superconducting qubit readout by qubit-induced nonlinearities," *Physical review letters*, vol. 105, no. 10, p. 100504, 2010. (Cited on page 32.)

[75] M. Boissonneault, J. Gambetta, and A. Blais, "Improved qubit bifurcation readout in the straddling regime of circuit QED," *Physical Review A*, vol. 86, no. 2, p. 022326, 2012. (Cited on page 32.)

[76] D. M. Pozar, *Microwave engineering*. John Wiley & Sons, 2009. (Cited on page 33.)

[77] K. L. Geerlings, *Improving Coherence of Superconducting Qubits and Resonators*. PhD thesis, YALE UNIVERSITY, 2013. (Cited on pages 33, 35, 40, and 68.)

[78] R. Schoelkopf, A. Clerk, S. Girvin, K. Lehnert, and M. Devoret, "Qubits as spectrometers of quantum noise," in *Quantum noise in mesoscopic physics*, pp. 175–203, Springer, 2003. (Cited on page 35.)

[79] M. Boissonneault, J. M. Gambetta, and A. Blais, "Dispersive regime of circuit QED: Photon-dependent qubit dephasing and relaxation rates," *Physical Review A*, vol. 79, no. 1, p. 013819, 2009. (Cited on page 37.)

[80] A. Wallraff, D. Schuster, A. Blais, L. Frunzio, J. Majer, M. Devoret, S. Girvin, and R. Schoelkopf, "Approaching unit visibility for control of a superconducting qubit with dispersive readout," *Physical Review Letters*, vol. 95, no. 6, p. 060501, 2005. (Cited on page 37.)

[81] P. Campagne-Ibarcq, E. Flurin, N. Roch, D. Darson, P. Morfin, M. Mirrahimi, M. H. Devoret, F. Mallet, and B. Huard, "Persistent control of a superconducting qubit by stroboscopic measurement feedback," *Physical Review X*, vol. 3, no. 2, p. 021008, 2013. (Cited on pages 39, 40, 41, 42, 56, 107, 109, 112, 129, and 172.)

[82] P. Campagne-Ibarcq, L. Bretheau, E. Flurin, A. Auffèves, F. Mallet, and B. Huard, "Observing interferences between past and future quantum states in resonance fluorescence," *Physical review letters*, vol. 112, no. 18, p. 180402, 2014. (Cited on pages 41, 42, 61, 64, 88, 129, and 172.)

[83] L. Bretheau, P. Campagne-Ibarcq, E. Flurin, F. Mallet, and B. Huard, "Quantum dynamics of an electromagnetic mode that cannot contain n photons," *to be published in Science*. (Cited on pages 41, 42, 143, and 172.)

[84] J. M. Martinis, K. Cooper, R. McDermott, M. Steffen, M. Ansmann, K. Osborn, K. Cicak, S. Oh, D. Pappas, R. Simmonds, *et al.*, "Decoherence in Josephson qubits from dielectric loss," *Physical Review Letters*, vol. 95, no. 21, p. 210503, 2005. (Cited on page 40.)

[85] J. M. Martinis and a. Megrant, "UCSB final report for the CSQ program: Review of decoherence and materials physics for superconducting qubits," p. 10, Oct. 2014. (Cited on page 40.)

[86] J. M. Martinis, M. Ansmann, and J. Aumentado, "Energy decay in superconducting Josephson-junction qubits from nonequilibrium quasiparticle excitations," *Physical review letters*, vol. 103, no. 9, p. 097002, 2009. (Cited on page 40.)

[87] M. Lenander, H. Wang, R. C. Bialczak, E. Lucero, M. Mariantoni, M. Neeley, A. O'Connell, D. Sank, M. Weides, J. Wenner, *et al.*, "Measurement of energy decay in superconducting qubits from nonequilibrium quasiparticles," *Physical Review B*, vol. 84, no. 2, p. 024501, 2011. (Cited on page 40.)

[88] C. Wang, Y. Y. Gao, I. M. Pop, U. Vool, C. Axline, T. Brecht, R. W. Heeres, L. Frunzio, M. H. Devoret, G. Catelani, *et al.*, "Measurement and control of quasiparticle dynamics in a superconducting qubit," *Nature communications*, vol. 5, 2014. (Cited on pages 40 and 172.)

[89] J. Wenner, Y. Yin, E. Lucero, R. Barends, Y. Chen, B. Chiaro, J. Kelly, M. Lenander, M. Mariantoni, A. Megrant, *et al.*, "Excitation of superconducting qubits from hot nonequilibrium quasiparticles," *Physical review letters*, vol. 110, no. 15, p. 150502, 2013. (Cited on page 40.)

[90] W. Gerlach and O. Stern, "Der experimentelle nachweis der richtungsquantelung im magnetfeld," *Zeitschrift für Physik A Hadrons and Nuclei*, vol. 9, no. 1, pp. 349–352, 1922. (Cited on pages 45 and 46.)

[91] W. H. Zurek, "Decoherence, einselection, and the quantum origins of the classical," *Reviews of Modern Physics*, vol. 75, no. 3, p. 715, 2003. (Cited on page 45.)

[92] K. Murch, S. Weber, C. Macklin, and I. Siddiqi, "Observing single quantum trajectories of a superconducting quantum bit," *Nature*, vol. 502, no. 7470, pp. 211–214, 2013. (Cited on pages 47 and 55.)

[93] M. Hatridge, S. Shankar, M. Mirrahimi, F. Schackert, K. Geerlings, T. Brecht, K. Sliwa, B. Abdo, L. Frunzio, S. M. Girvin, *et al.*, "Quantum back-action of an individual variable-strength measurement," *Science*, vol. 339, no. 6116, pp. 178–181, 2013. (Cited on pages 47 and 55.)

[94] D. Steck, *Quantum and atoms optics*. Oregon Center for Optics and Department of Physics, University of Oregon, 2007. (Cited on pages 47 and 189.)

[95] B. Johnson, M. Reed, A. Houck, D. Schuster, L. S. Bishop, E. Ginossar, J. Gambetta, L. DiCarlo, L. Frunzio, S. Girvin, *et al.*, "Quantum non-demolition detection of single microwave photons in a circuit," *Nature Physics*, vol. 6, no. 9, pp. 663–667, 2010. (Cited on page 49.)

[96] C. Deng, J. Gambetta, and A. Lupaşcu, "Quantum nondemolition measurement of microwave photons using engineered quadratic interactions," *Physical Review B*, vol. 82, no. 22, p. 220505, 2010. (Cited on page 49.)

[97] B. Peropadre, G. Romero, G. Johansson, C. Wilson, E. Solano, and J. J. García-Ripoll, "Approaching perfect microwave photodetection in circuit QED," *Physical Review A*, vol. 84, no. 6, p. 063834, 2011. (Cited on page 49.)

[98] W. K. Wootters and W. H. Zurek, "A single quantum cannot be cloned," 1982. (Cited on page 50.)

[99] M. Castellanos-Beltran and K. Lehnert, "Widely tunable parametric amplifier based on a superconducting quantum interference device array resonator," *Applied Physics Letters*, vol. 91, no. 8, p. 083509, 2007. (Cited on page 51.)

[100] M. Hatridge, R. Vijay, D. Slichter, J. Clarke, and I. Siddiqi, "Dispersive magnetometry with a quantum limited squid parametric amplifier," *Physical Review B*, vol. 83, no. 13, p. 134501, 2011. (Cited on page 51.)

[101] J. Mutus, T. White, E. Jeffrey, D. Sank, R. Barends, J. Bochmann, Y. Chen, Z. Chen, B. Chiaro, A. Dunsworth, *et al.*, "Design and characterization of a lumped element single-ended superconducting microwave parametric amplifier with on-chip flux bias line," *Applied Physics Letters*, vol. 103, no. 12, p. 122602, 2013. (Cited on page 51.)

[102] E. A. Tholen, A. Ergül, E. M. Doherty, F. M. Weber, F. Grégis, and D. B. Haviland, "Nonlinearities and parametric amplification in superconducting coplanar waveguide resonators," *Applied physics letters*, vol. 90, no. 25, p. 253509, 2007. (Cited on page 51.)

[103] D. Kinion and J. Clarke, "Microstrip superconducting quantum interference device radio-frequency amplifier: Scattering parameters and input coupling," *Applied Physics Letters*, vol. 92, no. 17, p. 172503, 2008. (Cited on page 51.)

[104] M. Castellanos-Beltran, K. Irwin, G. Hilton, L. Vale, and K. Lehnert, "Amplification and squeezing of quantum noise with a tunable Josephson metamaterial," *Nature Physics*, vol. 4, no. 12, pp. 929–931, 2008. (Cited on page 51.)

[105] A. Kamal, A. Marblestone, and M. Devoret, "Signal-to-pump back action and self-oscillation in double-pump Josephson parametric amplifier," *Physical Review B*, vol. 79, no. 18, p. 184301, 2009. (Cited on page 51.)

[106] L. Spietz, K. Irwin, M. Lee, and J. Aumentado, "Noise performance of lumped element direct current superconducting quantum interference device amplifiers in the 4–8 ghz range," *Applied Physics Letters*, vol. 97, no. 14, p. 142502, 2010. (Cited on page 51.)

[107] D. Hover, Y.-F. Chen, G. Ribeill, S. Zhu, S. Sendelbach, and R. McDermott, "Superconducting low-inductance undulatory galvanometer microwave amplifier," *Applied Physics Letters*, vol. 100, no. 6, p. 063503, 2012. (Cited on page 51.)

[108] B. H. Eom, P. K. Day, H. G. LeDuc, and J. Zmuidzinas, "A wideband, low-noise superconducting amplifier with high dynamic range," *Nature Physics*, vol. 8, no. 8, pp. 623–627, 2012. (Cited on page 51.)

[109] C. Bockstiegel, J. Gao, M. Vissers, M. Sandberg, S. Chaudhuri, A. Sanders, L. Vale, K. Irwin, and D. Pappas, "Development of a broadband NbTiN traveling wave parametric amplifier for mkid readout," *Journal of Low Temperature Physics*, vol. 176, no. 3-4, pp. 476–482, 2014. (Cited on page 51.)

[110] J. Mutus, T. White, R. Barends, Y. Chen, Z. Chen, B. Chiaro, A. Dunsworth, E. Jeffrey, J. Kelly, A. Megrant, *et al.*, "Strong environmental coupling in a Josephson parametric amplifier," *Applied Physics Letters*, vol. 104, no. 26, p. 263513, 2014. (Cited on page 51.)

[111] L. Zhong, E. Menzel, R. Di Candia, P. Eder, M. Ihmig, A. Baust, M. Haeberlein, E. Hoffmann, K. Inomata, T. Yamamoto, *et al.*, "Squeezing with a flux-driven Josephson parametric amplifier," *New Journal of Physics*, vol. 15, no. 12, p. 125013, 2013. (Cited on page 51.)

[112] C. Eichler, Y. Salathe, J. Mlynek, S. Schmidt, and A. Wallraff, "Quantum-limited amplification and entanglement in coupled nonlinear resonators," *Physical review letters*, vol. 113, no. 11, p. 110502, 2014. (Cited on page 51.)

[113] A. Narla, K. Sliwa, M. Hatridge, S. Shankar, L. Frunzio, R. Schoelkopf, and M. Devoret, "Wireless Josephson amplifier," *Applied Physics Letters*, vol. 104, no. 23, p. 232605, 2014. (Cited on page 51.)

[114] X. Zhou, V. Schmitt, P. Bertet, D. Vion, W. Wustmann, V. Shumeiko, and D. Esteve, "High-gain weakly nonlinear flux-modulated Josephson parametric amplifier using a squid array," *Physical Review B*, vol. 89, no. 21, p. 214517, 2014. (Cited on page 51.)

[115] J. Gambetta, A. Blais, M. Boissonneault, A. Houck, D. Schuster, and S. Girvin, "Quantum trajectory approach to circuit QED: Quantum jumps and the Zeno effect," *Physical Review A*, vol. 77, no. 1, p. 012112, 2008. (Cited on pages 53, 135, 142, 146, and 187.)

[116] G. De Lange, D. Riste, M. Tiggelman, C. Eichler, L. Tornberg, G. Johansson, A. Wallraff, R. Schouten, and L. DiCarlo, "Reversing quantum trajectories with analog feedback," *Physical Review Letters*, vol. 112, no. 8, p. 080501, 2014. (Cited on pages 55 and 139.)

[117] C. M. Caves, J. Combes, Z. Jiang, and S. Pandey, "Quantum limits on phase-preserving linear amplifiers," *Physical Review A*, vol. 86, p. 063802, Dec. 2012. (Cited on page 55.)

[118] A. N. Korotkov, "Quantum bayesian approach to circuit QED measurement," *Les Houches, Session XCVI*, 2011. (Cited on page 55.)

[119] B. Abdo, F. Schackert, M. Hatridge, C. Rigetti, and M. Devoret, "Josephson amplifier for qubit readout," *Applied Physics Letters*, vol. 99, no. 16, p. 162506, 2011. (Cited on page 55.)

[120] E. Flurin, *The Josephson mixer, a Swiss army knife for microwave quantum optics*. PhD thesis, Ecole Normale Superieure, 2014. (Cited on pages 55 and 173.)

[121] E. Flurin, N. Roch, F. Mallet, M. H. Devoret, and B. Huard, "Generating entangled microwave radiation over two transmission lines," *Physical review letters*, vol. 109, no. 18, p. 183901, 2012. (Cited on page 55.)

[122] M. Reed, L. DiCarlo, B. Johnson, L. Sun, D. Schuster, L. Frunzio, and R. Schoelkopf, "High-fidelity readout in circuit quantum electrodynamics using the Jaynes-Cummings nonlinearity," *Physical review letters*, vol. 105, no. 17, p. 173601, 2010. (Cited on page 60.)

[123] L. S. Bishop, E. Ginossar, and S. Girvin, "Response of the strongly driven Jaynes-Cummings oscillator," *Physical review letters*, vol. 105, no. 10, p. 100505, 2010. (Cited on page 60.)

[124] P. Carbonaro, G. Compagno, and F. Persico, "Canonical dressing of atoms by intense radiation fields," *Physics Letters A*, vol. 73, no. 2, pp. 97 – 99, 1979. (Cited on page 60.)

[125] G. Kirchmair, B. Vlastakis, Z. Leghtas, S. E. Nigg, H. Paik, E. Ginossar, M. Mirrahimi, L. Frunzio, S. M. Girvin, and R. J. Schoelkopf, "Observation of quantum state collapse and revival due to the single-photon Kerr effect," *Nature*, vol. 495, no. 7440, pp. 205–209, 2013. (Cited on pages 62, 136, 147, 150, 156, 159, and 160.)

[126] I. M. Pop, K. Geerlings, G. Catelani, R. J. Schoelkopf, L. I. Glazman, and M. H. Devoret, "Coherent suppression of electromagnetic dissipation due to superconducting quasiparticles," *Nature*, vol. 508, no. 7496, pp. 369–372, 2014. (Cited on page 62.)

[127] I. Nsanzineza and B. Plourde, "Trapping a single vortex and reducing quasiparticles in a superconducting resonator," *Physical review letters*, vol. 113, no. 11, p. 117002, 2014. (Cited on page 62.)

[128] U. Vool, I. M. Pop, K. Sliwa, B. Abdo, C. Wang, T. Brecht, Y. Y. Gao, S. Shankar, M. Hatridge, G. Catelani, *et al.*, "Non-poissonian quantum jumps of a fluxonium qubit due to quasiparticle excitations," *Physical review letters*, vol. 113, no. 24, p. 247001, 2014. (Cited on pages 62 and 69.)

[129] B. Mollow, "Power Spectrum of Light Scattered by Two-Level Systems," *Physical Review*, vol. 188, pp. 1969–1975, Dec. 1969. (Cited on page 64.)

[130] A. Abdumalikov Jr, O. Astafiev, Y. A. Pashkin, Y. Nakamura, and J. Tsai, "Dynamics of coherent and incoherent emission from an artificial atom in a 1D space," *Physical review letters*, vol. 107, no. 4, p. 043604, 2011. (Cited on page 64.)

[131] H. Amini, M. Mirrahimi, and P. Rouchon, "On stability of continuous-time quantum filters," in *Decision and Control and European Control Conference (CDC-ECC), 2011 50th IEEE Conference on*, pp. 6242–6247, IEEE, 2011. (Cited on pages 68 and 73.)

[132] P. Rouchon and J. F. Ralph, "Efficient quantum filtering for quantum feedback control," *arXiv preprint arXiv:1410.5345*, 2014. (Cited on pages 68 and 74.)

[133] D. Ristè, C. Bultink, M. Tiggelman, R. Schouten, K. Lehnert, and L. DiCarlo, "Millisecond charge-parity fluctuations and induced decoherence in a superconducting transmon qubit," *Nature communications*, vol. 4, p. 1913, 2013. (Cited on page 69.)

[134] K. W. Murch, S. J. Weber, C. Macklin, and I. Siddiqi, "Observing single quantum trajectories of a superconducting quantum bit.," *Nature*, vol. 502, pp. 211–4, Oct. 2013. (Cited on page 69.)

[135] P. Six, P. Campagne-Ibarcq, L. Bretheau, B. Huard, and P. Rouchon, "Parameter estimation from measurements along quantum trajectories," *arXiv preprint arXiv:1503.06149*, 2015. (Cited on page 75.)

[136] J. Gambetta and H. M. Wiseman, "State and dynamical parameter estimation for open quantum systems," *Physical Review A*, vol. 64, no. 4, p. 042105, 2001. (Cited on page 75.)

[137] B. A. Chase and J. Geremia, "Single-shot parameter estimation via continuous quantum measurement," *Physical Review A*, vol. 79, no. 2, p. 022314, 2009. (Cited on page 75.)

[138] Y. Aharonov, A. Botero, S. Popescu, B. Reznik, and J. Tollaksen, "Revisiting Hardy's paradox: counterfactual statements, real measurements, entanglement and weak values," *Physics Letters A*, vol. 301, no. 3, pp. 130–138, 2002. (Cited on page 81.)

[139] N. Ritchie, J. Story, and R. G. Hulet, "Realization of a measurement of a weak value," *Physical review letters*, vol. 66, no. 9, p. 1107, 1991. (Cited on page 81.)

[140] N. Williams and A. Jordan, "Weak Values and the Leggett-Garg Inequality in Solid-State Qubits," *Physical Review Letters*, vol. 100, p. 026804, Jan. 2008. (Cited on pages 81 and 94.)

[141] A. Palacios-Laloy, F. Mallet, F. Nguyen, P. Bertet, D. Vion, D. Esteve, and A. N. Korotkov, "Experimental violation of a Bell/'s inequality in time with weak measurement," *Nature Physics*, vol. 6, no. 6, pp. 442–447, 2010. (Cited on pages 81, 94, and 141.)

[142] J. Groen, D. Riste, L. Tornberg, J. Cramer, P. C. De Groot, T. Picot, G. Johansson, and L. DiCarlo, "Partial-measurement backaction and nonclassical weak values in a superconducting circuit," *Physical review letters*, vol. 111, no. 9, p. 090506, 2013. (Cited on pages 81 and 94.)

[143] T. White, J. Mutus, J. Dressel, J. Kelly, R. Barends, E. Jeffrey, D. Sank, A. Megrant, B. CampBell, Y. Chen, *et al.*, "Violating the Bell-Leggett-Garg inequality with weak measurement of an entangled state," *arXiv preprint arXiv:1504.02707*, 2015. (Cited on page 81.)

[144] J. Dressel, M. Malik, F. M. Miatto, A. N. Jordan, and R. W. Boyd, "Colloquium: Understanding quantum weak values: Basics and applications," *Reviews of Modern Physics*, vol. 86, no. 1, p. 307, 2014. (Cited on pages 81 and 88.)

[145] O. Hosten and P. Kwiat, "Observation of the spin hall effect of light via weak measurements," *Science*, vol. 319, no. 5864, pp. 787–790, 2008. (Cited on pages 81 and 95.)

[146] P. B. Dixon, D. J. Starling, A. N. Jordan, and J. C. Howell, "Ultrasensitive beam deflection measurement via interferometric weak value amplification," *Physical review letters*, vol. 102, no. 17, p. 173601, 2009. (Cited on pages 81 and 95.)

[147] J. S. Lundeen, B. Sutherland, A. Patel, C. Stewart, and C. Bamber, "Direct measurement of the quantum wavefunction," *Nature*, vol. 474, no. 7350, pp. 188–191, 2011. (Cited on pages 81 and 94.)

[148] Y. Aharonov and L. Vaidman, "The two-state vector formalism of qauntum mechanics: an updated review," *arXiv preprint quant-ph/0105101*, 2001. (Cited on page 81.)

[149] G. C. Knee, G. A. D. Briggs, S. C. Benjamin, and E. M. Gauger, "Quantum sensors based on weak-value amplification cannot overcome decoherence," *Physical Review A*, vol. 87, no. 1, p. 012115, 2013. (Cited on page 81.)

[150] C. Ferrie and J. Combes, "Weak value amplification is suboptimal for estimation and detection," *Physical review letters*, vol. 112, no. 4, p. 040406, 2014. (Cited on pages 81 and 95.)

[151] S. Tanaka and N. Yamamoto, "Information amplification via postselection: A parameter-estimation perspective," *Physical Review A*, vol. 88, no. 4, p. 042116, 2013. (Cited on page 81.)

[152] W. H. Press, *Numerical recipes 3rd edition: The art of scientific computing*. Cambridge university press, 2007. (Cited on page 81.)

[153] A. Barchielli and M. Gregoratti, *Quantum Trajectories and Measurements in ContinuousTime: the Diffusive Case*. Springer Verlag, 2009. (Cited on page 87.)

[154] D. Tan, S. Weber, I. Siddiqi, K. Mølmer, and K. Murch, "Prediction and retrodiction for a continuously monitored superconducting qubit," *arXiv preprint arXiv:1409.0510*, 2014. (Cited on page 88.)

[155] H. M. Chrzanowski, N. Walk, S. M. Assad, J. Janousek, S. Hosseini, T. C. Ralph, T. Symul, and P. K. Lam, "Measurement-based noiseless linear amplification for quantum communication," *Nature Photonics*, vol. 8, no. 4, pp. 333–338, 2014. (Cited on page 95.)

[156] S. Weber, A. Chantasri, J. Dressel, A. Jordan, K. Murch, and I. Siddiqi, "Mapping the optimal route between two quantum states," *Nature*, vol. 511, no. 7511, pp. 570–573, 2014. (Cited on page 99.)

[157] T. Rybarczyk, S. Gerlich, B. Peaudecerf, M. Penasa, B. Julsgaard, K. Moelmer, S. Gleyzes, M. Brune, J.-M. Raimond, S. Haroche, *et al.*, "Past quantum state analysis of the photon number evolution in a cavity," *arXiv preprint arXiv:1409.0958*, 2014. (Cited on page 99.)

[158] A. H. Kiilerich and K. Mølmer, "Estimation of atomic interaction parameters by photon counting," *Physical Review A*, vol. 89, no. 5, p. 052110, 2014. (Cited on page 100.)

[159] J. P. Pekola, "Towards quantum thermodynamics in electronic circuits," *Nature Physics*, vol. 11, no. 2, pp. 118–123, 2015. (Cited on page 100.)

[160] H. Mabuchi, "Coherent-feedback quantum control with a dynamic compensator," *Physical Review A*, vol. 78, no. 3, p. 032323, 2008. (Cited on page 105.)

[161] P. Facchi and S. Pascazio, "Quantum Zeno subspaces," *Physical review letters*, vol. 89, no. 8, p. 080401, 2002. (Cited on page 105.)

[162] S. O. Valenzuela, W. D. Oliver, D. M. Berns, K. K. Berggren, L. S. Levitov, and T. P. Orlando, "Microwave-induced cooling of a superconducting qubit," *Science*, vol. 314, no. 5805, pp. 1589–1592, 2006. (Cited on pages 111 and 129.)

[163] M. Grajcar, S. Van der Ploeg, A. Izmalkov, E. Il'ichev, H.-G. Meyer, A. Fedorov, A. Shnirman, and G. Schön, "Sisyphus cooling and amplification by a superconducting qubit," *Nature physics*, vol. 4, no. 8, pp. 612–616, 2008. (Cited on pages 111 and 129.)

[164] M. Mariantoni, H. Wang, T. Yamamoto, M. Neeley, R. C. Bialczak, Y. Chen, M. Lenander, E. Lucero, A. O'Connell, D. Sank, *et al.*, "Implementing the quantum von Neumann architecture with superconducting circuits," *Science*, vol. 334, no. 6052, pp. 61–65, 2011. (Cited on pages 111 and 129.)

[165] J. Johnson, C. Macklin, D. Slichter, R. Vijay, E. Weingarten, J. Clarke, and I. Siddiqi, "Heralded state preparation in a superconducting qubit," *Physical review letters*, vol. 109, no. 5, p. 050506, 2012. (Cited on pages 111 and 129.)

[166] D. Riste, J. Van Leeuwen, H.-S. Ku, K. Lehnert, and L. DiCarlo, "Initialization by measurement of a superconducting quantum bit circuit," *Physical review letters*, vol. 109, no. 5, p. 050507, 2012. (Cited on pages 111 and 129.)

[167] A. N. Jordan and M. Büttiker, "Quantum nondemolition measurement of a kicked qubit," *Physical Review B*, vol. 71, no. 12, p. 125333, 2005. (Cited on page 114.)

[168] A. Palacios-laloy, F. Mallet, F. Nguyen, P. Bertet, D. Vion, D. Esteve, and A. N. Korotkov, "Experimental violation of a Bell s inequality in time with weak measurement," *Nature Physics*, vol. 6, no. 6, pp. 442–447, 2010. (Cited on page 114.)

[169] M. Mirrahimi, B. Huard, M. Devoret, *et al.*, "Strong measurement and quantum feedback for persistent rabi oscillations in circuit QED experiments.," in *CDC*, pp. 3646–3651, 2012. (Cited on page 114.)

[170] H. M. Wiseman, S. Mancini, and J. Wang, "Bayesian feedback versus markovian feedback in a two-level atom," *Physical Review A*, vol. 66, no. 1, p. 013807, 2002. (Cited on pages 118 and 127.)

[171] H. Hofmann, G. Mahler, and O. Hess, "Quantum control of atomic systems by homodyne detection and feedback," *Physical Review A*, vol. 57, no. 6, pp. 4877–4888, 1998. (Cited on page 118.)

[172] J. Wang and H. M. Wiseman, "Feedback-stabilization of an arbitrary pure state of a two-level atom," *Physical Review A*, vol. 64, no. 6, p. 063810, 2001. (Cited on page 118.)

[173] A. Blais, J. Gambetta, A. Wallraff, D. Schuster, S. Girvin, M. Devoret, and R. Schoelkopf, "Quantum-information processing with circuit quantum electrodynamics," *Physical Review A*, vol. 75, no. 3, p. 032329, 2007. (Cited on page 125.)

[174] S. Lloyd, "Coherent quantum feedback," *Physical Review A*, vol. 62, no. 2, p. 022108, 2000. (Cited on page 129.)

[175] H. Nyquist, "Thermal agitation of electric charge in conductors," *Physical review*, vol. 32, no. 1, pp. 110–113, 1928. (Cited on page 131.)

[176] L. Szilard, "Über die entropieverminderung in einem thermodynamischen system bei eingriffen intelligenter wesen," *Zeitschrift für Physik*, vol. 53, no. 11-12, pp. 840–856, 1929. (Cited on page 137.)

[177] R. Hamerly and H. Mabuchi, "Advantages of coherent feedback for cooling quantum oscillators," *Physical review letters*, vol. 109, no. 17, p. 173602, 2012. (Cited on page 140.)

[178] Z. Leghtas, U. Vool, S. Shankar, M. Hatridge, S. M. Girvin, M. H. Devoret, and M. Mirrahimi, "Stabilizing a Bell state of two superconducting qubits by dissipation engineering," *Physical Review A*, vol. 88, no. 2, p. 023849, 2013. (Cited on pages 140 and 161.)

[179] S. Shankar, M. Hatridge, Z. Leghtas, K. Sliwa, A. Narla, U. Vool, S. M. Girvin, L. Frunzio, M. Mirrahimi, and M. H. Devoret, "Autonomously stabilized entanglement between two superconducting quantum bits," *Nature*, vol. 504, no. 7480, pp. 419–422, 2013. (Cited on pages 140 and 161.)

[180] Y. Lin, J. Gaebler, F. Reiter, T. R. Tan, R. Bowler, A. Sørensen, D. Leibfried, and D. Wineland, "Dissipative production of a maximally entangled steady state of two quantum bits," *Nature*, vol. 504, no. 7480, pp. 415–418, 2013. (Cited on pages 140 and 161.)

[181] Z. Leghtas, S. Touzard, I. M. Pop, A. Kou, B. Vlastakis, A. Petrenko, K. M. Sliwa, A. Narla, S. Shankar, M. J. Hatridge, *et al.*, "Confining the state of light to a quantum manifold by engineered two-photon loss," *arXiv preprint arXiv:1412.4633*, 2014. (Cited on pages 140 and 142.)

[182] R. Ruskov and A. N. Korotkov, "Entanglement of solid-state qubits by measurement," *Physical Review B*, vol. 67, no. 24, p. 241305, 2003. (Cited on pages 140 and 161.)

[183] N. Roch, M. E. Schwartz, F. Motzoi, C. Macklin, R. Vijay, A. W. Eddins, A. N. Korotkov, K. B. Whaley, M. Sarovar, and I. Siddiqi, "Observation of measurement-induced entanglement and quantum trajectories of remote superconducting qubits," *Physical review letters*, vol. 112, no. 17, p. 170501, 2014. (Cited on pages 140 and 161.)

[184] D. Riste, M. Dukalski, C. Watson, G. de Lange, M. Tiggelman, Y. M. Blanter, K. Lehnert, R. Schouten, and L. DiCarlo, "Deterministic entanglement of superconducting qubits by parity measurement and feedback," *Nature*, vol. 502, no. 7471, pp. 350–354, 2013. (Cited on pages 140 and 161.)

[185] W. M. Itano, D. J. Heinzen, J. Bollinger, and D. Wineland, "Quantum Zeno effect," *Physical Review A*, vol. 41, no. 5, p. 2295, 1990. (Cited on page 141.)

[186] C. Balzer, R. Huesmann, W. Neuhauser, and P. Toschek, "The quantum Zeno effect–evolution of an atom impeded by measurement," *Optics Communications*, vol. 180, no. 1, pp. 115–120, 2000. (Cited on page 141.)

[187] J. Bernu, S. Deléglise, C. Sayrin, S. Kuhr, I. Dotsenko, M. Brune, J.-M. Raimond, and S. Haroche, "Freezing coherent field growth in a cavity by the quantum Zeno effect," *Physical review letters*, vol. 101, no. 18, p. 180402, 2008. (Cited on page 141.)

[188] J. Gambetta, A. Blais, D. Schuster, A. Wallraff, L. Frunzio, J. Majer, M. Devoret, S. Girvin, and R. Schoelkopf, "Qubit-photon interactions in a cavity: Measurement-induced dephasing and number splitting," *Physical Review A*, vol. 74, p. 042318, Oct. 2006. (Cited on page 146.)

[189] F. Motzoi, J. Gambetta, P. Rebentrost, and F. K. Wilhelm, "Simple pulses for elimination of leakage in weakly nonlinear qubits," *Physical review letters*, vol. 103, no. 11, p. 110501, 2009. (Cited on page 147.)

[190] J. Chow, L. DiCarlo, J. Gambetta, F. Motzoi, L. Frunzio, S. Girvin, and R. Schoelkopf, "Optimized driving of superconducting artificial atoms for improved single-qubit gates," *Physical Review A*, vol. 82, no. 4, p. 040305, 2010. (Cited on page 147.)

[191] J. Johansson, P. Nation, and F. Nori, "Qutip 2: A python framework for the dynamics of open quantum systems," *Computer Physics Communications*, vol. 184, no. 4, pp. 1234–1240, 2013. (Cited on page 153.)

[192] W. P. Schleich, *Quantum optics in phase space*. John Wiley & Sons, 2011. (Cited on page 153.)

[193] L. Lutterbach and L. Davidovich, "Method for direct measurement of the wigner function in cavity QED and ion traps," *Physical review letters*, vol. 78, no. 13, p. 2547, 1997. (Cited on page 153.)

[194] P. Bertet, A. Auffeves, P. Maioli, S. Osnaghi, T. Meunier, M. Brune, J.-M. Raimond, and S. Haroche, "Direct measurement of the wigner function of a one-photon fock state in a cavity," *Physical Review Letters*, vol. 89, no. 20, p. 200402, 2002. (Cited on page 153.)

[195] B. Vlastakis, G. Kirchmair, Z. Leghtas, S. E. Nigg, L. Frunzio, S. M. Girvin, M. Mirrahimi, M. H. Devoret, and R. J. Schoelkopf, "Deterministically encoding quantum information using 100-photon Schrödinger cat states," *Science*, vol. 342, no. 6158, pp. 607–610, 2013. (Cited on pages 153 and 156.)

[196] B. Yurke and D. Stoler, "The dynamic generation of Schrödinger cats and their detection," *Physica B+ C*, vol. 151, no. 1, pp. 298–301, 1988. (Cited on page 160.)

[197] S. Maniscalco, F. Francica, R. L. Zaffino, N. L. Gullo, and F. Plastina, "Protecting entanglement via the quantum Zeno effect," *Physical review letters*, vol. 100, no. 9, p. 090503, 2008. (Cited on page 160.)

[198] X.-B. Wang, J. You, and F. Nori, "Quantum entanglement via two-qubit quantum Zeno dynamics," *Physical Review A*, vol. 77, no. 6, p. 062339, 2008. (Cited on page 160.)

[199] Z. Shi, Y. Xia, H. Wu, and J. Song, "One-step preparation of three-particle Greenberger-Horne-Zeilinger state via quantum Zeno dynamics," *The European Physical Journal D-Atomic, Molecular, Optical and Plasma Physics*, vol. 66, no. 5, pp. 1–6, 2012. (Cited on page 160.)

[200] X.-Q. Shao, L. Chen, S. Zhang, and K.-H. Yeon, "Fast CNOT gate via quantum Zeno dynamics," *Journal of Physics B: Atomic, Molecular and Optical Physics*, vol. 42, no. 16, p. 165507, 2009. (Cited on page 160.)

[201] M. Mirrahimi, Z. Leghtas, V. V. Albert, S. Touzard, R. J. Schoelkopf, L. Jiang, and M. H. Devoret, "Dynamically protected cat-qubits: a new paradigm for universal quantum computation," *New Journal of Physics*, vol. 16, no. 4, p. 045014, 2014. (Cited on page 161.)

[202] M. Reed, L. DiCarlo, S. Nigg, L. Sun, L. Frunzio, S. Girvin, and R. Schoelkopf, "Realization of three-qubit quantum error correction with superconducting circuits," *Nature*, vol. 482, no. 7385, pp. 382–385, 2012. (Cited on page 161.)

[203] L. Sun, A. Petrenko, Z. Leghtas, B. Vlastakis, G. Kirchmair, K. Sliwa, A. Narla, M. Hatridge, S. Shankar, J. Blumoff, *et al.*, "Tracking photon jumps with repeated quantum non-demolition parity measurements," *Nature*, vol. 511, no. 7510, pp. 444–448, 2014. (Cited on page 161.)

[204] D. Ristè, S. Poletto, M.-Z. Huang, A. Bruno, V. Vesterinen, O.-P. Saira, and L. DiCarlo, "Detecting bit-flip errors in a logical qubit using stabilizer measurements," *arXiv preprint arXiv:1411.5542*, 2014. (Cited on page 161.)

[205] J. Kelly, R. Barends, A. Fowler, A. Megrant, E. Jeffrey, T. White, D. Sank, J. Mutus, B. CampBell, Y. Chen, *et al.*, "State preservation by repetitive error detection in a superconducting quantum circuit," *arXiv preprint arXiv:1411.7403*, 2014. (Cited on page 161.)

[206] R. Barends, J. Wenner, M. Lenander, Y. Chen, R. Bialczak, J. Kelly, E. Lucero, P. O'Malley, M. Mariantoni, D. Sank, *et al.*, "Minimizing quasiparticle generation from stray infrared light in superconducting quantum circuits," *Applied Physics Letters*, vol. 99, no. 11, p. 113507, 2011. (Cited on page 170.)

[207] P. Campagne-Ibarcq, E. Flurin, N. Roch, D. Darson, P. Morfin, M. Mirrahimi, M. H. Devoret, F. Mallet, and B. Huard, "Persistent control of a superconducting qubit by stroboscopic measurement feedback," *Physical Review X*, vol. 3, no. 2, p. 021008, 2013. (Cited on page 172.)